UNIVERSITY OF SZEGED

Faculty of Science and Informatics
Doctoral School of Geosciences
Department of Geoinformatics, Physical and Environmental Geography

A multi-scale investigation of sediment and plastic pollution transport in the Tisza River applying remote sensing and machine learning: A hydrological perspective

Ph.D. Dissertation

Ahmed Mohsen Abdelsadek Metwaly

Supervisors:

Dr. Tímea Kiss

Dr. Ferenc Kovács

Szeged

2024

TABLE OF CONTENTS

1. INTRODUCTION

Plastic pollution is one of the growing environmental challenges in terrestrial and aquatic ecosystems. Rivers play a significant role in connecting land-based plastic pollution sources to oceans since riverine plastic transport is responsible for 80% of the marine annual plastic input (14 million tons) (Jakovljević et al., 2019; Zhang et al., 2020). However, rivers not only serve as conveyor belts, but also as reservoirs, as plastic debris [including microplastics (MP) and macroplastics (MaP)] can be trapped by vegetation on floodplains or accumulate within the river channel. The variability of the river`s role as a conduit or reservoir is influenced by several interfering hydrological, meteorological, and morphological factors (Van Emmerik et al., 2018). Although many studies have recently attempted to investigate these factors for MP (Zhang et al., 2020; Kiss et al., 2021; Balla et al., 2022) and MaP (Crosti et al., 2018; Van Emmerik et al., 2018; Van Emmerik and Schwarz, 2020), there are still many conflicting findings and unsolved questions.

Plastic debris and natural sediment have similar transport mechanisms in rivers since they are transported as bedload and suspended load, and the particles are vertically stratified according to their size and density (Cowger et al., 2021). Furthermore, they often aggregate with organic materials, organisms, and metal oxides during transport (Yan et al., 2021). Despite these similarities, most studies investigated their transport individually. However, if their transport correlation is well-explored, it is possible to transfer many concepts and theories from the long-studied hydrology and sediment transport into the plastic transport field.

Though the general aim of the dissertation is to investigate both MP and MaP pollution transport, the focus is on the MP concentration in water and its relationship with suspended sediment concentration (SSC). Some studies (Piehl et al., 2020; Buwono et al., 2021; Chen et al., 2021) investigated this correlation but with limitations in terms of spatial scales (e.g., snapshot measurements at limited sites) and temporal resolution (e.g., not repeated or monthly measurements), thus, they reached conflicting findings. This refers to the complexity of their correlation at the multi-scale level, which may arise from the differences in their densities, sources, shapes as well as fragmentation, and degradation rates (Waldschläger et al., 2022).

The spatiotemporal distribution of SS and MP concentrations in rivers is influenced by various processes operating at multiple scales (Fryirs, 2013). While SS has both natural (e.g., soil erosion in the catchment and/or river channel, landslides, and surface runoff) and anthropogenic (e.g., road construction, mining activities, and channel dredging) origins, MP has only an anthropogenic origin [e.g., landfills, wastewater treatment plants (WWTPs) and industrial effluents] since it is a synthetic polymer (Vercruysse et al., 2017; Kiss et al., 2021). Once SS and MP are produced, their spatiotemporal distribution is influenced by the topographical features, land use patterns, climatic conditions, and river hydrodynamics of the sub-catchments (Fryirs, 2013). Although SS and MP share the same transporting process from the catchment into the river channel, their spatial and temporal distributions could be affected by different factors (Vercruysse et al., 2017). For instance, the location and timing of mining activities, landslides, and riverbank erosion could influence the spatiotemporal distribution of SS without any impact on MPs. Conversely, the locations and discharges of WWTP and industrial effluents have an adverse effect

(Vercruysse et al., 2017). Given the complexity of factors affecting the spatiotemporal distribution and correlation of SS and MP concentrations, intensive spatiotemporal measurements are warranted.

In the meantime, the situation is more complicated at confluences and in reservoirs upstream dams (Ahmed et al., 2016; Serra et al., 2022). At tributaries the SS and MP concentrations can experience sudden increase (Balla et al., 2022) or dilution (Barrows et al., 2018) in the mainstream depending on the sediment and plastic yield of the tributary. However, it is important to note that they are not necessarily having the same influence simultaneously. For instance, a tributary with a high sediment load could only yield high plastics if it is accompanied by inadequate waste management practices at the sub-catchment (Ahmed et al., 2016). To our knowledge, no study has compared the influence of tributaries on the transport of SS and MP in the mainstream.

Specifically focusing on a confluence zone, the SS and MP transport is influenced by intricate hydrodynamic processes (Park and Latrubesse, 2015). These processes resulted in various water mixing patterns with spatiotemporal dynamism governed by the hydrological characteristics of the joining rivers and the geometrical settings of the confluence (e.g., bed discordance and confluence angle). Hence, the SS and MP concentration measurements should be conducted only after defining the actual mixing condition to avoid misleading findings. Although some studies (Park and Latrubesse, 2015; Marinho et al., 2018) had investigated the spatiotemporal mixing patterns in confluences, their investigations were limited to short durations (e.g., 1–3 years). Besides, to my knowledge, no study has considered the connection between hydrological parameters of the joining rivers (e.g., water stage, water slope, and discharge) and the spatiotemporal dynamics of water mixing patterns.

On the other hand, dams disconnect the longitudinal profile of sediment transport (Watkins et al., 2019; Serra et al., 2022). Particularly, a considerable amount of sediment tends to deposit upstream of a dam due to its impoundment effect and reduced stream power. In contrast, the diminished sediment supplies downstream cause sediment starvation and clear water erosion affecting not only channel stability but also sediment-dependent habitats (Serra et al., 2022). The behavior of MP transport at dams is still unclear. While some studies reported a similar transport mechanism to SS (Watkins et al., 2019; Balla et al., 2022), others reported dissimilar patterns (Balla et al., 2022; Liu et al., 2022b) considering that MPs are often less efficiently trapped compared to SS.

To uncover the spatiotemporal distribution and correlation of SS and MP transport at local and global scales of rivers, intensive in-situ measurements are required. However, these measurements are costly, time-consuming, and labor-intensive (Mohsen et al., 2018; 2020 and 2022a). In addition, there is a lack of financial resources devoted to river monitoring programs worldwide, resulting in a significant decline in the number of gauging sites for measuring not only SS and MP concentrations but also water discharge (Q) (Flores et al., 2020). This decline obscures our understanding of sediment and plastic pollution transport and fluxes to oceans. In the meantime, remote sensing could offer a more sustainable and cost-effective monitoring option for these variables (i.e., SS, MP concentrations, and Q) given the great development in the spatial, spectral, and temporal resolutions of satellite constellations (Mohsen et al., 2018). Besides, their global coverage and frequent imaging prove particularly beneficial for providing valuable SS and MP

transport data for physically inaccessible river sections and during extreme weather conditions, especially for radar (Mohsen et al., 2023c).

Remote sensing of Q in rivers is a growing research topic. The majority of studies have focused on integrating remote sensing data with hydrological (Chen et al., 1998; Stisen et al., 2008; Hartanto et al., 2017) or hydraulic (Bates et al., 1997; Bjerklie et al., 2003; Neal et al., 2009) models. Yet, developing these models requires several supplementary in-situ measurements, which may not be available for many rivers. Alternatively, the hydraulic geometry theory (Leopold and Maddock, 1953) offers potential for remote sensing-based estimation of Q by a single hydraulic parameter (e.g., water width, depth, and slope) derived from satellite images. However, few studies investigated this approach, and they achieved only a moderate to low estimation accuracy. Also, to my knowledge, no study integrated hydraulic geometry theory with machine learning algorithms, which could enhance the estimation accuracy of Q significantly (Mohsen et al., 2022a).

Suspended sediment (SS) has a characteristic pattern in the visible and near-infrared (VIS–NIR) bands making it detectable by satellite sensors (Mohsen et al., 2022a). Several studies developed SS concentration (SSC) models by establishing regressions between the reflectance of these bands and in-situ SSC measurements, using semi-empirical (Duan et al., 2010; Mohsen et al., 2022b), bio-optical (Ammenberg et al., 2002; Manuel et al., 2020) and machine learning methods (Peterson et al., 2018; Mohsen et al., 2022a). However, few studies compared the estimation accuracy of these models across different satellite sensors with varying spatial and spectral characteristics, including active sensors. Furthermore, the suitability of SSC as a proxy for MP concentration has not been evaluated. In this regard, it is important to distinguish between SSC and surficial SSC (SSC at the water surface) models since MP measurements are usually conducted at the water surface (20–30 cm depth) (Chen et al., 2021). However, most studies did not consider their differences.

The field of remote sensing of MP concentration by satellite sensors is in its infancy with conflicting findings regarding its feasibility. While some studies reported that MPs have a distinct spectral signature in the NIR bands (Bentley, 2019), others argued that remote sensing of MP is impossible by any current or planned unmilitary satellite sensors owing to its subtle contribution to the sensor signal (Hu, 2021). To date, no study has specifically investigated the potential of various passive and active satellite sensors to estimate MP concentration in rivers, since most studies were conducted in oceanic environments (Davaasuren et al., 2018; Evans and Ruf, 2022). Also, these studies relied primarily on active sensors leveraging their capability to capture the changes in water surface roughness affected by MP colonization and the formation of surfactants.

On the other hand, many studies proved the potential of satellite sensors in detecting MaP debris or riverine litter as a proxy for MaP, due to their wider coverage and higher influence on the sensor signal; yet, the spatial and spectral characteristics of the employed sensor are still questionable (Goddijn-Murphy et al., 2018; Hu, 2021). Similarly, most studies were conducted in marine environments (Biermann et al., 2020; Themistocleous et al., 2020; Evans and Ruf, 2022) and very few in rivers (Jakovljević et al., 2019; Solé Gómez et al., 2022). Various remote sensing approaches have been implemented to detect MaP debris, including bio-optical modeling (Goddijn-Murphy et al., 2018), deep learning modeling using techniques such as image segmentation (Mifdal et al., 2021), image classification (Jakovljević et al., 2019) and object detection (Hegde et al., 2021) as well as

indices approach (Biermann et al., 2020). However, bio-optical modeling is quite complex, very sensitive to slight changes in water`s optical properties, and reliant on many auxiliary optical data. The indices approach, while simpler, has low detection accuracy and needs further analysis post-application (Biermann et al., 2020). Deep learning modeling is quite an accurate and useful approach; however, it requires the availability of a large MaP dataset, which is often scarce (Themistocleous et al., 2020). Hence, further research exploring traditional machine learning algorithms [e.g., Support Vector Machine (SVM), Random Forest (RF), Naïve Bayes (NB), Decision Tree (DT), and Artificial Neural Network (ANN)] is warranted since these algorithms require less extensive datasets.

1.1. Research objective

The main objective of this study is to investigate the spatiotemporal dynamics of sediment (mainly SS) and plastics (including MP and MaP) transport in rivers, as well as develop remote sensing-based models for these variables.

1.2. Research hypothesis, and questions

1.2.1. *Spatiotemporal distribution of riverine litter/macroplastic (Map) in the Tisza River*
Hypothesis 1: The spatiotemporal distribution of riverine litter/MaP in the Tisza River is influenced by the hydrological conditions and locations of hydraulic structures, particularly dams.

– How is riverine litter/MaP distributed spatiotemporally in the Tisza River based on the analysis of in-situ surveys and satellite images?

Hypothesis 2: The riverine litter/MaP lifting campaigns should be applied at the end of flood waves when aggregation occurs at defined locations.

– What are the temporal characteristics of riverine litter/MaP aggregates e.g., upstream of dams?
– When should riverine litter/MaP lifting campaigns be conducted by the authorities and voluntary groups?

1.2.2. *Remote sensing-based riverine litter/macroplastic (MaP) modelling*
Hypothesis 1: The very high spatial resolution (VHR) images from Google Earth (GE) Satellites can partially resolve the riverine litter/MaP data shortage by providing data about litter accumulation spots for developing satellite-based riverine litter/MaP models.

– Can VHR images from GE be integrated with Sentinel-2 images to develop satellite-based riverine litter/MaP models?

Hypothesis 2: The SVM algorithm may provide the best riverine litter/MaP model owing to the dual-class nature of the classification problem (i.e. litter and non-litter classes).

– What is the most effective machine learning algorithm for developing a riverine litter/MaP model, considering the lack of riverine litter/MaP data?

Hypothesis 3: The models may detect riverine litter/MaP items up to a pixel size; however, sub-pixel detection is uncertain.

– What is the minimum areal extent of riverine litter/MaP items that can be detected by Sentinel-2 images?

1.2.3. Remote sensing-based water discharge (Q) modelling

Hypothesis 1: Integrating hydraulic geometry theory with machine learning algorithms could enhance the estimation accuracy of Q due to the potential of these algorithms in dealing with complex and non-linear problems.

– Would integrating hydraulic geometry theory with machine learning algorithms provide better Q estimates than traditional methods?

Hypothesis 2: The model's accuracy of Q will be bound to the bankfull level due to the absence of hydraulic geometry characteristics above this level.

– To what extent can the hydraulic geometry theory be used to estimate Q in rivers based on satellite images considering various water stages?

1.2.4. Spatiotemporal distribution of water mixing in the Tisza–Maros confluence in response to rivers` hydrology

Hypothesis 1: Mixing patterns in confluences are significantly influenced by hydrological parameters of the joining rivers, especially during floods, since they could impound each other.

– How does the hydrology of the Tisza–Maros Rivers influence the water mixing process in their confluence area, utilizing satellite images and in-situ data?

Hypothesis 2: In-situ measurements of sediment and microplastics in confluences should be conducted after identifying the actual mixing pattern.

– How do the mixing patterns change in the Tisza–Maros confluence over space and time?
– Where and when representative SS and MP concentration samples should be collected in the Tisza–Maros confluence to avoid misleading conclusions?

1.2.5. Spatiotemporal distribution and correlation of surficial suspended sediment (SS) and microplastic (MP) concentrations in the Tisza River

Hypothesis 1: The temporal distribution and correlation of surficial SS and MP concentrations may change throughout different hydrological conditions due to changes in their sources.

– How similar is the temporal distribution and correlation of surficial SS and MP concentrations in the Tisza River, both collectively considering all hydrological conditions and individually?

Hypothesis 2: The longitudinal distribution and correlation of MP concentration may differ from that of surficial SSC since the measurements were conducted during low stages.

– How similar are the spatial distribution and correlation of surficial SS and MP concentrations along the Tisza River based on intensive in-situ measurements and satellite images?

Hypothesis 3: The longitudinal measurements of surficial SS and MP concentrations at a particular time of the year may exhibit persistence in a subsequent year due to common influencing factors.

– To what extent does the spatial pattern of surficial SS and MP concentrations observed at a particular time of year in the Tisza River persist in the subsequent year?

Hypothesis 4: The influence of tributaries in surficial SS and MP concentrations in the Tisza River may vary depending on waste management practices in the sub-catchments.

–   Do tributaries of the Tisza River have a similar influence on MP transport as surficial SS based on intensive in-situ measurements and satellite images?

Hypothesis 5: Dams may influence MP concentration similarly to surficial SSC due to shared physical characteristics.

–   Do the three dams in the Tisza River have a similar influence on MP transport as surficial SS based on intensive in-situ measurements and satellite images?

1.2.6. *Remote sensing-based surficial suspended sediment (SS) and microplastic (MP) concentration modelling*

Hypothesis 1: The spectral signature of surficial SSC may differ from MP concentration due to variations in their concentration levels and uniformity.

–   What are the spectral signature differences between surficial SS and MP concentrations considering the bands of two optical satellite sensors (i.e., Sentinel-2 and PlanetScope) in the Tisza River?

Hypothesis 2: Spatial and spectral resolutions of satellite sensors may influence the estimation of surficial SS/MP concentrations significantly, as they determine sub-pixel coverage and noise level.

–   To what extent do the differences in the spatial and spectral resolutions of Sentinel-2 and PlanetScope satellites affect their estimation accuracy for surficial SS and MP concentrations in the Tisza River?

Hypothesis 3: Surficial SSC may serve as a good proxy for MP concentration due to shared characteristics.

–   What is the strength of the correlation between surficial SS and MP concentrations, both collectively considering all hydrological conditions and individually in the Tisza River?
–   Can surficial SSC be used as a viable proxy for MP concentration in the Tisza River?

Hypothesis 4: Sediment and plastic particles influence the dielectric constant of river water, detectable by active sensors.

–   What is the correlation between surficial SS, MP concentrations, and channels' backscattering of active sensors (i.e., Sentinel-1) in the Tisza River?
–   Can surficial SS and MP concentrations influence the dielectric constant of river water, in which, to be detected by active sensors?

1.3. Research motivation

The Tisza River is a highly dynamic system in space and time since it has two flood periods and its channel has several morphological, hydrological, and slope conditions. In addition, the river is influenced by various levels of manmade activities including mining activities, industrial and WWTP effluents, and the presence of levee systems. Moreover, the catchment of the river is shared by five European Countries implementing different waste management practices and environmental protection regulations leading to varying levels of communal waste production and wastewater treatment capabilities. These variabilities have a

significant impact on the spatiotemporal distribution of not only plastic pollution but also SS which is still understudied and unclear.

In the meantime, the Tisza River is monitored only at eight sites along its extensive 962 km length (Mohsen et al., 2022a). Besides, the measurements are conducted only monthly solely for Q and SSC, and no regular monitoring specifically focused on plastic contamination. Hence, there is an urgent necessity for remote sensing-based monitoring tools for comprehensive assessment of plastic and sediment transport in the river. These tools would support future riverine litter/MaP removal initiatives by identifying their accumulation hotspots and defining the most suitable timing for removal efforts. In addition, they would streamline the process of measuring SS and MP concentrations, particularly considering the substantial volume of river water required to obtain representative MP samples. This would efficiently save time and effort applied to manual sampling procedures.

2. STATE OF THE ART

The intricate interplay between plastic and SS transport, as well as their spatiotemporal dynamics in rivers at various scales, remains relatively understudied. Besides, their correlations and responses to various spatiotemporal variables remain unclear. The integration of cutting-edge remote sensing and artificial intelligence techniques in plastic and sediment monitoring would enhance our understanding of their spatiotemporal dynamism in the various compartments of rivers. However, many questions are still unanswered regarding the feasibility and efficiency of existing satellites in detecting various plastic sizes and measuring SSC and water discharge. Therefore, this chapter provides a comprehensive overview of the existing scientific knowledge while shedding light on areas requiring further research exploration.

2.1. Origin and transport of fluvial sediments

Sediment transport in rivers is an intricate process that has a profound influence on shaping the morphology, ecology, and functionality of the fluvial system (Vercruysse et al., 2017). The transport of sediment encompasses three main phases including erosion, transfer, and deposition (Amissah, 2020). Although the three phases may manifest at any section of the river, their prevalence at particular reaches (Figure 2.1) gives rise to the classification of the river reaches into sediment source zone (upper reach), transfer zone (middle reach), and accumulation zone (lower reach) (Church and Rice, 2009; Fryirs and Brierley, 2012).

Upland	Upland Valley	Floodplain Valley	Unconfined Floodplain
Erosion dominant	Erosion/deposition (aggradation/degradation)		Depositon dominant
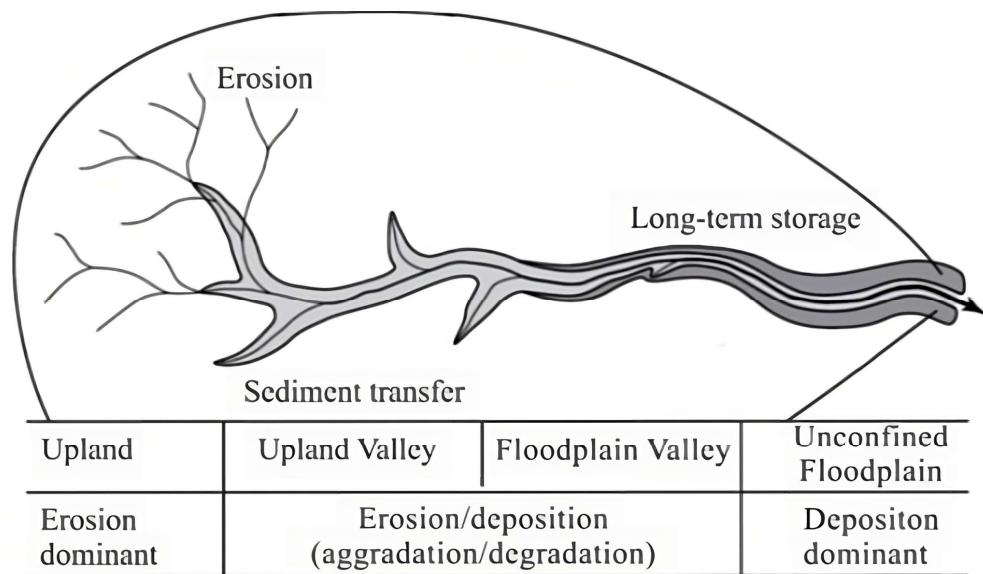
Figure 2.1. The dominant fluvial process at the three (i.e., upper, middle, and lower) reaches of a river (source: Church and Rice, 2009).

The origins of sediment in rivers (Figure 2.2) encompass out-of-channel and/or in-channel sources (Vercruysse et al., 2017). Out-of-channel sediment principally arises from soil erosion and mass movements (Vercruysse et al., 2017). While soil erosion can occur across a wide range of environmental settings, mass movements are confined to steep terrain, mainly in mountainous and hilly regions, though they can appear also along the channel banks (Church and Rice, 2009). Soil erosion typically provides rivers with fine sediments owing to the composition of soils, consisting of silt, clay, sand, or their combinations; meanwhile, mass movements deliver all size ranges (Figure 2.2; Vercruysse et al., 2017).

In-channel sediment sources include the erosion of channel banks and/or beds. Commonly, the upper segments of channel banks release fine sediment due to their cohesive nature, while the lower, non-cohesive segments supply coarser sizes (e.g., sand and boulders)

(Figure 2.2). Typically, the coarsest sediment is found within the channel bed; however, the size range depends on the influx of out-of-channel sources and the hydrodynamic potential of a river to transport a particular size range (Vercruysse et al., 2017).

Sediment transport in rivers encompasses wash load, suspended load, and bed load (Figure 2.2 and Figure 2.3; Fryirs and Brierley, 2012). However, different types of sediment transport are not mutually exclusive and frequently occur simultaneously (Bettes, 2008). While wash load consists of fine silt and clay (particle size <0.063 mm), suspended load consists of sand and may include small pebbles in high turbulent flow conditions (Bettes, 2008). Notably, the wash load is less reliant on the river`s hydraulic conditions compared to the suspended load given the size range of their constituents (Vercruysse et al., 2017). Both loads have out-of-channel and in-channel sources, though out-of-channel sources (i.e., soil erosion and mass movements) typically dominate over in-channel sources (Bettes, 2008).

On the other hand, bed load consists of fine sand to large boulders and is strongly related to the river`s hydraulic conditions (Bettes, 2008). The main origin of the bed load is the riverbed; however, mass movements from the slopes and bank erosion (lower segments) may also contribute to the load (Vercruysse et al., 2017). In lowland rivers (e.g., the Tisza River), suspended load usually dominates the total sediment load of the river (Mohsen et al., 2022a), therefore, my study focused mainly on this load.
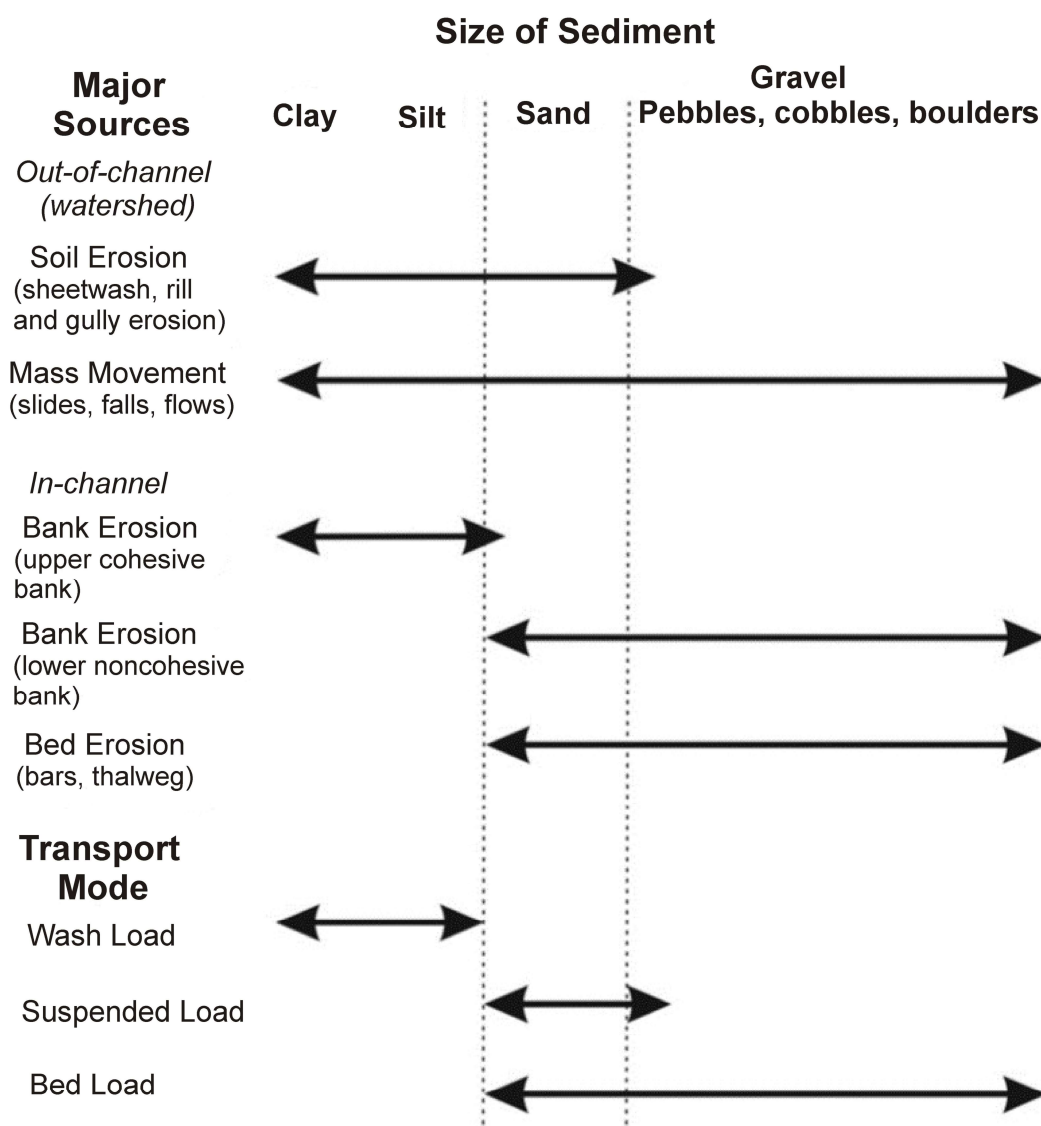
Figure 2.2. The main sources of sediment and transport modes for the various grain-size classes transported within river systems (adapted after: Vercruysse et al., 2017).

14
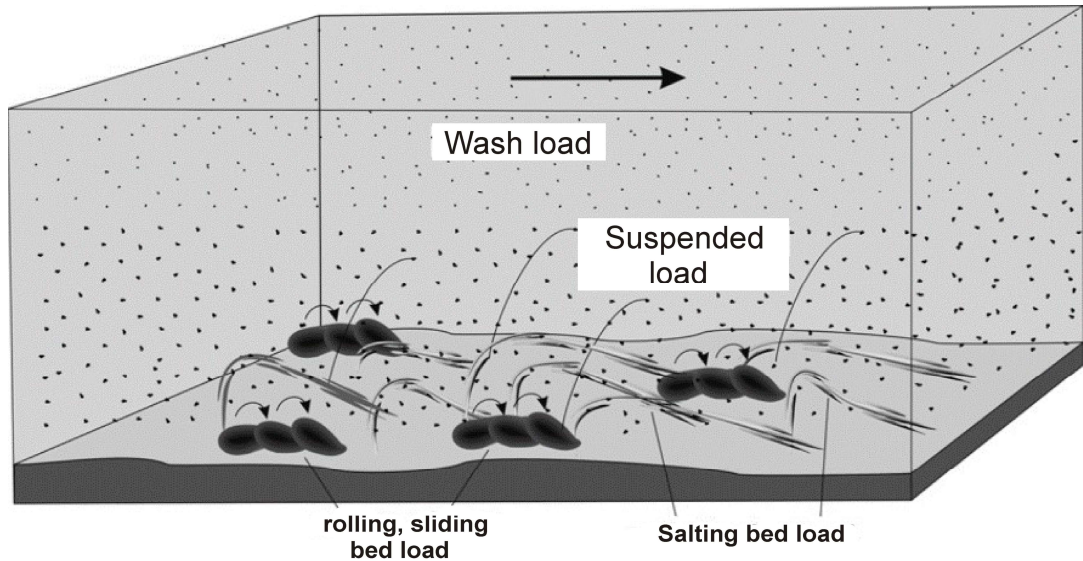
Figure 2.3. Schematic diagram representing different transport modes of sediment in rivers (adapted after: Vercruysse et al., 2017).

2.1.1. *Spatiotemporal dynamics of suspended sediment transport in rivers*

Temporal changes in SS transport in rivers are influenced by several natural and anthropogenic factors varying with the time scale, i.e., event, seasonal, and inter-annual scales (Vercruysse et al., 2017). Seasonal fluctuations of precipitation characteristics (e.g., intensity, pattern, duration, and frequency) exert a profound impact on the runoff, soil erosion, and consequently, the SS transport (Vercruysse et al., 2017). Changes in precipitation characteristics at the event scale (i.e., storm event) may influence SS load through alterations in catchment connectivity and channel conductivity. Seasonal variations in vegetation density and farming practices strongly influence SS load due to their soil stabilization effects (Talbot and Chang, 2022). Climate change was also reported as a driving factor affecting interannual SS load by either increasing or decreasing trends (Du et al., 2021). Additionally, various anthropogenic activities e.g., dam operations, mining activities, and land use/cover changes have been linked to SS load fluctuations.

The complexity of the temporal changes of SS transport and concentrations (SSCs) in rivers can be inferred from the fact that the sediment wave usually has a different velocity than the Q wave, leading to hysteresis in the Q–SSC relationship (Bussi et al., 2017). The specific type of hysteresis is determined through the interplay of various factors, that occur during storm events, including sediment flushing, exhaustion, storage, delayed activation, and remobilization (Vercruysse et al., 2017). Clockwise hysteresis occurs when SSC peaks before the Q peak (Figure 2.4A), probably due to the availability of sediment in the catchment preceding the wet period and/or the proximity of sediment sources to the river (Bussi et al., 2017). Although clockwise hysteresis is the most common type, several studies reported the occurrence of anticlockwise hysteresis too (Figure 2.4C) (Wulf et al., 2012). This phenomenon is likely due to the location of sediment sources farther from the river channel and/or the delayed activation of new sources during the storm event (Vercruysse et al., 2017).

Given the complexity of the interfering factors influencing sediment transport in rivers, frequent spatiotemporal measurements collected at various event, seasonal, and inter-annual scales are required. This would provide more insights into temporal variations in sediment transport and its relationship with the transport of anthropogenic contaminants, such as MPs. Additionally, there is an urgent need to incorporate new techniques (e.g., remote sensing) in sediment transport data acquisition to overcome the limitations of in-situ measurements and obtain more frequent data.
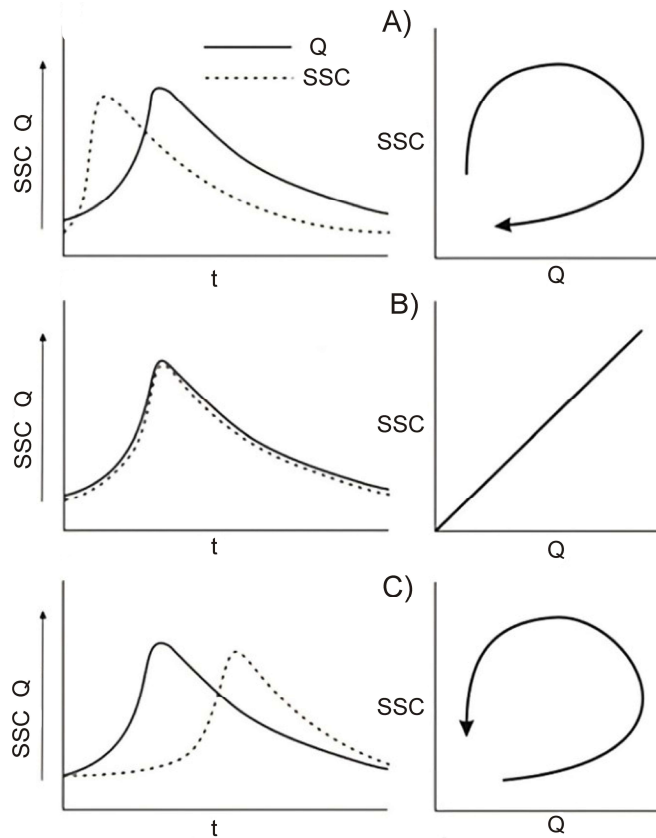
Figure 2.4. Temporal changes between suspended sediment concentration (SSC) and water discharge (*Q*) waves resulted in clockwise hysteresis (A) no hysteresis (B) and anticlockwise hysteresis (C) (adapted after: Vercruysse et al., 2017).

The spatial dynamics of SS transport in rivers are also influenced by a complex interplay of diverse natural and anthropogenic factors. Variability of sub-catchment characteristics (e.g., topography, relief, soil type, geology, and rainfall pattern) and land use practices (e.g., urbanization, cultivation, and forestation activities) influence sediment production and availability for transport, thereby shaping the spatial distribution of SS transport (Mohsen et al., 2023a). In-channel characteristics, including channel morphology, sinuosity, slope condition, and roughness, exert a significant influence on the spatial variability of flow velocity, turbulence, shear stress, and sediment transport capacity along the river (Knighton, 2014). Hydrological variations across different river reaches driven by the macro-climate of sub-catchments (e.g., precipitation and temperature) and tributary inputs lead to further spatial heterogeneity of SS transport (Walling, 1983).

In addition to natural impacts, the disparity of anthropogenic activities (e.g., urbanization, mining activities, channelization, deforestation, construction of roads and levee system) along the river, contribute to spatial heterogeneity of SS transport, irrespective of runoff and discharge conditions (Vercruysse et al., 2017). Furthermore, the presence of dams affects the longitudinal profile of SS transport due to its trapping effect upstream and alterations of channel morphology and flow regimes downstream (Watkins et al., 2019; Serra et al., 2022).

Along the 962 km of the Tisza River, there are only eight gauging sites, and there is only one site along the 750 km of the Maros River where SSC and *Q* are monitored by the water directorate authorities. Moreover, these measurements are performed once a month, regardless of the water stage condition, and during snowy months (e.g., December and January), sampling is prohibited. These sampling schedules are insufficient for tracking the highly dynamic spatiotemporal distribution of SS transport in the rivers, highlighting the crucial need for a more representative sampling strategy incorporating new advanced data acquisition techniques.

2.1.2. *Spatiotemporal dynamics of suspended sediment transport in confluences*

Confluences are pivotal areas in riverine systems where significant alterations in hydrodynamics, sediment transport, channel morphology, water quality, and ecological features often occur (Yuan et al., 2021 and 2022). The most common confluence types are symmetrical, asymmetrical, and bifurcation (Shaheed et al., 2019). While symmetrical confluences occur when two channels merge at an obtuse angle, asymmetrical confluence involves a tributary joining the mainstream laterally, forming an acute angle (Yuan et al., 2021). In the case of bifurcation confluences, the mainstream splits into two or more channels forming an island (Shaheed et al., 2019). In terms of confluence scale, Yuan et al. (2021) suggested a classification based on the width (w) to depth (H) ratio of the joining rivers as small (w/H<10), medium (10<w/H<50), and large scales (w/H> 50).

The differences in flow velocity, momentum, and Q between the joining rivers often result in the formation of shear layers, primarily attributed to the Kelvin-Helmholtz instability phenomenon (Yuan et al., 2021). Also, secondary circulation (helical flow in the cross-sectional plane of a channel) arises because the geometric characteristics of the confluence [e.g., curvature, width variation, and bed condition (i.e., discordant, or concordant)] generate a centrifugal force. These flow structures (i.e., shear layers and secondary circulation) stimulate turbulent mixing affecting not only sediment transport and ecology of the mainstream but also the hydraulic condition and geomorphological evolution of the river system (Yuan et al., 2022).

The spatiotemporal dynamism of SS transport in confluences is a quite complex process. The spatial distribution of the hydrodynamic zones and flow structures in confluences were conceptualized by Mosley (1976), who identified six zones in the confluence area: separation, stagnation, deflection, recovery, maximum velocity, and shear layer zones (Figure 2.5). Each zone has characteristic patterns affecting water, sediment, and contaminant transport. For instance, the stagnation and separation zones are marked by low flow velocities and calm conditions, stimulating sediment deposition and contaminant absorption. Conversely, the highest velocities and turbulent flow conditions are located in the maximum velocity and shear layer zones, accelerating sediment and contaminant mixing (Yuan et al., 2022). The spatiotemporal distribution of these zones is influenced by various factors, including the geometry and morphology of the confluence (e.g., planform geometry, confluence angle, and bed discordance), as well as the relative Q, momentum, and water density of the joining rivers (Yuan et al., 2022). Based on the experimental study of Best and Reid (1984), the dimensions of the flow separation zone (L and h in Figure 2.5) are positively correlated to the Q ratio of the joining rivers (Q_2/Q_3 in Figure 2.5), especially at high confluence angles (e.g., 70° and 90°).

Knowledge of sediment transport dynamics in confluences is far from being completed (Yuan et al., 2022). Most studies have primarily focused on evaluating the degree of longitudinal and/or lateral mixing of SS until complete mixing is achieved (Guyot et al., 1998; Umar et al., 2018; Mohsen et al., 2021). Guyot et al. (1998) investigated SS transport in the confluence of the Negro and Solimões Rivers, Brazil, by mass balance technique, reporting that complete mixing occurs at ca. 25 km downstream with the Solimões River contributing the majority (96.5%) of the total downstream SS load. Similarly, the lateral and longitudinal mixing of SSC were investigated at the confluence of the Mississippi and Missouri Rivers, employing satellite images, and the findings of the mixing ratios were quantified by a mixing metric (Umar et al., 2018).

Fewer studies investigated the temporal mixing of SSC in confluences and just for limited periods. For instance, Marinho et al. (2018) examined the temporal mixing of SSC in the confluence of the Negro and Solimões Rivers over one year, revealing fluctuations in the dominance of water from the two rivers around the year. Another study conducted by Park and Latrubesse (2015) investigated the spatiotemporal mixing of SSC at the same

confluence, considering different hydrological conditions (i.e., drought, average, and flood conditions). The authors reported a high dependency of the mixing process on the hydrological condition, with the highest mixing rate occurred during floods, followed by drought and average conditions.
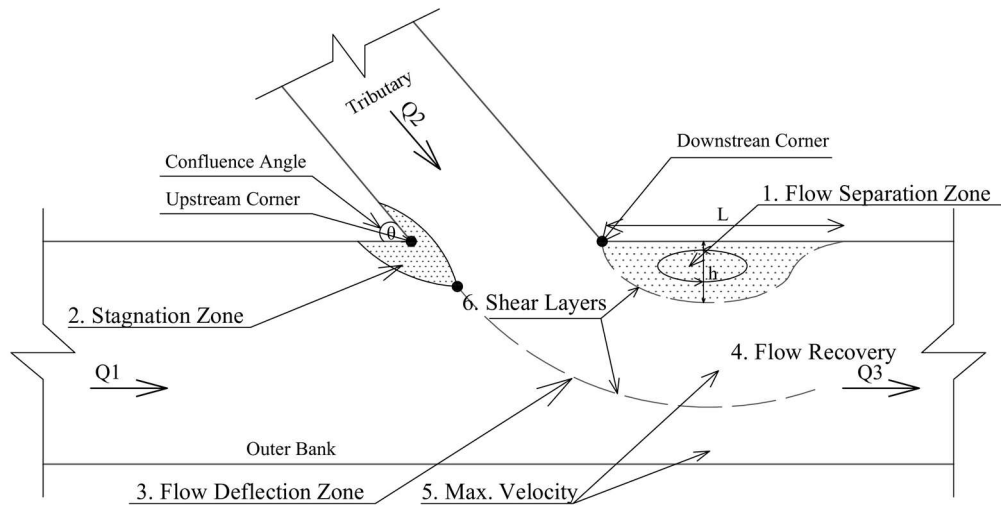
Figure 2.5. Conceptual model of hydrodynamic zones and flow structures in a confluence area *(Q: water discharge; L and h: dimensions of the flow separation zone; θ: confluence angle)* (adapted after: Mosley, 1976).

However, to my knowledge, no study has explored the correlation between hydrological parameters (e.g., water stage, water slope, and Q) of the joining rivers and spatiotemporal mixing patterns of SSC in confluences. Hence, further research addressing this research gap is warranted to enhance our understanding of confluence dynamics. Additionally, at the Tisza–Maros confluence, SSC measurements are conducted downstream monthly without considering the actual mixing pattern, which may lead to a misleading interpretation of findings. Therefore, there is a need for more intensive SSC data collection through the incorporation of remote sensing techniques to identify the dynamism of mixing patterns and their connection to variations in the hydrology of the joining rivers.

2.2. Plastic pollution transport in rivers

Plastic pollution is one of the contemporary environmental risks negatively affecting human well-being and ecosystems. Besides, its impacts are likely to be exaggerated in the future, given the projected sixfold rise in global annual plastic production between 2015 and 2050 (Zalasiewicz et al., 2019). Rivers play a crucial role in connecting terrestrial sources of plastic pollution (e.g., mismanaged waste, sewage discharge, and industrial leakage) to marine environments due to their proximity to various anthropogenic activities (Kiss et al., 2021; Mohsen et al., 2023a). However, there are conflicting findings regarding plastic contribution of rivers worldwide to marine systems (Newbould et al., 2021). While Lebreton et al. (2017) and Schmidt et al. (2017) suggested that only 47 and 5 of the world`s rivers, respectively, are responsible for 80% of the global riverine plastic emissions, Meijer et al. (2021) reported a much higher number, exceeding 1000 rivers. The substantial disparity in the number of rivers indicates a lack of sufficient data on plastic transport in rivers worldwide, emphasizing the necessity for enhanced plastic transport models with reduced uncertainty. Also, contradictory findings were reported regarding the spatiotemporal dynamics of plastics in riverine systems, influenced by different longitudinal and temporal factors, thus many aspects of plastic transport in rivers remain poorly understood (Zhang et al., 2020; Kiss et al., 2021).

2.2.1. *Plastic characteristics, sources, and impacts*

The physical characteristics (e.g., size, shape, and density) of plastic particles play a profound role in their transport within aquatic systems. However, there is an ongoing debate regarding the precise definitions of these characteristics (Waldschläger et al., 2022).

The most common classification of plastic particles is based on their size: nano plastic (≤ 1 μm), microplastic (MP; 1 μm<MP$\leq$5 mm), mesoplastic (5 mm<mesoplastic$\leq$ 25 mm), and macroplastic (MaP; >25 mm) (Shamskhany et al., 2021). Each size range originates from different sources and exerts specific environmental impacts. For instance, while MPs usually originate from sewage discharges, MaPs originate from mismanaged solid waste, though MaP degradation contributes to the formation of smaller plastic fractions (Newbould et al., 2021). Regarding their impacts, the small size and heightened hydrophobicity of MP particles enhance their ability to absorb toxic substances that can subsequently enter the food web (Lu et al., 2023). MaPs, on the other hand, can increase flood risk through their clogging effects, they damage habitats and leach toxic chemicals into aquatic systems (Lu et al., 2023).

Plastic shape is not only a fundamental feature influencing their transport, but it is also commonly used as a proxy for determining the origin of the particles (Waldschläger et al., 2022). Metz et al. (2020) suggested the terms "fragments" and "pellets" for plastic particles having three dimensions, "foil" for those with two dimensions, and "fiber" for one-dimensional particles (Figure 2.6). However, there remains a lack of precise definitions for plastic shapes, as within every category, shapes can vary. For instance, pellets could be lenticular, cylindric, or any other shape. Also, some plastic particles, such as foam, undergo continuous shape changes during transport (Waldschläger et al., 2022).
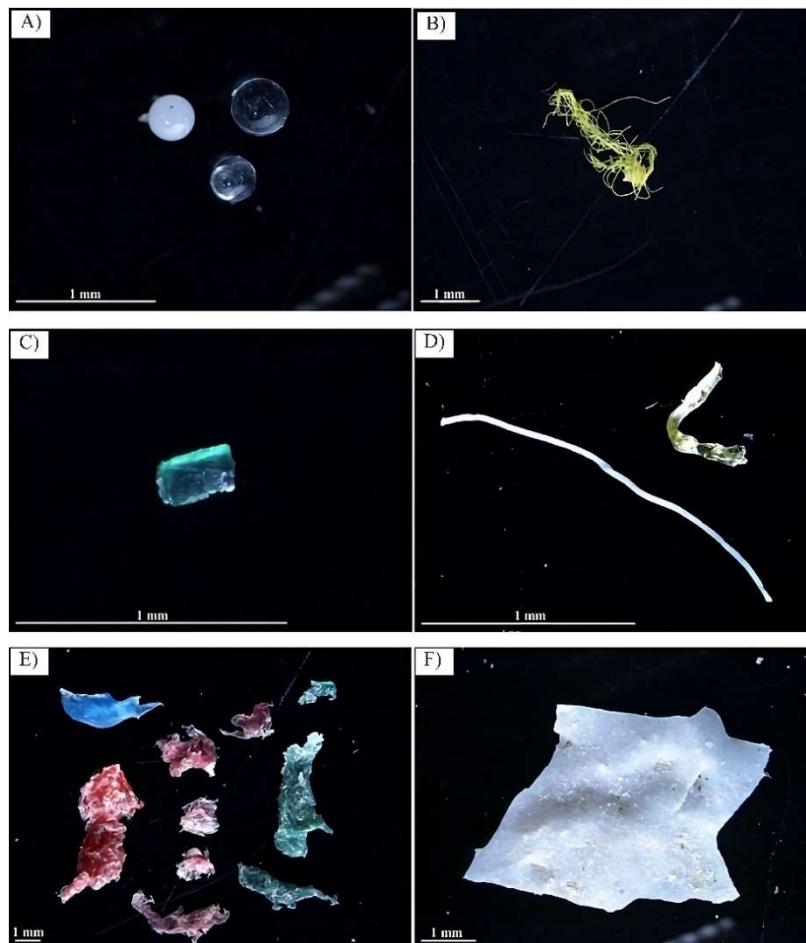
Figure 2.6. Different microplastic (MP) shapes including: spheres (A), fibers (B), fragments (C–D), irregular particle shapes (E), and film (F) (adapted after: D'Hont et al., 2021).

Another physical characteristic influencing plastic transport in aquatic systems is density. The density of a plastic particle is determined by the type of polymer it comprises and can range from ≤0.05 g/cm^3 (in the case of expanded polystyrene) to 2.3 g/m^3 (in the case of Teflon) (D'Hont et al., 2021). However, it`s important to note that the density of plastic particles often undergoes changes during their transport or over time due to the biofouling process (Waldschläger et al., 2022). Although the distribution of polymer types in riverine plastic pollution is primarily influenced by local anthropogenic activities and consumption patterns, it's noteworthy that lightweight plastics e.g., Polyethylene (PE), Polypropylene (PP), and Polystyrene (PS) are among the most frequently reported polymer types in rivers worldwide (Van Emmerik and Schwarz, 2020).

2.2.2. Mechanisms governing plastic pollution transport in rivers

Plastic pollution transport in riverine systems is still in an early research stage due to the complex interaction of plastic particles with various riverine compartments. Although rivers are the primary conveyor belts of terrestrial plastic to oceans, an increasing body of evidence suggests that most of this plastic input never reaches oceans (Van Emmerik et al., 2022). This can be interpreted by Newbould et al. (2021) conceptualization of plastic transport in rivers as it consists of a series of detached "step" (transport phase) and "rest" (stationary phase) periods between temporary storage sites (i.e., trapping sites). Tramoy et al. (2020) reported a similar transport mechanism in the River Seine, France since the GPS trackers of plastic particles showed intermittent paths and their residence time was significantly longer than the transit time of water. However, to date, little is known about dominant modes of transport, accumulation patterns in the trapping sites, and residence periods at various reach types and under varying hydraulic regimes (Van Emmerik et al., 2018; Newbould et al., 2021). During the transport phase, plastics exhibit different modes of transport, including surface, suspended, and bed loads. These modes are governed by the physical characteristics of plastic particles and the river`s hydrodynamic condition (Waldschläger et al., 2022). Surface mode occurs for positively buoyant particles with high rising velocity, and it is considered the most common mode owing to the domination of lightweight plastic particles in rivers (Lenaker et al., 2019). The suspended mode occurs when the settling or rising velocities of plastic particles are counteracted by flow turbulence (Waldschläger et al., 2022). The dynamics of this transport mode are governed by the advection-diffusion equations (Fischer, 1979). Denser plastic particles with elevated settling velocities are usually transported as bed load, through sliding, rolling, and saltation (Waldschläger and Schüttrumpf, 2019). This transport mode is initiated when the bed shear stress exceeds the critical stress.

The stationary phase of plastic transport, on the other hand, occurs at trapping sites (pollution hot-spots; Hurley et al., 2023) which may arise due to hydraulic conditions, including the existence of the flow separation zone, and/or physical obstacles such as hydraulic structures, channel bars, bends, and vegetation (Newbould et al., 2021).

The complexity of plastic transport in rivers could be inferred from the fact that for every size range (e.g., MP and MaP) the transport rate and consequently the spatiotemporal distribution may differ from one another (Newbould et al., 2021). For example, several studies reported higher trapping rates for MaP particles in river compartments than MPs, indicating that MP particles have a greater chance of reaching oceans (Newbould et al., 2021). MP tends to exhibit a more uniform distribution along rivers, while MaP distribution is more heterogeneous and closely linked to distances from contamination sources (Newbould et al., 2021). Also, MaPs are mainly transported by traction, floating, and rolling, while MPs rely on surface currents, suspension, and saltation (Lahens et al., 2018). These differences suggest potential variations in the sources, transport mechanisms, drivers, and ultimate fates of MaP and MP in rivers (Van Emmerik and Schwarz, 2020). However, further research is warranted to assess similarities and differences in their transport dynamics.

2.2.3. Spatiotemporal dynamics of plastic pollution transport in rivers

There are conflicting results regarding the spatial distribution of MP in response to various longitudinal variables in rivers. For instance, while numerous studies reported a positive correlation between MP concentration and urban land cover and population density (Feng et al., 2020; de Carvalho et al., 2021; Sang et al., 2021), others reported no correlation (Feng et al., 2020; Mai et al., 2021), attributing this to rigorous waste management practices applied in these areas. Similarly, many studies reported no apparent connection between MP concentration in rivers and proximity to agricultural lands (Barrows et al., 2018; He et al., 2020) or even observed a negative correlation (Huang et al., 2020), though agricultural lands usually apply wastewater sludge and greenhouses which are sources of MPs (Saadu et al., 2023). Also, both the concentration (McCormick et al., 2016) and dilution (McCormick et al., 2016) effects of WWTP effluents have been reported in river reaches downstream. Therefore, the precise influences of longitudinal variables on MP distribution in rivers remain unclear and warrant further research, considering intensive spatial sampling plans with appropriate repetition.

Similar conflicting findings were reported regarding the influence of temporal changes of hydro-meteorological variables on MP distribution in rivers. For instance, Ockelford et al. (2020) reported that the MP concentration follows a similar pattern as of a storm hydrograph, as the highest concentrations were recorded during the rising and peak phases, while it decreased during the falling phase and low stages. Hence, they considered rivers as sources of MP during high stages, and as sinks during low stages. Although, this finding was supported by many studies (Kumar et al., 2021; Laermanns et al., 2021), other research reported a negative correlation between MP concentration and Q, suggesting that high Q dilutes MP concentration (Barrows et al., 2018; Wu et al., 2020). Therefore, further investigations into the role of the temporal changes in hydro-meteorological variables on MP distribution in rivers, considering extended and more frequent sampling, are needed.

2.2.4. Roles of tributaries and dams on plastic pollution transport

Tributaries play a significant role in plastic transport in mainstream rivers; however, their impact depends on local anthropogenic activities, waste management practices, and sewage discharge in sub-catchments (Ahmed et al., 2016; Kiss et al., 2021). Although most studies reported an increase in the plastic abundance downstream of confluences (Balla et al., 2022; Xia et al., 2023), fewer reported a decline, considering that their diluting impacts outweigh the concentration effects (Kukkola et al., 2023; Mohsen et al., 2023a). However, most of these studies build their conclusions based on snapshot measurements without evaluating their persistence over time. Besides, the extent to which tributaries exert comparable or disparate influences on MP and SS in the mainstream remains uncertain.

Dams and their reservoirs, on the other hand, change the river`s connectivity due to the deposition behavior upstream and clear water erosion downstream. However, their influence on plastic transport is still understudied, and conflicting findings were reported. For instance, both the increasing and decreasing trends of MP concentrations upstream of dams were reported in several studies (Watkins et al., 2019; Balla et al., 2022). Hence, further research identifying the precise role of tributaries and dams on plastic transport is necessary.

2.2.5. Monitoring and analysis of micro- and macro plastics in water: potentials and limitations

Although plastic contamination in aquatic environments has received significant global research attention, there is still a lack of standardized schemas for sampling and subsequent analysis of samples, which obscure cross-study interpretations and comparisons (Mohsen et

al., 2023a). For instance, several studies used different mesh sizes for MP sampling from the water, resulting in different MP size ranges that complicate direct comparisons of the findings (Dris et al., 2015). Nevertheless, some organizations attempted to publish guidelines towards the harmonization of methodologies and establishing standardized protocols for plastic monitoring and analysis (Masura et al., 2015; Wendt-Potthoff et al., 2020). Notable, this harmonization is promising and feasible, practically given the comparable sampling approaches of plastics in fresh and saltwater environments.

The choice of plastic sampling methods, including MP and MaP, is contingent upon the desired research question, the targeted spatiotemporal scales, and the availability of resources (Hurley et al., 2023). Also, the quantity of the collected water plays a significant role in the representativeness of the sample. Lenz and Labrenz (2018) recommended to collect at least 1000 liters of water when MP concentration falls below 1 item/m^3.

The most common methods for MP sampling are nets, including neuston/manta trawl nets (Morét-Ferguson et al., 2010), zooplankton nets (Dris et al., 2015), and continuous plankton recorders (Thompson et al., 2004), as well as pumps, including teflon pump (Zhao et al., 2014), submersible pump (Setälä et al., 2016) and centrifugal jet pump (Lenz and Labrenz, 2018). Nets collect samples by towing their openings behind a boat at a constant velocity and for a fixed duration or distance when the sample is stored at the cod end (Morét-Ferguson et al., 2010). The size range of the collected MP samples is determined by the mesh size of the net. Also, the volume of the collected water is calculated based on the net`s dimensions, the towing velocity, and the sampling duration or distance (Morét-Ferguson et al., 2010). However, in this way, the exact amount of sampled water could be calculated roughly. Pumps, on the other hand, collect samples by immersing a suction pipe (in an above-water pump) or the entire pump (in submersible pumps) into the water, passing the outlet pipe through a sieving cascade or filter stack, and measuring the exact volume of collected water by a flow meter (Figure 2.7). While nets are convenient, efficient for large water volumes, and capable of detecting MPs down to 100 μm size (plankton net), they are costly, unsuitable for small water bodies, and require navigation vehicles (e.g., boats) (Bordós et al., 2019). Pumps can partially overcome the limitations of nets; however, they are still costly, less mobile, and could be a source of MP contamination (Prata et al., 2019).
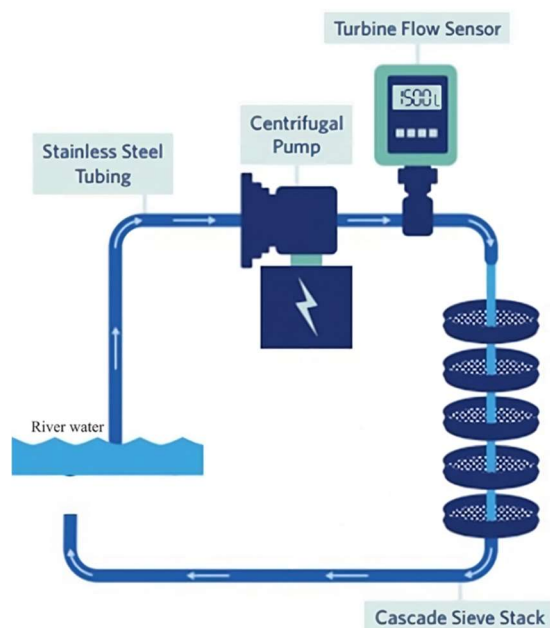
Figure 2.7. Example of the general setup of a pumping system used to sample water for microplastic (MP) concentration (adapted after: Bryksa, 2021).

In the meantime, the in-situ monitoring of MaP particles can be accomplished by physical sampling, including nets, and visual counting by trained observers (Mohsen et al., 2023b). While these methods provide detailed data about the physical characteristics of MaP particles, they are labor-intensive, costly, and prone to human errors (Armitage et al., 2022). Hence, remote sensing methods have recently been integrated into the monitoring process by using unmanned aerial vehicles (UAVs) (Wolf et al., 2020), bridge cameras (De Giglio et al., 2021), and satellite images (Mohsen et al., 2023b). These methods provide large-scale and frequent data about MaP variations as well as saving time and effort. However, they are somewhat less accurate, require advanced image processing techniques, and don't provide data on submerged MaP particles (Armitage et al., 2022). For a detailed illustration of remote sensing techniques, please refer to section 2.5.

Water samples for MP are remedied by various methods to measure the MP concentration and the physical characteristics of MP particles. These methods can be summarized into three steps, including density separation, digestion, and identification (Prata et al., 2019). The density separation process leverages the density difference between plastic (0.8–1.6 g/cm^3) and sediment particles (2.7 g/cm^3) to isolate MP particles. This can be accomplished by adding a salt-saturated solution, with an elevated density, and collecting the supernatant (suspected MP and organic materials) for further analysis. Quinn et al. (2017) recommended using reagents with a density greater than 1.4 g/cm^3 to enhance the separation process. Several solutions have been applied in the literature, including water, sodium chloride (NaCl), sodium iodide (NaI), zinc bromide (ZnBr$_2$), and zinc chloride (ZnCl$_2$) resulting in different capabilities in recovering various polymer types (Table 2.1; Prata et al., 2019). Rodrigues et al. (2020) suggested using zinc chloride, despite its high cost, as it can potentially be reused at least five times while maintaining a recovery rate of over 95%.

Table 2.1. To recover polymer types several density separation solutions could be used with different capabilities, where + refers to good separation, ±: possible separation, and – not separated (adapted after: Prata et al., 2019).

Polymer type	Density (g/cm^3)	Water 1 g/cm^3	NaCl 1.2 g/cm^3	NaI 1.6 g/cm^3	ZnBr$_2$ 1.7 g/cm^3	ZnCl$_2$ 1.8 g/ cm^3
Polypropylene (PP)	0.9–0.91	+	+	+	+	+
Polyethylene (PE)	0.92–0.97	+	+	+	+	+
Polyamide (PA)	1.02–1.05	–	+	+	+	+
Polystyrene (PS)	1.04–1.1	–	+	+	+	+
Acrylic	1.09–1.2	–	+	+	+	+
poly methyl acrylate (PMA)	1.17–1.2	–	+	+	+	+
Polyurethane (PU)	1.2	–	+	+	+	+
Polyvinylchloride (PVC)	1.16–1.58	–	±	+	+	+
Polyvinyl alcohol (PVA)	1.19–1.31	–	±	+	+	+
Alkyd	1.24–2.1	–	–	+	+	+
Polyester	1.24–2.3	–	–	+	+	+
Polyethylene terephthalate (PET)	0.9–0.91	–	–	+	+	+
Polyoxymethylene (POM)	0.9–0.91	–	–	±	+	+

For samples with a high content of organic materials, it is vital to be digested to destroy the organic content and to avoid the misidentification of plastic particles. Prata et al. (2019) categorized the digestion agents applied in the literature into (a) acid agents [e.g., hydrochloric acid (HCl) and nitric acid (HNO_3)] (b) alkali agents [e.g., potassium hydroxide (KOH) and sodium hydroxide (NaOH)] (c) oxidizing agents [e.g., hydrogen peroxide (H_2O_2] (d) enzymatic agents (e.g., proteinase K, collagenase, papain, protease and cellulase). While acid and alkali agents could degrade, melt, or discolor certain polymer types, oxidizing agents, particularly hydrogen peroxide, have been considered as a preferable alternative, since they preserve the structure and chemical composition of the particles while achieving a higher recovery rate (Qiu et al., 2016). Enzymatic agents proved efficient in the digestion process too, but they are less commonly applied due to their higher cost (Prata et al., 2019).

To identify the physical characteristics of MP particles (e.g., count, size, shape, and polymer type) researchers have employed visual inspection and/or chemical quantification and characterization (Prata et al., 2019). Visual inspection is typically carried out by stereoscopes or microscopes; however, it is less accurate, prone to human errors, can`t detect MP particles smaller than 0.5 mm, and does not provide information on polymer types (Zhao et al., 2014; Prata et al., 2019). The effectiveness of visual inspection by microscopes was enhanced by using a staining dye (e.g., Nile red, rose bengal, and oil red dyes) and prodding particles with a hot needle (Maes et al., 2017). Chemical quantification and characterization, on the other hand, are widely performed by Fourier transform infrared spectroscopy (FTIR) and Raman spectroscopy (Prata et al., 2019). FTIR develops an infrared spectrum created by the change in dipole moment, while Raman produces a molecular fingerprint spectrum created by chemical bonds' polarizability (Elert et al., 2017). Although these techniques are quite accurate and have the potential to identify tiny MP particles (down to 20 μm; Raman spectroscopy), they are costly and time-consuming (Prata et al., 2019).

2.3. Similarities and differences between suspended sediment and microplastic transport in rivers

The connection between MP and SS transport in rivers remains understudied, though they share many characteristics that suggest potential similarities in their transport mechanisms (Mohsen et al., 2023a). Thus, many concepts and theories from sediment transport research could be transferred to MP research, particularly the MP research still experiences challenges with fundamental concepts such as particle characteristic definitions, elucidation of transport mechanisms, and identification of representative sampling (Hoellein et al., 2019).

The MP size range (1 μm–5 mm) is very similar to fine natural sediment, particularly sand and silt sediments (Mohsen et al., 2023a). Moreover, the MP and natural sediment particles exhibit inherent heterogeneity in terms of shapes, sizes, and densities and often form aggregates with other organic and inorganic materials during their transport (Yan et al., 2021). Additionally, MP and natural sediments share the same transport modes, encompassing surface or wash load, suspended, and bed loads, and the particles are vertically stratified in the water column based on their size and density (Cowger et al., 2021). Also, MP and fine sediment have similar hyporheic filtration mechanisms at the channel bed and both of them are affected by the ratio between their respective diameters and bed sediment diameter (Waldschläger et al., 2019).

On the other hand, MP and sediment have contrasting buoyancies with MPs being positively buoyant and natural sediment being negatively buoyant. Hence, MPs are more likely to be transported as surface load, whereas the natural sediment is conveyed as suspended and bed loads (Waldschläger et al., 2022). In contrast to sediment, MPs usually deform during their transport and are characterized by higher degradation and fragmentation rates than sediment (Waldschläger et al., 2022). Notably, MPs have higher mobility at the riverbed than sediment, as the experimental study of Waldschläger and Schüttrumpf (2019)

revealed that the MP particles (a mixture of various shapes, sizes, and polymer types) moved earlier than anticipated by the Shields` diagram. Also, Waldschläger et al. (2019) highlighted significant differences in the settling and rising velocities of MP particles than sediment, emphasizing that sediment transport formulas should be treated with caution before being applied to MP transport.

Few studies assessed the spatiotemporal correlation between SS and MP concentrations in rivers and they reported conflicting findings (Waldschläger and Schüttrumpf, 2019; Chen et al., 2021; Laermanns et al., 2021). These discrepancies may arise from the inherent similarities and differences between MP and sediment characteristics, and variations in sampling scales among studies. A significant correlation (R^2=0.65) between SS and MP concentrations was reported in the Langat River, Malaysia, especially during high stages; however, the established relationship was based on monthly measurements (Chen et al., 2021). Similarly, Buwono et al. (2021) reported a strong correlation between MP concentration and certain physicochemical water quality parameters, including SSC; however, the assessment was based on only four sites sampled once every three months. Piehl et al. (2020) reported a good correlation between SS and MP concentrations (R^2=0.60) in the estuary of the Trave River; however, no correlation was found in the Elbe and Po Rivers, but the assessment was based on snapshot measurements. Atwood et al. (2019) hypothesized that the accumulation pattern of MP follows a similar pattern as of SS in the Po River; however, no correlation was found between both variables until some tourist, aquaculture, and public parking sites were excluded from the analysis. Therefore, more studies investigating the connection between SS and MP concentrations in rivers, considering long-term, spatially, and temporally detailed monitoring programs, are warranted.

2.4. Remote sensing-based suspended sediment discharge modelling in rivers

Suspended sediment discharge (Q_s) monitoring is of utmost importance for gaining insights into the hydrology, geomorphology, water quality, and riparian ecological system. To accurately measure Q_s, data on Q and SSC are needed. However, the accurate in-situ monitoring of these variables requires the availability of intensive resources, besides it is laborious, time-consuming, and often impractical during extreme events. Hence, many researchers and monitoring agencies opt to integrate in-situ measurements with remote sensing and numerical modeling techniques (Mohsen et al., 2022a).

The estimation of Q and SSC could be retrieved by several sensor types, including optical, thermal, radar, or altimetry sensors (Bjerklie et al., 2018). However, only a few studies have attempted to estimate them simultaneously using remote sensing sensors. Alternatively, most studies focused on estimating SSC only by remote sensing sensors and relying on in-situ measurements of Q for Q_s estimation (Stumpf and Goldschmidt, 1992; Martinez et al., 2009). Others gave rough estimates of Q_s to oceans at a global scale, employing GRACE satellite data (Mouyen et al., 2018). Hence, further research is needed to advance the field of remote sensing of Q_s.

2.4.1. Remote sensing of water discharge

Remote sensing of Q in rivers can provide spatially and temporally continuous data for large and inaccessible rivers as well as reducing the cost and risk of in-situ measurements (Gleason and Durand, 2020). Several attempts aimed to estimate Q by combining remote sensing data with hydrological models (Chen et al., 1998; Stisen et al., 2008) or hydraulic models (Bates et al., 1997; Bjerklie et al., 2003; Neal et al., 2009). However, these models often rely on many auxiliary in-situ measurements; thus, hindering the full automation of Q estimation. Other studies applied near-field remote sensing of surface velocity by Doppler radars, thermal infrared images, or particle tracking algorithms. Although this method is

effective, it is costly and requires additional measurements of the channel`s cross-sectional area (Fulton et al., 2020). Therefore, research efforts were geared towards the integration of the hydraulic geometry method (Leopold and Maddock, 1953) with remote sensing data since it could estimate Q based on a single hydraulic parameter such as water width, depth, and velocity (Equation 2.1–Equation 2.3) (Gleason and Smith, 2014; Flores et al., 2020).

$$w = aQ^b; \log(w) = \log(a) + b.\log(Q) \qquad \text{Equation 2.1}$$

$$H = cQ^f; \log(H) = \log(c) + f.\log(Q) \qquad \text{Equation 2.2}$$

$$v = kQ^m; \log(v) = \log(k) + m.\log(Q) \qquad \text{Equation 2.3}$$

where w: water surface width; H: mean water depth; v: mean flow velocity; Q: water discharge; a, c and k: numerical coefficients; b, f, and m: numerical exponents.

For decades, hydraulic geometry-based Q estimates were the backbone of water management decisions and hydrological developments (Gleason and Durand, 2020). These power-law relationships are typically established based on measured or estimated water width, depth, or velocity and measured Q by an Acoustic Doppler Current Profiler (ADCP) or weir equations (Gleason and Durand, 2020). However, they should be calibrated regularly, particularly in mobile bed streams to overcome any factual errors that may arise due to changes in river channel morphology (Mohsen et al., 2022a). These changes might be occurred at short scales, like flood events, causing hysteresis in the established relationships, or over the long term due to various anthropogenic activities (e.g., cut-offs, construction of revetments, groynes, and levee systems) (Sipos et al., 2007; Kiss et al., 2019b).

Birkinshaw et al. (2010) and Michailovsky et al. (2012) employed altimetry data obtained from TOPEX/Poseidon and ENVISAT/ERS-2 satellites to estimate water depth (H) and consequently Q by the *H–Q* hydraulic geometry equation (Equation 2.2) for the Ob, Mekong and Zambezi Rivers. However, the water depth is unattainable through optical sensors; hence, other studies exploited another form of hydraulic geometry equations that involve water width (w) and Q (Equation 2.1), known as at-station-hydraulic-geometry (AHG) (Leopold and Maddock, 1953). Later on, the AHG method evolved into the at-many-station hydraulic geometry (AMHG) method through a breakthrough study by Gleason and Smith (2014). The study revealed a log-linear relationship between the AHG coefficients and exponents of the river`s cross sections along a mass-conserved reach. Optimizing these coefficients and exponents to minimize the Q difference between every pair of cross-sections results in better estimates of Q than the original AHG method.

The AMHG was applied to estimate Q in four Indian rivers based on a time series of *w* data obtained by Landsat/IRS images and measured Q (Durga Rao et al., 2020). The results showed high estimation accuracy, especially during low and medium flow conditions. A similar approach was followed in the Mekong River; but, instead of optical sensors, Sentinel-1 SAR data were used to produce a time series of *w* (Mengen et al., 2020). To our knowledge, no study integrated the AHG method with machine learning algorithms, which may result in comparable accuracy to AMHG while simplifying the process.

2.4.2. *Remote sensing of suspended sediment concentration*

Optical remote sensing is the most prominent sensor type for estimating SSC in rivers (Bjerklie et al., 2018). The interaction of light with the river water surface is intricate, influenced by not only the scattering and absorption of light by the water-sediment mixture, but also by the initial solar input, atmospheric condition, and specular reflection of sunlight (Arisanty and Saputra, 2017). These factors collectively influence surface reflectance, and

consequently the feasibility of SSC estimation (Bjerklie et al., 2018). Typically, elevated SSCs correspond to higher surface reflectance in the VIS–NIR bands (Mohsen et al., 2022b). However, the degree of sensitivity varies with the wavelength of the spectral band (Bjerklie et al., 2018). Numerous studies exploited the existence of this correlation and developed calibration models by empirical (Mohsen et al., 2022b), semi-empirical (Duan et al., 2010), bio-optical modeling (Ammenberg et al., 2002; Manuel et al., 2020), machine learning (Flores et al., 2020; Mohsen et al., 2022a) and indices (Arisanty and Saputra, 2017) approaches. Also, a wide range of satellite missions spanning from coarse spatial resolution e.g., MODIS and MERIS (Feng et al., 2012) to relatively finer resolutions e.g., Landsat and Sentinel-2 (Mohsen et al., 2022a) have been applied.

Larson et al. (2018) derived SSC regression models by simple linear and stepwise regression techniques, employing the reflectance data from the MicaSense Sequoia sensor on UAV, and a field spectroradiometer over the Maumee River, USA. The field spectroradiometer models showed a higher accuracy (adjusted R^2=0.7) than the UAV sensor (adjusted R^2=0.56). Bio-optical modeling in the Barra Bonita Reservoir (Tietê River, Brazil) achieved even higher estimation accuracy (R^2=0.77) than the empirical and semi-empirical methods (Bernardo et al., 2015). While this approach is accurate, it requires the availability of extensive optical data, is very sensitive to environmental fluctuations, and has complex structures (Yang et al., 2022).

Recently, many studies employed several machine learning algorithms in deriving SSC models to overcome the limitations of the empirical, semi-empirical, and bio-optical modeling methods. Peterson et al. (2018) tested three neural network algorithms for estimating Landsat-based SSC models in the Missouri and Mississippi Rivers, USA. Their results revealed that the extreme learning machine algorithm outperformed others (R^2=0.9). Similarly, Dehkordi et al. (2021) compared random forest (RF) and support vector machine (SVM) for deriving Sentinel-2-based SSC models in the Missouri River, with the RF algorithm demonstrating the best estimation accuracy ($R^2 = 0.79$ and Pearson's r = 0.88).

Radar images, on the other hand, could partially overcome some of the limitations of optical sensors since they provide images during day or night and regardless of cloud condition (Mohsen et al., 2023c). However, few studies have assessed its potential to estimate SSC, especially in rivers (Shao et al., 2021). Notably, radar images are sensitive to changes in surface roughness and dielectric constant; thus, I hypothesize that they are sensitive to fluctuations in active water constituents, including SSC. Given the intricate interfering factors affecting surface roughness in rivers, such as Q, topography, size, and hydraulic structures, it is challenging to employ surface roughness as a proxy for SSC changes. In light of these considerations, I attempted to examine the feasibility of the other component of the radar images (i.e., dielectric constant) as a potential proxy for SSC. Particularly, Shao et al. (2021) reported a linear relationship between the backscattering of Sentinel-1 images and SSC, which was linked to changes in the dielectric constant.

2.5. Remote sensing-based plastic pollution modelling in rivers

In-situ monitoring of riverine large to small plastic particles (MaP, MP) is often limited to individual campaigns since regular surveys are costly, time-consuming, and labor-intensive. Hence, most plastic sampling schemas in rivers worldwide are insufficient to track the highly dynamic plastic transport (Mukonza and Chiang, 2022). To overcome the limitations of in-situ measurements, some studies developed numerical models for plastic transport monitoring e.g., CaMPSim-3D (Pilechi et al., 2022) and INCA (Whitehead et al., 2021); however, these models require many hydrological, morphological, and plastic characteristics data, which might not be easily available for most rivers. Remote sensing, on the other hand, could overcome these limitations owing to its large-scale coverage and frequent imaging (Mohsen et al., 2022a). Yet, the application of remote sensing for plastic

27

monitoring in aquatic ecosystems, particularly MPs, is still in the research and development phase with many conflicting findings regarding its viability (Bentley, 2019; Hu, 2021). Furthermore, an overwhelming amount of research was devoted towards marine ecosystems, and very few was conducted in rivers (Davaasuren et al., 2018; Evans and Ruf, 2022).

The incident light on river water has a distinct behavior with floating plastic, especially MaPs than water in terms of reflection at the surface, transmission into the water, and upwelling from the subsurface passing through plastic items (Goddijn-Murphy et al., 2018). However, the spectral characteristics of plastics in aquatic systems can be challenging to discern owing to the diversity of their polymer types, sizes, shapes, and colors. Polyethylene (PE) and polypropylene (PP) are the most studied polymer types due to their prevalence in aquatic systems (Law, 2017). Their spectral responses in the VIS–NIR (400–1000 nm) and NIR (1000–1700 nm) wavelengths were examined by hyperspectral imaging, FTIR, and Raman spectroscopy (Serranti and Bonifazi, 2010). The results revealed that the PE has high reflectance variability in the VIS portion and a distinct signature in the NIR, while the PP has a distinct signature throughout the investigated spectral range (400–1700 nm). Themistocleous et al. (2020) explored the spectral response of a PET plastic bottle target (3×10 m^2) by the SVC HR-1024 spectroradiometer at different heights, concluding that the plastic target has a spectral signature at the NIR and short-wave infrared (SWIR) wavelengths. However, SWIR may not be ideal for plastic detection since water absorbs it strongly, making it ineffective for detecting plastic even under a thin water layer. Similarly, many other studies reported the usefulness of the NIR for plastic detection (Masoumi et al., 2012; Bentley, 2019).

Plastic color has a notable influence on the reflectance, primarily within the visible spectrum, where darker colors result in lower levels of reflectance; meanwhile, it has a subtle impact on the NIR wavelengths (Bentley, 2019). Plastic additives, used for decoration and reinforcement, have a similar spectral response as of color; however, an exception is made for the black carbon pigment as this additive increases the absorption in the ultraviolet (UV) and NIR wavelengths (Wiesinger et al., 2021). The size and thickness of plastics also play a significant role in their spectral response and detection possibility, as the larger plastic items may exhibit more pronounced scattering and absorption features than the smaller ones (Mohsen et al., 2023b). Therefore, it is necessary to develop and compare methods for remote sensing of both the MP and MaP size ranges, utilizing a variety of both active (e.g., Sentinel-1 SAR) and optical (e.g., Sentinel-2 and PlanetScope) satellite missions.

2.5.1. *Remote sensing of microplastic*

Direct detection of MP particles in aquatic ecosystems is quite challenging due to the low spatial resolution of satellite sensors accompanied by the small size range of MP particles (Mohsen et al., 2023c). To date, no dedicated satellite sensors for MP detection have been devised, hence, many studies relied on existing satellites. However, these satellites are susceptible to atmospheric interference, the complex background of MP particles (e.g., waves and foam), and the presence of other materials in water (e.g., phytoplankton blooms, sediments, and organic matter) which can obscure any potential signal from MP particles (Evans and Ruf, 2022). Hu (2021) argued that direct detection of MP in marine ecosystems is virtually impossible using any current or even planned unmilitary satellite sensors due to the very subtle contribution of MP particles to the sensor signal, even at the highest reported concentration in the literature. In contrast, Bentley`s (2019) study stands alone in implying that direct detection of MPs through bio-optical modeling is feasible, as he reported a strong relationship between MP concentrations in the Great Pacific garbage patch and the predicted reflectance from his model.

Given the challenges of direct sensing of MPs in aquatic systems, most studies, including my study, have explored indirect methods using simulated proxy measurements employing

existing active and optical sensors. Davaasuren et al. (2018) assumed that microbial colonization of MP particles and the formation of surfactants can alter fluid characteristics (e.g., viscosity and surface tension) and consequently water surface roughness conditions in oceans, which could be detected by SAR images. However, Sun et al. (2023) remarked that it is true only in the case of high MP concentrations. The surfactant concept was exploited by Evans and Ruf (2022) to develop an empirical algorithm for estimating MP concentration in oceans by connecting the concentration changes to variations in wind-driven water surface roughness affected by surfactant release. However, unlike oceans where wind is the dominant factor influencing surface roundness, rivers are subject to several interfering factors (e.g., river Q, size, topography, and hydraulic structures) besides wind, that may complicate similar model derivation (Martin and McCutcheon, 1998). Hence, research efforts are needed to explore the connection between variations of MP concentration and water dielectric constant, which can be sensed by SAR images.

Active water constituents, such as SSC, chlorophyll-a, and colored dissolved organic matter, accurately measurable with optical sensors, can serve as a viable proxy for MP concentration (Piehl et al., 2020; Chen et al., 2021; Mohsen et al., 2022b). Mercedes et al. (2003) stated a similarity between the spatial distribution of chlorophyll-a and MP concentrations in the northwestern Mediterranean Sea as algae very often attach to plastic particles. A moderate to strong positive relationships between the spatial distribution of MP concentration and colored dissolved organic matter (R^2=0.60), chlorophyll-a (R^2=0.57), and SSC (R^2=0.38) were reported in the estuary of the Trave River, Germany (Piehl et al., 2020). Similarly, a strong positive relationship (R^2=0.65) between the spatiotemporal distribution of SS and MP concentrations was reported in the Langat River, Malaysia (Chen et al., 2021). However, so far, no study has combined optical sensors and any of the active water constituents to estimate MP concentration either in oceans or in rivers.

2.5.2. *Remote sensing of macroplastic*

Remote sensing of large plastic debris (MaP) in aquatic systems at a large scale has garnered more research attention than the micro-scale. Most studies on floating MaP were conducted in oceans (Biermann et al., 2020; Themistocleous et al., 2020) and fewer in rivers (Jakovljević et al., 2019; Solé Gómez et al., 2022). Although several studies reported the applicability of optical sensors in detecting MaPs, their detection capabilities are still bound to over sub-pixel coverage (Themistocleous et al., 2020). Rußwurm et al. (2023) stated that MaP particles in oceans usually aggregate with other organic and inorganic materials in lines hammered by environmental forces (e.g., wind, waves, and coastal fronts) making them detectable by medium-resolution satellite images, like Sentinel-2. However, the segregation of floating objects of natural origins (e.g., wood, algae, and sargassum) from anthropogenic origin (e.g., plastics) by medium-resolution images is still challenging and it requires further research (Hu, 2021). Also, the effectiveness of large-scale satellite images (e.g., Sentinel-2) in detecting heterogeneous aggregates of riverine litter is still understudied, though this approach could enhance our understanding of riverine litter transport and serve as an effective proxy for MaP contamination hot spots.

The literature outlined three main approaches for remote sensing of aquatic litter/MaP, including bio-optical modeling, indices, and deep learning algorithms. The development of bio-optical modeling depends on determining the optical properties of water both with and without the presence of litter (Goddijn-Murphy et al., 2018). Although this method could detect litter with an elevated accuracy, few studies have attempted to apply it due to its complexity and high sensitivity to subtle changes in environmental conditions (Moore et al., 2014). Goddijn-Murphy et al. (2018) developed a reflectance model for detecting the fraction of the surface area of a MaP item to the total surface area of water, based on the geometrical optics and the spectral signatures of water and plastics.

The indices method aims to develop an index that can discriminate litter/MaP from its background water based on their spectral signatures. This approach is less accurate than bio-optical modeling and usually requires further refinement after its application. Biermann et al. (2020) proposed a floating debris index (FDI) based on amplifying the disparity in the reflectance between the NIR band and the baseline NIR. However, the detection results of the FDI were enhanced by applying the Normalized Difference Vegetation Index (NDVI) to eliminate false identifications of vegetation and the NB machine learning algorithm for further classification of different litter types. Similarly, Themistocleous et al. (2020) developed a plastic index (PI) based on the spectral reflectance of the red and NIR bands.

The deep learning method focuses on automating litter/MaP detection by computer vision (CV) tasks, such as image classification (Jakovljević et al., 2019), image segmentation (Mifdal et al., 2021), and object detection (Hegde et al., 2021). Although deep learning algorithms could detect litter with high accuracy, they usually require large datasets, which are currently not available due to litter dataset shortage (Jakovljević et al., 2019; Solé Gómez et al., 2022; Mohsen et al., 2023b). Therefore, further research is necessary to explore traditional machine learning classification algorithms (e.g., RF, DT, SVM, and NB) for riverine litter detection. These algorithms are favored for their simplicity, high detection accuracy even with limited datasets, and strong generalization capabilities (Szeliski, 2010).

De Giglio et al. (2021) compared the detection accuracy of supervised (ISO-DATA and K-means), unsupervised (Maximum likelihood), and machine learning (DT) methods to detect litter in the Reno River, Italy, by applying a multispectral camera. They revealed that the DT exhibited the best detection accuracy (>80%). Conventional Neural Network (CNN)-based models were developed to detect and quantity MaPs in different aquatic settings in Cambodia based on the data collected by drones (Wolf et al., 2020). They achieved a detection accuracy of 83% and a discrimination accuracy of 71%. Similarly, a recent study developed a deep learning-based (i.e., U-Net and DeeplabV3+ image segmentation structures) riverine litter detector with an accuracy of 0.82 (Solé Gómez et al., 2022).

2.6. Research problems and gaps

The spatiotemporal transport and distribution of large and small plastic debris (MaP and MP) in rivers are influenced by various spatial (e.g., sub-catchment characteristics, tributaries, dams, WWTPs) and temporal (e.g., event, seasonal and inter-annual variations in hydro-metrological) variables that remain inadequately understood. Also, the connection between the transport of natural SS and plastics is still unclear and many conflicting findings were reported due to the lack of sufficient spatiotemporal data and unified sampling scales. To address these knowledge gaps, further research is imperative, necessitating denser and more frequent sampling plans that integrate advanced data acquisition techniques (e.g., remote sensing) and artificial intelligence.

Similarly, at the confluences, the intricate interplay of hydrological, morphological, and hydraulic factors of the joining rivers has substantial influences on mixing patterns downstream. Yet, these aspects, especially the connection between hydrological parameters and mixing patterns are still understudied and require further research based on intensive spatiotemporal data employing remote sensing techniques.

Remote sensing of water discharge and natural sediment requires further development in the estimation accuracy incorporating concurrent data science techniques (e.g., machine learning) with various active (e.g., Sentinel-1) and optical (e.g., Sentinel-2 and PlanetScope) satellite sensors. On the other hand, remote sensing of large and small plastics, especially MPs, is still in its early stages of research, with conflicting findings regarding its feasibility. Besides, most research efforts were geared toward marine systems, leaving rivers understudied. Therefore, further research is necessary to assess the potential of satellite sensors for direct MP and MaP detection and indirect estimation through a proxy [i.e., MP:

active water constituents (e.g., SSC); MaP: litter accumulation hot spots] incorporating various machine learning algorithms.

The Tisza River and its tributaries, especially the Maros River, serve as an ideal case study for addressing my research questions. This choice is justified by the river`s elevated sediment load, moderate plastic pollution levels, and the availability of hydrological data along with our intensive in-situ measurements of natural sediment and plastic pollution.

3. STUDY AREA

3.1. Geographical settings

The lowland, medium-sized Tisza River, and its main tributary Maros/Mures River (Central Europe) were selected for the case studies (Figure 3.1A). The Tisza River is the longest tributary (962 km) of the Danube and contributes to the Danube`s discharge by 13% ($Q_{mean}$: 930 m$^3$/s; Lászlóffy, 1982). Meanwhile, the Maros River is the longest tributary of the Tisza (750 km) and contributes with 17% ($Q_{mean}$: 161 m$^3$/s) of the Tisza`s discharge (Mohsen et al., 2021). The catchment area of the Tisza (157,200 km^2) drains the eastern part of the Carpathian Basin, including the catchment of the Maros (30,000 km^2) which is located in the southeast part of the basin (Sipos et al., 2007; Amissah, 2020). The mountainous and hilly sub-catchments in Romania, Ukraine, and Slovakia contribute with the vast majority of the Tisza`s discharge (93.8%), while the lowland sub-catchments in Hungary and Serbia contribute minimally (6.2%) (ICPDR, 2007). Similarly, most of the Maros`s discharge (92%) originates in the Carpathians and Transylvanian Plateau, while only 8% originates from the Great Hungarian Plain (Sipos et al., 2014).
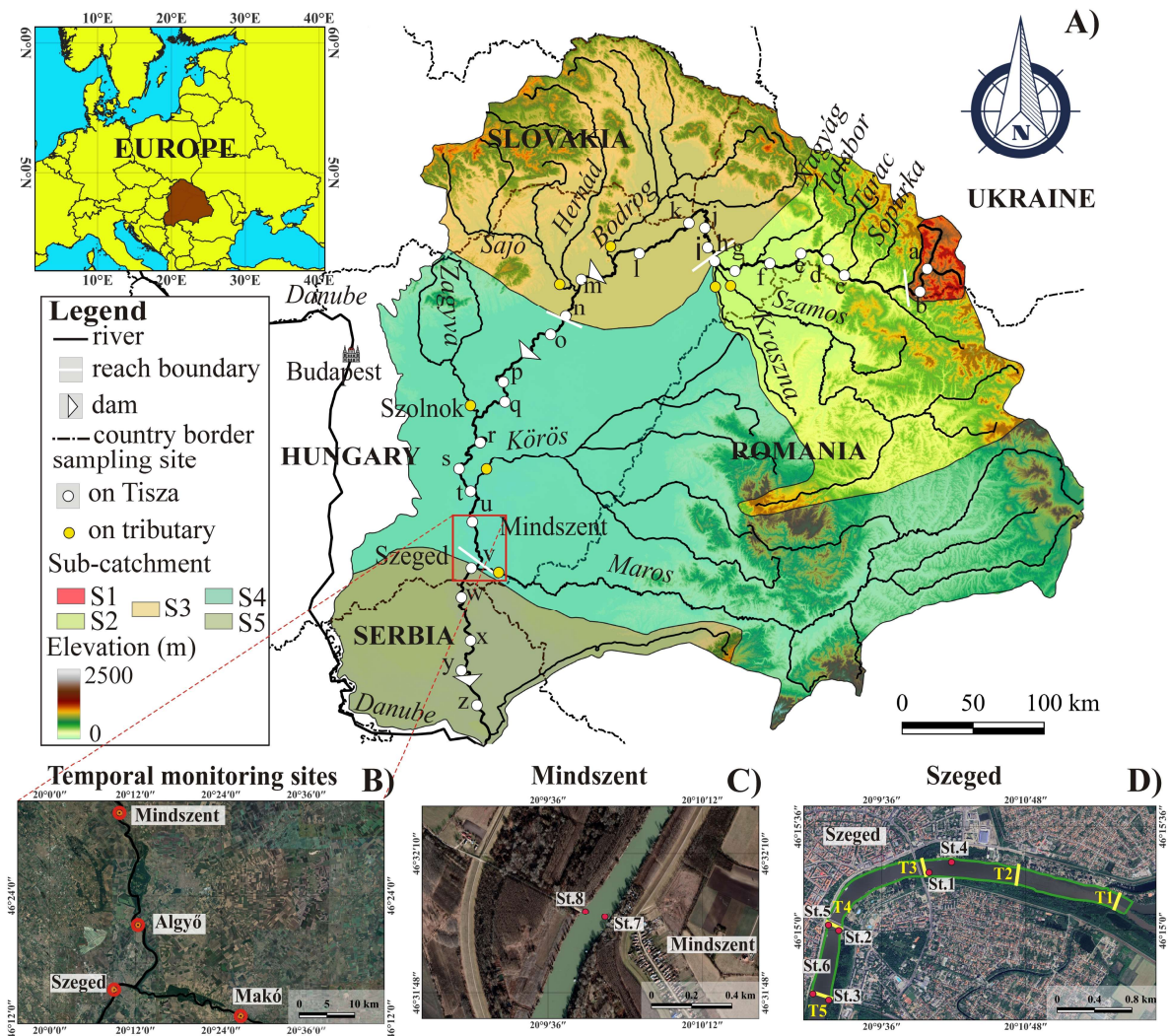
Figure 3.1. Along the Tisza River (S1–S5) and its tributaries 26 sites (a–z) were selected for annual water sampling in 2021 and 2022 (A). Detailed measurements were performed in the close vicinity of fluviometers (B). Frequent samplings were performed in Mindszent and Szeged (St.1–8) and in the confluence area of the Tisza and Maros, five transects (T1–T5) were investigated (C–D).

Based on the hydrological, morphological, meteorological, and relief characteristics of the Tisza`s sub-catchments, the river was divided into three reaches (Upper, Middle, and Lower Tisza) and divided further into five sections (S1–S5) (Figure 3.1A). The upstream section of the Upper Tisza (S1) (964–688 river km) drains the Carpathian Mountains in Ukraine through a steep-sided, incised valley, while the downstream section (S2) drains hilly Ukraine and lowland Hungary sub-catchments, through an anastomosing-meandering channel (Kiss et al., 2022; Figure 3.1A). Similarly, the Middle Tisza (688–177 river km) is further subdivided into sections S3 and S4. While the S3 drains mainly the hilly Slovakian sub-catchment, the S4 collects the water from the lowland Hungarian and hilly Romanian sub-catchments. In both sections, the channel displays a meandering/sinuous pattern (Kiss et al., 2022). Given the homogeneity of the hydro-morphological characteristics along the Lower Tisza (177–0 river km), it was considered as one section (S5). This section is mainly located in Serbia, and its channel has a meandering/sinuous pattern too (Kiss et al., 2022).

3.2. Hydrological, meteorological, and hydraulic characteristics

The catchment of the Tisza River belongs to the temperate continental climate zone; though, the meso- and micro-climate conditions in its sub-catchments are variable and influenced by various factors (e.g., vegetation, relief, and land use/land cover) (TERRA, 2000). The mean annual precipitation in the mountainous sub-catchments is ca. 1750 mm but decreases to 550 mm in the lowland sub-catchments (ICPDR, 2018). The prevailing wind direction is from the west, though influences of the Eastern-European and Mediterranean air masses can be significant (Sipos et al., 2014). The mean annual temperature ranges from 4–11°C, with notable spatial variations primarily driven by topography (Sipos et al., 2014).

The occurrence of floods in the Tisza and Maros Rivers is not significantly related to temporal variations in precipitation patterns; instead, it is primarily influenced by snowmelt (Sipos et al., 2014). Both the Tisza and Maros Rivers typically experience two flood periods within the year, including the early spring flood (March–April) caused by snowmelt and the early summer flood (June–July) resulting from summer rainfall (Sipos et al., 2014). Following these flood periods, the remainder of the year is characterized by prolonged low stages and is frequently associated with droughts (Kiss et al., 2021). Typically, the early spring flood transports more Q and sediment (15% of the annual transport) than the early summer flood (Sipos et al., 2007; Kiss et al., 2011). Occasionally, the summer flood overlaps the spring flood (e.g., in 1941, 1970, 1975, 2000, and 2006) due to the gentle slope of the Tisza, leading to the formation of high, impounded flood waves (Sipos et al., 2007). The Maros`s floods usually precede that in the Tisza by a few days; however, they might also occur concurrently during prolonged floods (Kiss et al., 2011).

Given the steep slopes of the Maros`s catchment (28 cm/km in the alluvial fan and 13 cm/km in the lowland region), floods typically rise rapidly and inundate its floodplain for a short period (1–2 weeks) (Mohsen et al., 2021). Meanwhile, floods persist longer (2–3 months) in the Tisza River, especially in the lowland reach (Mohsen et al., 2021). During floods, the Tisza and Maros Rivers can impound each other, or they can both be impounded by the Danube. However, the impounded section of the Maros is significantly shorter (25 km; up to Makó) than the Tisza (330 km; up to Szolnok) due to their considerably different slope conditions (Sipos et al., 2007; Kiss et al., 2019b; Figure 3.1A).

The mean Q of the Tisza (930 m^3/s) is six times higher than the Maros (161 m^3/s), though they have smaller differences between their maximum (Tisza: 4346 m^3/s; Maros: 2450 m^3/s) and minimum (Tisza: 58 m^3/s; Maros: 21 m^3/s) Q (Sipos et al., 2007). Also, both rivers have a similar mean flow velocity (Tisza: 0.54 m/s; Maros: 0.66 m/s), though the slope of the Maros (28 cm/km) is significantly higher than the Tisza (2.4 cm/km) (Sipos et al., 2007). Both rivers experience significant fluctuations in water levels since the maximum recorded water stage difference was 13.6 m in the Tisza and 7.3 m in the Maros (Mohsen et al., 2021).

Concerning the hydraulic characteristics of the Tisza`s sections (S1–S5), the steepest slope and highest flow velocity are in the upstream section of the Upper Tisza (S1) (Table 3.1; Lászlóffy, 1982). However, they decline suddenly by 82% and 60%, respectively, towards the S2 section, and then gradually decline by a further 17% and 33%, respectively, from S3 to S5. The mean Q is the lowest in S1 (22 m³/s) and increases steadily towards S5 (864 m³/s). Also, the fluctuation in the water stage gradually increases from the Upper Tisza (S2: 10 m) to the Lower Tisza (S5: 12.6 m) (Kiss et al., 2021).

The increase in Q downstream is mainly attributed to the joining tributaries, such as the Szamos (Q_{mean}: 131 m³/s) and Kraszna (Q_{mean}: 7 m³/s) in the Upper Tisza, and the Bodrog (Q_{mean}: 115 m³/s), Sajó (Q_{mean}: 27 m³/s), Zagyva (Q_{mean}: 5 m³/s) and Körös (Q_{mean}: 107 m³/s) in the Middle Tisza (Figure 3.1A; OVF, 2019). Remarkably, the hydrology of the river is under the influence of three dams, namely the Tiszalök and the Kisköre Dams in the Middle Tisza, and the Novi Becej Dam in the Lower Tisza (Figure 3.1A; Mohsen et al., 2023a).

Table 3.1. Hydraulic parameters and sediment characteristics of the five sections of the Tisza River (S1–S5) (data source: Bogárdi, 1974; Lászlóffy, 1982; Kiss et al., 2021; Balla et al., 2022).

River reach	Upper Tisza		Middle Tisza		Lower Tisza
Section (gauging site)	*S1 (Rakhiv)*	*S2 (Tivadar)*	*S3 (Dombrád)*	*S4 (Szolnok)*	*S5 (Szeged)*
Slope (cm/km)	200–500	110–13	≥ 3	1-3	< 2.5
Flow velocity (m/s)	2–3	1	0.1–0.5	0.1–0.2	< 0.2
Mean discharge (m³/s)	22	207	346	509	864
Annual bed load (t/year)	No data	41.8×10^3	16.28×10^3	20.4×10^3	16.7×10^3
Annual suspended load (t/year)	No data	1.7×10^6	9.3×10^6	22.6×10^6	23.8×10^6

3.3. Sediment transport characteristics

Both the Tisza and Maros Rivers transport substantial amounts of sediment loads. Given the highly erodible catchment and steep slope of the Maros River, it has a 2.5 times higher SSC (mean:1600 g/m³) than the Tisza (mean: 640 g/m³) (Bogárdi, 1971 and 1974). However, the annual SS load of the Maros (8.7 million t/y) is only half of the Tisza (18.7 million t/y) due to its lower discharge (Maros: 161 m³/s; Tisza: 930 m³/s) (Bogárdi, 1971 and 1974). In contrast, the bed load transport of the Maros (28,000 t/y) is three times higher than the Tisza (9000 t/y) due to its significantly higher concentration (5.5 g/m³) compared to the Tisza (0.31g/m³) and steeper slope (Bogárdi, 1971 and 1974). The medium grain size of the suspended and bed loads of both rivers are comparable and ranges between 0.01–0.05 mm and 0.2–5 mm, respectively, with coarser grain sizes typically found in the upper reaches (Kiss et al., 2018).

Concerning sediment transport at the various sections of the Tisza (S1–S5), the bed load dominates the upper mountain sections and declines by 60% towards the lower section (Table 3.1; Bogárdi, 1974). Meanwhile, the SS load has an adverse pattern, as it increases steadily by 14 times towards the lower section. It's worth noting that there is an increase in the suspended and bed load transport between S3 and S4, probably due to sediment input from large tributaries located within this section (Table 3.1).

Tributaries have a profound impact on shaping the sediment transport dynamics of the Tisza, especially when the elevated SSC is associated with high Q (OVF, 2019). For instance, although the Szamos and Hernád Rivers have higher SSCs (max for Szamos: 36,461 g/m³; for Hernád: 31,229 g/m³), than the Maros River (max: 8988 g/m³), their annual contribution to the Tisza`s SS load is lower than the Maros (Szamos: 4.6 million t/y; Hernád:

0.4 million t/y; Maros: 18.7 million t/y) due to their smaller water Q (Q_{mean}: Szamos: 131 m^3/s; Q_{mean}: Hernád: 27 m^3/s) than the Maros (Q_{mean}: 161 m^3/s) (OVF, 2019).

The SS transport in the Tisza is highly dynamic and has significant spatiotemporal variability. For instance, although similar hydrographs were recorded during the floods of 2001 and 2002 at the Kisköre (403 river km) and Szolnok (334 river km) gauging sites, the average SS load in 2001 was 50% higher than in 2002 in both sites (Figure 3.2; Csépes et al., 2000 and 2003). Also, the spatial variability is evident in the fact that, on average, the transported SS at the Kisköre site was 49% higher than at the Szolnok site in both years (i.e., 2001 and 2002). This difference may be attributed to overbank sediment accumulation between the two sites. Notably, the Q_s peak precedes the Q peak at the two measuring sites in both years, indicating the prevalence of a clockwise hysteresis pattern in the Tisza River
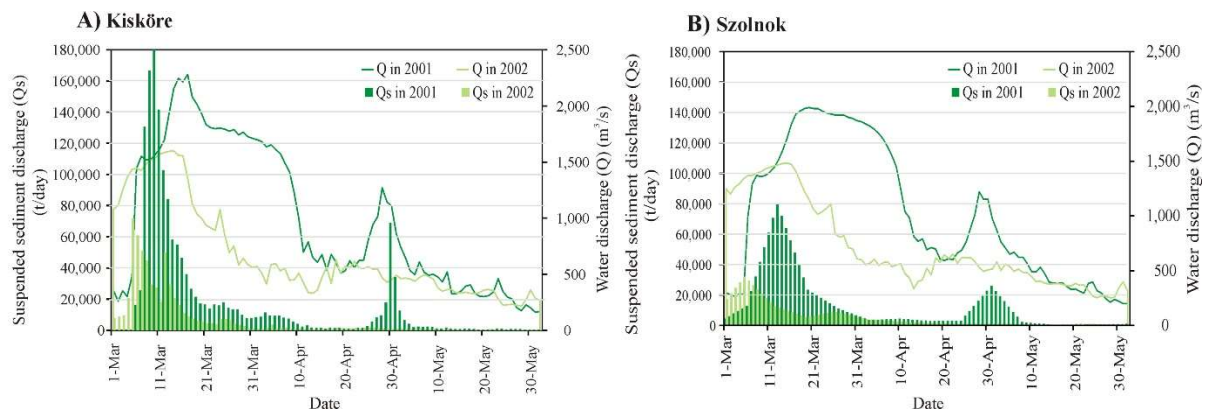
Figure 3.2. Transported water (Q) and sediment discharges (Q_s) during the 2001 and 2002 early spring floods along the Middle Tisza at two adjacent gauging sites at Kisköre (A) and Szolnok (B) (Data source: Csépes et al., 2000 and 2003).

3.4. Plastic pollution in the Tisza River`s sub-catchments

The catchment of the Tisza is shared between five countries (i.e., Romania: 46.2%, Hungary: 29.4%, Slovakia: 9.7%, Ukraine: 8.1%, and Serbia: 6.6%) applying different waste management practices and environmental protection strategies (Mohsen et al., 2023b). This leads to environmental conflicts between the upstream and downstream countries. The upper and lower reaches of the river are more prone to communal waste pollution than the middle reach. This can be inferred from the substantial production of communal waste in Ukraine (12 million t/y; the highest producer) and Serbia (3 million t/y), coupled with the lowest recycling ratio (1%) (Figure 3.3A; Cewep, 2021). On the other hand, countries in the middle reach, especially Slovakia and Hungary, produce less waste (Slovakia: 2.4 million t/y; Hungary: 3.8 million t/y) and boast higher recycling rates (Slovakia: 38%; Hungary: 36%) (Figure 3.3A). It is important to note that communal waste contributes significantly to MaP pollution, but it has minimal contribution to MP pollution owing to the limited degradation of floating MaPs during the transport process (Ronkay et al., 2021). Therefore, Kiss et al. (2021) and Balla et al. (2022) have reported a low abundance of MP fragments in the sediment and water of the Tisza River.

To gain an insight into the quantity and composition of riverine litter being transported in the Tisza one can rely on the data of waste-removal campaigns. Hungarian authorities annually remove 90–10,000 tons of litter, most of which (67%) originates from the Upper Tisza sub-catchments (Index.hu, 2019). The composition of litter consists mainly of organic material as evidenced by the fact that upstream of the Kisköre Dam, 88% of the removed litter consists of woody debris and other organic materials (e.g., branches, leaves, and grass), while only 12% is communal waste (Figure 3.4; Katona, 2019). Remarkably, the volume of the removed litter upstream of the dam varied between 200 and 1500 m^3 for most dates,

except for June 2010, April 2015, and February 2017, when it surged to 3450–4000 m^3. These heavily polluted periods correspond to the greatest flood waves recorded during the studied period (2007–2017) (Figure 3.4).
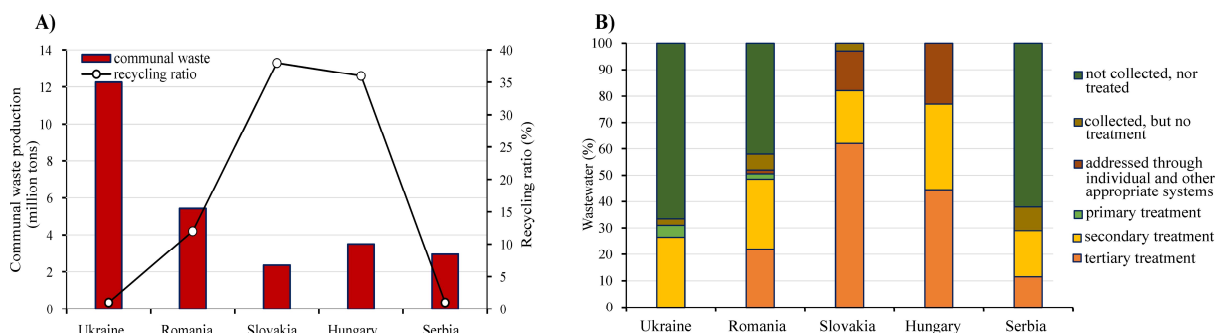
Figure 3.3. Production of communal waste and recycling rates (A), and proportions of the different wastewater treatment types (B) in the five countries sharing the Tisza`s catchment (data source: Interreg, 2018; Cewep, 2021; Eurostat, 2021).
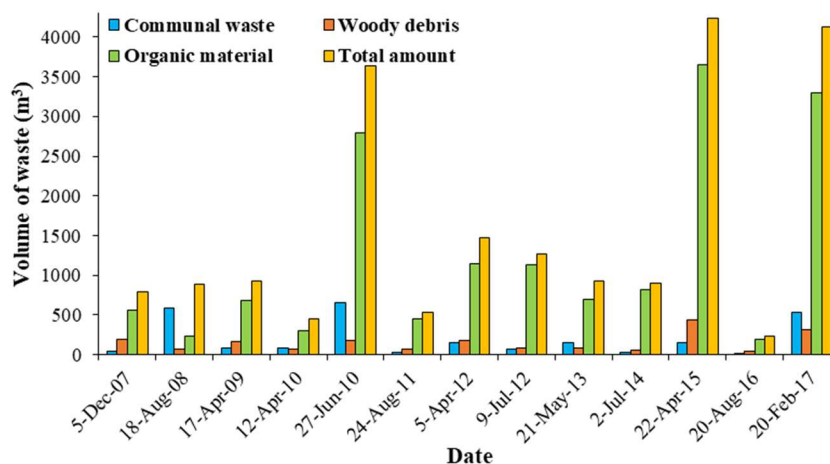
Figure 3.4. Quantity of removed litter upstream of the Kisköre Dam, Middle Tisza, between 2007 and 2017 (data source: Katona, 2019).

Microplastic transport is greatly influenced by wastewater treatment condition, as the most frequently observed MP morphotype is fiber in the water (Balla et al., 2022) and also in the sediment (Kiss et al., 2021) of the Tisza. This prevalence might be linked to the low proportion of houses connected to sewage systems, especially in the upper and lower reaches of Ukraine, where only 57% of the households have a connection to sewage systems, while in Serbia it is even lower (56%) (Interreg, 2018). Hence, a significant amount of wastewater (Ukraine: 69% and Serbia: 71%) is neither collected nor treated, instead, it drains directly into rivers (Figure 3.3B). For example, in 2011, around 7.8×10^6 m^3 of untreated wastewater was released directly into rivers within the upper sub-catchments of the Tisza in Ukraine (Tarpai, 2013). On the other hand, the situation is more favorable in the Middle Tisza, especially in Hungary and Slovakia, where 86% (Hungary) and 91% (Slovakia) of the houses are connected to sewage systems and almost all (98%) collected wastewater undergoes treatment (Figure 3.3B; Eurostat, 2021).

Yet, it is important to note that treated wastewater may also serve as a source of MPs, especially microfiber, as other morpho types are often eliminated during the settling process (Ngo et al., 2019). Thus, microfiber has been identified as the most dominant MP morpho type in wastewater effluents in many studies (Koyuncuoğlu and Erden, 2023). Also, the applied treatment technology in the WWTPs and their conditions influence the retention ratio of microfiber with primary treatment achieving up to 84% retention, secondary treatment

achieving 0–22%, and tertiary treatment achieving 0–12% retention (Tang and Hadibarata, 2021). Given that secondary treatment technology is widely applied in the shared countries, especially in the upper and lower reaches, it becomes obvious that the household-related wastewater input (either treated or untreated) represents the primary source of MP pollution in the fluvial system of the Tisza (Figure 3.3B; Tarpai, 2013).

3.5. Characteristics of spatiotemporal monitoring sites in the rivers

The longitudinal distribution of SS and MP concentrations along the Tisza River was monitored at 26 sites, spaced 50 km apart, over two consecutive years (August 2021 and July 2022) (Figure 3.1A). Also, the main tributaries of the river were monitored at 8 sites, located 15–20 km away from their confluences with the Tisza, but this monitoring occurred only during the 2022 campaign (Figure 3.1A).

Although the entire river was investigated at multiple spatiotemporal scales, my frequent and regular temporal monitoring effort was focused on specific locations. These locations include the Middle Tisza at Mindszent (217 river km) and Algyő (201 river km) and the Lower Tisza at Szeged (172 river km) for the Tisza River and Makó (24.5 river km) for the Maros River (Figure 3.1B–D). Also, the confluence of the Tisza and Maros Rivers was monitored and studied in detail.

The temporal monitoring sites at Mindszent (bankfull width: 108 m; thalweg depth: 11 m; Q: 550 m^3/s) and Algyő (bankfull width: 120 m; thalweg depth: 12.6 m; Q: 575 m^3/s) exhibit similar hydro-morphological characteristics (Sipos and Fiala, 2008; Amissah et al., 2018). Yet, these parameters increase on average by 43%, 19.5%, and 27%, respectively, towards the Szeged site (bankfull width: 164 m; thalweg depth: 14.1 m; Q: 702 m^3/s) due to the additional Q from the Maros River (Sipos and Fiala, 2008; Amissah et al., 2018). The temporal monitoring site in the Maros River at Makó has a comparable bankfull width (126 m) to the Middel Tisza sites (i.e., Mindszet and Algyő). However, its thalweg depth (5.5 m) and Q (157 m^3/s) are almost half and one-third of their counterparts at the Tisza sites, respectively (Mohsen et al., 2022a). Notably, while the Maros River has a trapezoidal cross-section shape, the Tisza River has a V-shaped cross-section (Sipos and Fiala, 2008).

The Maros River joins the Tisza River with a confluence angle of 23° at 177 river km (Figure 3.1D). My study area extends from this point downstream for 4.2 kilometers (172.8 river km). Here, the mean channel width is 170 m, and the thalweg depth is 13.6 m, though there are substantial depth variations, especially near the confluence (Mohsen et al., 2021). The deepest channel depth (18.6 m) is associated with the narrowest width (149 m) at transect No. 4 (T4) (Figure 3.1D). Meanwhile, the widest cross-section (200 m) observed at T5 has a relatively shallow depth (11.6 m) (Figure 3.1D; Mohsen et al., 2021). Notably, upon entering the confluence area, the Tisza River has a lower flow velocity (0.54 m/s) compared to the Maros River (0.66 m/s) (Mohsen et al., 2021).

4. MATERIAL AND METHODS

The SS and plastic pollution transport in the Tisza River was analyzed based on intensive in-situ measurements and various satellite sensors and compared with various hydrological conditions and in response to longitudinal variables. This investigation spanned diverse spatiotemporal scales, meticulously revealing the nuanced dynamics governing their distribution and correlation (Appendix: Table A1). Furthermore, remote sensing-based models were developed for both variables incorporating an array of optical and active sensors. A detailed description of the collected data and applied methodology are illustrated in this chapter.

4.1. In-situ data

4.1.1. Hydrological condition of the Tisza and Maros Rivers during the studied periods

The hydrological condition of the Tisza and Maros Rivers was determined through the data of three fluviometers in the Tisza River at Mindszent, Algyő and Szeged and one fluviometer in the Maros River at Makó (Figure 3.1B). In Mindszent, a daily water stage (H) between March 2021 and May 2023 was used. Meanwhile, in Algyő, Szeged, and Makó, both daily water stage and Q (obtained by rating curves and monthly measurements) were employed, covering the period between January 2015 and May 2021. All the hydrological data were provided by the Hydrological Water Directorate of the Lower Tisza (ATIVIZIG).

4.1.2. Temporal monitoring of riverine litter/macroplastic (MaP) in the Tisza River

The floating riverine litter in the Tisza River, including macroplastics (MaPs) was monitored during an early spring flood on February 18th and 23rd; and March 5th and 10th, 2021. This monitoring period was deliberately chosen since the river is likely to exhibit the highest riverine litter transport rates during floods. The observation point was strategically positioned near the midpoint of a bridge located in Szeged, where the observer estimated the riverine litter transport rate and its composition (Figure 4.1). Every monitoring campaign lasted for one hour when continuous images were captured along with a 15-minute video recording.
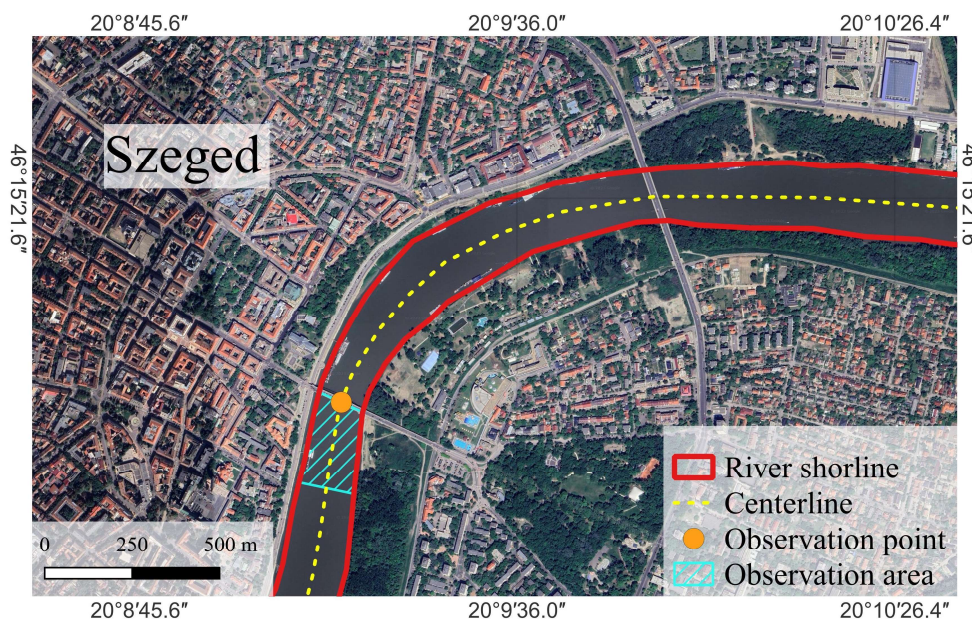
Figure 4.1. Temporal monitoring site of riverine litter, including macroplastics (MaP) during the early spring flood in the Lower Tisza River in Szeged.

4.1.3. Temporal measurements of suspended sediment concentration and water discharge in the Tisza and Maros Rivers

On the Lower Tisza near Szeged fluviometer (ca. at 171 river km) and in Makó fluviometer at the Maros River, the ATIVIZIG routinely conducts monthly measurements for SSC and Q (Figure 3.1B). The depth-integrated sampling approach was applied to measure SSC from 5 verticals along the river`s cross-sections using a pump (Figure 4.2D and E). Meanwhile, the Q is measured by an acoustic doppler current profiler (ADCP). Typically, ATIVIZIG employs these data to calibrate the established Q–H rating curves at the fluviometers. In this study, the SSC and Q data collected between February 2015 and November 2020 were utilized.

Given the variability of the water levels during various SSC measurements, the positions of the five verticals shifted from one campaign to another. Thus, all campaigns were clustered into two groups, (e.g., low and high stages), where the mean distances between the verticals (or to the riverbank) were considered for both stages (Figure 4.2D and E).
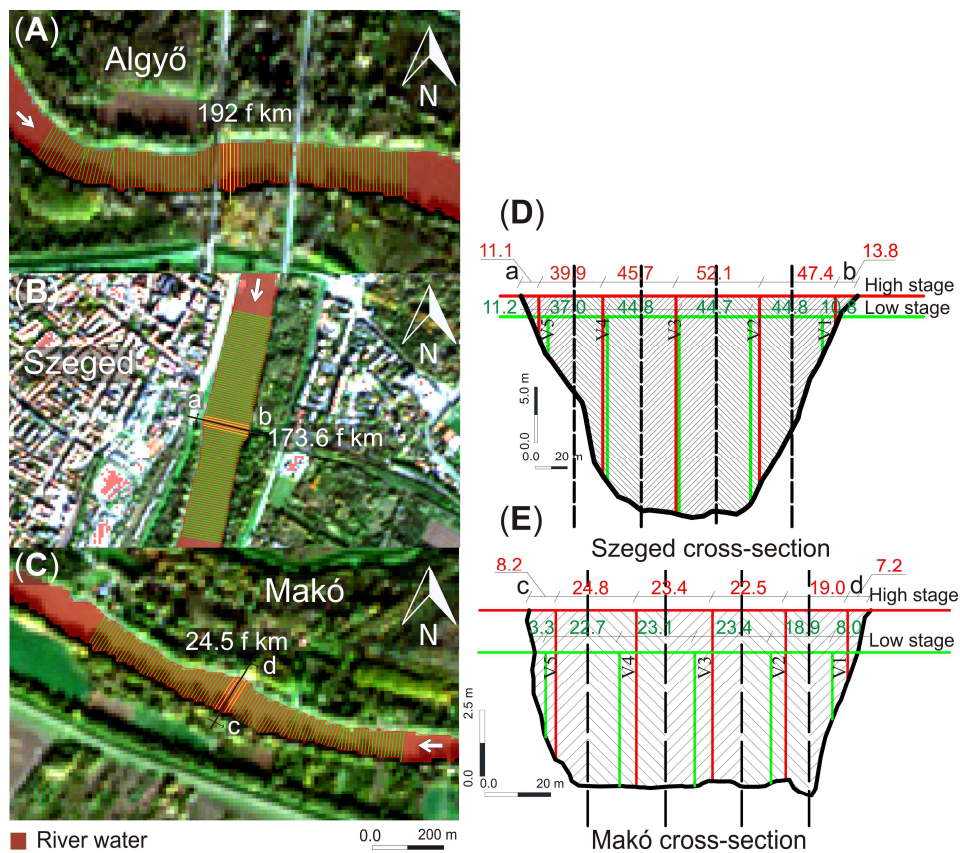
Figure 4.2. Locations of the 100 transects used for the development of the AMHG-based water discharge (Q) models in Algyő (A), Szeged (B), and Makó (C). The mean width of the five yellow transects at the three sites was employed to develop the AHG power-law and AHG machine learning-based Q models. Suspended sediment concentration (SSC) was measured at five verticals in Szeged (D) and Makó sites (E). The horizontal red and green lines indicate high and low stages, while the vertical red and green lines represent the locations of the SSC sampling during high and low stages.

4.1.4. Spatiotemporal measurements of surficial suspended sediment and microplastic concentrations in the Tisza River

The dynamics of surficial SS and MP concentrations were investigated through intensive spatiotemporal measurements. The entire Tisza was monitored at 26 sampling sites (a–z) during low stages in August 2021 (Figure 3.1A). A similar longitudinal measurement was repeated in July 2022, though the first five sites in Ukraine (a–e) were excluded due to the

ongoing war. MP concentration was measured in both years, while the surficial SSC was measured only in 2022 and estimated by satellite images in 2021. A detailed description of the remote sensing-based estimation of surficial SSC is provided in section 4.9. The main tributaries were also monitored in 2022 for surficial SS and MP concentrations (ca. 15–20 km upstream of their confluence; Figure 3.1A). All these measurements were performed from the riverbank.

Temporal measurements of surficial SS and MP concentrations were conducted every five days in Mindszent (site "u"; Figure 3.1A and C). The surficial SSC measurements were performed continuously for nearly two years, from March 2021 to May 2023, resulting in 154 samples at two sites (St.7–8). However, the MP concentration measurements started later in May 2021 and extended until May 2023, yielding 140 samples. MP concentration measurements were conducted across the entire river width from a moving ferry. Additional surficial SSC measurements were conducted in Szeged at six sites (St.1–6; Figure 3.1D) every five days for one year (March 2021–March 2022; 70 samples).

The SSC was measured by sampling 1.5 L of the river`s surface water. Meanwhile, MP concentration measurement involved pumping 1 m^3 of water using an above-water pump following Tamminga et al. (2018). The pumping duration lasted for 25–30 min, during which water was extracted from a depth of 20–30 cm and passed through two metal sieves (e.g., 90 and 2000 μm). Finally, residues from the sieves were washed into glass jars.

4.2. Laboratory analysis of surficial suspended sediment and microplastic concentrations

The surficial SSC was measured by applying the evaporation method, primarily due to the prevalence of fine grains in the natural sediment of the Tisza (Mohsen et al., 2021). Also, occasionally, the river experiences elevated SSC levels exceeding the applicability limit of the infiltration method (200 mg/l; Guy, 1969), especially during floods. The measurements adhered to the ISO 4365(A) and ASTM D3977-97(A) standards (ASTM, 2007). In this process, water samples were evaporated at 105 °C (48 h), then the remaining sediment was weighted, and the surficial SSC was expressed in g/m^3.

The residue of water samples collected for MP analysis was digested to destroy the organic content (cc. H_2O_2 30 %; for 48 h; Rodrigues et al., 2020; Balla et al., 2022). Then, samples with elevated SS content underwent a one-step density separation process using $ZnCl_2$ solution (1.8 g/cm^3) (Kiss et al., 2021). Finally, all samples were washed into a glass petri dish and dried (60 °C for 36 h) for further analysis.

The identification and quantification of MP particles were conducted by a light microscope (Ash Inspex II) at 60× magnification. The identification process followed prior research criteria (Hurley et al., 2018; Balla et al., 2022). Specifically, a particle was considered as a MP if (1) it did not have obvious cellular or organic structures; (2) the fiber exhibited uniform color and consistent thickness throughout; and (3) it responded to the hot needle test and retained its rigid shape with the movement. The precision of the MP identification was verified by the ATR-FTIR Shimadzu Infinity 1s device. The device was used within the range of 400–4000 cm-1 and the Shimadzu Standard Library database was employed. A randomly selected 150 particles were analysed which resulted in an identification precision of 98%. Three MP morpho-types were considered, including fiber (colored and non-colored), microbead, and fragment (Balla et al., 2022), and the MP concentration was expressed as item/m^3.

MP contamination mitigation measures outlined in Balla et al. (2022) were implemented during the sampling and laboratory work. Specifically, only glass and metal equipment were used after being cleaned in an ultrasonic bath and rinsed three times with distilled water. Also, samples were consistently shielded by an aluminium foil throughout the entire process. Yet, complete prevention of MP contamination is allusive, thus for every four samples a fifth

blank sample was included and followed the same process as the original samples. The mean of the identified MP particles in the blank samples was 5.72±3.37 item/sample and all of them were microfibers. Since the MP contamination in the blank samples accounted for 8.6% of the MP in the original samples, all samples were adjusted by subtracting the number of MP in the blank sample from the total number of a sample.

4.3. Remote sensing data

A diverse range of satellite images acquired at multiple spatiotemporal scales by optical and active sensors were employed. The optical sensors encompassed various spatial resolutions, including very high (i.e., Google Earth satellites and PlanetScope) and medium–high resolutions (i.e., Sentinel-2). In the meantime, Sentinel-1 images were exclusively employed among the active sensors. The subsequent sections provide a comprehensive overview of the employed images to achieve each of the study's goals (Appendix: Table A1).

4.3.1. *Optical sensors*

4.3.1.1. Very High spatial Resolution (VHR) images (Google Earth satellites)

Given the elevated spatial resolution (<1 m) of the VHR images from the Google Earth satellites, they could be employed to provide data about riverine litter accumulation spots. Hence, lower altitude orbiting satellites within the Google Earth satellite network [e.g., Airbus constellation, including Pléiades Neo and Pléiades (50 cm); Maxar constellation, including WorldView-3 (31cm); GeoEye (41 cm)] were deployed to search for any litter spots along the Tisza River in Hungary, between July 2015 and May 2021 (Figure 3.1A). Altogether 13 images encompassing litter spots were determined, comprising 3 images from the Maxar constellation and 10 images from the Airbus.

4.3.1.2. Sentinel-2 images

To study riverine litter/MaP in the Tisza River and develop litter models, 77 Sentinel-2A-B images covering the river between July 2015 and May 2021 were acquired from the Copernicus Open Access Hub (ESA). Among these, 16 images covering the same riverine litter spots in the VHR images were employed to develop Sentinel-2-based riverine litter/MaP models. The remaining 61 images were utilized to reveal the spatiotemporal dynamics of riverine litter/MaP in the Middle Tisza through the best-derived model. The set of 16 images used for model development encompasses 11 synchronous images with the VHR images (mean difference of the acquisition date: 2.6±0.1 days) and 5 historical images for the same litter spots to expand the riverine litter dataset size. Notably, the 16 images were acquired from three tiles covering almost the whole river in Hungary, including "T34UEU", "T34TDT" and "T34TDS", while the 61 images were from a single tile "T34TDT" in the Middle Tisza.

To develop remote sensing-based suspended sediment discharge (Q_s) models and investigate its spatiotemporal dynamics in the Tisza and Maros Rivers, a total of 122 Sentinel-2A-B images covering the lower reaches of the rivers (at Algyő, Szeged, and Makó) were acquired (Figure 3.1B). The image acquisition period spanned from July 2015 to May 2021. However, since the in-situ campaigns of the ATIVIZIG for SSC and Q were conducted monthly, only 29 images for the Tisza and 27 images for the Maros were used to develop the models. The images were chosen to be as synchronous as possible with the in-situ measurements with a maximum deviation of ± three days. The rest of the images (93 images) served the purpose of assessing the generalization capability of the developed models and investigating the spatiotemporal change of the Q_s in the rivers.

Focusing on the confluence area of the Tisza–Maros Rivers (Figure 3.1D), the spatiotemporal dynamism of the SS mixing patterns and its relationship to hydrological

parameters of the rivers were investigated by 143 Sentinel-2A-B images. The employed images covered the period between July 2015 and May 2021.

To develop remote sensing-based surficial SS and MP concentration models and investigate their dynamism in the Tisza River, 122 Sentinel-2A-B images were employed. The acquired images covered the longitudinal measurements of both variables in August 2021 (8 images) and July 2022 (7 images) (Figure 3.1A), as well as the temporal measurements in Mindszent (March 2021–May 2023; 75 images) and Szeged (March 2021–March 2022; 47 images) (Figure 3.1C and D). The images were cloud-free at the designated sites and synchronous with the in-situ measurements. Additional PlanetScope and Sentinel-1 images specifically utilized for this study goal are outlined in the next two sections.

Sentinel-2A-B satellites provide images in 13 spectral bands (443–2190 nm), with varying spatial resolutions (10–60 m; Table 4.1). The temporal resolution is typically five days, though it reaches three days at mid-latitudes (Mohsen et al., 2021).

Table 4.1. The spatial and spectral characteristics of the different bands of the Sentinel-2 and PlanetScope satellites (data source: Wang and Atkinson, 2018).

Spectral band	Sentinel-2			PlanetScope		
	Central wavelength (nm)	Spatial resolution (m)	Bandwidth (nm)	Central wavelength (nm)	Spatial resolution (m)	Bandwidth (nm)
B1	443[a]	60	20	443[a]	3	21
B2	492[b]	10	65	490[b]	3	50
B3	560[c]	10	35	531	3	36
B4	665[d]	10	30	565[c]	3	36
B5	704[e]	20	15	610	3	20
B6	741	20	15	665[d]	3	30
B7	783	20	20	705[e]	3	16
B8	833	10	115	865[f]	3	40
B8a	865[f]	20	20	–	–	
B9	945	60	20	–	–	
B10	1374	60	30	–	–	
B11	1614	20	90	–	–	
B12	2202	20	180	–	–	

Alphabetical letters indicate the compatible bands of both satellites

4.3.1.3. PlanetScope images

An additional 177 PlanetScope images covering the longitudinal measurements of surficial SS and MP concentrations in August 2021 (26 images) and July 2022 (21 images), as well as the temporal measurements in Mindszent (March 2021–May 2023; 79 images) and Szeged (March 2021–March 2022; 51 images) were acquired from the planet explorer (Planet). These images served for developing remote sensing-based surficial SS and MP concentration models. Notably, the images were acquired to be as synchronous as possible with the in-situ measurement dates with a maximum deviation of $\pm$ 1-day timeframe.

PlanetScope constellation comprises over 180 sun-synchronous CubeSats, offering daily image coverage for nearly the entire globe (Tan et al., 2021). The images employed in my study were captured by the Super Dove sensor (PSB.SD), offering 8 band images (wavelength: 431–885 nm) with a spatial resolution of 3 m (Table 4.1) (Tan et al., 2021).

4.3.2. Active sensor: Sentinel-1 images

Given the potential of Synthetic Aperture Radar (SAR) to provide reliable terrestrial images irrespective of the weather condition or time, it emerges as a beneficial tool for

monitoring the spatiotemporal distribution of surficial SS and MP concentrations in rivers. Altogether 169 Sentinel-1A-B images covering the longitudinal measurements in August 2021 (8 images) and July 2022 (7 images), as well as the temporal measurements in Mindszent (March 2021–May 2023; 154 images) and Szeged (March 2021–March 2022; 70 images) were acquired from the Copernicus Open Access Hub program. The images were captured every five days in the C-band (5.405 GHz) with dual polarimetric channels (i.e., VH and VV channels) and a spatial resolution of 10 m. The level 1 Ground Range Detected (GRD) products with the Interferometric Wide Swath (IW) acquisition mode were used.

4.4. Pre-processing of the satellite images

The Sentinel-2 images were acquired at level 2A and the PlanetScope at level 3B, hence, they had already undergone the atmospheric and radiometric corrections. Yet, older Sentinel-2 images (2015–2016) were only available in level 1C. To rectify them, they were atmospherically corrected by the Sen2Core 255 processor in SNAP 8.0 software. The correction process is implemented through three steps, including cloud detection, determination of water vapor content and aerosol optical thickness, and finally, converting the top of atmosphere reflectance to the bottom of the atmosphere (Louis et al., 2016).

Given the variability of the spatial resolution of the Sentienl-2 bands (10–60 m), all bands were uniformly resampled to 10 m using the nearest neighbor resampling technique. To reduce image processing time in both satellites, the river water pixels were extracted from the images by applying the Normalized Difference Water Index (NDWI) (McFeeters, 1996). The NDWI thresholds were automatically determined using the OTSU method (Otsu, 1979) in the scikit-image library. All these pre-processing procedures were implemented in the Sentinel Application Platform (SNAP) software, version 8.0 (ESA) and Python 3.0.

Similarly, river water pixels in the Sentinel-1 images were extracted using the derived Sentinel-2 water mask to reduce image processing time. The images were radiometrically corrected by converting backscattering intensity to normalized radar cross section (Sigma 0: σ_0), considering the incidence angle and the sensor characteristics. Speckle noise was eliminated by applying the Lee sigma speckle filter (window size 7×7 pixels; sigma=0.9), and the images were georeferenced to the WGS 84/UTM 34N zone. Finally, geometric distortion was corrected by the SRTM 1sec HGT digital elevation model (DEM) and the bilinear interpolation resampling method. The visibility of images was enhanced by converting the σ_0 to a log scale expressed in dB.

4.5. Development of remote sensing-based riverine litter/macroplastic (MaP) models in the Tisza River

Sentinel-2 images could be employed as a reliable and recurring monitoring tool for riverine litter (including MaP), due to its free accessibility, frequent imaging (3–5 days), and broad spectral coverage (13 bands). Yet, its moderate spatial resolution (10–60 m) obscures the direct detection of riverine litter manually. Therefore, The VHR images from Google Earth satellites with their elevated spatial resolutions (<1 m) were utilized to identify litter spots along the Tisza River in Hungary. The identified spots were used to train, validate, and test five machine learning algorithms to detect riverine litter in Sentinel-2 images (Figure 4.3). The best-performing model was used to explore the spatial and temporal dynamics of riverine litter/MaP along 175 km long reach in the Middle Tisza.

4.5.1. Derivation of the models

The identified litter spots in the Sentinel-2 images, based on the VHR images, were labeled, and the reflectance of bands: B2–B8a and B11–B12 was extracted for each litter

pixel. Given the medium spatial resolution of the Sentinel-2 images, which makes the pixel-scale labeling process challenging, only pixels that showed significant reflectance anomalies were considered as litter. My goal was to distinguish riverine litter from its background; therefore, another class, namely, the non-litter class was identified. Within this class, pixels of water and hydraulic structures (e.g., dams, and bridges) were considered during the training, validating, and testing, with the same number of pixels as of the litter class.

To enhance the detection accuracy of the developed models, the Plastic Index (PI), Floating Debris Index (FDI), NDWI, and Normalized Difference Vegetation Index (NDVI) (Rouse et al., 1974) (Equation 4.1–Equation 4.4) were calculated and considered as independent variables, besides the reflectance of the spectral bands. Since the FDI, NDWI, and NDVI range between -1 and +1, they were normalized using the min-max normalization technique (Equation 4.5; Yu et al., 2009) to align with the reflectance domain of the PI and spectral bands (i.e., 0–1).
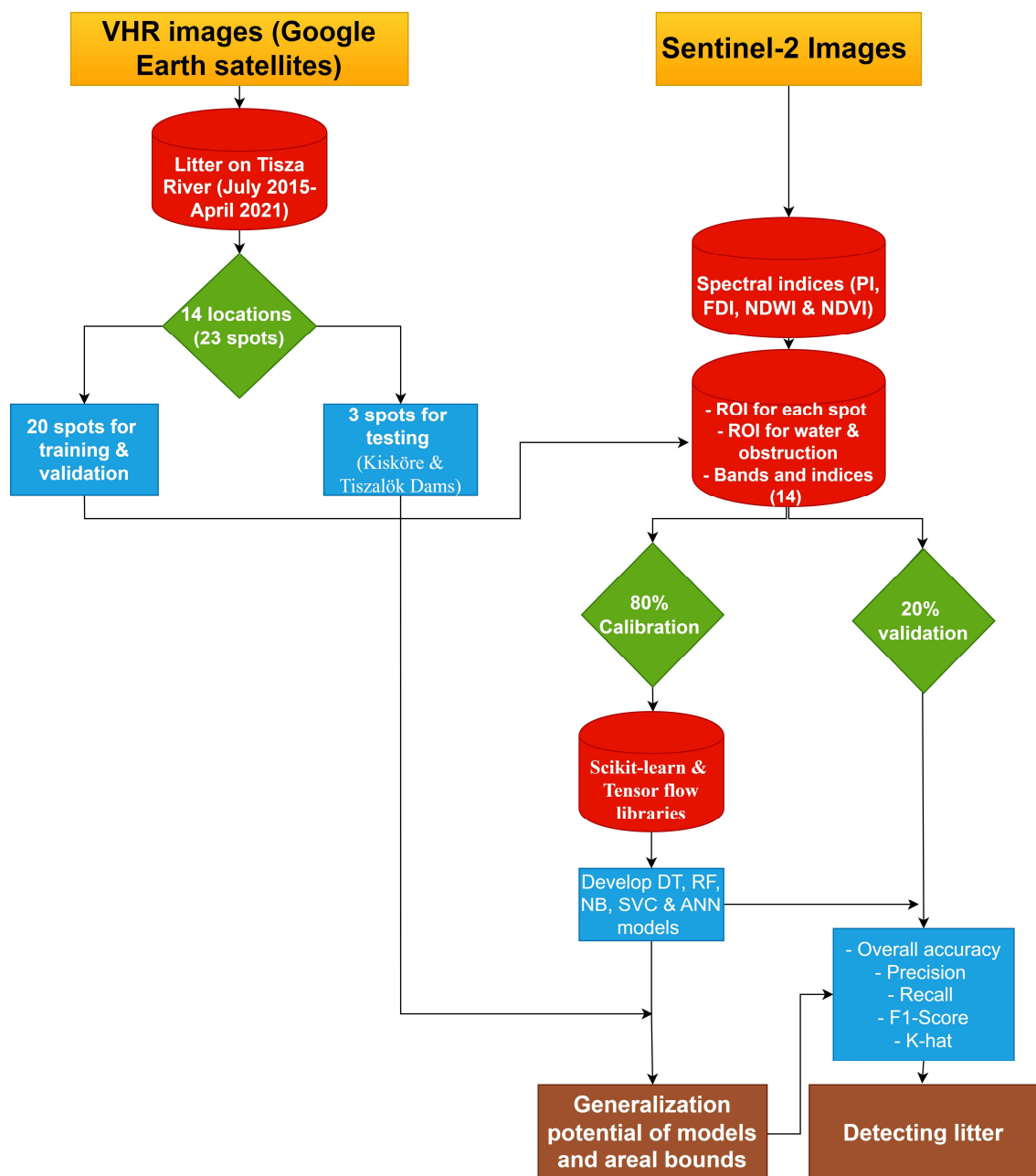
Figure 4.3. Integration of the very high spatial resolution (VHR) images from Google Earth satellites with Sentinel-2 images to develop riverine litter (including macroplastics) detector models through different machine learning algorithms.

$$PI = \frac{R_{NIR}}{R_{NIR} - R_{RED}} \qquad \text{Equation 4.1}$$

$$FDI = R_{NIR} - \left[R_{RE2} + (R_{SWIR1} - R_{RE2}) \times \frac{(\lambda_{NIR} - \lambda_{RED})}{(\lambda_{SWIR1} - \lambda_{RED})} \times 10 \right] \qquad \text{Equation 4.2}$$

$$NDWI = \frac{R_{GREEN} - R_{NIR}}{R_{GREEN} + R_{NIR}} \qquad \text{Equation 4.3}$$

$$NDVI = \frac{R_{NIR} - R_{RED}}{R_{NIR} + R_{RED}} \qquad \text{Equation 4.4}$$

$$X` = \frac{X - \min(X)}{\max(X) - \min(X)} \qquad \text{Equation 4.5}$$

Where: $R_{NIR}, R_{RED}, R_{RE2}, R_{SWIR1}$ and R_{GREEN}: reflectance of the various bands, including near-infrared, red, red edge 2, shortwave-infrared 1 and green bands respectively; $\lambda_{NIR}, \lambda_{RED}$, and λ_{SWIR1}: central wavelength of the near-infrared, red, and shortwave-infrared 1 bands; X and X`: original and normalized pixel values, respectively; min(X) and max(X): minimum and maximum values of the original pixel value.

All pixels from two classes [i.e., litter and non-litter (water and obstruction) classes] were divided into datasets: training, validation, and testing. The training dataset was used to develop the models, the validation dataset assessed model accuracy and the testing dataset evaluated model generalization capability and areal detection bounds. For the testing dataset, three litter spots with various areas and their surroundings ($\approx$ 1.0 km of the river) were separated, while the rest of the data were used for the training and validation process. Within the training and validation dataset (1974 pixels), a random 80% (calibration), and 20% (validation) split was applied using the scikit-learn library.

Five supervised machine learning algorithms, including the DT, RF, NB, Support Vector Classifier (SVC), and ANN were utilized to develop binary riverine litter models. The DT is a non-parametric, supervised machine learning algorithm that can be applied in classification and regression tasks (Breiman et al., 1984). It splits the dataset into subsets recursively based on the features of the data. At each step, the algorithm decides the features that give the best separation of data into distinct classes and subsequently minimizes the classification error. In this study, the classification and regression trees (CART) algorithm in the scikit-learn library was applied. Within this algorithm, the "Gini" criterion was used to measure the impurity in the dataset, and the "best" splitter to select the features and their thresholds that give the best split at each node.

The RF primarily relies on combining multiple DTs to improve prediction accuracy and mitigate overfitting (Breiman, 2001). The input data is divided randomly into subsets by bagging or bootstrap aggregation approaches forming multiple DTs. Each DT gives its prediction based on the included features and data. The final decision of the RF is based on the average (in the case of regression tasks) or majority voting (in the case of classification tasks) of the predictions made by the DTs. In this research, the RF classifier in the scikit-learn library was used to build the riverine litter model, utilizing 150 trees for the ensemble.

The NB is a probabilistic, supervised machine learning algorithm used for mainly classification tasks (Friedman et al., 1997). The algorithm is built based on bayes' theorem of probability and the naïve assumption of independent features. I have used the Gaussian NB algorithm in the scikit-learn library to develop the litter model, assuming that features (i.e., spectral bands and indices) follow a normal distribution (Biermann et al., 2020). Default values for the hyperparameters were used, with priors set to "none", and smoothing to "1e-09". The algorithm estimates the probability of each pixel belonging to the litter or non-litter based on the feature values and assigns it to the class with the highest probability.

The SVM is a powerful machine learning algorithm capable of handling complex data

distributions and high-dimensional features (Cortes and Vapnik, 1995). The classifier module of this algorithm, known as the SVC, aims to identify a hyperplane in "n" dimensions with the maximum margins. This maximization provides the best possible separation of classes and improves the generalization capability of the model to unseen data. In this study, the SVC module in the scikit-learn library was applied with the Radial Basis Function (RBF) kernel and regularization parameter (c) of 1000.

The ANN is inspired by the structure and operation of the human brain and serves as the fundamental building block of deep learning models (McCulloch and Pitts, 1943). An ANN consists of inter-connected cells (neurons) organized in three layers, including one input layer, one (or more) hidden layers, and one output layer. The input layer receives data features, the hidden layers perform some data transformations, and the output layer produces the final prediction. The training process begins by randomly selecting weights that connect neurons to each other. Each neuron applies an activation function to the weighted sum of its inputs, introducing non-linearity into the model and enabling it to learn complex patterns. The weights are iteratively updated through backpropagation to minimize loss/cost function using optimization techniques. In this study, the sequential model in Tensor Flow`s Keras library was employed to develop the riverine litter model. The model was structured with 14 neurons in the input layer, three hidden layers containing 14, 12, and 8 neurons each, and one neuron in the output layer. The Rectified Linear Unit (ReLU) activation function was considered for the hidden layers and the sigmoid function for the output layer. The loss/cost function was set to "binary crossentropy" and the optimizer to "adam". Also, a batch size of 32 and 400 epochs were employed. To avoid overfitting, a dropout layer with a rate of 0.5 was applied.

The performance of these algorithms is significantly influenced by the adjusted hyperparameters. Hence, they were fine-tuned automatically by the Optuna open-source Python library (Optuna) after defining a search space for every hyperparameter. The library contains many algorithms, yet the tree-structured parzen estimator (TPE) algorithm that models the objective function as a probability distribution was employed. This algorithm explores the search space of the hyperparameters through a tree structure which is updated iteratively based on the resulting accuracy. The optimizer function within the algorithm aimed to minimize the score (Equation 4.6) across 300 trials. The resulting optimized hyperparameter combinations for each machine learning algorithm (DT, RF, NB, SVC, and ANN) were then used to build the riverine litter model.

The contribution of the features (i.e., spectral bands and indices) to the overall accuracy of the derived models was revealed by the Shapley additive explanations (SHAP) Python library (Lundberg and Lee, 2017). This technique draws inspiration from cooperative game theory, and it quantifies the contribution of each feature through a SHAP value. This value is calculated based on the accuracy difference between a model with and without the existence of a particular feature, across all possible permutations. Since this study applied different machine learning algorithms with various structures, the three explainers of the SHAP library were used, including the tree explainer for the DT and RF algorithms, the kernel explainer for the NB and SVC algorithms, and the deep explainer for the ANN algorithm. The SHAP values for the features were visualized by a summary plot and the features were sorted in descending order of importance.

The models were validated by the overall accuracy, recall, precision, F1-score, and Cohen kappa score (Equation 4.6–Equation 4.10; Congalton, 1991), considering the validation dataset (20% of the dataset). These metrics were computed by the classification report and the Cohen kappa score functions available in the scikit-learn library. Remarkably, the overall accuracy, recall, precision, and F1-score range between 0 and 1, while the Cohen kappa score ranges between -1 and +1.

$$\text{Overall accuracy} = \frac{TP + TN}{TP + TN + FP + FN} \qquad \text{Equation 4.6}$$

$$\text{Precision (user's accuracy)} = \frac{TP}{TP + FP} \qquad \text{Equation 4.7}$$

$$\text{Recall (producer's accuracy)} = \frac{TP}{TP + FN} \qquad \text{Equation 4.8}$$

$$\text{F1-score} = 2 * \frac{Recall * Precision}{Recall + Precision} \qquad \text{Equation 4.9}$$

$$\text{K-hat} = \frac{(observed\ agreement - expected\ agreement)}{(1 - expected\ agreement)} \qquad \text{Equation 4.10}$$

$$\text{observed agreement} = \frac{(TP + TN)}{(TP + TN + FP + FN)}$$

$$\text{expected agreement} = \frac{[(TP + FP) * (TP + FN) + (TN + FN) * (TN + FP)]}{(TP + TN + FP + FN)^2}$$

Where: TP: true positive, TN: true negative, FP: false positive, and FN: false negative numbers.

4.5.2. *Testing the generalization capability of the developed models and revealing the spatiotemporal distribution of riverine litter in the Middle Tisza*

The testing dataset included three litter spots and their surrounding area. These spots varied in size, with a small spot (≤ 1 pixel), a medium spot (2–4 pixels), and a large spot (≥ 4 pixels). While the small and medium spots were located upstream of the Tiszalök Dam (1/6/2019), the large spot was located upstream of the Kisköre Dam (1/8/2020) (Figure 5.1). To evaluate the areal detection bounds of the models, the areal estimates of the three spots were compared to the actual areas derived by the VHR image. Also, the generalization capability of the models was evaluated by computing the overall accuracy, recall, precision, F1-score, and K-hat (Equation 4.6–Equation 4.10) based on the testing dataset.

The best-performing riverine litter model was employed to study its spatiotemporal distribution in the Middle Tisza (175 km long section; 276–451 river km), utilizing 61 historical Sentinel-2 images (2015–2021). Also, I investigated in detail the temporal trend of the areal extent of the litter spot located upstream of the Kisköre Dam (Figure 5.1) (2015–2021) by applying the seasonal Mann-Kendall trend analysis test (Mann, 1945; Kendall, 1975). This test type was applied since the river behaves differently during the low and high stages. Thus, two seasons were considered, including flood periods (March–April and June–July) and low stage (August–February).

4.6. Development of remote sensing-based suspended sediment discharge models in the Tisza and Maros Rivers

As at-a-site Q_s measurements are not frequently performed, I aimed to build a model on it, where both components of Q_s, i.e., Q and SSC were derived by satellite images (Figure 4.4). The in-situ measurements of Q were combined with Sentinel-2 images and hydraulic geometry theory to produce Q models. Similarly, the in-situ measurements of SSC at specific sites were combined with Sentinel-2 images using some machine learning algorithms (i.e., ANN, SVM, and RF) to produce SSC models. The top-performing Q and SSC models were then used to investigate the temporal change in Q_s within the Lower Tisza and Maros Rivers, utilizing historical Sentinel-2 images acquired between 2015 and 2021.

4.6.1. *Water discharge models*

The Q was modeled by the at-a-station-hydraulic geometry (AHG) power law method and its modified version at-many-station hydraulic geometry (AMHG) method. These

methods are based on the river width–*Q* relationship (Equation 2.1), with the width data obtained by the Sentinel-2 images. Additionally, a novel AHG machine learning (AHG ML) method was developed by combining the AHG theory with some machine learning algorithms, including the ANN, SVM, and RF.
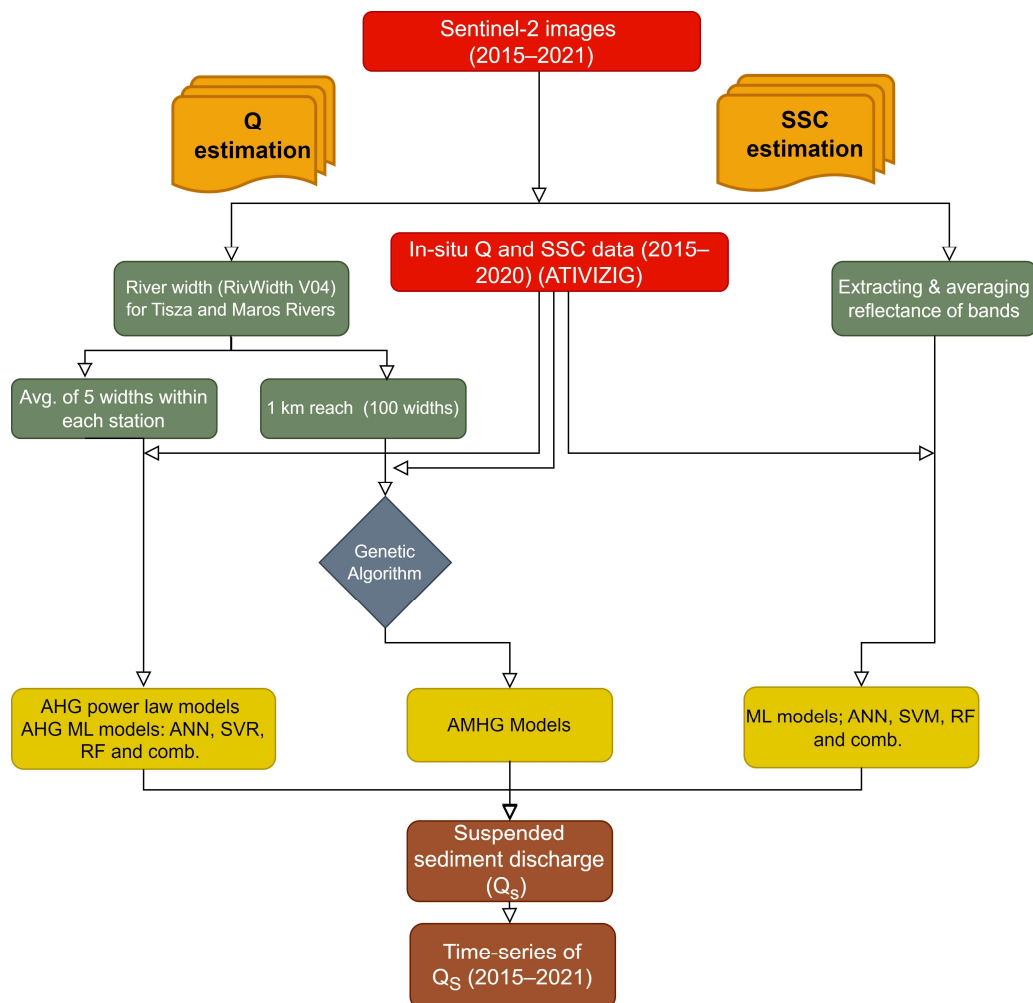
Figure 4.4. Applied methodology to estimate the suspended sediment discharge (Q_s), and its two components: water discharge (Q) and suspended sediment concentration (SSC) by satellite images, hydraulic geometry theory, and various machine learning (ML) algorithms.

4.6.1.1. At-a-station hydraulic geometry (AHG) power law, and machine learning models

A time-series of the river width at the three gauging sites in the Tisza (Algyő and Szeged) and Maros (Makó) Rivers (Figure 4.2A–C) was obtained by the Sentinel-2 images (Tisza: 29 images and Maros: 27 images; 2015–2020) and combined with in-situ measurements of the *Q* through the AHG power law method (Equation 2.1). The river width was estimated by the RivWidth V04 software (Pavelsky and Smith, 2008) based on a water mask derived from the application of the NDWI and the OTSU automatic thresholding method. To minimize errors associated with width estimations, five cross-sections spaced 10–20 m upstream and downstream of the original cross-section were estimated and averaged (yellow transects in Figure 4.2A–C). The time-series of the averaged widths and the corresponding *Q* were fitted by a power-law function in the SciPy library.

This study represents a pioneering effort in combining the AHG theory with machine learning algorithms, leveraging the potential of machine learning algorithms for dealing with intricate, non-linear problems. Specifically, the regression module of three machine learning algorithms, including ANN, SVM, and RF was used to formulate *Q* models. These models

were based on the time-series of river width and Q data at the three gauging sites. The data was randomly divided into 80% for calibration and 20% for validation by the train-test-split function in the Scikit-learn library. The average prediction of the three models was also calculated and considered as a "combined model". All hyperparameters were finetuned by the Optuna library (Table 4.2).

Table 4.2. Finetuned hyperparameters obtained by the Optuna library for developing water discharge (Q) models based on artificial neural network (ANN), support vector machine (SVM), and random forest (RF) algorithms.

Artificial Neural Network (ANN)	Support Vector Machine (SVM)	Random Forest (RF)
Input and output layers: 1 neuron Two hidden layers: 20 neurons each Activation function: relu Solver: lbfgs Max iterations: 200	Kernel: polynomial (2nd degree) ε: 0.01 Regularization parameter (c): 2	Number of estimators: 300 Maximum feature: auto Minimum sample split: 2 Minimum sample leaf: 4 Cost function: mse

4.6.1.2. At-many-stations hydraulic geometry (AMHG) models

In the AMHG method, the estimation of the Q relies on the application of the AHG power law method across several transects within a mass-conserved reach of a river. This approach is grounded in the study of Gleason and Smith (2014), who proved a log-linear relationship between the coefficients *a* and exponents *b* of these transects. In this study, a 1 km long reach was considered at the three gauging sites (i.e., Algyő, Szeged, and Makó) where 100 transects were defined (green transects in Figure 4.2A–C). The water width at the transects was measured by the RivWidth software based on the Sentinel-2 images (Tisza: 29 images; Maros: 27 images). For each transect, the time-series of the estimated water width and corresponding Q, consistent for all transects on a particular date, were fitted by the power law formula in the SciPy library. The resulting 100 sets of *a* and *b* values at each gauging site were then fitted by a log-linear relationship to determine their domains.

The optimization of the resulting *a* and *b* values to minimize the Q difference between every pair of transects was implemented by the genetic algorithm (GA; Holland, 1992). The GA is a powerful optimization algorithm inspired by the natural selection and genetic evolution process. The optimization process was initiated by selecting 10 random solutions (i.e., *a* and *b* values for both transects) from the predefined domains in the log-linear relationship. This solution is denoted as a chromosome and the individual coefficient *a* or exponent *b* is a gene.

Before proceeding with the optimization process, the validity of the selected chromosomes was evaluated. The validation process involved combining them with the transect widths to ensure that they provide reasonable Q values falling between the minimum and maximum Q limits of the river. Chromosomes that provide unreasonable Q values were replaced iteratively until they reached 10 valid chromosomes. The Q limits can be determined from historical Q in the river or empirically estimated by Equation 4.11 and Equation 4.12 (Gleason and Smith, 2014). The Tisza River's discharge limits were specified as a minimum of 50 m³/s and a maximum of 4000 m³/s, while their counterparts in the Maros River were 10 m³/s and 850 m³/s, respectively.

$$Q_{min} = w_{min} \times 0.5\,m\,(depth) \times 0.1\,m/s\,(velocity) \qquad\qquad \text{Equation 4.11}$$

$$Q_{max} = w_{max} \times 10\,m\,(depth) \times 5.0\,m/s\,(velocity) \qquad\qquad \text{Equation 4.12}$$

where: w_{min} and w_{max}: minimum and maximum river width observed throughout the studied period.

The 10 valid chromosomes proceeded through the selection phase, where they were ranked based on their fitness (Q conservation). Then, chromosomes underwent crossover and mutation processes. While crossover aims to exchange genes between chromosomes, mutation aims to alter a few genes randomly in a chromosome, which was particularly valuable in cases where unsuitable genes were present. The crossover and mutation rates were adjusted to 0.8 and 0.1, respectively (Gleason and Smith, 2014). Following these genetic operations, the order of the modified chromosomes was rearranged based on their updated fitness scores. Subsequently, the five least fit chromosomes are replaced by another fresh chromosome from the population domain. Once the selection, crossover, and mutation processes had been completed, the chromosomes passed the first generation. In this study, altogether 20 generations were applied for every pair of cross-sections.

Every transect within the 1 km reach was paired with the rest of the transects which resulted in 990,000 (Equation 4.13) estimates of a and b values. The median of the resulting a and b values was calculated and considered as the final optimized constants for each transect. Based on these constants and the corresponding water width at each transect, 100 estimates of Q were calculated, and their median was considered as the final optimized Q for the reach. The GA code developed in this study can be found on the GitHub repository: https://github.com/AMohsenMetwaly/Genetic-Algorithm.

$$\text{Number of } a \text{ and } b \text{ estimates for each transect} = (n^2 - n) \times 100 \qquad \text{Equation 4.13}$$

where n: is the number of transects (100 transects in this study).

The performance of the AHG power law, AHG machine learning, and AMHG methods was evaluated by three metrics, including the coefficient of determination (R^2), root mean square error (RMSE), and mean absolute error (MAE) (Equation 4.14–Equation 4.16).

$$R^2 = 1 - \frac{\sum_{i=1}^{N}(y_i - \hat{y}_i)^2}{\sum_{i=1}^{N}(y_i - \bar{y})^2} \qquad \text{Equation 4.14}$$

$$RMSE = \sqrt{\frac{\sum_{i=1}^{N}(y_i - \hat{y}_i)^2}{N}} \qquad \text{Equation 4.15}$$

$$MAE = \frac{1}{N}\sum_{i=1}^{n}|y_i - \hat{y}_i| \qquad \text{Equation 4.16}$$

where: y_i: observed value, $\hat{y}_i$: predicated value by a model, $\bar{y}$: mean of the observed values, and N: number of observations.

The generalization capability of the best-performing Q model was assessed by comparing its predictions over totally ungauged dates between July 2015 and May 2021 (93 Sentinel-2 images) with daily Q data obtained from ATIVIZIG at the three gauging sites.

4.6.2. *Suspended sediment concentration and discharge modeling*

The measured SSC at five verticals in the cross-sections of the Tisza River at Szeged and the Maros River at Makó (Figure 4.2D–E), along with the acquired Sentinel-2 images (Tisza: 29 images and Maros: 27 images) were used to develop SSC models employing machine learning algorithms. Specifically, the images were divided into two groups based on the

hydrological condition of the river, including floods and low stage images. For flood images, the high stage verticals (red lines in Figure 4.2D–E) were considered, while for low stage images, the low stage verticals (green lines in Figure 4.2D–E) were utilized. In both cases, the entire cross-section was divided into five segments, with each vertical approximately in the middle of its respective segment. Afterward, the average reflectance of the pixels (B2–B8a) within each segment was calculated and correlated with the SSC measured at the corresponding vertical, by the ANN, SVM, and RF. The reflectance and SSC data were divided into 80% (calibration) and 20% (validation) by the scikit-learn library. The hyperparameters of the algorithms were finetuned using the Optuna library (Table 4.3). Also, the three developed models were integrated into a "combined model" by averaging their predictions, and the outcomes were compared with the individual original models. The models` performance was evaluated by the R^2 and RMSE (Equation 4.14–Equation 4.15).

Table 4.3 Finetuned hyperparameters obtained by the Optuna library for developing suspended sediment concentration (SSC) models based on artificial neural network (ANN), support vector machine (SVM), and random forest (RF) algorithms.

Artificial Neural Network (ANN)	Support Vector Machine (SVM)	Random Forest (RF)
Input layer: 8 neurons One hidden layer: 50 neurons Output layer: 1 neuron Activation function: relu Solver: lbfgs Max iterations: 20	Kernel: polynomial (4th degree) ε: 0.1 Regularization parameter (c): 0.7	Number of estimators: 600 Maximum feature: auto Minimum sample split: 2 Minimum sample leaf: 4 Cost function: mse

The best-derived Q and SSC models were employed to investigate the temporal change of the Q_s at the three gauging sites (i.e., Algyő, Szeged, and Makó) for a relatively long period (July 2015–May 2021; 93 images) applying Equation 4.17 (Porterfield, 1972).

$$Q_s = K \times Q \times SSC \hspace{4cm} \text{Equation 4.17}$$

where: Q_s: suspended sediment discharge (ton/day); K: conversion unit constant (0.0864 SI units); Q: water discharge (m^3/s); SSC: suspended sediment concentration (g/m^3).

4.7. Exploring the dynamics of water mixing patterns in the Tisza–Maros confluence and their connection to hydrological parameters

The spatiotemporal dynamics of the water mixing patterns in the Tisza–Maros confluence and its relationship to the changes in the rivers` hydrological parameters were investigated by the Sentienl-2 images and in-situ hydrological data (Figure 4.5). The K-means unsupervised algorithm was applied to 143 Sentinel-2 images, classifying the surface water at the confluence area (Figure 3.1D) into Tisza water (TW), Maros water (MW), and mixed water (MIX) exploiting clear watercolor difference. The areal coverage (%) of the three classes along with the longitudinal extent (L) of the MW into the Tisza were correlated to measured (e.g., water stage and discharge) and calculated (e.g., the difference and ratio of daily water change, water slope, and water discharge difference and ratio) hydrological parameters in the rivers, to assess the strength of their correlation. Also, predictive equations for the TW, MW, MIX, and L were developed based on the hydrological parameters of the rivers (as independent variables) considering both collective and individual hydrological scenarios. The study also identified the predominant mixing patterns that occur throughout the year to support future measurements in the confluence area.
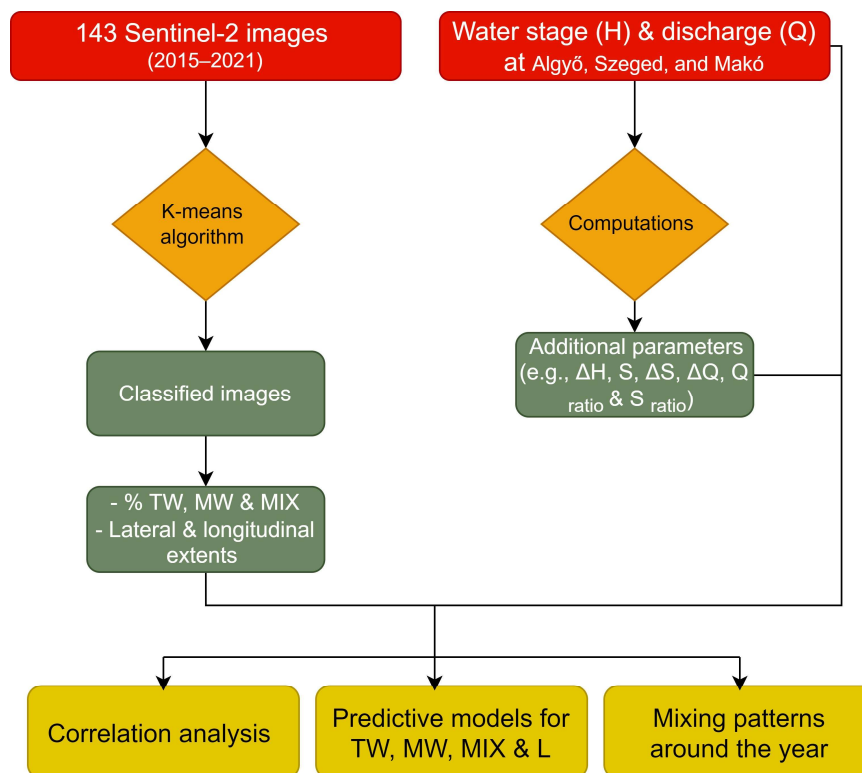
Figure 4.5. Applied methodology to investigate the dynamics of water mixing patterns in the Tisza–Maros confluence and its relationship to changes in the hydrological parameters.

4.7.1. *Classifying water types in the confluence area by Sentinel-2 images*

Given the elevated SSC of the Maros River (1600 g/m^3) compared to the Tisza River (640 g/m^3), usually they exhibit dissimilar colors in the confluence area, detectable by satellite sensors (Bogárdi, 1971 and 1974). As such, to study the mixing process in the confluence area, the K-means classification algorithm (Lloyd, 1982) was used to classify the acquired 143 Sentinel-2 images. Three classes were identified, including the water of the Tisza (TW), the water of the Maros (MW), and their mixture (MIX). These classes represent the gradient in SSC and consequently reflectance from the highest in the case of MW, to moderate in the case of MIX, to the lowest in the case of TW. The bands with high sensitivity to SSC changes along with high spatial resolution of 10 m, including the B2–B4, were employed for performing the classification task (Dekker et al., 2002). The algorithm initializes the classification process by identifying a random centroid for each cluster (i.e., TW, MW, and MIX) and then assigns the pixels to the nearest cluster centroid (the lowest sum of square errors) based on the selected source bands (i.e., B2–B4). Afterward, the centroid positions are optimized iteratively, and consequently, the pixels, until the maximum number of iterations is achieved, or the centroids stabilize (Lloyd, 1982; Likas et al., 2003).

The K-means algorithm was applied due to its potential to accommodate the threshold dynamism of the three classes (TW, MW, and MIX) that may arise from temporal changes in the SSC as well as chemical and biological processes of both rivers. The images were analyzed individually to ensure that the actual mixing pattern was well-depicted. Occasionally, the images contain some shadow of trees and/or bridges, which is misrepresented by defining three classes only, thus, an additional class for shadow was defined in these cases. The area of the shadow class was subtracted from the total area of the confluence and the areal coverage of the three water classes was recalculated accordingly.

Based on the classified images, the areal coverage (%) of TW, MW, and MIX was quantified as a percentage (%). The longitudinal mixing was investigated by estimating the longitudinal extent (L) of the MW into the Tisza expressed as a function of the Tisza`s

52

average width (162.2 m in the confluence area). The lateral mixing was assessed by estimating the lateral extent of the TW, MW, and MIX at five transects (T1–T5), spaced 1 km apart (Figure 3.1D), expressed as a percentage of the transect width.

4.7.2.   Determining hydrological parameters of the joining rivers

Additional hydrological parameters were calculated at the three gauging sites (i.e., Algyő, Szeged, and Makó) to assess their correlation with the water mixing process in the confluence area. Daily water level change (ΔH) was calculated by subtracting the water level on a particular day from its counterpart on the previous day. Also, the difference between the daily ΔH of the Tisza (at Algyő) and the daily ΔH of the Maros (at Makó) was calculated ($\Delta H_{Algyő}$–$\Delta H_{Makó}$). Both the absolute difference (ΔQ) and ratio (Q_{ratio}) in the water discharge of the rivers were calculated. While the absolute difference (ΔQ) was calculated by subtracting Q at Algyő ($Q_{Algyő}$) from its counterpart at Makó ($Q_{Makó}$), the discharge ratio was obtained by dividing the Q at Makó ($Q_{Makó}$) by the Q at Szeged (Q_{Szeged}). To calculate the daily water slope of the rivers (S), the relative daily water levels were transformed into absolute levels based on the zero-point altitudes at the gauging sites (i.e., Algyő: 74.0 m, Szeged: 73.7 m and Makó: 79.5 m). Then, the distance between Algyő and Szeged (for the Tisza slope) and between Makó and Szeged (for the Maros slope) were measured along the centerlines. The elevation differences between sites were combined with the measured distances to estimate the daily water slopes of the rivers (S_{Tisza} and S_{Maros}). Also, the slope difference between both rivers (ΔS) was estimated by subtracting the slope of the Tisza from its counterpart of the Maros.

4.7.3.   Correlation between hydrology and water mixing process in the confluence area

The correlation between measured and calculated hydrological parameters and the spatiotemporal dynamism of the water mixing process in the confluence area, represented by TW, MW, MIX, and L was evaluated by the Pearson correlation test (Freedman et al., 2007). The correlation coefficient (r) ranges between -1 and +1, and it was categorized as very weak for $0.0 \leq r \leq 0.19$ (-0.19), weak for 0.2 (-0.2) $\leq r \leq 0.39$ (-0.39), moderate for 0.4 (-0.4) $\leq r \leq 0.59$ (-0.59), strong for 0.6 (-0.6) $\leq r \leq 0.79$ (-0.79) and very strong for 0.8 (-0.8) $\leq r \leq 1.0$ (-1.0) (Stigler, 1989).

Predictive equations for the areal coverage of the TW, MW, and MIX and the longitudinal extent of the MW into the Tisza (L) were developed based on the hydrological parameters as independent variables using the stepwise multilinear regression technique. The predictive equations were developed based on three scenarios, including case 1: all data considered, case 2: low and medium stages data considered, and case 3: high stage data considered. The classification of the data was achieved by the hierarchical cluster analysis (HCA), specifically Ward's algorithm (Ward, 1963), based on the hydrological parameters and the areal percentages of TW, MW, and MIX. While case 1 predictive equations can be applied across all water stages, providing rough estimates, case 2 and 3 equations are suited for specific hydrological conditions and provide better estimates than case 1. The statistical analysis was performed by the IBM SPSS software V26.0 (IBM).

4.8. Analyzing the spatiotemporal distribution and correlation of surficial suspended sediment and microplastic concentrations in the Tisza River

The spatiotemporal distribution and correlation of surficial SS and MP concentrations in the Tisza River were investigated in detail based on intensive spatial (26 sites; August 2021 and July 2022) and temporal (140 samples collected every 5 days; May 2021–May 2023) in-situ data (Figure 4.6). Also, Sentinel-2 images were used to fill surficial SSC data shortage in 2021. The hydrological condition of the river was divided into low stages and flood waves based on daily water stage data recorded in the Mindszent site. Moreover, flood waves were

categorized into minor and medium floods, each further subdivided into rising, peak, and falling phases. Parametric and non-parametric tests were applied to scrutinize potential statistical differences in the spatial and temporal distributions of both surficial SS and MP concentrations. Furthermore, their correlation was systematically assessed in space in time.
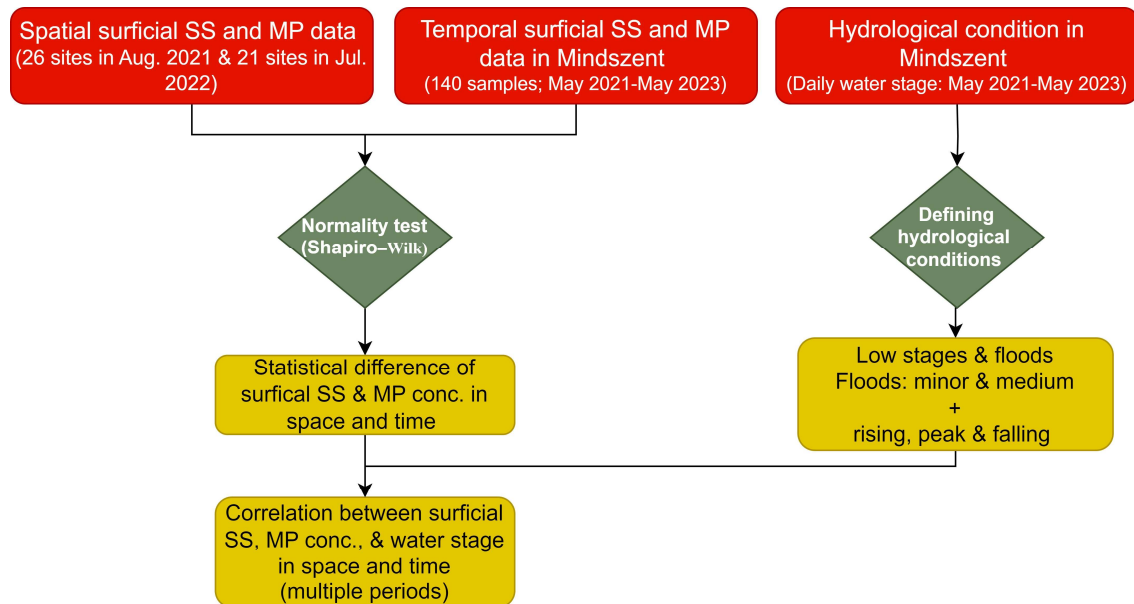
Figure 4.6. Applied methodology to investigate the spatiotemporal distribution and correlation of surficial suspended sediment (SS) and microplastic (MP) concentrations in the Tisza River.

4.8.1.   Defining hydrological periods and statistical analysis

The longitudinal measurements were performed in summer during low stages, while the temporal measurements in Mindszent covered various hydrological conditions. Thus, they were classified into low stages and flood waves. Low stages were recognized based on daily water level (H≤100 cm) and limited variations in daily water level (≤15 cm/day). Flood waves, on the other hand, were identified based on significant daily water level changes (>15 cm/day). Also, they were divided into minor (≤3 weeks) and medium floods (>3 weeks), based on flood duration, and subdivided further into rising, peak, and falling phases.

The statistical differences in surficial SS and MP concentrations were investigated in space and time. The assumptions of normality and equal variance were not achieved for the spatial data of MP concentration along the Tisza in 2021 and 2022 (Shapiro–Wilk normality test; $p=0.028$) and for the temporal data of surficial SS and MP concentrations in the Mindszent site (Shapiro–Wilk normality test; SSC: $p<0.001$; MP: $p=0.003$); thus, the non-parametric Kruskal-Wallis H and post hoc tests were applied to perform the statistical difference evaluation (Kruskal and Wallis, 1952). In the meantime, the spatial data of surficial SSC along the Tisza in 2021 and 2022 followed the normal distribution (Shapiro–Wilk normality test; $p=0.395$); hence, the parametric one-way ANOVA test was employed. The findings were represented by alphabetical letters in boxplots following Mattos et al. (2017). Datasets with the same letters in a single (e.g., "a") or a double form (e.g., "ab") indicate no statistical difference, while different letters represent statistically significant differences. The p-values were also provided for statistically different datasets.

The spatial correlation between surficial SS and MP concentrations along the river was assessed in both measuring years (i.e., 2021 and 2022) by the Spearman's rank-order correlation test. Similarly, the same test was employed to evaluate the strength of correlation between surficial SSC, MP concentrations and water stage (H) at the temporal monitoring site ($\rho_{SSC–H}$, $\rho_{MP–H}$, $\rho_{SSC–MP}$) during various hydrological periods (ρ_{low}: low stages; ρ_{minor}: minor floods; ρ_{medium}: medium floods; ρ_{rising}: rising limb; ρ_{peak}: peak; $\rho_{falling}$: falling limb). The

correlation was labeled as very strong for correlation coefficient (ρ) ≥0.7 (-0.7), strong for 0.4 (-0.4) ≤ ρ ≤ 0.69 (-0.69), moderate for 0.3 (-0.3) ≤ ρ ≤ 0.39 (-0.39), weak for 0.2 (-0.2) ≤ ρ ≤ 0.29 (-0.29) and negligible for 0.01 (-0.01) ≤ ρ ≤ 0.19 (-0.19) (Dancey and Reidy, 2007). All statistical analysis was performed by the IBM SPSS software V26.0 (IBM).

4.9. Development of remote sensing-based surficial suspended sediment and microplastic concentration models in the Tisza River

To develop remote sensing-based surficial SS and MP concentration models, the correlation between reflectance or backscattering of the various optical (i.e., Sentinel-2 and PlanetScope) and active (i.e., Sentinel-1) sensors and the surficial SS and MP concentration measurements (i.e., spatial: 26 sites: 2021 and 2022; temporal: 140 in Mindszent and 70 in Szeged) was tested in advance (Figure 4.7). Direct models for both variables were developed considering reflectance or backscattering of satellite sensors as independent variables. Besides, in-direct models for MP concentration were developed based on surficial SSC as a proxy. The generalization capability of the developed models was tested in space and time.
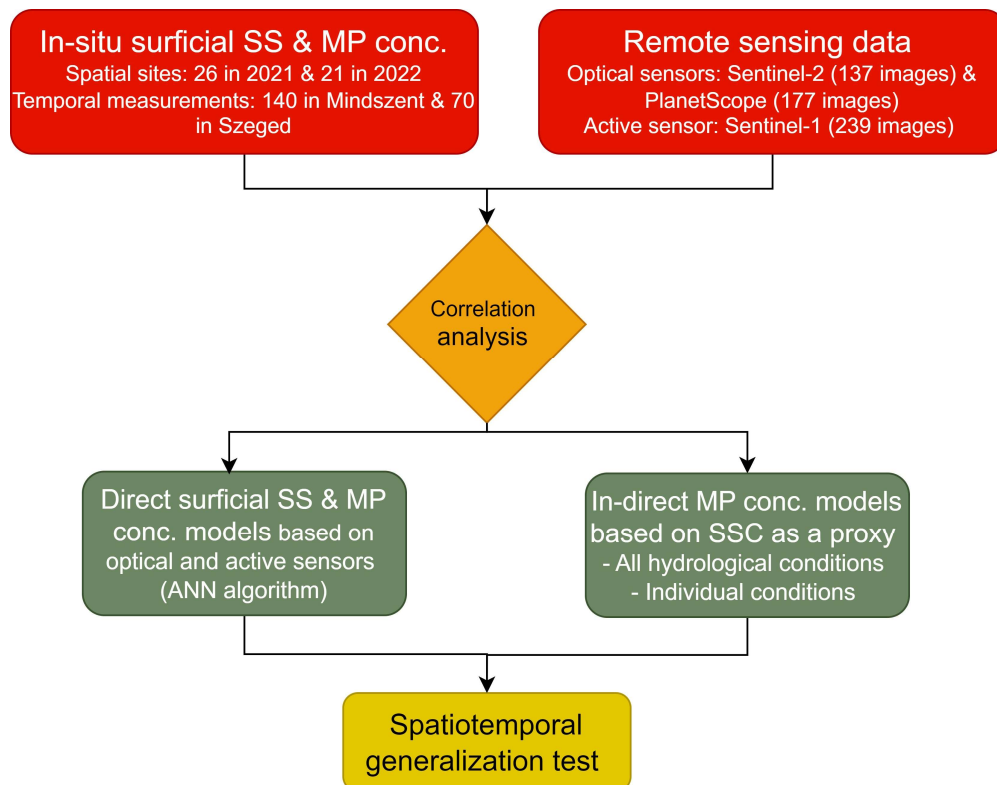
Figure 4.7. Applied methodology to develop surficial suspended sediment (SS) and microplastic (MP) concentration models based on optical (Sentinel-2 and PlanetScope) and active sensors (Sentinel-1).

4.9.1. Correlation test and direct models of surficial suspended sediment and microplastic concentrations

A region of interest (ROI) of 2×2 pixels (i.e., 20×20 m) in Sentinel-2 and Sentinel-1 and 6×6 pixels (i.e., 18×18 m) in PlanetScope were identified around every spatiotemporal sampling site in the Tisza River. Then, the reflectance of the various bands of Sentinel-2 (137 images) and PlanetScope (177 images) satellites, as well as the backscattering of the Sentinel-1 channels (239 images), were extracted from these ROIs. Spearman`s rank-order correlation test was applied to assess the correlation between both variables (i.e., surficial SS and MP concentrations) and reflectance or backscattering data, as the assumption of normality of both variables was rejected (Shapiro–Wilk normality test; *p*<0.001).

The ANN algorithm was applied to develop surficial SS and MP concentration models based on the reflectance of Sentinel-2 and PlanetScope images, along with the backscattering of the Sentinel-1 channels. This algorithm was chosen owing to its potential in dealing with complex, non-linear, and high-dimensional problems. In the case of Sentinel-2, all but bands with a coarse spatial resolution of 60 m (i.e., B1, B9, and B10) and bands with low sensitivity to surficial SSC variations (i.e., B11 and B12) were selected as independent variables. Likewise, all bands but B1 and B8 were chosen as independent variables in the case of the PlanetScope images. Both the VV and VH channels in Sentinel-1 images were used.

To develop the models, the datasets of the surficial SS and MP concentrations and reflectance or backscattering data were divided into five training and validating sets by the k-fold cross-validation in the scikit-learn library. The models` hyperparameters were automatically finetuned by the Optuna library (Table 4.4). The models were evaluated by the $R^2$, RMSE, and MAE (Equation 4.14–Equation 4.16). Finally, the contribution of each band to the models` performance was identified by the SHAP library.

Table 4.4. Finetuned hyperparameters obtained by the Optuna library for developing the surficial suspended sediment and MP concentration models based on the reflectance of optical (Sentinel-2 and PlanetScope) and active sensors (Sentinel-1).

	Model	Hyperparameters						
		Hidden layer sizes	Activation function	Solver	Alpha	Learning rate	Maximum iteration	Batch size
SSC	Sentinel-2	(100, 5, 20)	logistic	lbfgs	0.0003	invscaling	604	67
SSC	PlanetScope	(40, 10, 20)	relu	lbfgs	0.0239	constant	669	120
SSC	Sentinel-1	(50, 50)	tanh	adam	0.0001	constant	521	44
MP	Sentinel-2	(100)	relu	adam	0.0191	invscaling	985	33
MP	PlanetScope	(150, 150)	tanh	adam	0.0001	adaptive	865	121
MP	Sentinel-1	(10, 15)	relu	sgd	0.0011	adaptive	748	116

4.9.2. *Proxy models of microplastic concentration by surficial suspended sediment concentration and spatiotemporal generalization capability of models*

The MP concentration models developed directly based on passive and active sensors exhibited low estimation accuracy. Therefore, indirect MP concentration models based on surficial SSC as a proxy were developed, exploiting their elevated correlation coefficients (ρ), especially during flood waves. The models were developed considering collectively all hydrological conditions, and individually during low stages and rising, peak, and falling phases of flood waves. To streamline the regression process, simpler regression techniques, such as linear and polynomial regressions were tested.

The generalization capability of both the direct and indirect models was evaluated in space and time. Certain surficial SS and MP concentration measurements, obtained in various spatiotemporal scales, were omitted, and used as a testing dataset, before partitioning the data into training and validation sets. The temporal testing data covered all hydrological scenarios, including low stages and rising, peak, and falling phases of flood waves. Meanwhile, the spatial testing data involved eight sites "i" (Aranyosapáti)–"p" (Tiszaroff) located upstream of the Kisköre Dam, measured during the July 2022 campaign.

5. RESULTS AND DISCUSSION

The integration of satellite sensors with in-situ measurements has elucidated characteristic patterns in the spatiotemporal dynamics of not only SS but also plastic pollution (MP and MaP) transport in the Tisza River. This comprehensive analysis highlights the similarities and distinctions in their transport behaviors under various hydrological scenarios and in response to longitudinal variables, such as tributaries and hydraulic structures. The frequent samplings and the utilization of optical (i.e., Sentinel-2 and PlanetScope) and active (i.e., Sentinel-1) satellite sensors have facilitated the development of reliable SS, MP, and MaP concentration models, albeit with inherent limitations. Yet, they still furnish valuable data for decision-makers across multiple spatiotemporal scales. A detailed exposition of these findings is presented within this chapter.

5.1. Spatiotemporal distribution of riverine litter/macroplastic (MaP) in the Tisza River

5.1.1. *Riverine litter composition and transport rate*

Based on my in-situ observations in the Tisza River in Szeged, organic materials, mainly woody debris dominated the riverine litter transport (Figure 5.1A). This is likely associated with the elevated bank erosion rate (1.7 m/year; Kiss et al., 2019a) at the meandering sections of the Tisza, where organic debris regularly enters the river. Some MaP were observed too (Figure 5.1A); however, they usually accumulate in larger clusters and drift together. Similar riverine litter composition was documented by Katona (2019) in the Middle Tisza, upstream of the Kisköre Dam, where only 12.5 % of the floating debris consisted of MaPs, while the rest were organic materials. Moreover, in February 2021, around 22 tons of riverine litter were retrieved in the Upper Tisza near the Ukrainian border (Vásárosnamény) with MaPs accounting for just 17.3% (PETKUPA, 2021).
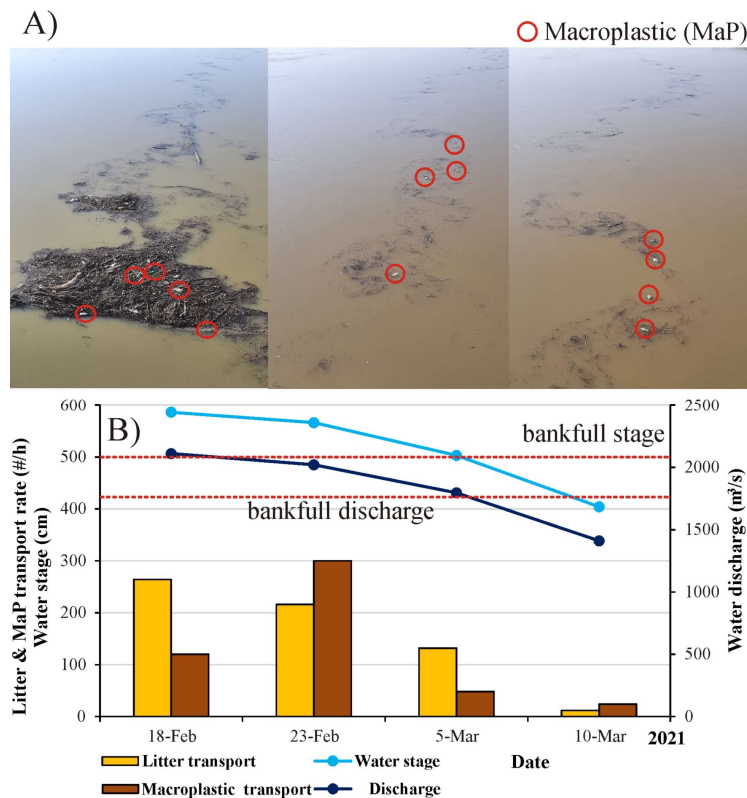

Figure 5.1. During the in-situ campaigns in Szeged, litter spots were identified with different shapes and sizes (Images captured on February 23rd, 2021; 9:40 UTC) (A). The litter and macroplastic (MaP) transport rate was compared to the water stage and discharge of the Tisza at Szeged (B).

57

To quantify the transport rate of riverine litter, a single spot was defined as a continuous litter irrespective of its size. For instance, in Figure 5.1A, the entire litter mass in the three shots was treated as a single spot due to its continuity. Based on this assumption, the mean litter transport rate during the study period (February–March 2021) was 156 spot/h. The transport rate was strongly associated with water stage and discharge conditions since the highest rate (264 spot/h) was observed with the greatest water stage and discharge (586 cm and 2110 m^3/s), and the lowest rate (12 spot/h) occurred during the period of the lowest water stage and discharge (404 cm and 1410 m^3/s) (Figure 5.1B). However, it should be noted that the river was already on a falling limb at the beginning of the observation; thus, the transport rate probably was higher in the earlier rising or peak stages.

This high transport rate is explained by the high stream power of the river during flood waves, allowing it to drag litter from floodplains and riverbanks, along with the contributions from tributaries. As soon as the water stage drops, the transport rate diminishes as the river becomes isolated from floodplain sources (Van Emmerik et al., 2022) (Figure 5.1B). The observed transport rate in the Tisza (12–264 spot/h) was comparable to that in the Rhone River, France (0–293 spot/h; Castro-Jiménez et al., 2019); however, it was slightly higher than the Tiber River, Italy (10–130 spot/h; Crosti et al., 2018).

Concerning MaP transport, it showed a similar trend over the study period. However, the highest transport rate (300 items/h) was observed a week later (on February 23rd), following the highest stage and discharge (Figure 5.1B). Afterward, it dropped substantially to 48 items/h on March 5th and further declined to 24 items/h on March 10th. The mean MaP transport rate in the Tisza during the study period (123 items/h) was approximately three times higher than that observed in the Rhine River (42 items/h; Vriend et al., 2020). However, the Rhine was monitored during a low stage, while the Tisza was during a flood wave. Although the Klang River was monitored during the low stage, it showed a 12 times higher transport rate than the Tisza (1500 items/h; Geraeds et al., 2019).

5.1.2. Spatiotemporal dynamics of riverine litter in the Tisza River (Hungary) based on very high spatial resolution (VHR) Google Earth satellite images

The visual analysis of the VHR images from the Google Earth satellites, between July 2015 and May 2021, identified 14 litter spots along the Hungarian section of the river (Figure 5.2 and Table 5.1). The areal extent of the spots varied between 25 m^2 (smaller than a Sentinel-2 pixel) to 9600 m^2 ($\approx$ 96 pixels). Typically, the spots appear just once in most locations. However, a notable exception was observed upstream of hydraulic structures, primarily dams (e.g., the Kisköre Dam; spots 8A–G in Table 5.1). The temporal distribution of the spots showed a characteristic pattern, as they typically appear in March, June, and August, with a notable occurrence in 2020.

5.1.3. Spatiotemporal dynamics of riverine litter in the Middle Tisza based on Sentinel-2-based models

The best-derived Sentinel-2-based riverine litter model was applied to unveil its spatiotemporal dynamics along a 175-km long reach in the Middel Tisza, employing 61 images (2015–2021). Three states representative for the various hydrological conditions were depicted, including bankfull flood, minor flood, and low stages (Figure 5.3). The area of the detected spots along the reach ranged between 36,900 and 99,000 m^2 (369–990 pixels) across the three hydrological conditions. However, the largest (2300–28,000 m^2; 23–288 pixels) and most persistent litter spot was noticed upstream of the Kisköre Dam. This finding consists with similar patterns observed in many other rivers worldwide, e.g., the Three Georges Dam in the Yangtze River, China due to the trapping effect of dams (Zhang et al., 2015).
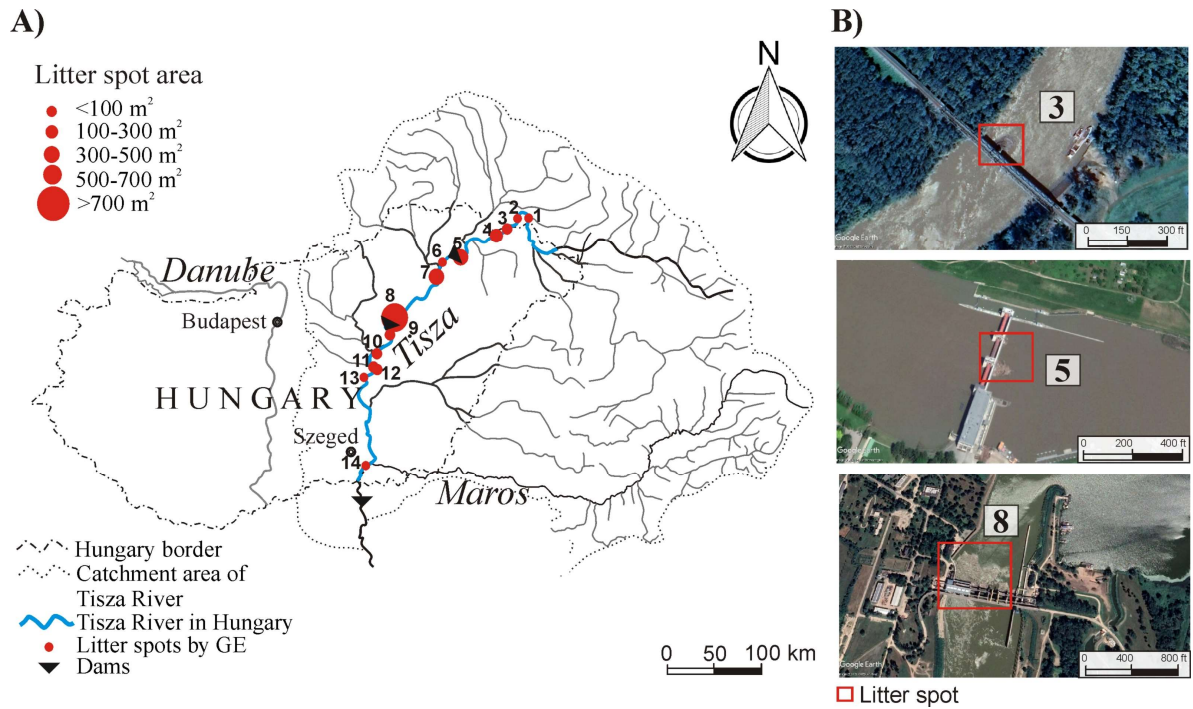
Figure 5.2. The 14 litter spots were identified along the Hungarian section of the Tisza River by very high spatial resolution (VHR) images from the Google Earth (GE) satellites (A). Examples of the identified spots, including spots no. 3, 5, and 8 (B).

Table 5.1. Features of the identified litter spots along the Hungarian section of the Tisza River, determined by very high spatial resolution (VHR) images. The spots designated in bold (i.e., 5/A, 5/B, and 8E) were used during the testing phase of the Sentinel-2-based models.

ID	Latitude	Longitude	Date (VHR)	Date (S–2)	Area (m²) (pixels)
1	48°22'26"N	22°15'24"E	31/3/2019	23/3/2019	88 (<1)
2	48°23'13"N	22°08'02"E	31/3/2019	23/3/2019	75 (<1)
3/A			–	23/3/2019	140 (≈1)
3/B	48°15'59"N	21°57'36"E	5/4/2019	2/4/2019	130 (≈1)
3/C			28/6/2019	26/6/2019	130 (≈1)
4	48°11'20"N	21°43'38"E	3/6/2017	4/6/2017	267 (≈3)
5/A	**48°01'33"N**	**21°18'30"E**	**1/6/2019**	**1/6/2019**	**345 (≈3)**
5/B			**1/6/2019**	**1/6/2019**	**25 (<1)**
6	47°52'06"N	21°03'58"E	20/3/2020	20/3/2020	40 (<1)
7	47°49'17"N	21°01'17"E	20/3/2020	20/3/2020	520 (≈5)
8/A			27/6/2017	24/6/2017	3405 (≈34)
8/B			–	3/8/2017	4000 (40)
8/C			–	24/4/2020	4300 (43)
8/D	47°29'37.4"N	20°30'53.8"E	–	28/7/2020	9500 (95)
8/E			**1/8/2020**	**2/8/2020**	**9474 (≈95)**
8/F			–	12/8/2020	9000 (90)
8/G			–	22/8/2020	9600 (96)
9	47°22'14.54"N	20°26'7.66"E	29/7/2020	28/7/2020	204 (≈2)
10	47°15'11.18"N	20°23'51.50"E	9/8/2020	12/8/2020	220 (≈2)
11	47° 2'35.30"N	20°16'20.18"E	14/8/2017	8/8/2017	266 (≈3)
12	47° 2'35.30"N	20°16'20.18"E	9/8/2020	12/8/2020	181 (≈2)
13	46°57'1.78"N	20° 6'10.71"E	2/4/2020	4/4/2020	67 (<1)
14	46°14'40"N	20°09'02"E	3/3/2021	7/3/2021	90 (<1)
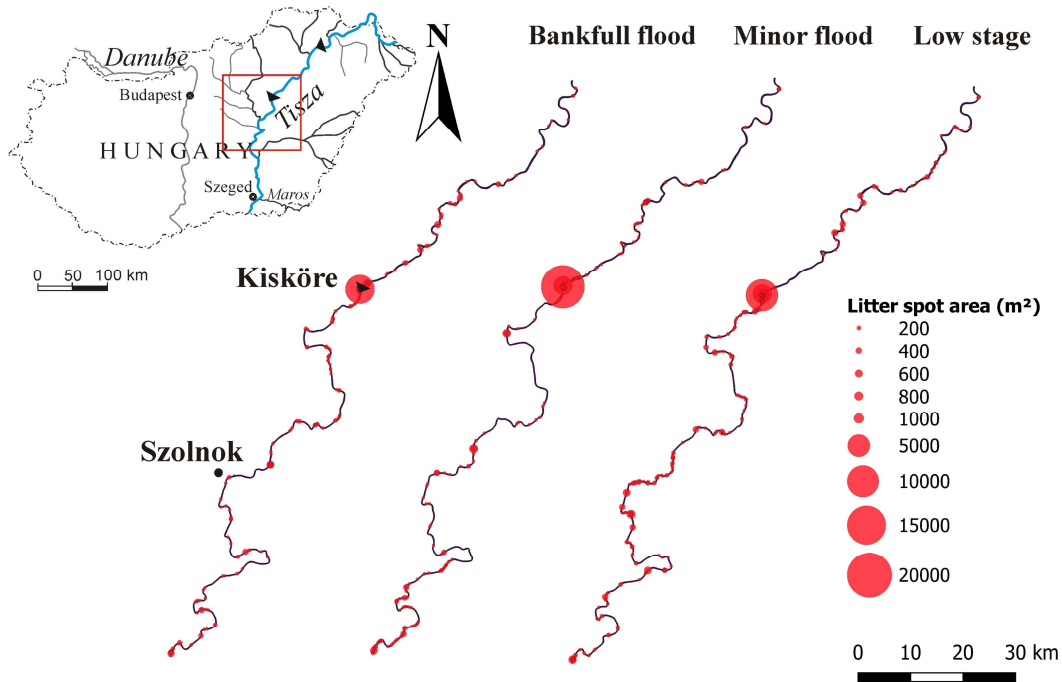
Figure 5.3. Detected riverine litter spots along a 175-km long reach in the Middle Tisza by Sentinel-2-based model under various hydrological conditions: bankfull flood (31/03/2019), minor flood (09/06/2019) and low stage (22/09/2019).

Medium to small spots appeared too, primarily along the riverbanks in meandering sections with high bank erosion, fallen trees, and low flow velocity (Figure 5.3). Also, some spots were noticed near docks, but none were observed upstream of bridges, within this reach. Remarkably, the density of litter spots downstream of the dam (1.2–1.6 spot/km) exceeded that upstream (0.85–1 spot/km) under the three hydrological conditions. This disparity suggests the presence of local litter sources downstream. Although Sentinel-2 proved its potential as a valuable tool for riverine litter monitoring, caution is needed in interpreting its results, especially along the riverbanks due to the misclassification of mixed pixels.

To investigate the temporal change of riverine litter, this study specifically focused on the litter spot located just upstream of the Kisköre Dam (spot no.8; Figure 5.2). Although the highest riverine litter transport rate usually occurs during bankfull floods (Van Emmerik and Schwarz, 2020), the largest spot was noticed at the end of the minor flood event (Figure 5.3). This observation underscores the significance of gradual fluxes in litter accumulation. Typically, litter accumulates progressively during bankfull and minor floods, reaching its peak at the end of the flood period. Notably, the area of the litter spot declined during the low stages (Figure 5.3), probably due to the litter removal efforts by Hungarian authorities.

The areal coverage of the litter spot upstream of the Kisköre Dam almost doubled between 2015 and 2019; however, it dropped by 30% in 2020 and then slightly increased by 12% in 2021 (Figure 5.4A). The seasonal Mann-Kendall test revealed an overall upward trend of the areal extent of the litter spot throughout the study period (2015–2021) (Figure 5.4B). This increasing trend might be attributed to the absence of large flood events during the study period.

5.2. Remote sensing-based riverine litter/macroplastic (MaP) modelling in the Tisza River

5.2.1. *Spectral signature of riverine litter*

The spectral signature of riverine litter was compared to those of river water and obstructions (i.e., bridges and dams) (Figure 5.5). Riverine litter showed the highest reflectance across the entire spectrum (490–2190 nm), and its spectral signature was

60

comparable to obstructions. Both riverine litter and obstructions exhibited low reflectance in the VIS bands (especially 490 and 665 nm), high reflectance in the SWIR bands (1610 and 2190 nm), and significant reflectance in the NIR bands (740–865 nm). The river water, on the other hand, showed high reflectance solely in the VIS bands (especially the 560 nm) and low reflectance in the NIR and SWIR bands. Therefore, the NIR and SWIR bands are the most suitable for discriminating riverine litter and obstructions from river water, consistent with Bentley (2019) and Biermann et al. (2020). Given the resemblance in the spectral signature of riverine litter and obstructions, their differentiation presents a challenge. However, the bands 842 and 1610 nm may be valuable for this purpose, owing to the slight drop in the obstruction reflectance in comparison to the elevated reflectance of riverine litter.
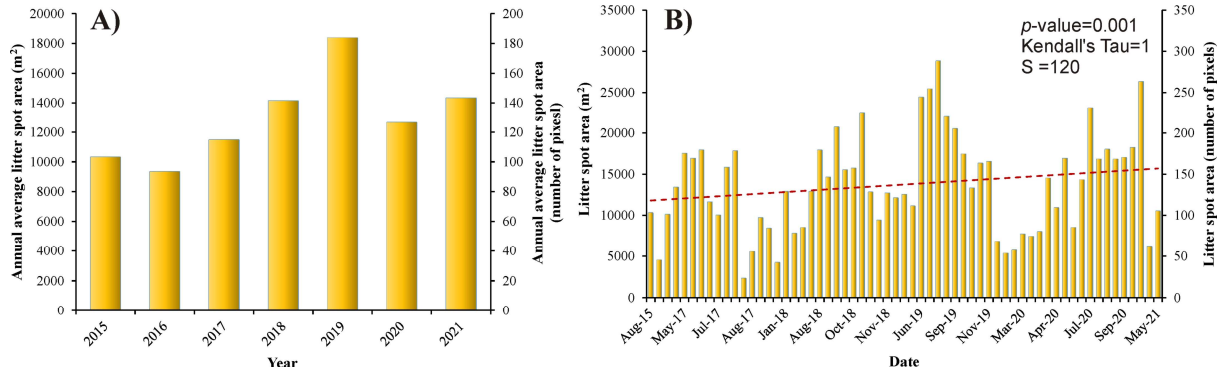
Figure 5.4. Mean annual coverage of the riverine litter spot located upstream of the Kisköre Dam, estimated by 61 Sentinel-2 images (applying the best-derived model) between 2015 and 2021 (A). A Comprehensive time-series of the litter spot areal coverage throughout the study period (B).
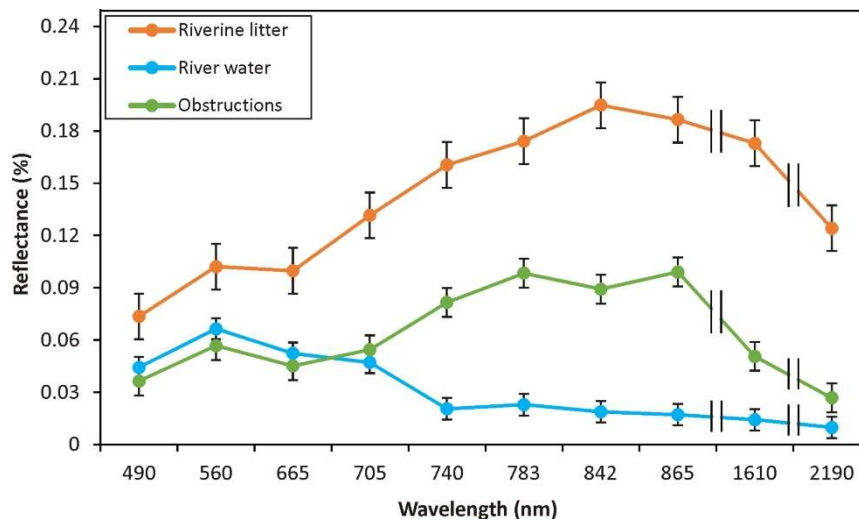
Figure 5.5. Spectral signature of the riverine litter in comparison to river water and obstructions (e.g., bridges and dams) considering the Sentinel-2 bands.

5.2.2. Evaluation of the riverine litter models

The developed riverine litter models showed promising metrics based on the validation dataset, as the overall accuracy ranged between 0.89 (NB) and 0.96 (SVC) (Table 5.2). Given the tradeoff between precision and recall, the algorithm that gave the highest precision (ANN: 0.98) was associated with a moderate recall (0.89). Similarly, the highest recall that was achieved by the SCV (0.99) was associated with a moderate precision (0.9). The F1-score and K-hat followed a similar performance ordering pattern to the overall accuracy, highlighting SVC and ANN as the top-performing algorithms; meanwhile, NB performed less effectively. However, it is important to acknowledge that the validation dataset contained relatively limited data, due to riverine litter data shortage. Consequently, the models`

performance may vary with larger datasets. Therefore, their generalization performance and detection bounds were tested in the next section over a large dataset.

Table 5.2. Evaluation metrics of the developed riverine litter models based on the validation dataset.

Algorithm	Overall accuracy	Precision	Recall	F1-score	K-hat
Decision Tree (DT)	0.93	0.89	0.92	0.90	0.77
Naïve Bayes (NB)	0.89	0.86	0.80	0.83	0.58
Support Vector Classifier (SVC)	0.96	0.9	0.99	0.94	0.85
Random Forest (RF)	0.94	0.88	0.95	0.91	0.84
Artificial Neural Network (ANN)	0.95	0.98	0.89	0.93	0.82

The elevated detection accuracy of the models can be related to the inherent potential of machine learning algorithms in dealing with continuous and non-linear datasets, and high dimensional classification problems (Mohsen et al., 2023c). The superiority of the SVC over the tested algorithms may be attributed to the binary nature of the classification problem (i.e., litter and non-litter classes). This is due to the creation of hyperplane and support vectors in the SVC which provides the best possible separation of both classes. Conversely, the relatively low metrics of the NB may stem from the violation of the independent feature of Bayes` assumption, since the spectral bands and indices were correlated.

The classification accuracy of the riverine litter models developed in this study was comparable to their counterparts in rivers and seas worldwide. For instance, an NB-based model classified marine litter with an overall accuracy of 0.86 (Biermann et al., 2020), which is very similar to the NB model in this study (0.89). However, the marine litter model addressed a multiclass problem, in contrast to the binary classification undertaken in this study, accounting for the accuracy difference between both models. A similar riverine litter model was developed in the Drina River, Bosnia and Herzegovina based on the ANN (Jakovljević et al., 2019). This model achieved a higher overall accuracy (0.97) than the ANN-based model in this study (0.95). The main challenge affecting their classification accuracy was the mixed pixels (pixels covered by both litter and non-litter classes), which was also observed in this study. Besides, active water constituents, mainly SSC, have a profound impact on classification accuracy. However, the training water pixels data applied in this study were gathered during almost all hydrological scenarios to overcome this issue.

5.2.2.1. Contribution of spectral bands and indices in the performance of models

The highly contributing features (i.e., spectral bands and indices) in the DT model were B11, PI, NDVI, and B12; in the RF model were PI, B11, NDVI, and NDWI; in the NB model were B11, B12, B8, and NDWI; in the SVC model were B11, B12, B8, and B7 and in the ANN model were B11, B8, B12, and NDVI. However, the SHAP summary plots were depicted only for the SVC and ANN-based models as examples (Figure 5.6). The features are sorted on the vertical axis based on their contribution importance, while their affection manner is represented on the horizontal axis through a SHAP sign.

Considering SHAP analysis across all models, the most effective bands for riverine litter detection are B11, B12, and B8. This finding aligns with the spectral signature analysis (Figure 5.5), as these bands showed unique signatures for riverine litter compared to river water and obstructions. The noteworthy implication of this finding is that these bands could be employed for the future development of a riverine litter index. Notably, some spectral indices contributed significantly to the enhancement of models` performance, particularly the PI, NDWI, and NDVI, while the FDI showed the least contribution.
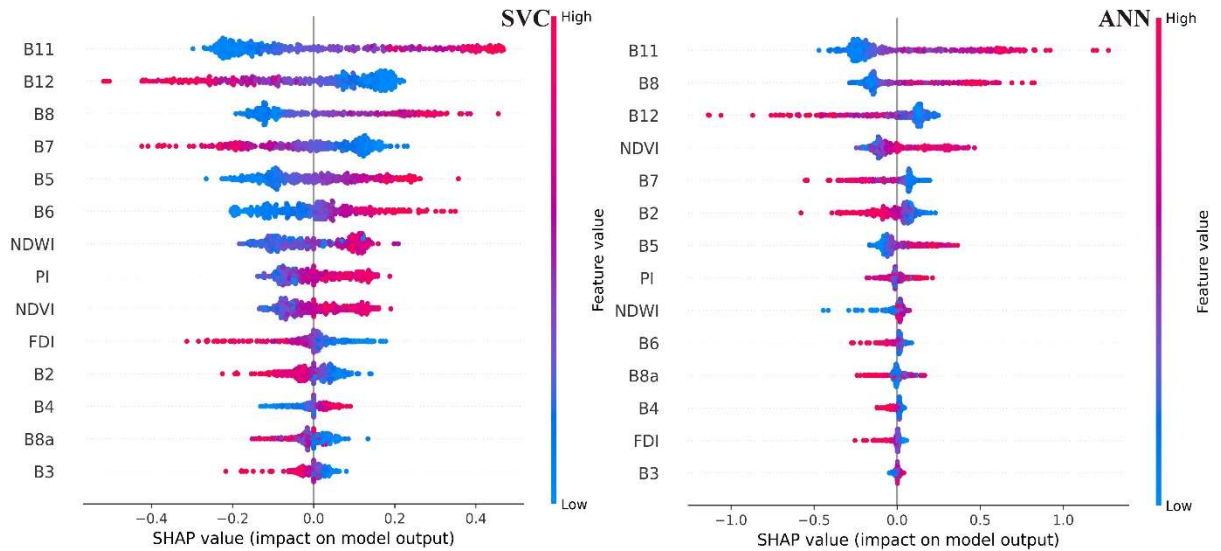
Figure 5.6. SHAP summary plots for the support vector classifier (SVC) and artificial neural network (ANN) riverine litter models represent the contribution of the spectral bands and indices in descending order of importance.

5.2.3. *Generalization capability and detection bound of the developed riverine litter models*

The testing dataset (bold spots in Table 5.1) was used to assess the generalization capability of the developed models (Table 5.3, Figure 5.7, and Figure 5.8), and determine their detection bounds (Table 5.4). Although the models exhibited elevated classification metrics during the validation process (Table 5.2), they showed various metrics during the testing process, spanning from medium for SVC, RF, and ANN (F1-score: 0.62–0.69), to poor accuracy for DT and NB (F1-score: 0.45–0.48). This discrepancy returns to the limited size of the validation dataset (365 pixels), in contrast to the more extensive and diverse testing dataset.

Table 5.3. Evaluation metrics of the developed riverine litter models based on the testing dataset.

Algorithm	Overall accuracy	Precision	Recall	F1-score	K-hat
Decision Tree (DT)	0.89	0.30	0.9	0.45	0.44
Naïve Bayes (NB)	0.92	0.32	0.98	0.48	0.48
Support Vector Classifier (SVC)	0.97	0.51	0.8	0.62	0.62
Random Forest (RF)	0.96	0.56	0.9	0.69	0.68
Artificial Neural Network (ANN)	0.97	0.51	0.8	0.62	0.62

The models showed an elevated potential in detecting litter pixels, especially the large spot, thus their recall ranged between 0.8 and 0.98 (Table 5.3). However, they struggled to avoid the false classification of non-litter pixels (i.e., water and obstructions) as litter, especially the DT and NB. Thus, they showed low to medium precisions (0.3–0.56). Notably, the overall accuracy of the models was 1.6 times higher than their F1-score and K-hat, primarily due to their higher performance with the majority non-litter class, which overshadowed their poor to medium performance with the minority litter class.

To reveal the detection bounds of the developed riverine litter models, their areal estimates of the testing litter spots (i.e., large, medium, and small spots) were compared to their actual area obtained from the VHR Google Earth images (Table 5.4, Figure 5.7 and Figure 5.8). Concerning the large spot [upstream of the Kisköre Dam; 9474 m^2 (ca. 95 pixels)], all models were able to detect it successfully, though most of them slightly

overestimated its area (Table 5.4 and Figure 5.7). The greatest overestimation was achieved by the DT (ca. 40 pixels difference) and RF (ca. 26 pixels) models. However, they gave good classification for the river water and obstructions (dam), especially the RF model. Although the NB model provided the most accurate area of this particular spot (only ca. 6 pixels difference), it performed badly with the dam and misclassified it as litter. The best classification for this spot was achieved by the ANN and SVC models, as they provided a moderate overestimation of its area (ANN: ca. 18 pixels and SVC: ca. 21 pixels difference) while maintaining a correct classification of most river water and dam.
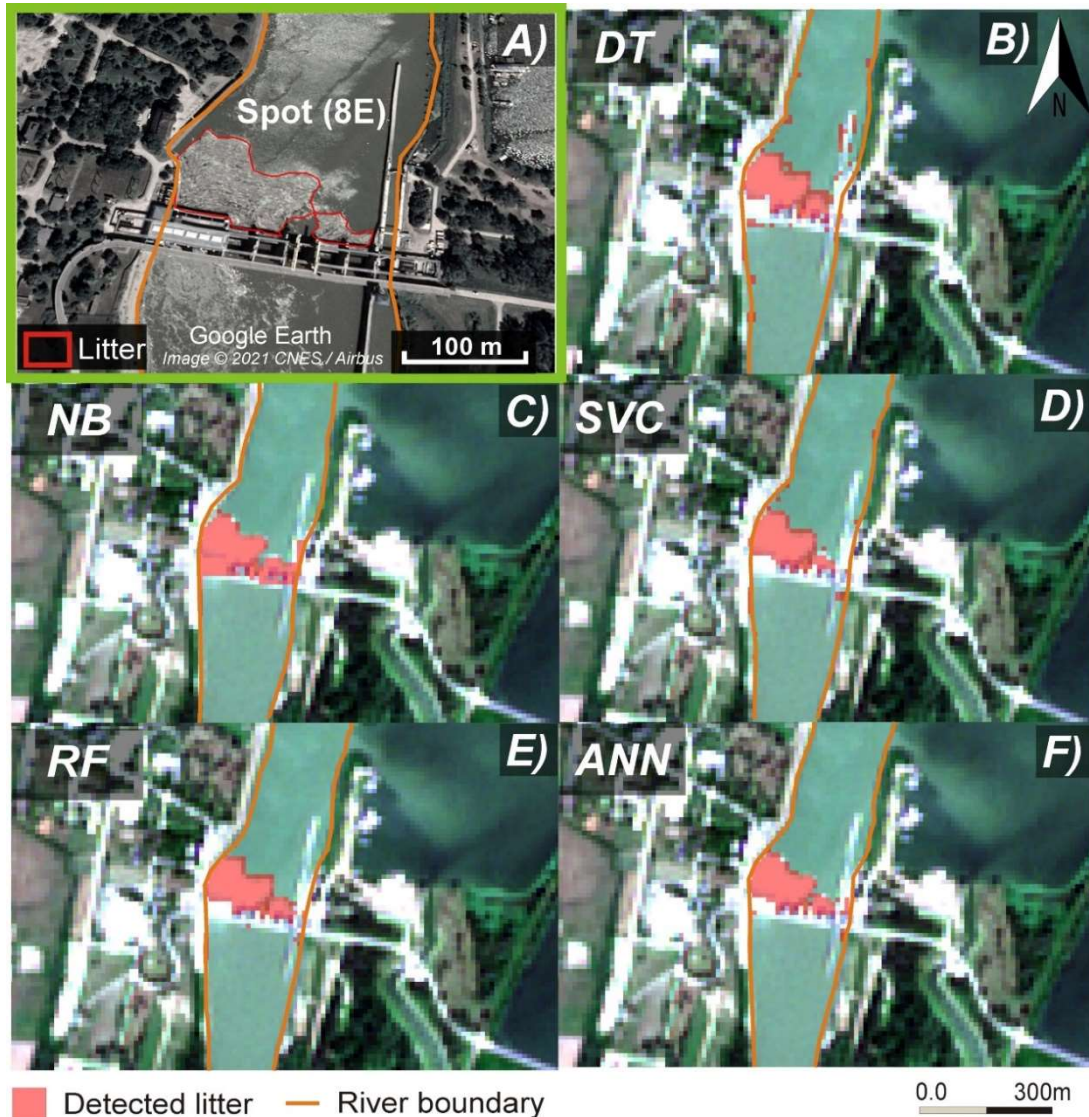
Figure 5.7. Performance of the derived riverine litter models in detecting the large spot in (A), based on the decision tree (DT) (B), naïve bayes (NB) (C), support vector classifier (SVC) (D), random forest (RF) (E) and artificial neural network (ANN) (F) algorithms.

The medium spot [upstream of the Tiszalök Dam; 345 m^2; (ca. 4 pixels)] was fully (DT, NB, RF, ANN) to partially (SVC) detected by the models; however, the small spot [upstream of the Tiszalök Dam; 25 m^2; (< 1 pixel)] was detected only by the NB model, despite having limited accuracy (Table 5.4 and Figure 5.8). The DT model provided the worst classification performance, as it misclassified a significant area of river water as litter; however, it correctly classified most of the dam and successfully detected the 4 pixels of the medium spot. Although the NB was the sole model that detected all pixels of the medium and small spots, it usually misclassifies the dam as litter, which was also noticed with the large spot (Figure 5.7). The

SVC model detected only half of the medium spot (2 pixels); however, its superiority arises from the correct classification of the river water and dam. Both the RF and ANN models showed similar classification performance, as they detected the full pixels of the medium spot and none of the small spot while maintaining accurate classification of river water and dam.
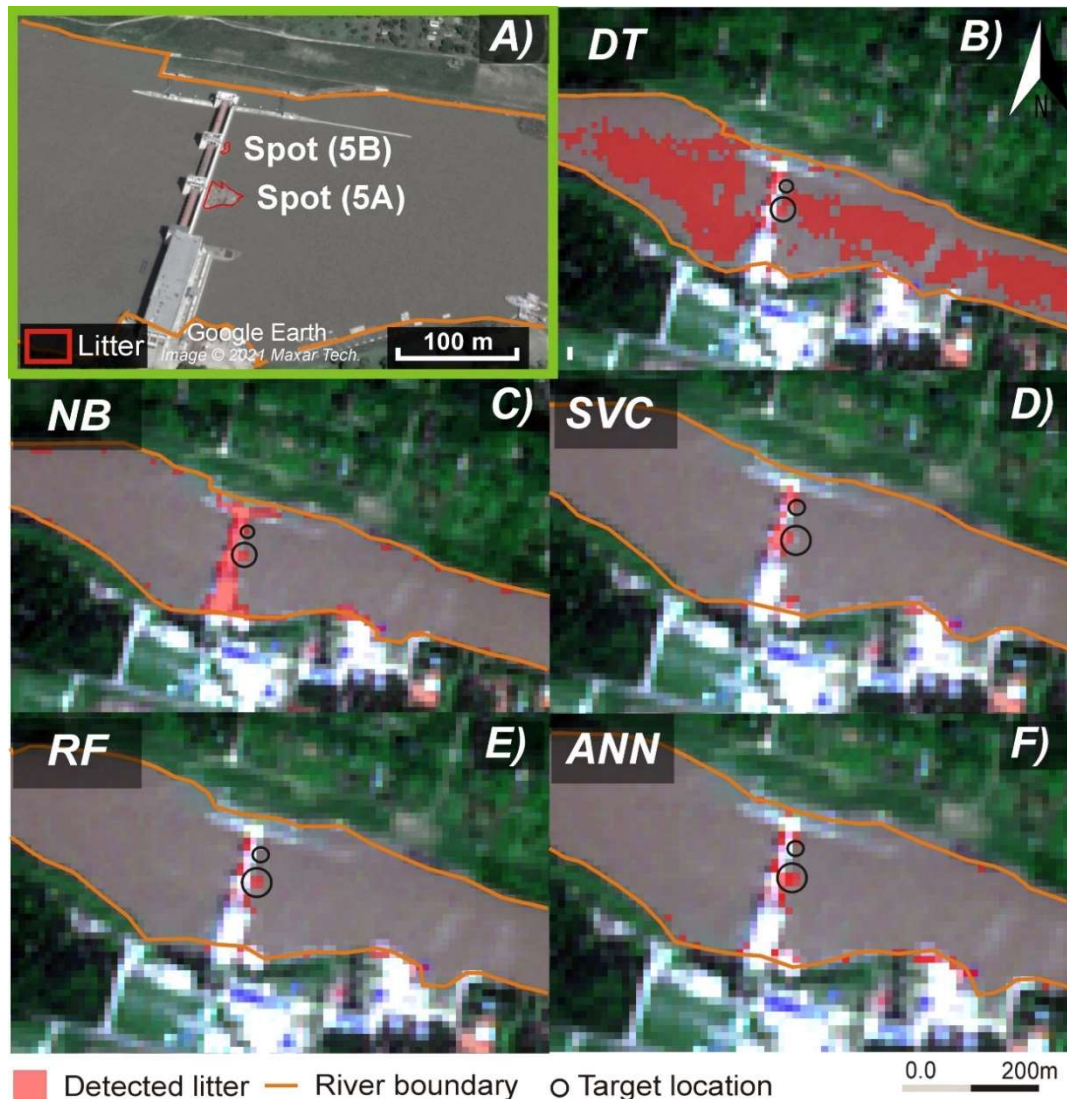
Figure 5.8. Performance of the derived riverine litter models in detecting small and medium spots in (A), based on the decision tree (DT) (B), naïve bayes (NB) (C), support vector classifier (SVC) (D), random forest (RF) (E) and artificial neural network (ANN) (F) algorithms.

Table 5.4. The estimated area of the three tested litter spots (i.e., large, medium, and small spots) by the five developed models, in comparison to the actual area detected by the very high spatial resolution (VHR) Google Earth (GE) images.

Method	Large spot m^2 (pixels)	Medium spot m^2 (pixels)	Small spot m^2 (pixels)
	Kisköre Dam	*Tiszalök Dam*	
VHR images from GE	**9474 (95)**	**345 (4)**	**25 (<1)**
Decision tree (DT)	13400 (134)	400 (4)	0.0 (0)
Naïve Bays (NB)	10100 (101)	400 (4)	100 (1)
Support Vector Classifier (SVC)	11500 (115)	200 (2)	0.0 (0)
Random Forest (RF)	12000 (120)	400 (4)	0.0 (0)
Artificial Neural Network (ANN)	11200 (112)	400 (4)	0.0 (0)

The models excelled at detecting large and medium spots owing to their higher reflectance, while they struggled with the small spot due to its lower reflectance. This finding aligns with Topouzelis et al. (2019) who reported that a litter area of $\geq 10 \times 10$ m^2 is a vital requirement to be detected by Sentinel-2 images. On the contrary, Hu (2021) argued that litter with a sub-pixel coverage of $\geq 0.8\%$ could be detected by the Sentinel-2 sensor. However, this percentage is a theoretical value and neglects practical noise that may originate from the sensor`s artifacts, such as the hardware parallax impacts in push-broom and pepper noise. Yet, further studies are warranted to explore the potential of satellite images in the sub-pixel detection of riverine litter, as the percentage of the small spots used in the training and validating dataset in this study was very limited (1%) and underrepresented.

Based on the evaluation metrics of the models on the validation and testing datasets and their performance in detecting litter spots of varying sizes, I argue that the SVC, ANN, and RF are the best-performing models, while the DT and NB models are the worst. The shortcoming of the DT model stems from its misclassification of river water as litter, especially during high SSCs, while the NB model misclassifies obstructions as litter. This may partially be attributed to the imbalanced dataset applied in this study (non-litter: litter class=67:33). Although this`ratio is considered relatively low (Zou et al., 2016), its influence on a simple algorithm like DT and NB may be more pronounced. Also, the similarity in the spectral signature of litter and obstruction (Figure 5.5) may have influenced the potential of these models to achieve better results, particularly the NB model.

5.2.4. *Assessment of remote sensing-based riverine litter/macroplastic (MaP) modelling*

This study is an initial attempt towards automatic detection of riverine litter/MaPs employing satellite images and machine learning algorithms. The results are promising, especially for the large and medium litter spots; however, further research on the sub-pixel detection is vital incorporating a larger dataset with more representative small spots. The Sentinel-2 MSI sensor with its 13 spectral bands, including the NIR and SWIR bands, as well as its frequent imaging (3–5 days), provide a valuable tool for riverine litter monitoring. The main challenge of this sensor is its low signal-to-noise ratio (SNR; 12–15 dB), as well as its moderate spatial resolution and variability among bands (10–60 m). This complicates sub-pixel detection, especially in medium-sized rivers, such as the Tisza River (w=164 m), where the river is covered by just 16–3 pixels. Therefore, applying the same approach on a finer spatial resolution image with similar spectral and temporal characteristics as of the Sentinel-2 may provide better results in medium-sized rivers.

5.3. Remote sensing-based suspended sediment discharge modelling in the Tisza and Maros Rivers and its spatiotemporal dynamism

5.3.1. *Temporal dynamics of Q and SSC in the Tisza and Maros Rivers (in-situ data)*

The monthly measurements of *Q* and SSC (2015–2020) at the three gauging sites (i.e., Algyő, Szeged, and Makó) were analyzed to reveal their temporal dynamics in the Lower Tisza (Figure 5.9A) and Maros Rivers (Figure 5.10A). The mean *Q* at Algyő (575 m^3/s) formed 80% of the mean *Q* at Szeged (702 m^3/s), while the rest originates from the Maros River (mean at Makó: 157 m^3/s), as the Szeged site is located 4.2 km downstream of their confluence. The mean SSC in the Maros River at Makó (129 g/m^3) was two-fold higher than the Tisza River at Szeged (58 g/m^3), due to the intensive mining activities and highly erodible rocks in the Maros`s catchment along with its steep slope (Kiss et al., 2018).

The largest flood wave during the study period occurred in 2016. In this year, the peak *Q* of the Tisza (Algyő: 1640 m^3/s; Szeged:1760 m^3/s) occurred during the early spring flood in March, while the peak *Q* of the Maros (465 m^3/s) occurred during the early summer flood in

June (Figure 5.9A and Figure 5.10A). Typically, flood waves are associated with high SS load, but the transported load is not necessarily proportional to the magnitude of Q. For instance, although the magnitude of the Q during the 2016 flood in the Tisza was similar to those in the 2019 flood, the SSC in 2016 (248 g/m^3) was 1.8 times higher than in 2019 (138 g/m^3). Another typical phenomenon in the Tisza is the clockwise hysteresis in the SSC–Q relationship, as the SSC peak usually precedes the Q peak. This can be observed, for example, in the early spring flood of 2016 (Figure 5.9B) and the early summer flood of 2019 (Figure 5.9C). This finding consists with the temporal measurements in the Middle Tisza at Szolnok and Kisköre sites (Figure 3.2; Csépes et al., 2000 and 2003), as well as many other rivers worldwide, such as the Save River, France (Oeurng et al., 2010) and the Rybárik Basin, Slovakia (BaČA, 2008). In the Maros River, the peaks of SSC and Q are likely to occur simultaneously (Figure 5.10A). This disparity between the two rivers was supported by the Pearson correlation coefficient (r) between SSC and Q, which was 0.88 in the Maros River and 0.72 in the Tisza River.
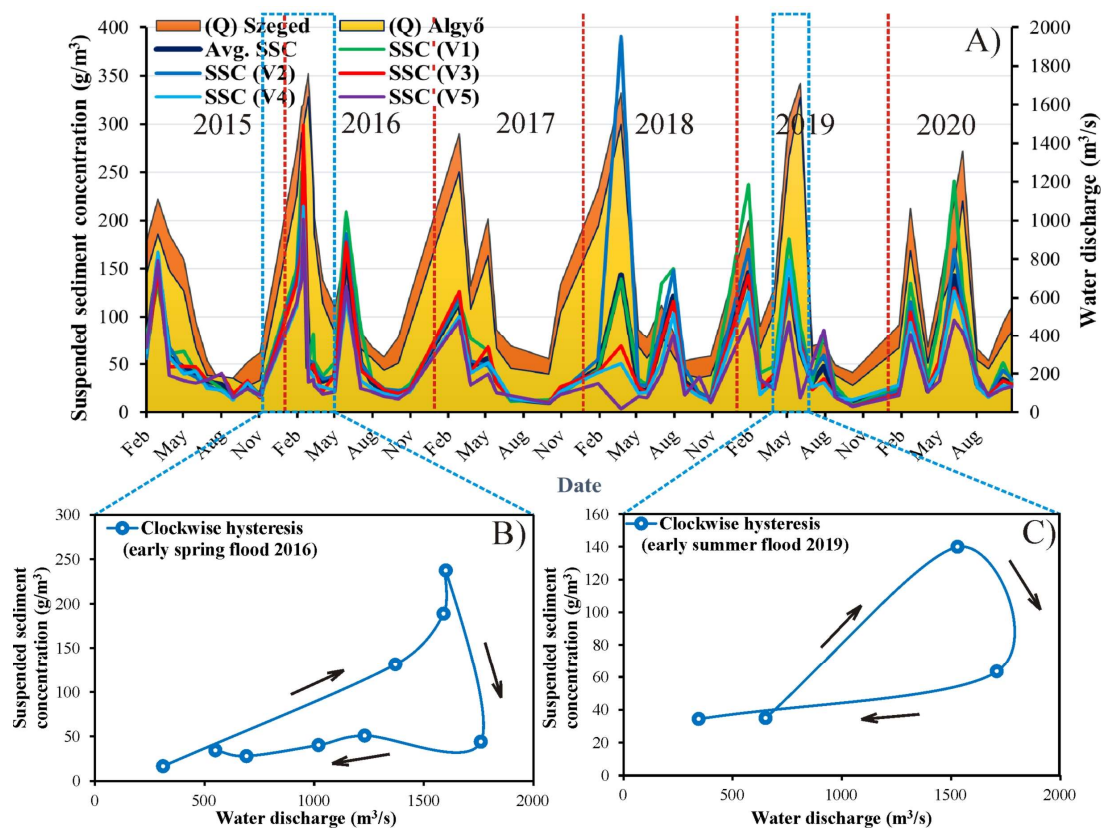
Figure 5.9. Temporal dynamics of water discharge (Q) and suspended sediment concentration (SSC) in the Lower Tisza River (2015–2020) at Algyő (Q only) and Szeged sites (A). Examples of the clockwise hysteresis in the Q–SSC relationship, observed during the 2016 (B) and 2019 (C) floods.

Typically, both rivers are in low stages between August and December (Figure 5.9A and Figure 5.10A). Throughout the study period, the lowest recorded Q in the Tisza (141 m^3/s) occurred in Szeged in August 2015, while its counterpart in the Maros at Makó (51 m^3/s) was in October 2019. During low stages, both rivers transport minimal SS loads, though the Maros maintains a higher concentration than the Tisza. Yet, the lowest concentrations during the study period were comparable in both rivers (Tisza: 8.3 g/m^3; Maros: 8.2 g/m^3) and occurred simultaneously in October 2019.

Given that the SSC measurements in Szeged (Tisza) and Makó (Maros) were conducted at five verticals (V1–V5; Figure 4.2D and E), its spatiotemporal dynamics along the cross-sections could be revealed (Figure 5.9A and Figure 5.10). The lateral distribution of SSC in

the cross-section of Szeged showed more variability than Makó; however, both rivers have the greatest variability during floods, while it declines during low stages. The lateral distribution of SSC usually corresponds to velocity distribution (Hashiba et al., 2014). This was applied to the cross-section at Makó, where the highest concentrations usually occur at the thalweg (ca. V3); meanwhile, the highest concentration in the Tisza, at Szeged, typically occurs at the low velocity left bank (ca. V1) (Figure 5.10B). This unusual SSC distribution at the Szeged cross-section returns to the site's specific configuration, which is located only 4.2 km downstream of the Tisza–Maros confluence, where the Maros join the Tisza from the left. Thus, the waters of both rivers are still mixing at this gauging site, as the complete mixing occurs 15–150 km downstream (Jirka, 2004).
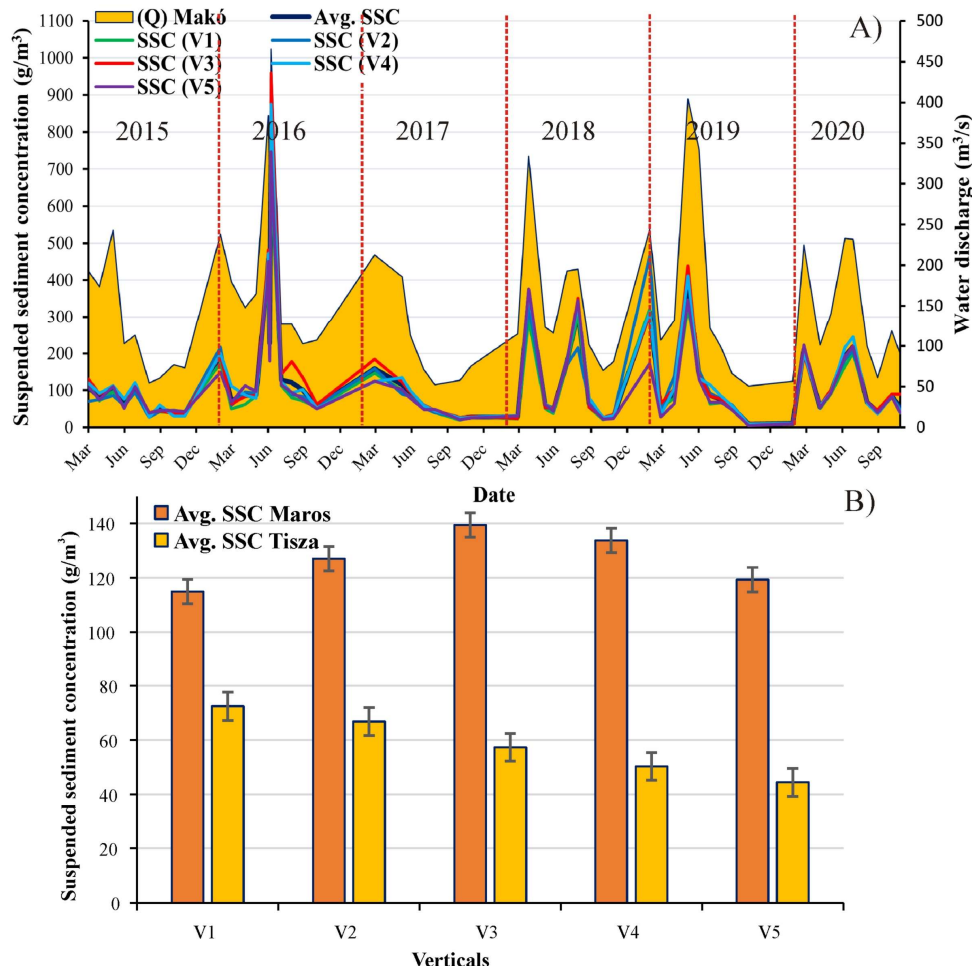
Figure 5.10. Temporal dynamics of water discharge (Q) and suspended sediment concentration (SSC) in the Lower Maros River (2015–2020) at Makó gauging site (A). Mean SSC of the five verticals (V1–V5) at Szeged and Makó cross-sections (2015–2020) (B).

5.3.2. Evaluation of the derived water discharge models

Water discharge (Q) was modelled as it is an essential prerequisite for Q_s estimation, providing increased availability of Q_s estimation in longer ungauged sections. Three Q models were developed in this study: the at-a-station hydraulic geometry (AHG) power-law model, the AHG machine learning model, and the at-many-station hydraulic geometry (AMHG) model. These models were developed by integrating remote sensing-based water width time series data (2015–2020) with concurrently measured Q. Finally, their performance was compared, and the most accurate model was employed to explore Q_s dynamics in the Lower Tisza and Maros Rivers over a relatively long period (2015–2021).

5.3.2.1. At-a-station hydraulic geometry (AHG) power-law and AHG machine learning (ML) models

The AHG power-law models developed at the three gauging sites (i.e., Algyő, Szeged, and Makó) revealed moderate and comparable R^2 values spanning between 0.54 and 0.6 (Appendix: Figure A1). The models` performance was visualized by comparing their predicted Q with the measured values over the study period (2015–2020) (Figure 5.11). Typically, they provide good predictions for discharges below the bankfull discharge (i.e., Algyő: 1600 m^3/s, Szeged: 1628 m^3/s, and Makó: 412 m^3/s), while they overestimate Q close or exceed this level (e.g., in March 2017 at Szeged and Algyő, and in June 2019 at Makó). This overestimation is attributed to the loss of hydraulic geometry of the channel`s cross-section above the bankfull level.

Notably, the RMSE and MAE showed similar performance patterns for the three models, as the best model was at Makó (RMSE/mean observed: 0.88) and the worst at Algyő (RMSE/mean observed: 2.6). However, they differed from the R^2 pattern, where the best model was at Szeged and the worst at Makó. This discrepancy may return to the significant overestimation of high discharges in Szeged and Algyő (e.g., in March 2017 and July 2020), in comparison to moderate overestimation in Makó (e.g., June 2019).
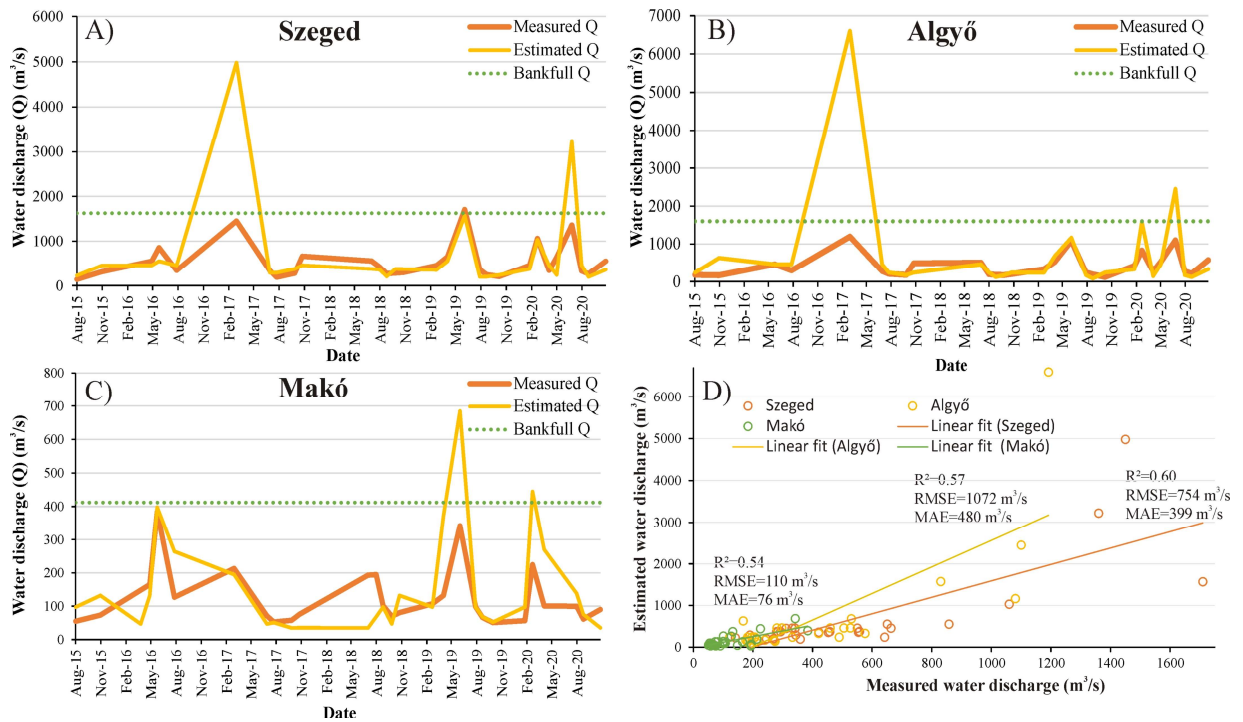
Figure 5.11. The estimated water discharge (Q) by the developed AHG power-law models was compared to the measured Q during the study period in Szeged (A), Algyő (B), and Makó (C). Both the estimated and measured Q were linearly fitted, and the evaluation metrics were annotated (D).

The evaluation metrics of the AHG ML models (i.e., SVC, RF, ANN, and combined models) at the three gauging sites (i.e., Szeged, Algyő, and Makó) were tabulated (Table 5.5). It is noteworthy that these metrics were calculated based on the validation dataset (20% of data). The models showed promising results as the R^2 ranged between 0.65 (SVR model at Szeged) and 0.88 (combined model at Makó). Also, the RMSE in the Tisza varied between 154.1 m^3/s (RF model at Szeged) and 98.9 m^3/s (SVR model at Algyő), and in the Maros at Makó between 33.7 m^3/s (SVR model) and 25.4 m^3/s (RF model). Considering the R^2 as the criteria of models` superiority, the combined model was the best-performing in Szeged (0.83) and Makó (0.88), and the ANN model was the best in Algyő (0.79).

Table 5.5. Evaluation metrics of the AHG machine learning (ML) models at the three gauging sites (i.e., Szeged, Algyő, and Makó) based on the validation dataset (20% of data).

Gauging site	AHG Machine-Learning (ML) models		
	Algorithm	R^2	RMSE (m^3/s)
Szeged	Support Vector Regression (SVR)	0.65	132.0
	Random Forest (RF)	0.71	154.1
	Artificial Neural Network (ANN)	0.76	119.9
	Combined model	**0.83**	**99.9**
Algyő	Support Vector Regression (SVR)	0.72	98.9
	Random Forest (RF)	0.68	123.6
	Artificial Neural Network (ANN)	**0.79**	**123.3**
	Combined model	0.77	107.8
Makó	Support Vector Regression (SVR)	0.85	33.7
	Random Forest (RF)	0.81	25.4
	Artificial Neural Network (ANN)	0.85	31.0
	Combined model	**0.88**	**25.9**

The evaluation metrics of the AHG power-law and AMHG models were calculated based on the entire dataset (2015–2020), while they were calculated based on the validation dataset (20% of data) in the AHG ML models (Table 5.5). To allow direct comparison between the adopted methods, the AHG ML metrics were recalculated considering the entire dataset, applying the best-performing models (i.e., combine model in Szeged and Makó; ANN model in Algyő) (Figure 5.12). The AHG ML models outperformed the AHG power-law models at the three gauging sites, as the R^2 increased by 23% on average. These ML models avoided significant overestimation of Q above the bankfull level, leading to a significant decline in the RMSE at the three sites (i.e., 80% in Algyő, 75% in Szeged, and 58% in Makó). The superiority of the AHG ML models returns to the inherent capabilities of ML algorithms in detecting intricate, non-linear relationships and patterns in data, allowing for more precise predictions and adaptability to changing conditions (Mohsen et al., 2023c).
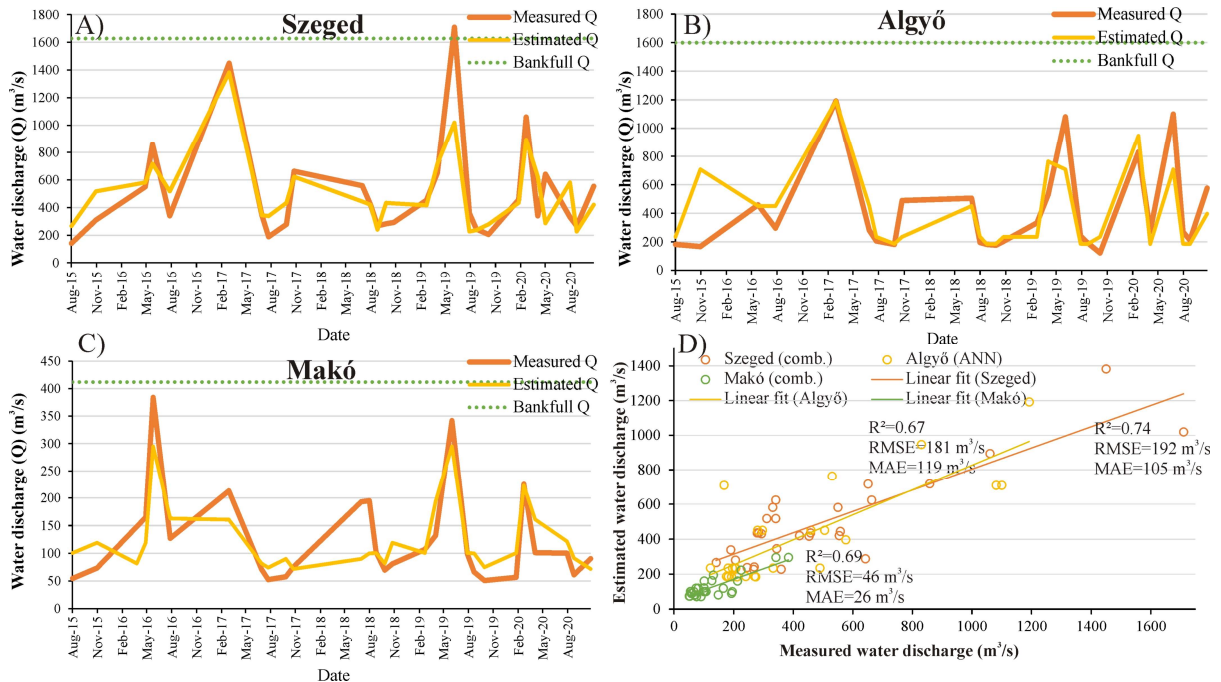
Figure 5.12. The estimated water discharge (Q) by the best-performing AHG machine learning (ML) models (i.e., combine model in Szeged and Makó; ANN model in Algyő) was compared to the measured Q throughout the study period in Szeged (A), Algyő (B) and Makó (C). Both the estimated and measured Q at the three sites were linearly fitted, and the evaluation metrics were annotated (D).

Based on the evaluation metrics at the three gauging sites, the best performance of the models was achieved in Szeged (R^2=0.74; RMSE/mean observed=0.38; MAE/mean observed=0.21), while the worst was in Algyő (R^2=0.67; RMSE/mean observed=0.45, and MAE/mean observed=0.29).

5.3.2.2. At-many-station hydraulic geometry (AMHG) models

The AMHG method was applied to develop Q models at the three gauging sites (i.e., Algyő, Szeged, and Makó) incorporating water width data from 100 transects within 1 km reach at these sites. The resulting 100 AHG coefficients log (a) and exponents (b) were fitted by a log-linear relationship at the three sites, aligning with the observations of Gleason and Smith (2014) (Figure 5.13). However, the best regression was achieved in the Szeged site (R^2=0.88) and the worst was in Makó (R^2=0.47). Following the regression analysis, the bounds of coefficients and exponents were determined and applied in the genetic algorithm (GA) to perform the optimization process. The optimized coefficients and exponents were clustered around the regression lines at the three sites. However, their dispersion was closely related to the strength of correlation, with the lowest dispersion at the Szeged site and the highest at the Makó site.
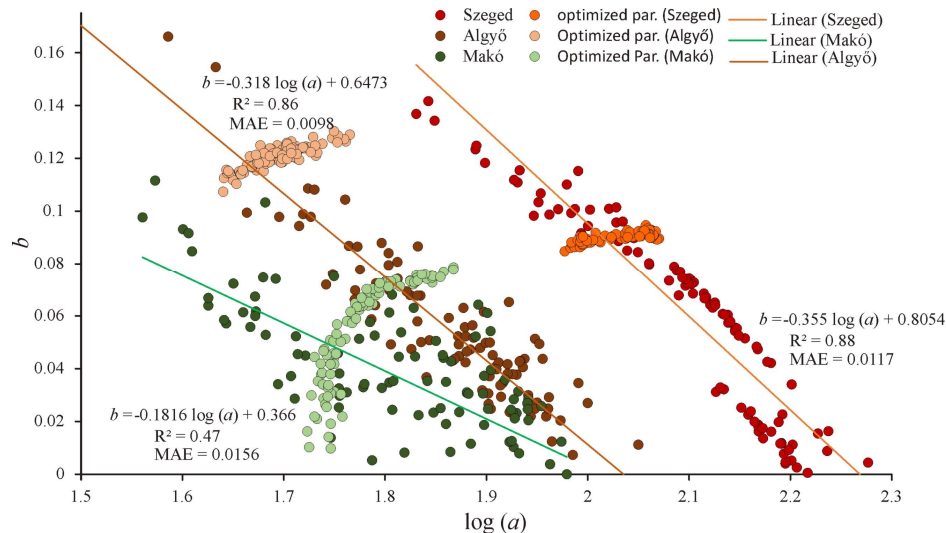
Figure 5.13. The AHG coefficients and exponents [i.e., log (a) and (b)] for the 100 transects in the 1-km reach in Szeged, Algyő and Makó sites. Their optimized values that were obtained by the genetic algorithm (GA) were also depicted.

The AMHG models outperformed the AHG power-law models, as the mean R^2 at the three gauging sites increased from 0.57 to 0.62, and the mean RMSE declined from 645 m^3/s to 172 m^3/s (Figure 5.14). Although the AMHG mitigated the significant over-estimation of Q during floods seen in the AHG power-law models, they had a tendency to slightly underestimate Q during these periods (e.g., Tisza: March 2017 and June 2019; Maros: June 2016 and June 2019; Figure 5.14). A similar superiority of the AMHG method over the AHG-power law method was reported in four Indian rivers, as the AHG power-law models estimated Q with a Nash coefficient of 0.69, while it was 0.8 in the case of AMHG models (Durga Rao et al., 2020). This can be attributed to the potential of the AMHG method to leverage hydraulic geometry data from multiple cross-sections, in contrast to the single cross-section in the case of the AHG power-law method (Durga Rao et al., 2020).

The performance of the AMHG models was comparable, or slightly lower than the novel AHG ML models developed in this study. This can be noticed from its slightly lower R^2 (mean of the three sites: 0.62) and higher RMSE (172 m^3/s) than the AHG ML models (R^2=0.7 and RMSE=140 m^3/s). Therefore, the ML algorithms have the potential to substitute

the hydraulic geometry feature of multi transects in the AMHG method. Consequently, the employment of the AHG ML method can circumvent the intricate optimization process in the AMHG method, which would increase the number of monitored sections along rivers.

The R^2 and MAE/mean observed revealed that the performance of the models was the best in Szeged (R^2=0.67; MAE/mean observed=0.17) and the worst in Makó (R^2=0.55; MAE/mean observed=0.38). Meanwhile, the best and worst performances occurred in Algyő and Szeged, according to the RMSE/mean observed (Algyő: 0.47; Szeged: 0.53).
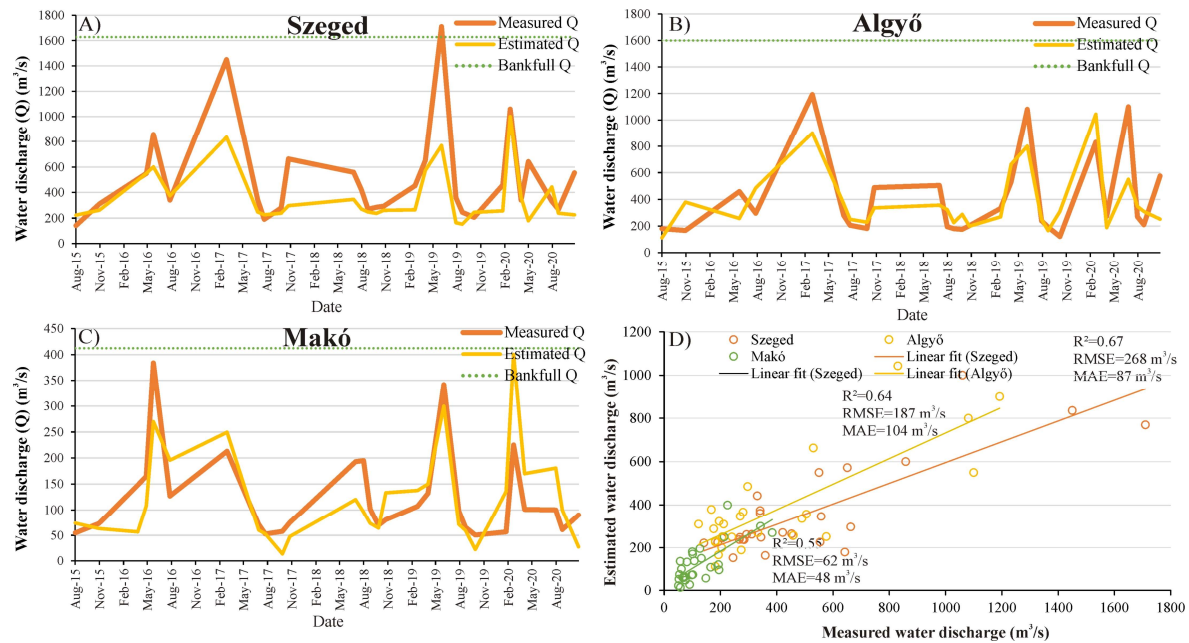
Figure 5.14. The estimated water discharge (Q) by the AMHG models was compared to the measured *Q* throughout the study period in Szeged (A), Algyő (B), and Makó (C). Both the estimated and measured *Q* at the three sites were linearly fitted, and the evaluation metrics were annotated (D).

5.3.2.3. Generalization capability of the best-performing water discharge model

Based on the performance of the three tested *Q* models (i.e., AHG power-law, AHG ML, and AMHG models), the AHG ML models, specifically the combined model in Szeged and Makó and the ANN model in Algyő were the best-derived models. Therefore, their generalization capability was tested over a relatively long period (July 2015–May 2021) utilizing 93 Sentinel-2 images (Figure 5.15). The models showed promising predictions, as the R^2 values ranged between 0.87 and 0.61, confirming their reliability and generalization capability. Notably, the evaluation metrics (i.e., R^2, RMSE/mean observed, and MAE/mean observed) consistently identified that Szeged was the site where the models performed the best, while Makó showed the poorest results. This underscores the importance of channel size and cross-section shape in *Q* estimation following this approach.

5.3.2.4. Potentials and limitations of the derived water discharge models

According to the findings of this study, I argue that the integration between hydraulic geometry theory and remote sensing data is a promising approach toward the automatic estimation of *Q* in rivers. Following my best-developed models (i.e., AHG ML), the *Q* could be estimated with an RMSE of 187 m^3/s (RMSE/mean observed=0.29) in the Tisza and 46 m^3/s (RMSE/mean observed=0.29) in the Maros Rivers. However, the accuracy of these models relies on the precision of water width data obtained from satellite images, which, in turn, depends on its spatial resolution and the adopted water pixel extraction technique. The combination of the NDWI and OTSU automatic thresholding proved its potential for water

pixel extraction in this study, as the RMSE of the estimated water width was 8.17 m at Szeged and 9.9 m at Makó sites. These values are close to the pixel size of the Sentinel-2 images (10 m), indicating that the application of a similar approach at finer spatial resolution images could lead to more accurate water width data and consequently better Q estimations.
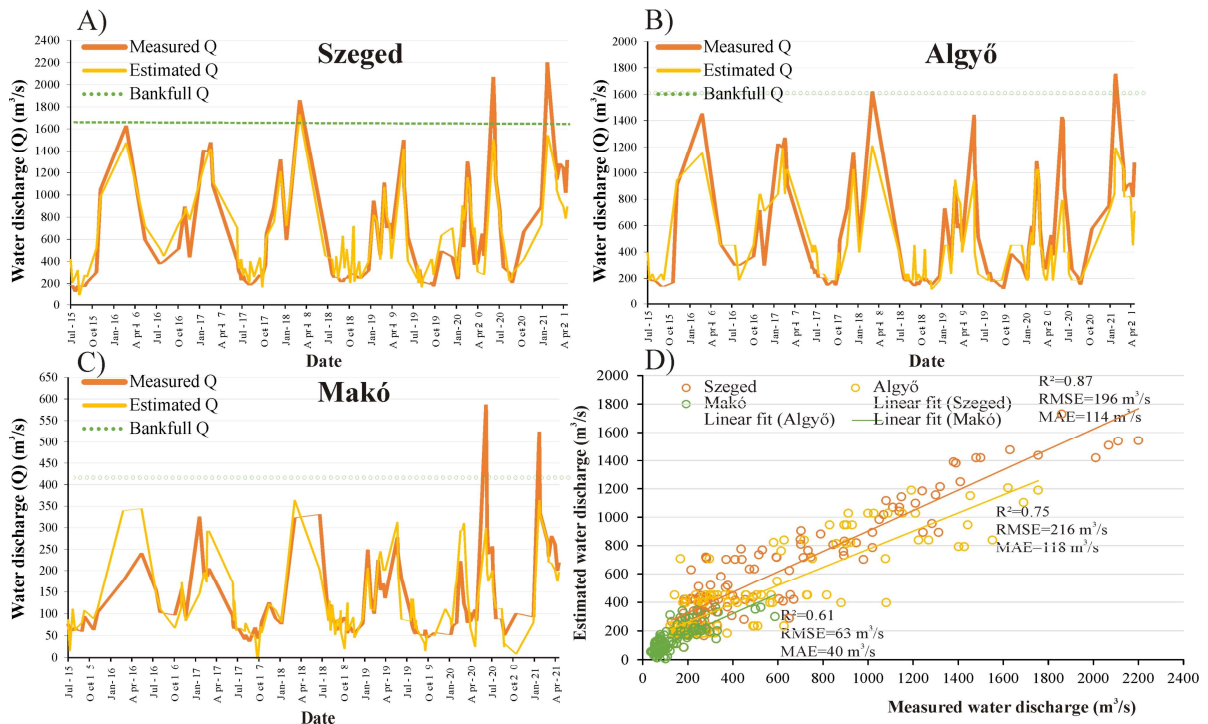
Figure 5.15. The estimated water discharge (Q) by the best performing AHG ML models was compared to the measured ones over a relatively long period (July 2015–May 2021; 93 Sentinel-2 images) in Szeged (A), Algyő (B) and Makó (C). Both the estimated and measured Q at the three sites were linearly fitted, and the evaluation metrics were annotated (D).

The developed Q models have limitations primarily linked to channel characteristics and remote sensing data availability. The estimation accuracy varied across the three sites, with the best performance achieved in Szeged followed by Algyő and the worst in Makó (Figure 5.15D). This discrepancy is attributed to the cross-section size and the precision of water width data estimated by Sentinel-2 images. Therefore, the widest cross-section in Szeged (203 m) was associated with the highest accuracy, and the narrowest in Makó (94 m) with the lowest accuracy. Furthermore, the cross-section shape in Szeged and Algyő (V-shape), outperformed the trapezoidal, or near rectangular shape in Makó (Figure 4.2D and E), from the w–Q relationship perspective (Equation 2.1) (Leopold and Maddock, 1953).

An additional limitation of the developed Q models is associated with bankfull level, especially for the AHG power-law models. The models tend to under or overestimate the actual Q values above this level, due to losing the hydraulic geometry characteristics of the original cross-section. Another limitation is related to the availability of remote sensing data as cloud cover can disrupt frequent monitoring of Q, especially during wet periods. However, this issue could be solved by integrating SAR images in future research.

5.3.3. Suspended sediment concentration models

5.3.3.1. Spectral signature of water of the Tisza and Maros Rivers

The spectral signature of the Tisza and Maros Rivers was analyzed by the mean reflectance of the Sentinel-2 bands (B2–B8a and B11–B12). The signatures were depicted considering all hydrological conditions (Figure 5.16A), and the individual low and high

stages (Figure 5.16B). Typically, the reflectance of the Maros was higher than the Tisza, and the reflectance during the high stage was higher than the low stage. The highest reflectance values were noticed between the green band (B3) and the red edge 1 band (B5) during all conditions in both rivers, consistently with several studies (Liu et al., 2017; Mohsen et al., 2020; Marinho et al., 2021). The sensitivity of this particular spectral range to SSC changes may return to the moderate to high absorption characteristics of the SS particles with this range. Remarkably, the highest reflectance in the Tisza occurred at B3, while it occurred at B5 in the Maros. Also, the highest reflectance during the low stages was B3 and the high stages was B5, which may indicate the potential utility of B3 for estimating low SSCs and B5 for high concentrations.
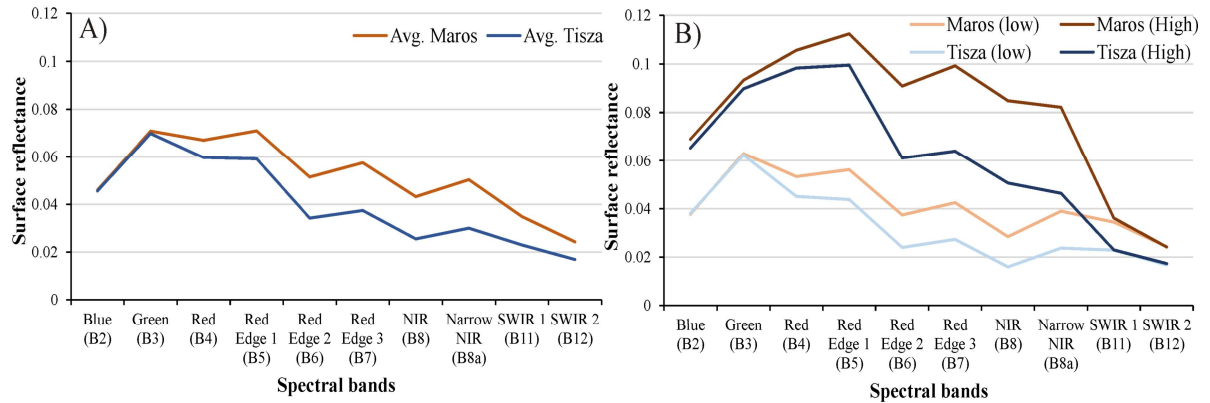
Figure 5.16. The spectral signature of the Tisza (at Szeged) and Maros (at Makó) Rivers is based on the mean reflectance of the Sentinel-2 bands, considering all hydrological conditions (A) and the individual low and high stages (B).

5.3.3.2. Evaluation of the derived suspended sediment concentration models

The evaluation metrics of the machine learning-based SSC models were calculated based on the validation dataset (20%) (Table 5.6). Generally, the models showed comparable and high accuracies, as the R^2 ranged between 0.76 and 0.9, the RMSE between 24.9 and 15.2 g/m^3, and the RMSE/mean observed between 0.22 and 0.44. The accuracy of Maros`s models was slightly higher (mean R^2=0.85) than the Tisza (mean R^2=0.8). The combined model was the best-derived SSC model in the Tisza and the RF model in the Maros, thus, these models were applied during the subsequent Q_s estimation.

Table 5.6. Evaluation metrics of the suspended sediment concentration (SSC) models in the Tisza (at Szeged) and Maros (at Makó) Rivers, based on the validation dataset (20%), utilizing different machine learning algorithms.

(Gauging site)	Algorithm	R^2	RMSE (g/m^3)	RMSE/mean observed
Tisza River (Szeged)	Support Vector Regression (SVR)	0.78	17.28	0.42
	Random Forest (RF)	0.76	15.23	0.37
	Artificial Neural Network (ANN)	0.82	17.96	0.44
	Combined model	**0.82**	**15.43**	**0.38**
Maros River (Makó)	Support Vector Regression (SVR)	0.78	24.9	0.28
	Random Forest (RF)	**0.90**	**19.97**	**0.22**
	Artificial Neural Network (ANN)	0.85	22.72	0.25
	Combined model	0.88	19.75	0.22

To gain deeper insights into the performance of the best-derived SSC models, a graphical comparison was made between their predictions and measured concentrations across the

validation dataset (Appendix: Figure A2). Both variables showed a high degree of consistency, especially in the Maros River. However, the models slightly underestimated the actual concentrations; though, the percent bias between mean estimated and measured concentrations in the Maros (-3.18%) was lower than in the Tisza (-5.31%).

The accuracy of the developed SSC models in this study was comparable to similar models in rivers worldwide. For instance, Peterson et al. (2018) employed the extreme learning machine algorithm for developing a remote sensing-based SSC model in the Missouri–Mississippi Rivers, achieving an R^2 of 0.9. A similar SSC model was developed in the confluence of these rivers, based on the RF algorithm with a slightly lower R^2 of 0.72 (Umar et al., 2018). Meanwhile, the developed machine learning-based models in this study outperformed statistical-based models in rivers worldwide. For instance, linear regression was applied to develop SSC models in the Maumee (Larson et al., 2018) and Mississippi, (Kröger et al., 2010) Rivers, USA, revealing an R^2 of 0.56 and 0.62, respectively.

Although all employed algorithms revealed promising SSC estimation accuracy, RF performed the best in the Maros River, consistently with Larson et al. (2018) (Table 5.6). This superiority returns to the data partitioning approach followed by the RF algorithm, as it divides data into multiple sub-models, and the final estimation is based on their average, enhancing the overall estimation accuracy of the model (Breiman, 2001). This study also demonstrated the effectiveness of combining multiple algorithms, as the combined model achieved the best performance in the Tisza River (Table 5.6).

To visualize the spatiotemporal performance of the best-derived SSC models (i.e., Szeged: combined model; Maros: RF model), they were applied to 20 km long reaches of the Lower Tisza and Maros Rivers, during high and low stages (Figure 5.17). Remarkably the SSC during the high stage (Tisza: 106.2 g/m^3; Maros: 211 g/m^3) was higher than low stage (Tisza: 17 g/m^3; Maros: 40.8 g/m^3), with the Maros having higher concentrations than the Tisza during both hydrological conditions. The lateral distribution of the SSC along Tisza`s cross-sections was more consistent during low stages than high stages. This can be noticed at the Algyő cross-section, where the highest concentrations occurred at ca. the middle and declined gradually to the riverbanks during the high stage (Figure 5.17AI); meanwhile, it was consistent along the cross-section during the low stage (Figure 5.17BI). On the other hand, the lateral distribution in the Maros River was consistent along channel cross-sections, regardless of the hydrological condition (Figure 5.17IV and V). However, the concentration at some pixels along the riverbanks, especially the left bank, was misestimated due to the coverage of the shadow tree. The confluence area revealed an intricate spatial SSC pattern (Figure 5.17II and III), which is discussed in detail in the next section (5.4).
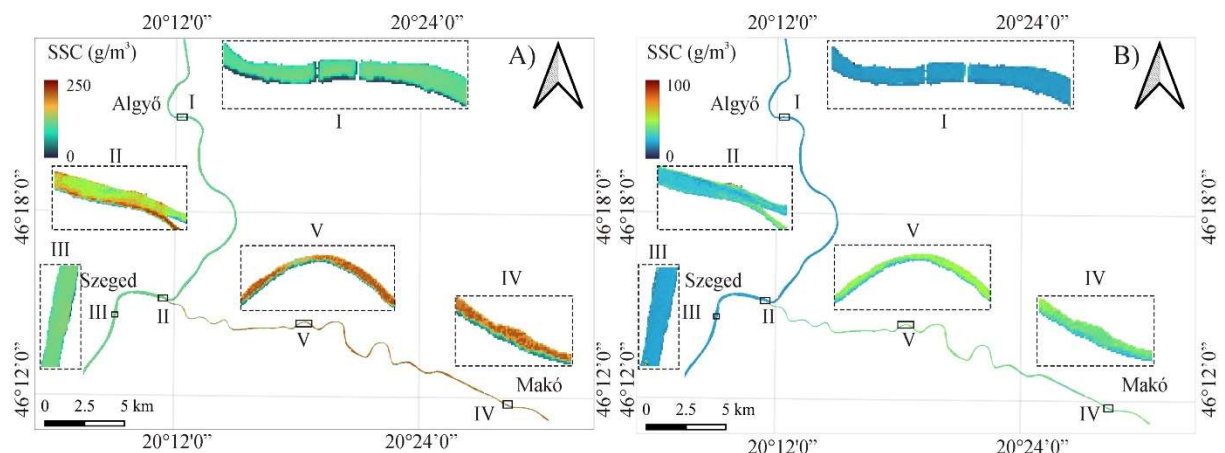
Figure 5.17. The spatiotemporal distribution of the suspended sediment concentration (SSC) along 20 km reach in the Lower Tisza and Maros Rivers, based on the best-derived SSC models during high stage (5/3/2020) (A) and low stage (6/9/2020) (B). Specific sites (I–IV) were selected on both rivers to provide detailed insights into the SSC distribution.

5.3.4. *Exploring suspended sediment discharge in the Lower Tisza and Maros Rivers based on the developed models*

The best-performed Q (i.e., AHG ML models) and SSC (i.e., Szeged: combined model; Maros: RF model) models were employed to investigate the temporal dynamics of the Q_s in the Lower Tisza (at Algyő and Szeged) and Maros (at Makó), based on 122 Sentinel-2 images (July 2015–May 2021) (Figure 5.18). The Q_s in the Tisza was 2–3.5 times higher than the Maros, though the Maros consistently had 2–3 times higher SSC than the Tisza, which is interpreted by the elevated Q of the Tisza (4 times higher than the Maros). Mostly, the Q_s of the Tisza at Algyő (average: 2584 t/d) is higher than the Maros at Makó (average: 1264 t/day), though during some exceptional hydrological scenarios (e.g., June and August 2016, July 2017, July–August 2018, June–July 2019) the adverse condition occurred. This typically occurs during low stage periods, which is characterized by higher SSC of the Maros than the Tisza, induced by minor flood waves. On the other hand, the Q_s in the Tisza at Szeged (average: 4385 t/d) is the highest, owing to its special spatial configuration just 4.2 km downstream of the Tisza–Maros confluence.

Typically, the temporal change of Q_s follows a similar pattern as of the Q in both rivers (Figure 5.18). The Q_s peak in the Maros at Makó usually occurs concurrently with its counterpart in the Tisza at Algyő, though occasionally, it may precede (e.g., February 2019 and February 2021) or follow it (e.g., June 2016 and March 2017), due to differences in the timing and magnitude of flood waves induced in the rivers. In the case of the Szeged site, which is located downstream of the confluence, its Q_s temporal changes occasionally diverge from the upstream section at Algyő. For instance, the Q_s peak in Szeged preceded its counterpart in Algyő during the February 2021 flood wave, and followed it during the March 2017 flood wave, due to the influence of Q_s from the Maros River.
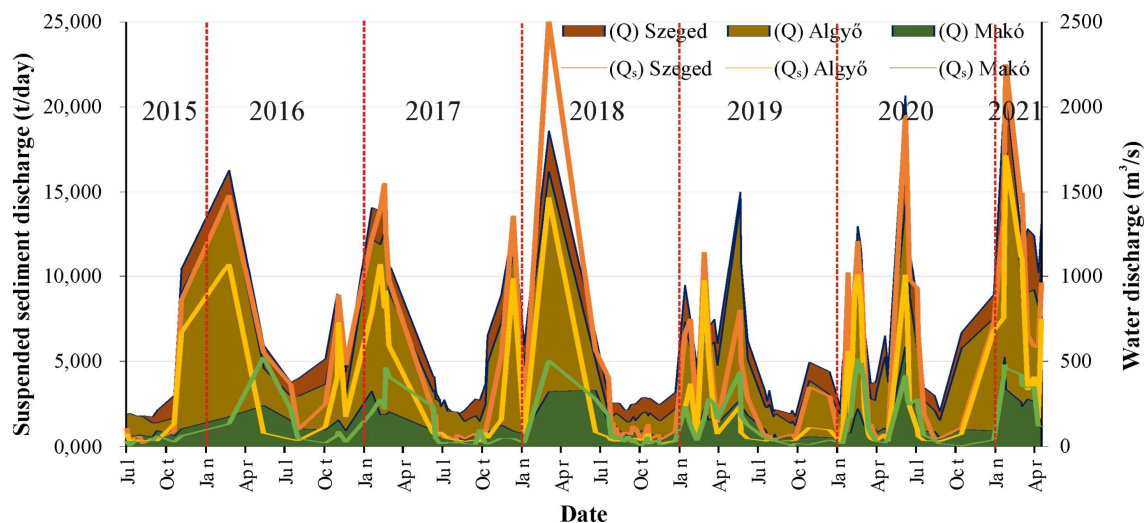
Figure 5.18. Estimated suspended sediment discharge (Q_s) in the Lower Tisza (at Algyő and Szeged) and Maros (at Makó) Rivers, based on the best-derived water discharge (Q) and suspended sediment concentration (SSC) models and 122 Sentinel-2 images (July 2015–May 2021). The estimated Q at the three sites is indicated in the background.

Based on my findings, I argue that the fusion of satellite images, hydraulic geometry theory, and machine learning algorithms, offered a promising approach towards automatic monitoring of Q_s in rivers worldwide. Although the developed monitoring technique was applied in medium-sized rivers utilizing Sentinel-2 images with 10–60 m spatial resolution, it demonstrated accurate Q_s estimates. Thus, enhanced performance is expected in larger rivers employing finer spatial resolution images.

5.4. Spatiotemporal dynamics of water mixing in the Tisza–Maros confluence and its relationship to rivers` hydrology

5.4.1. *Measured and calculated hydrological parameters of the rivers (2015–2021)*

Based on the daily water stage measurements in the three gauging sites (Algyő and Szeged in the Tisza; Makó in the Maros) during the study period (January 2015–May 2021), no considerable floods occurred in either river. However, five minor overbank flood waves (Algyő: ≥610 cm; Szeged: ≥500 cm) occurred in the Tisza, while only two occurred in the Maros (Makó: ≥310 cm) (Figure 5.19). These floods resulted in shallow floodplain inundation (Algyő: 59–98 cm; Szeged: 6–30 cm and Makó: 18–65 cm). Typically, flood waves developed between February and July in both rivers; however, their overbank flood coincided only during the June 2020 flood throughout the study period. The near bankfull stages (stages at or 1 m below the bankfull level) were the most common flood wave types, and they were recorded during the same period as the overbank floods (i.e., February–July). During flood waves, the peak water stage in the Tisza usually coincided with or slightly followed its counterpart in the Maros, by a 1–2 days shift.
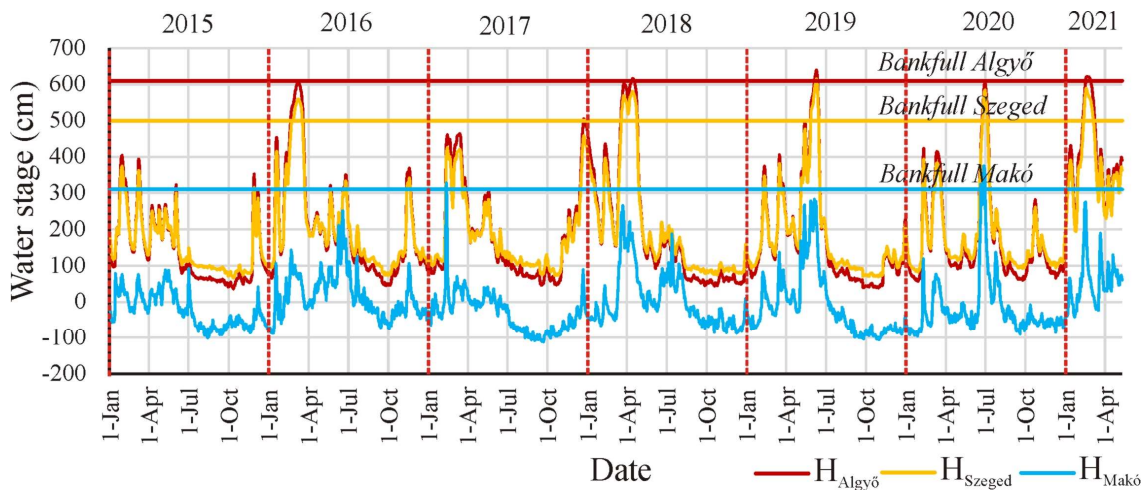
Figure 5.19. Daily water stage measurements and bankfull levels in two gauging sites in the Tisza (i.e., Algyő and Szeged) and one site in the Maros (i.e., Makó) between January 2015 and May 2021.

Apart from the flood period, the rivers experience prolonged low stages for the rest of the year (August–January). The onset of the low stage period in the Tisza usually occurs simultaneously or slightly later (i.e., 1–4 days shift) than in the Maros (Figure 5.19). The lowest water stages (i.e., Szeged and Algyő <60 cm; Makó<-100 cm) were recorded between August and November during the study period (Appendix: Table A2).

The daily water level change (ΔH) at the three gauging sites (i.e., $\Delta H_{Algyő}$, ΔH_{Szeged} and $\Delta H_{Makó}$), as well as the absolute difference in ΔH between the Tisza (at Algyő) and the Maros (at Makó) ($\Delta H_{Algyő}$-$\Delta H_{Makó}$) were calculated, as they may influence the mixing process in the confluence area (Appendix: Figure A3). The Maros showed higher water level variations than the Tisza since the fastest rising (145 cm/day) and falling (−151 cm/day) rates were recorded in the Maros in February 2017, indicating the flashy regime of the river. On the other hand, the Tisza had lower rates, as the fastest rising (January 2016) and falling (June 2019) rates were 113 cm/day and -81 cm/day, respectively and both were recorded in Algyő. The most significant ΔH difference between both rivers (>80 cm), occurred during floods (e.g., November 2015, January 2016, and February 2017), while remaining relatively stable during other periods.

During floods, the Q of the Tisza varied between 827 and 2087 m³/s, while it ranged only between 70 and 731 m³/s in the Maros (Figure 5.20A). Apart from this period, the Q range

drops to 128–1045 m³/s in the Tisza and 30–393 m³/s in the Maros. Based on the Q ratio between the rivers ($Q_{Makó}/Q_{Szeged}$), the greatest Q contribution of the Maros into the Tisza (37–57%), primarily occurred during low stages in summer or early autumn (Figure 5.20B). This is due to the significantly higher slope of the Maros, compared to the impounded Tisza by the Törökbecse Dam. Meanwhile, this contribution declines to just 6–10% during floods in winter months, due to the Tisza's impoundment effect on the Maros. In the meantime, the Q difference between the rivers (i.e., $Q_{Algyő}$-$Q_{Makó}$) displayed an opposite trend.
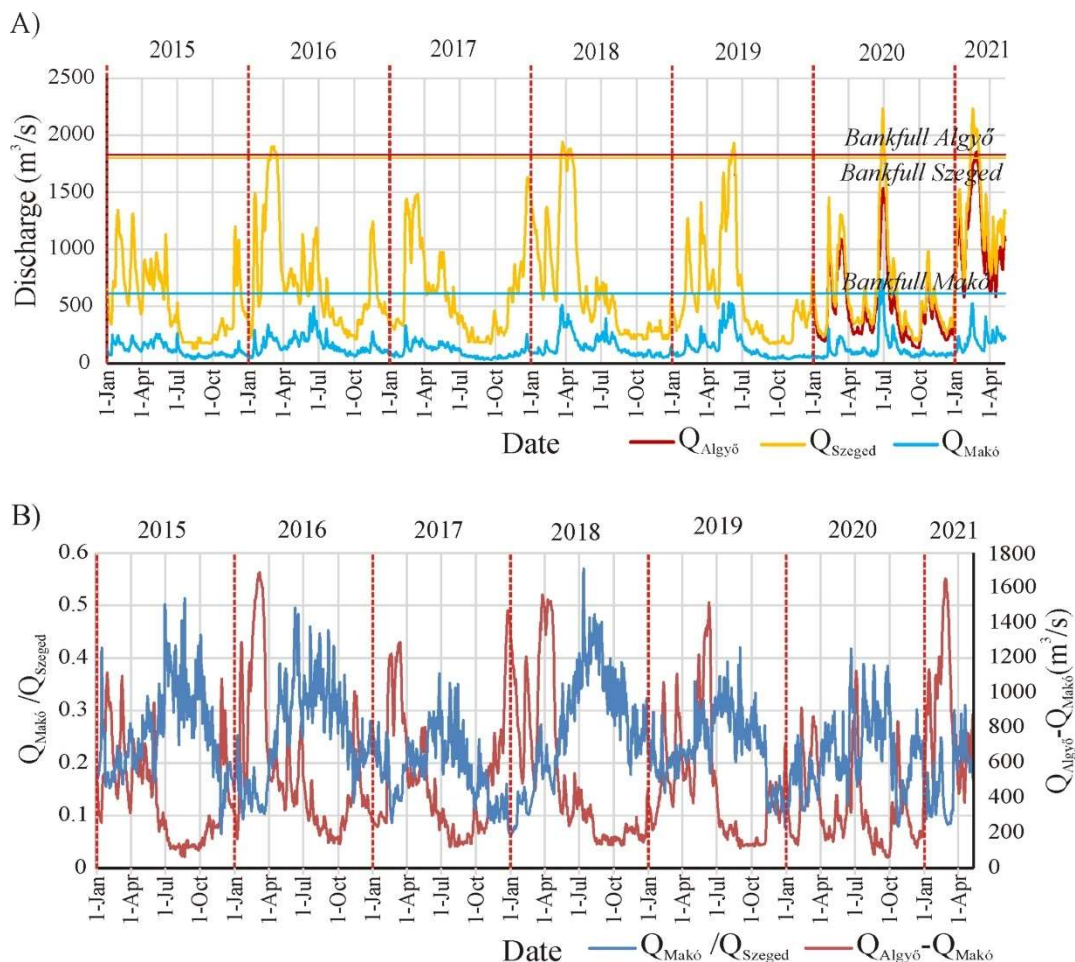
Figure 5.20. Daily discharge (Q) and bankfull value at the three gauging sites (i.e., Algyő, Szeged, and Makó) between January 2015 and May 2021 (A). The discharge ratio and difference between the rivers were calculated throughout the study period (B).

Throughout the study period, the Maros slope was nine-fold higher than the Tisza and exhibited greater variations too (Maros: 2.7–19.6 cm/km; Tisza: 0.0–5.5 cm/km) (Figure 5.21 and Table A2 in Appendix). Interestingly, the Maros slope during floods (2.7–19 cm/km) was comparable to the non-flood period (8.4–19.6 cm/km). However, a significant contrast was noticed in the Tisza`s slope between both hydrological conditions (floods: 1.3–5.5 cm/km; non-flood: 0–3.4 cm/km). During floods, the Maros slope usually opposes its counterpart in the Tisza, as it usually increases in the Tisza and simultaneously declines in the Maros. This discrepancy could be interpreted by the impoundment effect of the high-power Tisza to its tributary, the Maros, during this period. In non-flood periods, both rivers showed similar fluctuation patterns, though the Maros showed higher fluctuation magnitudes. The highest slope difference between the rivers (0–2 cm/km) typically occurred during floods in late winter and early summer, while it declined to -17.4–-18.2 cm/km during non-flood periods in summer.
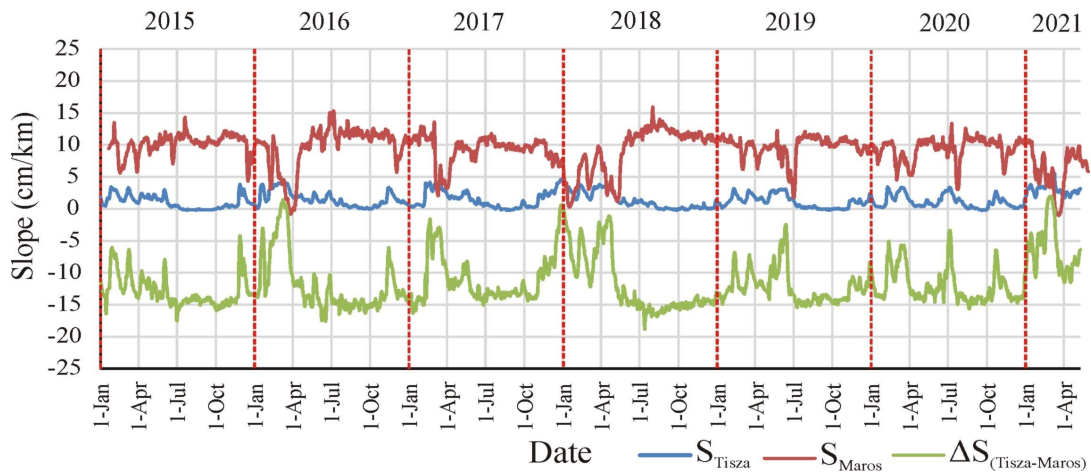
Figure 5.21. The calculated daily slope of the Tisza (S_{Tisza}) and Maros (S_{Maros}) Rivers, along with their difference ($\Delta S_{Tisza-Maros}$) during the study period: January 2015–May 2021.

5.4.2. *Temporal dynamics of mixing water from different origins in response to hydrological changes*

Based on the K-means classification of the 143 Sentinel-2 images (2015–2021), the areal percentage of the TW, MW, and MIX, along with the longitudinal extent of the MW into the Tisza (L) were calculated and compared to the hydrological parameters of the rivers (Figure 5.22). Over the study period, the TW dominated the confluence area, with 48.7%, exceeding the MW (12.4%) and the MIX (38.9%). Typically, the TW shows even more domination (60–100%) during simultaneous near bankfull/over bankfull stages in both rivers (e.g., January 2016, December 2017, and March 2018). The MW exhibited an intricate temporal change pattern, as its maximum areal coverage is achieved when the rivers have near-bankfull stages; however, it declines above this level, due to the domination of the TW and the impoundment of the MW. Hence, it seems that the coverage of MW is positively correlated with the water stage below the bankfull level and negatively correlated above it. An exception occurred only once throughout the study period during the June 2020 flood, as the MW covered a significant area of the confluence, though both rivers were at over bankfull flood. This case might have occurred due to an exceptional elevation in the Maros momentum, enabling it to overcome the impoundment effect of the Tisza. The MIX water, on the other hand, showed its lowest coverage during floods, while the greatest coverage typically occurs during low stages.
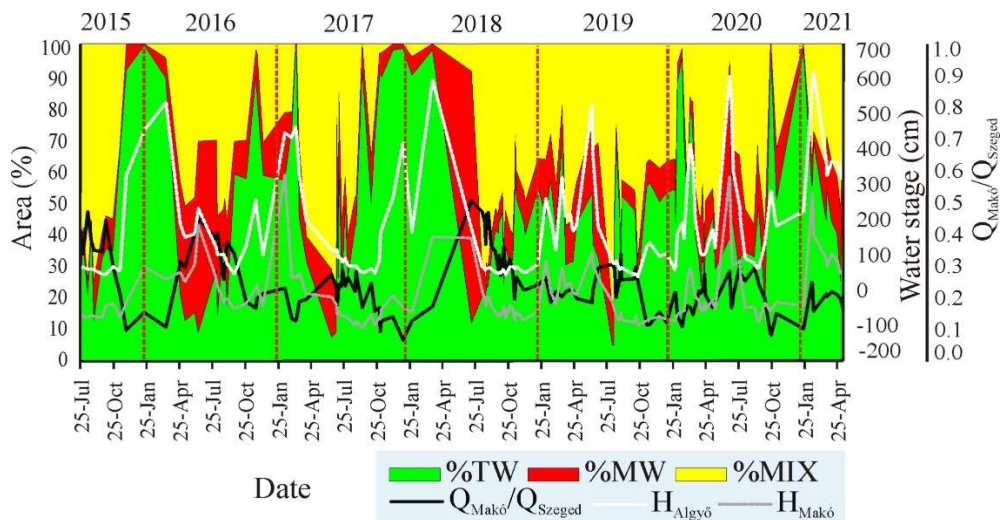
Figure 5.22. The areal coverage (%) of the Tisza water (TW), Maros water (MW), and mixture (MIX) in the confluence area was compared to measured and calculated hydrological parameters.

The lateral mixing in the confluence area was investigated by calculating the mean lateral coverage (%) of the TW, MW, and MIX within five transects (T1–T5; Figure 3.1D) (Figure 5.23). There was a decreasing trend in the lateral coverage of TW and MW towards downstream (T5), which was substituted by an increasing trend in MIX water, indicating gradual mixing downstream. Specifically, the lateral coverage of TW slightly increased by 3% between T1 and T2, gradually dropped by 29% between T2 and T4, and nearly stabilized at 32% between T4 and T5. However, this pattern is occasionally substituted by full TW coverage across all five transects during floods (Appendix: Figure A4).
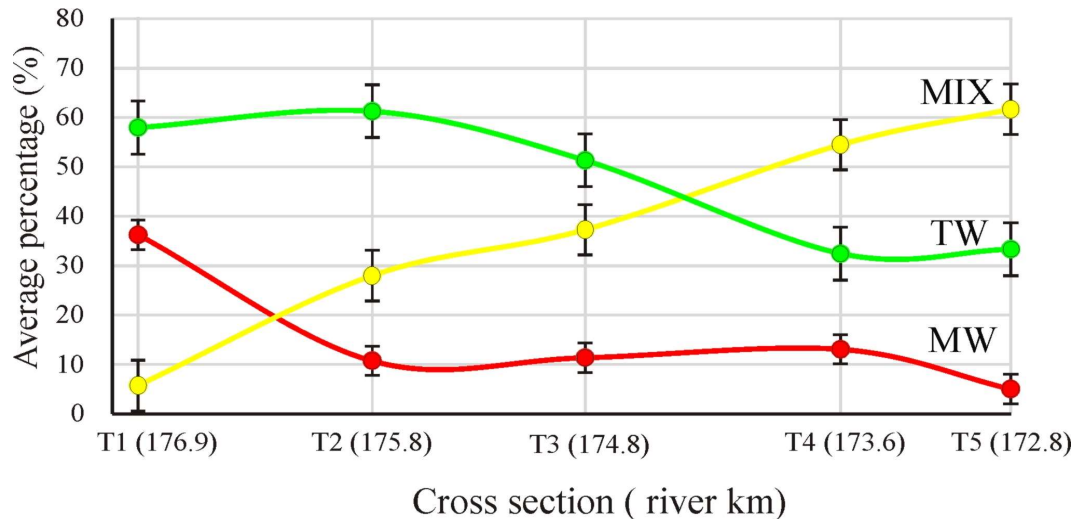
Figure 5.23. The mean lateral coverage (%) of the Tisza water (TW), Maros water (MW), and their mixture (MIX) was investigated along five transects (T1–T5) in the confluence area (2015–2021).

The lateral coverage of MW decreased from 36% at T1 to 11% at T2 due to the domination of TW at this section, then it stabilized at ca. 11% between T2 and T4. However, it declined by half (5%) at T5 due to the domination of MIX water. This pattern could also change during floods, with the MW covering ca. one-third of the channel at all transects (i.e., T1–T5) (Appendix: Figure A4).

The least lateral coverage of MIX water occurred at T1, as the TW and MW just interacted (Appendix: Figure A4). Afterward, it gradually increased by 13.8% per kilometer, reaching its peak (63%) at T5. The domination of MIX usually occurs during low stages in summer and autumn, while it almost has no coverage during floods, due to the prevalence of TW and/or MW (Appendix: Figure A4).

The longitudinal mixing was investigated through the distance (L) of the last MW pixel downstream of the confluence, which was estimated by the 143 Sentinel-2 images (2015–2021) (Figure 5.24). The distance L fluctuated significantly throughout the study period, ranging from just a few meters to several kilometers (1–26 w), with a mean extent of 1.3 km (7.8 w). Also, the temporal variation of L was closely associated with the areal coverage of MW, as it is an integral aspect of the MW dynamics.

The strength of the correlation between mixing water variables (i.e., TW, MW, MIX, and L) and various hydrological parameters of the rivers was investigated by the Pearson correlation test (Table 5.7). Besides, the correlations between these variables and the hypothesized most effective hydrological parameters were depicted (Appendix: Figure A5). The mixing water variables showed moderate to strong correlation with H, S, Q, Q_{Mako}/Q_{Szeged}, and $Q_{Algyő}-Q_{Makó}$, and very weak correlation with ΔH and $\Delta H_{Algyő}-\Delta H_{Makó}$. Remarkably, TW showed a better correlation with MIX (-0.91) than MW (-0.46), and both (i.e., TW and MIX) had similar correlation patterns with the hydrological parameters. Meanwhile, MW displayed its highest correlation (0.85) with L, and both also had similar correlation patterns with the hydrological parameters.
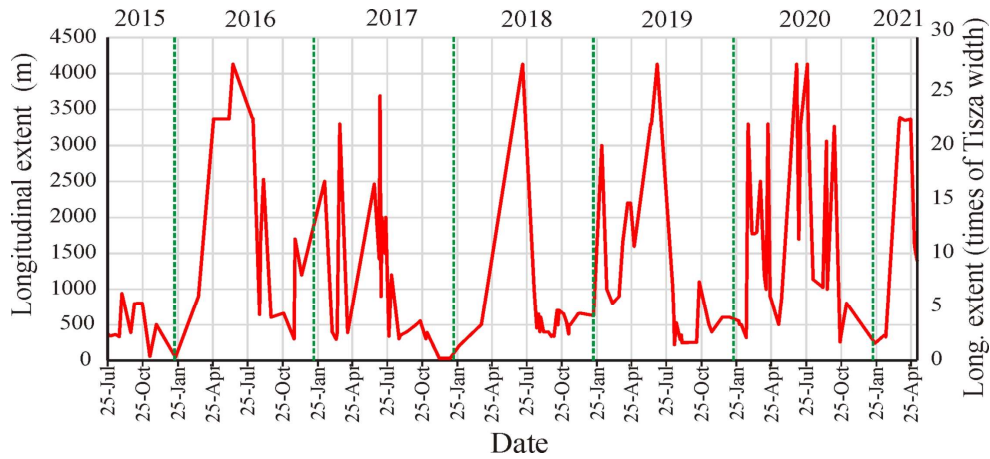
Figure 5.24. The longitudinal (L) extent of the Maros water (MW) into the Tisza water (TW), was estimated by 143 Sentinel-2 images (2015–2021).

Table 5.7. Correlation matrix between mixing water variables [i.e., Tisza water (TW), Maros water (MW), mixture (MIX), and longitudinal extent of MW into the Tisza (L)], measured and calculated hydrological parameters in the rivers (e.g., water stage, discharge, and slope).

	TW	MW	MIX	L
TW	1.00			
MW	-0.46	1.00		
MIX	-0.91	0.04	1.00	
$H_{Algyő}$	0.43	0.12	-0.54	
H_{Szeged}	0.40	0.13	-0.51	
$H_{Makó}$	0.02	0.47	-0.24	
S_{Tisza}	0.57	0.03	-0.66	
S_{Maros}	-0.65	0.27	0.60	
ΔS	0.65	-0.18	-0.64	
$\Delta H_{Algyő}$	0.01	-0.10	0.03	
ΔH_{Szeged}	0.01	-0.10	0.04	
$\Delta H_{Makó}$	-0.12	0.07	0.10	
$\Delta H_{Algyő}-\Delta H_{Makó}$	0.11	-0.15	-0.05	
$Q_{Algyő}$	0.48	0.10	-0.58	
Q_{Szeged}	0.42	0.13	-0.54	
$Q_{Makó}$	0.01	0.50	-0.24	
$Q_{Makó}/Q_{Szeged}$	-0.73	0.31	0.67	
ΔQ	0.57	-0.02	-0.63	
L	-0.36	0.85	-0.01	1.00

It seems that the most influential hydrological parameters on the areal coverage of TW and MIX are the *Q* ratio, *S*, and *S* difference. However, it is noteworthy that the *Q* ratio influences the mixing water variables regardless of the water stage condition, meanwhile, the influence of *S* and *S* difference relies on it, whether it is low or high. The superiority of the *Q* ratio affecting the mixing process downstream was also reported by Best and Reid (1984). The areal coverage of MW and its longitudinal extent *L*, on the other hand, are influenced the most by the Maros hydrology (e.g., $H_{Makó}$ and $Q_{Makó}$), with low sensitivity to the rest of the hydrological parameters. This behavior may return to the quick fade of MW in the confluence area, which does not proportionally correlate with the significant fluctuation in the hydrological parameters of the rivers.

To gain deeper insight into the influence of hydrology on the mixing process in the confluence area, specific hydrological events were analyzed. These events encompassed very different (i.e., low stages vs. high stages and vice versa) and similar (both have low or high stages) hydrological conditions in both rivers. Throughout the study period, the greatest stage

81

difference between the Tisza (491 cm) and Maros (33 cm) occurred on 18/3/2016. During this event, the TW dominated the confluence area (89.3%), the MW had limited coverage (6.4 %; between T1 and T3), and very limited mixing occurred (MIX: 4.4%). The opposite condition occurred on 14/7/2018 when a relatively high stage was recorded in the Maros (150 cm) and a relatively low stage in the Tisza (193 cm). During this event, the MW dominated the confluence area (79.3%) with an average lateral coverage of 65% along the five transects (T1–T5). The TW covered only 12.1% of the confluence area and the mixing was limited too (MIX: 8.5%). The Simultaneous floods in both rivers (Tisza: 585 cm; Maros: 324 cm) occurred just once during the study period on 30/6/2020. During this event, the mixing was severely restricted (MIX: 5.6%), as the confluence area was occupied by TW (38.8%) and MW (55.6%). The lowest water stages in the Tisza (72 cm) and Maros (-96 cm) occurred on 19/10/2019 throughout the study period. During this event, the MIX dominated the confluence area (67.7%) with limited coverage of TW (24.2%) and MW (8%) (Appendix: Figure A4).

5.4.3. *Mixing water patterns*

The spatiotemporal variation of the water types (i.e., TW, MW, and MIX) exhibited characteristic patterns throughout the year. Thus, three primary classes were established including 11 mixing patterns. These classes were defined based on the domination of each water type in the confluence area, resulting in TW, MW, and MIX mixing classes (Figure 5.25 and Table 5.8). Based on the spatial distribution of the water types and the likelihood of their upwelling at the end of the study area, 5 mixing patterns were determined within the TW and MIX classes, while only one pattern was observed within the MW class.
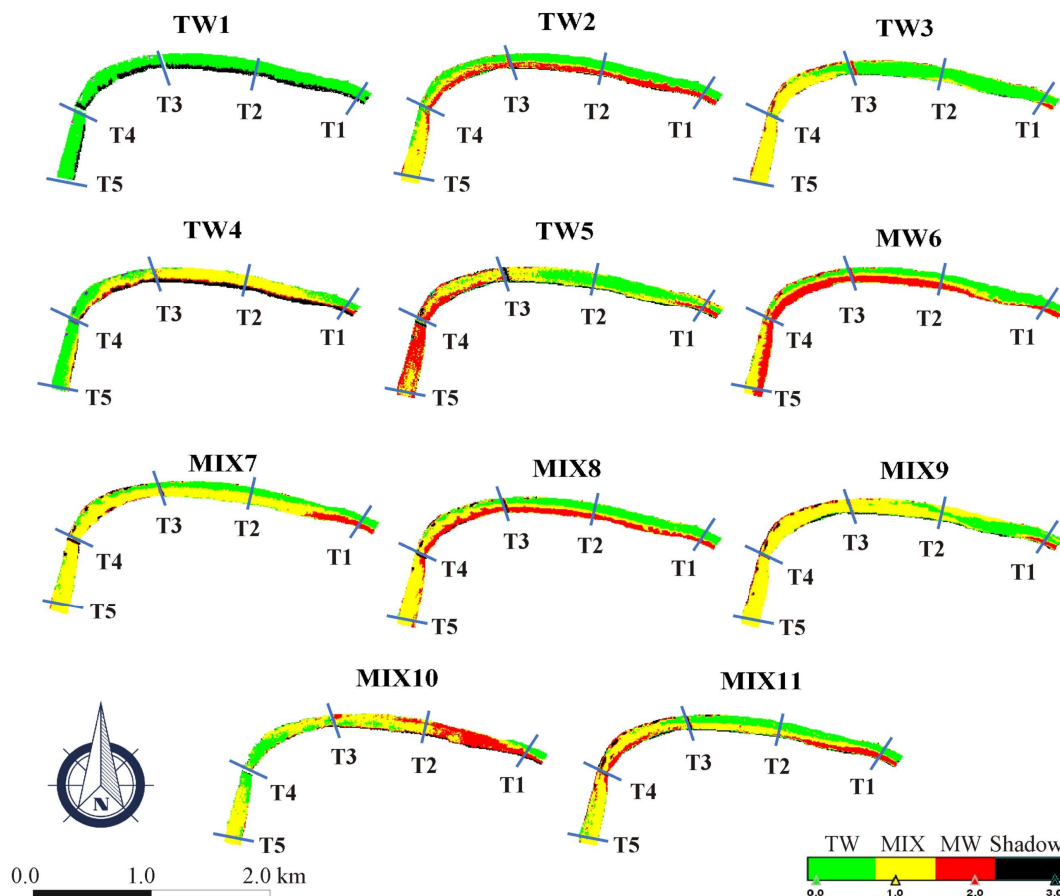
Figure 5.25. The most common mixing patterns in the Tisza–Maros confluence area are based on the domination of the water types [i.e., Tisza water (TW), Maros water (MW), and mixture (MIX)] in the confluence area. Each class was subdivided into several patterns considering the spatial distribution and upwelling of water types.

Table 5.8. Characteristics of the eleven mixing patterns, their frequency, and appearance months.

Mixing type	Up-welling	Sub-class	Characteristics of water types[1]			Characteristic hydrological parameters				Frequency (%)	Appearance (months)[2]
			TW	MW	MIX	$Q_{Makó}/Q_{Szeged}$	$Q_{Algyő}-Q_{Makó}$ (m^3/s)	$\Delta H_{Algyő}-\Delta H_{Makó}$ (cm/day)	$\Delta S_{(Tisza-Maros)}$ (cm/km)		
TW dominant	No	$TW1$	T1–T5: 70–100%	T1: 0–30%	no	0.1–0.34	151–1290	-27–54	-15.5–-1.4	18.9	**I–III**, IX–XI–XII
		$TW2$	T1–T4: 30–75%	T1–T4: 37–46%	T1–T5: 5–100%	0.11–0.26	142–1454	-56–56	-13.9–-0.3	17.5	I–III, VIII
		$TW3$	T1–T3: 30–100%	T1: 20–30%	T3–T5: 70–100%	0.17–0.26	142–1537	-11–22	-14.4–-2.3	4.9	III, IX–XII
	Tisza	$TW4$	T1 and T3–T5: 60–100%	T1–T4: 5–35%	T1–T5: 10–100%	0.11–0.29	102–597	-14–21	-14.7–-11.1	5.6	II, IX–XI
	Maros	$TW5$	T1–T3: 55–95%	T1 and T3–T5: 20–95%	T1–T5: 10–80%	0.15–0.25	103–511	-7–22	-13.8–-11	2.1	V, IX, XI
MW dominant	No	$MW6$	T1–T4: 10–75%	T1–T5: 30–80%	T1–T5: 10–60%	0.28–0.51	292–840	-42–35	-17.7–-8.2	4.9	IV, **VI–VIII**
MIX dominant	No	$MIX7$	T1–T4: 10–60%	T1–T2: 5–85%	T1–T5: 5–100%	0.2–0.41	108–617	-15–14	-15.5–-8.7	6.3	II, IV, V, VII–**VIII–X**
		$MIX8$	T1–T4: 10–70%	T1–T4: 30–40%	T1–T5: 5–100%	0.17–0.41	185–1104	-22–13	-15.7–-3.4	9.8	IV, VII–VIII, X
		$MIX9$	T1–T3: 5–95%	T1: 5–30%	T1–T5: 5–100%	0.2–0.5	68–544	-25–25	-16.6–-11.1	16.1	IV, VII–**VIII–IX, XI**
	Tisza	$MIX10$	T1 and T2–T4: 65–100%	T1–T2: 35–100%	T2–T3 and T4–T5: 10–100%	0.17–0.34	122–417	-16–11	-14.8–-11.6	12.6	III–IV, VII–VIII, X, XII
	Maros	$MIX11$	T1–T3: 45–65%	T1–T2 and T3–T4: 15–35%	T1–T5: 5–100%	0.22–0.3	265–548	-9–7	-14.5–-11.6	1.4	IV, VIII

[1] T1-T5: Those transects are indicated where the given water type appears. The % refers to the lateral contribution of the water type within these transects.
[2] Those months are highlighted in bold when the given pattern appears frequently.

Within the TW class (TW1–TW5), the water of the Tisza dominated the confluence area (Figure 5.25 and Table 5.8). While no upwelling appeared in the first three patterns (TW1–TW3), the water of the Tisza upwelled in the TW4 pattern and the water of the Maros upwelled in the TW5 pattern. In the TW1 no real mixing occurs, and the TW covered almost all the confluence area (T1–T5: 70–100%). The rest of the area is covered by MW (0–30%); however, it was restricted to the first transect T1. This pattern is the most common among the eleven identified patterns (frequency: 18%) and usually occurs in winter, especially between January and March, when the Tisza has an elevated discharge (mean $Q_{Makó}/Q_{Szeged}$: 0.16; mean ΔQ: 618 m³/s), water stage fluctuation (mean $\Delta H_{Algyő}-\Delta H_{Makó}$: 1.9 cm) and slope (mean ΔS: −9.6 cm/km) compared to the Maros.

Apart from the TW1 pattern, considerable mixing occurred at the remaining patterns of the TW class (i.e., TW2–TW5). However, these patterns differed mainly on the degree of MW coverage and the chance of TW or MW to upwell at the downstream end (Figure 5.25

and Table 5.8). In the TW2, the MW appeared at the first four transects (T1-T4) with an average lateral coverage of 41%. Meanwhile, the MIX appeared at all transects, with its lateral coverage gradually increasing from 5% (at T1) to full coverage downstream (at T5). This pattern usually develops in February and March when the Tisza has lower discharge ($Q_{Makó}/Q_{Szeged}$: 0.19) and water stage fluctuation ($\Delta H_{Algyő}$-$\Delta H_{Makó}$: -5.6 cm/day) compared to the TW1 pattern. However, the slope difference was similar to TW1 (ΔS: −8.2 cm/km). This pattern has the second highest frequency of occurrence (17.9%).

In the TW3 pattern, the MW showed quite limited coverage, as it appeared just within the first transect (T1) (Figure 5.25 and Table 5.8). The rest of the confluence area was divided into two parts: T1–T3 dominated by TW and T3–T5 dominated by MIX. This pattern has a moderate probability of occurrence (4.9%), and usually develops in December when the Tisza has lower discharge than the TW1 and TW2 patterns ($Q_{Makó}/Q_{Szeged}$: 0.22; mean ΔQ: 476 m^3/s), though minor flood wave appeared on the Tisza ($\Delta H_{Algyő}$-$\Delta H_{Makó}$: 3.9 cm/day). However, the Maros still maintains an elevated slope (ΔS: −11.6 cm/km).

Within the TW class, two upwelling patterns were identified, including the TW4 and TW5 (Figure 5.25 and Table 5.8). In the TW4 pattern, TW was blocked by MIX water near the junction; meanwhile, in the TW5 pattern, MW was blocked by TW; however, both water types reappeared at the downstream end (T3–T5). The explanation of these upwelling phenomena may return to different densities of the water types from different origins, resulting from variations in the transported SS load, depth, and water temperature of the rivers. As a result, the lower density water stratifies above the higher one. These patterns have a low to medium probability of occurrence (2.1–5.6%) and usually develop in September and November when the rivers are in low stages. The lowest discharge difference (ΔQ: 323 m^3/s) and the highest slope difference (ΔS: −12.9 cm/km) among the TW class occurred during these mixing patterns. However, they had comparable discharge ratio ($Q_{Makó}/Q_{Szeged}$: 0.2) and water stage difference ($\Delta H_{Algyő}$-$\Delta H_{Makó}$: −4.4 cm/day).

Within the MW dominant class, only one mixing pattern was noticed (MW6) (Figure 5.25 and Table 5.8). In the MW6 pattern, MW covered all transects (T1–T5) with a lateral coverage of 30–80%, while the TW covered the first four transects (lateral coverage: 10–75%), and the MIX presented at all transects (lateral coverage: 10–60%). This mixing pattern is similar to the TW2 pattern; however, they can be differentiated by the significantly higher coverage of MW in the MW6. The MW6 pattern has a moderate probability of occurrence (4.9%) and usually develops during summer in June and July, when the Maros has an elevated discharge ($Q_{Makó}/Q_{Szeged}$: 0.34; mean ΔQ: 454 m^3/s) and a steep slope (ΔS: −13.7 cm/km), allowing it to overcome the impoundment effect of the Tisza. However, owing to the elevated momentum of the Tisza during these periods, the MW could not penetrate deeper into the confluence area, instead, it extended longitudinally with a considerable strip.

Similar to the TW class, the MIX class comprises five mixing patterns (i.e., MIX7–MIX11) (Figure 5.25 and Table 5.8). While the MIX7–MIX9 patterns have no upwelling of any of the water types, the TW is upwelled in the MIX10, and the MW is upwelled in the MIX11. In the MIX7 the MIX water appeared at all transects (lateral coverage: 5–100%), the TW at most transects (i.e., S1–S4; 10–60%), and the MW at a short section between T1 and T2, with a wide strip (5–85%). This pattern has a moderate probability of occurrence (6.3%). Notably, MIX7–MIX9 patterns usually occur during low stages, when the discharge ratio is high ($Q_{Makó}/Q_{Szeged}$: 0.31), and the slope difference is low (ΔS: −13.9 cm/km).

The fact that the significant areal coverage of MIX usually occurs during low stages and the lowest coverage during floods in the Tisza–Maros confluence contradicts the findings of Park and Latrubesse (2015) in the Solimões–Negro confluence. However, this discrepancy may be raised from the elevated confluence angle of the Tisza–Maros and its gentler slopes than the Solimões–Negro. These factors may enhance the probability of Maro's impoundment during floods, leading to limited mixing. Meanwhile, during low stages, the

elevated slope of the Maros, and the low impounded Tisza enables better mixing.

The spatial pattern of MIX8 is similar to MIX7; however, the main difference is the longer extent of MW downstream (T1–T4: 30–40%) in MIX8, in comparison to the limited extent in MIX7 (T1–T2: 5–85%) (Figure 5.25 and Table 5.8). Also, the MIX8 has a similar spatial pattern as TW2 and MW6; however, the specialty of this pattern is the domination of the areal coverage of MIX water over TW and MW. This pattern has the second highest probability of occurrence (9.8%) among the MIX class, and usually develops in early summer (July and August).

The MIX9 is the most common pattern in the MIX class (frequency: 16.1%) (Figure 5.25 and Table 5.8). The pattern is characterized by the limited longitudinal extent of both MW (T1–T2: 5–30%) and TW (T1–T3: 5–95%), which is substituted by significant coverage of MIX (T1–T5: 5–100%). This pattern is typically in later summer (August and September). Interestingly, the highest discharge ratio ($Q_{Makó}/Q_{Szeged}$: 0.35) and the lowest slope difference (ΔS: -14.9 cm/km) occurred within this pattern, so far, which indicates that the elevated contribution from the Maros River doesn't necessarily translate as a domination of MW, but also the MIX.

The MIX10 and MIX11 patterns represent the upwelling of TW and MW within the MIX class (Figure 5.25 and Table 5.8). While the TW was blocked by MW near the junction in MIX10, the MW was blocked by MIX water in MIX11; however, both reappeared at the downstream end. The interpretation of the upwelling phenomenon may be attributed to the density difference of the water types (i.e., TW, MW, and MIX), similar to TW4 and TW5 patterns. Remarkably, the full lateral coverage of the MW (100 %) at the junction occurred only within the MIX10 pattern, though it still has a relatively short longitudinal extent (T1–T2). The spatial pattern of MIX11 resembles TW5; however, the significant coverage of TW and MW in TW5 is substituted by MIX water in MIX11. Both MIX10 and MIX11 usually occur during low stages, particularly in July and August in MIX10 and in August in MIX11. Yet, the MIX10 has a significantly higher probability of occurrence (12.6%) than MIX11 (1.4%). Both patterns tend to develop under similar hydrological conditions (i.e., MIX10: $Q_{Makó}/Q_{Szeged}$: 0.25, $\Delta H_{Algyő}-\Delta H_{Makó}$: -2.5 cm and ΔS: -13.7 cm/km; MIX11: $Q_{Makó}/Q_{Szeged}$: 0.25, $\Delta H_{Algyő}-\Delta H_{Makó}$: -1.0 cm and ΔS: -13.0 cm/km).

5.4.4. *Predictive equations for the mixing water types*

Predictive equations were produced for the mixing water variables (i.e., TW, MW, MIX, and *L*) in the confluence area, based on the measured and calculated hydrological parameters in both rivers (Table 5.9). The equations were established for three scenarios: all hydrological conditions (considering all data), low and medium discharge conditions (considering cluster I data), and high discharge conditions (considering cluster II data). This separation was established since some hydrological parameters (e.g., slope and slope difference) showed better correlations with the mixing water variables when flood periods were separated from low and medium discharges (Table 5.7 and Appendix: Figure A5).

Based on the R^2 values, the predictive accuracy is high for TW (0.6–0.63) and MW (0.61–0.7), and relatively low for MIX (0.4–0.55) (Table 5.9). Notably, the longitudinal extent of MW into the Tisza (L) could be predicted with the best possible accuracy (0.64–0.82) based on the areal coverage of MW, rather than the hydrological parameters.

The accuracy of the derived equations can be ranked as moderate to good; however, the complexity of the mixing process in the confluence area impedes better accuracy to be achieved. Specifically, the hydrological parameters do not exclusively influence the mixing process, but also several interacting factors, e.g., channel morphology and its dynamics along with temporal variations in sediment load, hydrology, and water temperature.

The predictive equations offer valuable support for planning sampling campaigns in the Tisza–Maros confluence area. This can be achieved by providing a near-future mixing

pattern based on measured or predicted hydrological parameters from the three neighboring gauging sites (Algyő, Szeged, and Makó). The main benefit of predicting the mixing pattern prior to the initiation of the sampling process is to avoid misinterpretations and wrong conclusions about the studied substance (e.g., pollutant, MP, SS, and phytoplankton).

Table 5.9. Predictive equations for the mixing water variables [i.e., Tisza water (TW), Maros water (MW), mixture (MIX), and longitudinal extent of MW into the Tisza (L)], based on measured and calculated hydrological parameters in the Tisza and Maros Rivers.

Data Group	Model	R^2
All Data	TW = 1076.84 - 87.55 ($Q_{Makó}$ / Q_{Szeged}) + 0.048 (ΔQ) - 12.96 ($H_{Makó}$)	0.63
	MW = -750.23 + 0.25 ($Q_{Makó}$) - 0.09 (Q_{Szeged}) + 8.03 (S_{Tisza}) - 52.94 ($Q_{Makó}$/Q_{Szeged}) +10.46 (H_{Szeged})	0.62
	MIX = 24.06 + 97.93 ($Q_{Makó}$ / Q_{Szeged}) - 6.93 (S_{Tisza})	0.55
	L = -83357.44 + 1077.04 ($H_{Makó}$) - 4.56 (ΔQ) + 940.93 (S_{Tisza})	0.41
	L = 97.92 (MW) - 4.61	0.73
Cluster I ($Q_{Algyő} \leq 747$ m^3/s and $Q_{Makó} \leq 150$ m^3/s)	TW = 14784.38 + 13.12 (S_{Maros}) - 190.83 ($H_{Makó}$) + 0.18 (Q_{Szeged}) + 0.94 ($Q_{Makó}$)	0.61
	MW = 2658.90 + 0.44 (QMakó) - 33.99 (HMakó)	0.61
	MIX = 23.42 + 99.45 ($Q_{Makó}$/ $_{Szeged}$) - 5.80 (S_{Tisza})	0.40
	L = 1374.5 + 23.97 ($Q_{Makó}$) - 5976.38 ($Q_{Makó}$/Q_{Szeged}) - 3.40 (ΔQ)	0.56
	L = 108.26 (MW) - 256.7	0.82
Cluster II ($Q_{Algyő} > 747$ m^3/s and $Q_{Makó} > 150$ m^3/s)	TW = 117.51 - 284.14 ($Q_{Makó}$/Q_{Szeged})	0.60
	MW = 53.36 - 2.09 (ΔS) + 0.20 ($Q_{Makó}$) - 0.06 (Q_{Szeged})	0.70
	MIX = -865.36 - 0.06 (ΔQ) + 12.12 (H_{Szeged})	0.40
	L = 996.37 + 11246.43 ($Q_{Makó}$/Q_{Szeged}) - 1.5 (ΔQ)	0.53
	L = 82.605 (MW) + 526.24	0.64

5.5. Spatiotemporal distribution and correlation of surficial suspended sediment and microplastic concentrations along the Tisza

5.5.1. *Temporal distribution and correlation of surficial suspended sediment, microplastic concentrations and water stage at Mindszent (temporal monitoring site)*

Altogether, 140 in-situ measurements were conducted between May 2021 and May 2023 at Mindszent (Figure 3.1C). Throughout this period, the maximum water stage fluctuation was 646 cm (H_{min}: -31 cm; H_{max}: 615 cm; Figure 5.26). Low stages were typical in summer and autumn (H_{mean}: 16.7±51 cm), and they were interrupted by 9 minor (H_{mean}: 118±84 cm), and 10 medium flood waves (H_{mean}: 339±150 cm), typically in winter and spring. Among them, only two waves (May 2021 and March 2023) exceeded the bankfull level (H≥560 cm) by a few centimeters (4–54 cm), while the rest were below the bankfull stage.
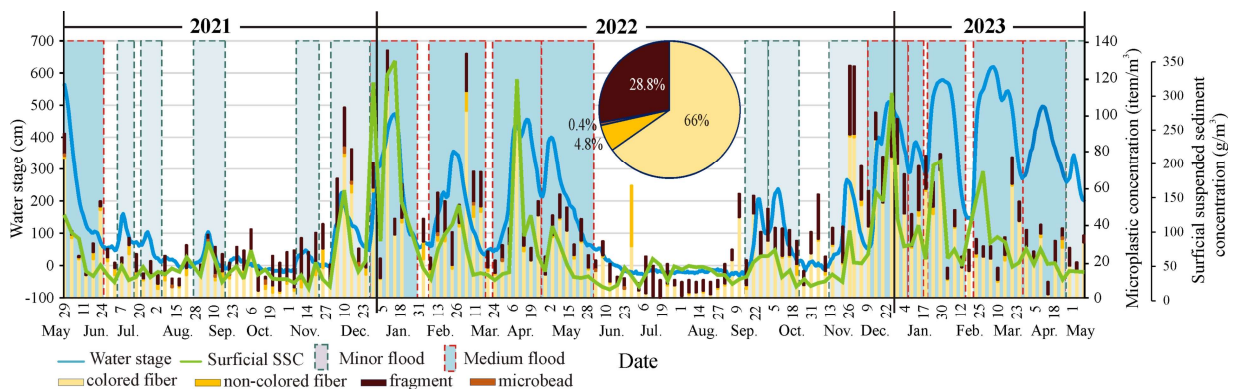

Figure 5.26. Temporal changes of surficial suspended sediment (SS) and microplastic (MP) concentrations during various hydrological conditions (i.e., low stage and flood waves) at Mindszent (May 2021–May 2023).

During the study period at Mindszent, the surficial SSC fluctuated between 11 and 323 g/m³ (SSC_{mean}: 60±57 g/m³) and MP concentration ranged between 2 and 129 item/m³ (MP_{mean}: 35±27 item/m³) (Figure 5.26). The surficial SS and MP concentrations followed a similar pattern as the stage hydrograph. Thus, the lowest concentrations occurred during low stages (SSC_{low}: 34±14 g/m³; MP_{low}: 21±16 item/m³) (Figures 5.26 and 5.27). Meanwhile, they increased by 32% (SSC_{minor}:45±27 g/m³) and 95% (MP_{minor}: 41±30 item/m³) during minor floods and further increased by 116% (SSC_{medium}:97±75 g/m³) and 15% (MP_{medium}: 47±27 item/m³) during medium floods. This is related to the low flow velocity (≤0.02 m/s) and stream power during low stages, which stimulate sediment and MP deposition. Meanwhile, during floods, the high flow velocity (>0.25 m/s) and highly turbulent flow mobilize the deposited sediments and MP from the riverbed into the water column. Additionally, slope sediments in the upland sub-catchments are mobilized, including MP sources (Mohsen et al., 2023a).

The average surficial SSC was comparable during the rising (43±22 g/m³) and falling (47±30 g/m³) phases of the minor floods; however, the MP concentration during the falling phase was 38% higher than during the rising phase. During the minor floods, the highest surficial SSC occurred during the peak phase (SSC_{peak}: 51±17 g/m³), in contrast to the lowest MP concentration (MP_{peak}: 22±6 item/m³). During medium floods, the mean surficial SSC during the rising phase was 1.6 times higher than the falling phase, due to the greater availability of sediment accompanied by an elevated stream power during the rising phase. The mean MP concentration was identical (45±27 item/m³) during the rising and falling phases, yet both surficial SS (171±93 g/m³) and MP (58±25 item/m³) concentrations were the highest during the peak phase. These temporal distribution patterns indicate a higher dependency of surficial SSCs on water stage changes than MP`s (Talbot and Chang, 2022).
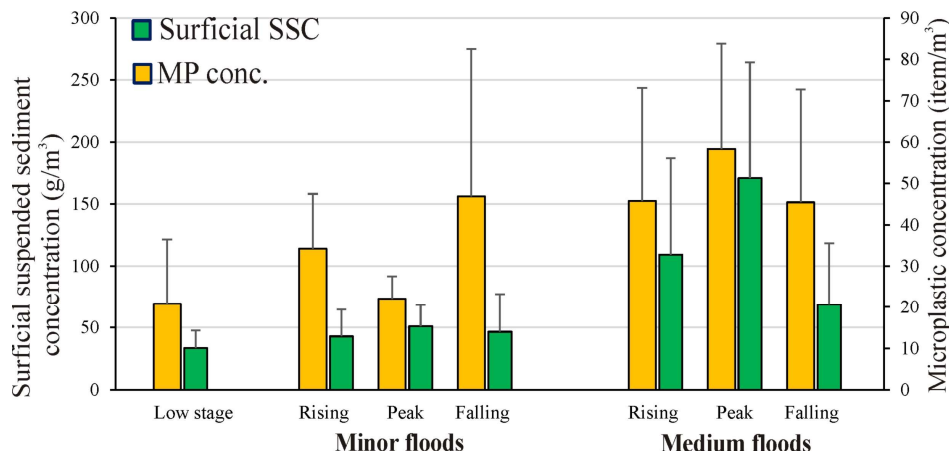
Figure 5.27. Average surficial suspended sediment (SS) and microplastic (MP) concentrations during different hydrological scenarios in the Mindszent site (May 2021–May 2023).

Remarkably, the magnitude of flood waves was not associated with the quantity of transported surficial SS and MP. Typically, the initial flood wave following a prolonged dry period carries higher surficial SS and MP loads compared to subsequent waves. For instance, the January 2022 flood wave transported concentrations twice and 1.4 times higher for surficial SS and MP, respectively, than the subsequent April 2022 wave, though their water stage magnitudes were similar (Figure 5.26). This highlights the importance of the first flush in the fluvial system of the Tisza caused by the higher availability of sediment and MPs in the channel and the upper sub-catchments at the beginning of flood wave, depleting with subsequent waves (Talbot and Chang, 2022). This observation aligns with the findings of Vercruysse et al. (2017), emphasizing the significance of event sequence.

During flood waves, the surficial SSC peak typically aligns with or precedes the water stage peak, while the peak of MP concentration may precede or follow it (Figure 5.26). This discrepancy could be attributed to variations in the transport lengths of SS and MPs

(Ockelford et al., 2020; Chen et al., 2021), as light MPs are likely to transport easier and earlier than SS (Waldschläger and Schüttrumpf, 2019).

The Spearman's rank correlation coefficient between surficial SSC and H was higher ($\rho=0.7$) than that between MP and H ($\rho=0.55$) across all hydrological periods (Figure 5.28A). For the individual periods, the lowest correlation between surficial SSC and H occurred during low stages ($\rho=0.16$), while the highest was observed during medium floods ($\rho=0.6$) (Figure 5.28A, Appendix: Table A3A). In contrast, the correlation between MP and H showed the lowest correlation during medium floods ($\rho=0.1$) and the highest during minor floods ($\rho=0.38$). Regarding flood phases, both surficial SS and MP concentrations exhibited the highest correlations with H during the peak phase, while their correlations during the rising and falling phases were lower, yet comparable (Figure 5.28B, Appendix: Table A3B).
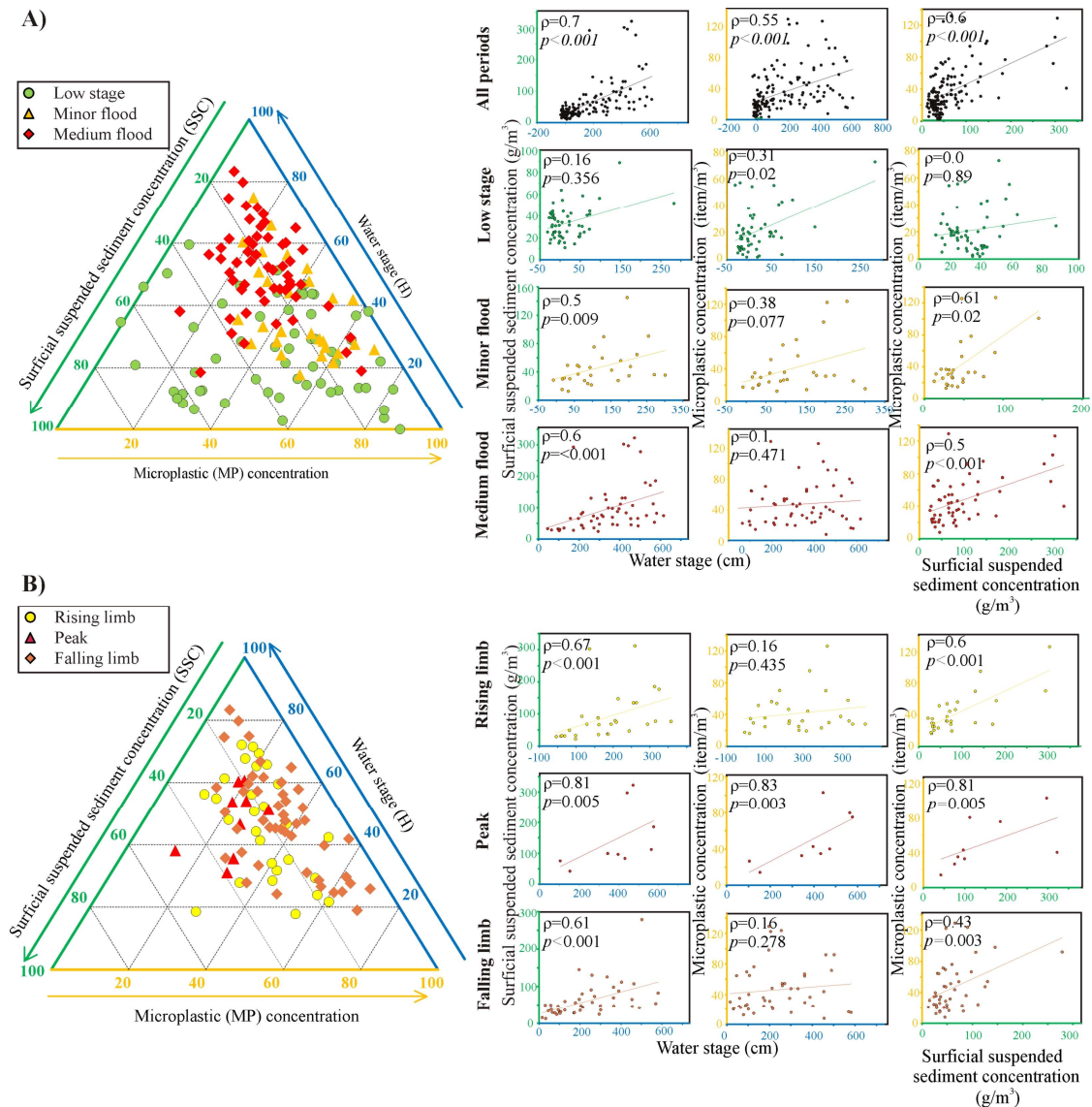
Figure 5.28. Correlations between water stage (H), surficial suspended sediment (SS), and microplastic (MP) concentrations during various hydrological periods (A) and flood phases (B) at Mindszent (May 2021–May 2023).

Based on the correlation findings, it becomes clear that both surficial SS and MP concentrations are positively correlated with H. However, the surficial SSC showed stronger correlations than MP`s, implying that the transport of SS in the Tisza is influenced more by the hydrological conditions than that of MP`s. Similar positive correlations have been observed in studies by Ockelford et al. (2020) and Laermanns et al. (2021), though negative

correlations have been reported by others (Barrows et al., 2018; Wu et al., 2020).

The Kruskal-Wallis H and post hoc tests revealed a significant difference in the surficial SSC among different hydrological periods. Meanwhile, it was evident between low stages and both the minor and medium floods in the case of MP concentration (Figure 5.29A, Appendix: Table A4–Table A5). During flood phases, a statistical difference in the surficial SSC was found only between the peak and falling phases, while no difference was noticed in the case of MP concentration among the three pairs (Figure 5.29B, Appendix: Table A6).

A strong positive correlation was found between surficial SS and MP concentrations ($\rho_{SSC–MP}$=0.6) across all hydrological periods (Figure 5.28A). Considering the individual periods, a negligible correlation occurred during low stages (ρ_{low}=0.0). However, during floods, the correlation strengthened, though the correlation during the minor floods (ρ_{minor}=0.61) was higher than the medium floods (ρ_{medium}=0.5) (Figure 5.28A; Appendix: Table A3B). The negligible correlation during low stages can be interpreted by the dominance of non-flood-related sources of MPs (e.g., wastewater input) and SS (e.g., bank erosion and tributaries), which have dissimilar impacts on surficial SS and MP transport in the Tisza. Meanwhile, during floods, probably the surface runoff and resuspension of deposited SS and MP have a common influence on both variables, leading to an elevated correlation. The discrepancy in correlation coefficients during minor and medium floods may be related to the appearance of surface runoff in the medium floods, and its absence in the minor floods. This additional source has a dissimilar influence on SS and MP transport owing to their heterogeneous distribution within different sub-catchments.
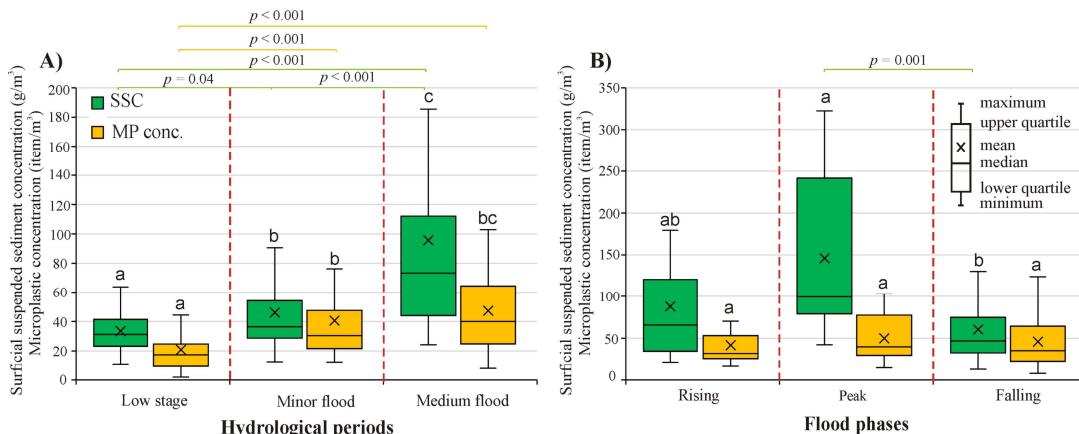
Figure 5.29. Distribution of surficial suspended sediment (SS) and microplastic (MP) concentrations during various hydrological periods (A) and flood phases (B) at Mindszent (May 2021–May 2023). Alphabetical letters indicate the statistical differences.

During flood phases, the correlation between surficial SS and MP concentrations was very strong (ρ_{peak}=0.81) during the peak, while it declined to strong during the rising and falling phases, though the correlation coefficient during the rising phase (ρ_{rising}=0.6) was higher than the falling phase ($\rho_{falling}$=0.43) (Figure 5.28B). The elevated correlation coefficients during the peak and rising phases can be attributed to the elevated kinetic energy in the river and the simultaneous influence of resuspension from the bottom sediment and/or surface runoff on surficial SS and MP transport. Meanwhile, during the falling phase, kinetic energy diminishes exponentially, and consequently the active layer thickness of the bottom sediment declines (Ockelford et al., 2020). Thus, flood-related sources of SS and MP (i.e., resuspension and surface runoff) are supplanted by low stage-related sources (e.g., WWTPs, bank erosion, and tributaries) which have dissimilar influences on surficial SS and MP transport in the Tisza.

The temporal measurements at Mindszent revealed a predominance of colored fiber (66%) and fragment (28.8%) over non-colored fiber (4.8%) and microbead (0.4%) (Figure

5.26). This is in line with the previous data of Balla et al. (2022) and Kiss et al. (2021) who reported the domination of colored fiber in freshly deposited sediment and water of the Tisza, suggesting wastewater as a major source of MP in the river. The domination of fibers among the MP morpho-types has been reported in other rivers, including the Yangtze and Ganges Rivers (He et al., 2021; Napper et al., 2021). The elevated proportion of fragments at Mindszent is likely connected to local anthropogenic activities, such as ferry movement, fishing, and tourism as the sampling site is in a port zone.

The occurrence of colored fiber (74%) and microbeads (0.65%) revealed a strong association with flood waves, while non-colored fiber (9%) and fragments (38%) with low stages. The Kruskal-Wallis H and post hoc tests revealed a statistical difference among the pre-defined hydrological periods (i.e., low stage, minor flood, and medium flood), but only for colored fibers and fragments (Appendix: Figure A6, Table A7, and Table A8). While colored fibers showed a statistical difference between low stages and both minor and medium floods, fragments differed only between low stage and medium floods. This variability in morpho-types across the hydrological periods may be indicative of the appearance of additional wastewater sources during floods (e.g., deliberate or accidental wastewater drainage), contributing to the observed statistical differences, particularly in colored fiber.

On the other hand, no statistical difference was found in morpho-types among various flood phases (i.e., rising, peak, and falling) (Appendix: Figure A6). However, colored fiber (80%) and microbeads (0.39 %) were strongly associated with the peak phase, while fragment (29%) and non-colored fiber (4%) were associated with the rising and falling phases, respectively.

5.5.2. Spatial distribution and correlation of surficial suspended sediment and microplastic concentrations along the Tisza

5.5.2.1. Bi-annual spatial changes of surficial suspended sediment concentration in the Tisza

The surficial SSC at the Tisza River sections (S1–S5) ranged between 26 and 44 g/m^3 (mean: 35±4.4 g/m^3) in 2021; meanwhile, it showed a wider range (24–65 g/m^3) and 16% higher mean concentration in 2022 (40 ± 9.8 g/m^3) (Figure 5.30). This difference may be linked to variations in the timing of sampling campaigns, though both were performed during low stages. The 2022 campaign was conducted in July just after heavy rainfalls in the catchment along with the beginning of the summer season, coincided with intensive touristic activities (e.g., motorboats and jet skis), leading to sediment resuspension. The 2021 campaign, on the other hand, was conducted at the end of the summer season in August when sediment deposition was prevalent.
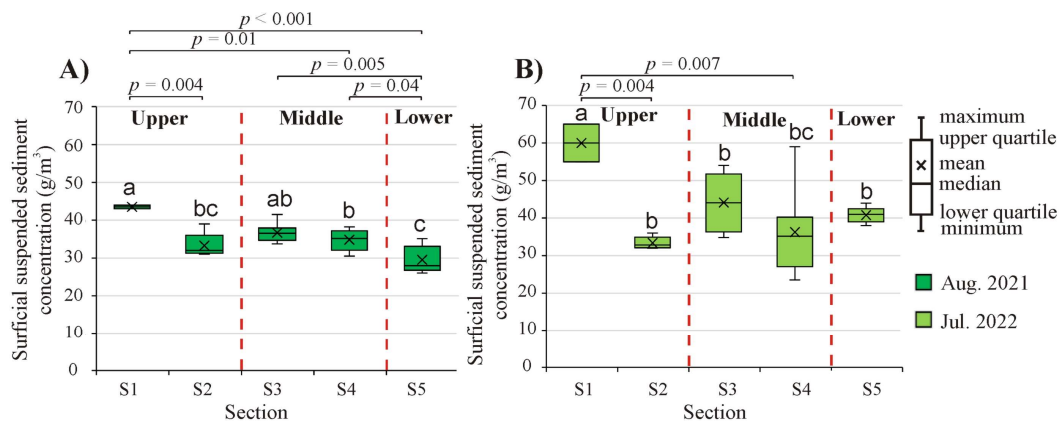
Figure 5.30. Distribution of the surficial suspended sediment concentration (SSC) at the five sections (S1–S5) of the Tisza in 2021 (A) and 2022 (B). Alphabetical letters refer to statistical differences.

A similar surficial SSC distribution pattern was observed in both years, especially in the

90

first four sections, as the highest concentrations were recorded in the S1 and S3 sections, albeit with greater magnitudes in 2022 (Figure 5.30). The lowest concentration in 2021 was recorded in S5, while it was in S2 in 2022. In 2021, the one-way ANOVA and Tukey post hoc tests revealed a statistical difference only in S1 and S5. Specifically, S1 differed significantly from S2, S4, and S5, while S5 differed significantly from S3 and S4 (Appendix: Table A9 and Table A10). In 2022, the statistical difference occurred only between S1 and both S2 and S4 (Appendix: Table A10).

Based on the surficial SSC measurements in 2022, tributaries showed three times higher concentrations (119.8 ± 59.6 g/m^3) than the Tisza (40 ± 9.8 g/m^3). The influence of tributaries on the SS transport was evaluated by comparing the surficial SSC at the sites located upstream and downstream of the confluences in 2021 and 2022 (Figure 5.31). Remarkably, various tributaries revealed different contributions. For instance, while the Szamos and Kraszna raised the surficial SSC downstream by 2.9–11.1% in both years, the Tarac, Sajó, and Körös declined it by 15.3–27.3%. In the meantime, some tributaries (e.g., Bodrog, Zagyva, and Maros) exhibited an adverse contribution in both years. For example, Maros raised surficial SSC downstream by 87.2% in 2022, whereas it declined by 9.8% in 2021.
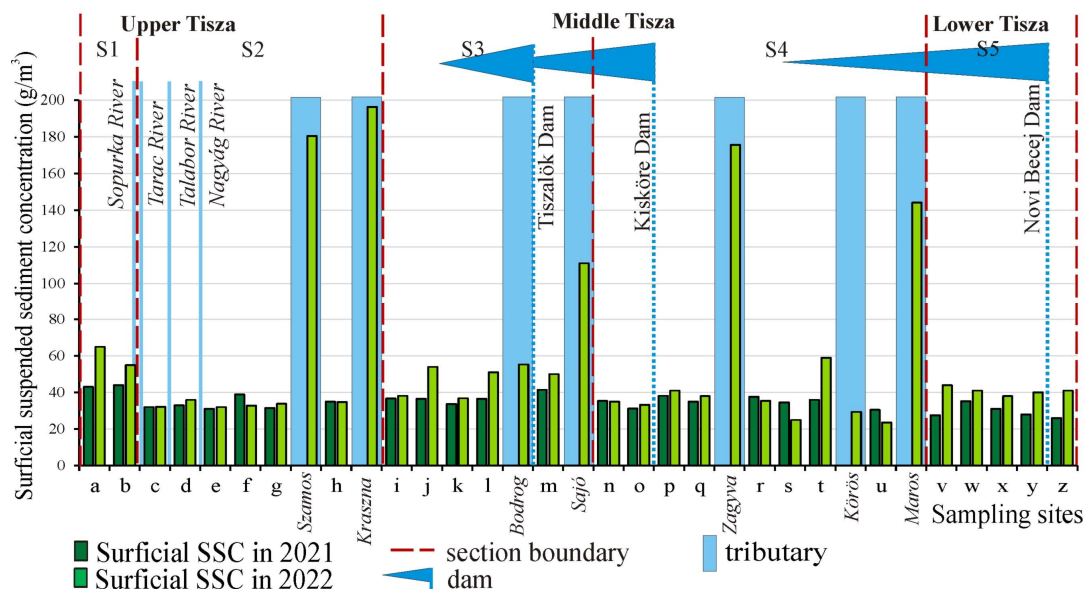
Figure 5.31. Spatial distribution of the surficial suspended sediment concentration (SSC) along the Tisza River at 26 sites in 2021 and 2022. The surficial SSC in the main tributaries was measured and represented only in 2022.

Dams induce sediment deposition upstream, as evidenced by a surficial SSC decline upstream of the Kisköre and Novi Becej Dams by 2.5–33.5%, (Figure 5.31). However, in the upstream end at the Tiszalök Dam, the surficial SSC increased by 8.1–38.5% (2021 & 2022).

5.5.2.2. Bi-annual spatial changes of microplastic concentration in the Tisza

The MP concentration in 2021 varied between 0 and 61 item/m^3 (mean: 19 ± 13.4 items/m^3); however, it showed a slightly wider range (4–63 items/m^3) and 18% higher mean concentration in 2022 (22.4 ± 14.8 item/m^3). This pattern resembles the surficial SSC pattern in both years, probably due to the differing timing of both campaigns. Based on our spatial (mean: 20.7 ± 14.1 item/m^3) and temporal (mean: 35 ± 27 item/m^3) MP measurements, the Tisza can be categorized as a moderately polluted river by MP among European Rivers. For instance, it has a higher contamination level than the Rhine (11.5 ± 6.3 item/m^3; Schrank et al., 2022) and the Elbe Rivers (5.57 ± 4.33 item/m^3; Scherer et al., 2020), while it was less polluted than the Danube (48.7 ± 53.7 item/m^3; Schrank et al., 2022). Internationally, the

Tisza can be classified as a slightly polluted river globally, as the median global MP pollution range is 0.17–3.4 × 10^5 items/m³ (Rodrigues et al., 2019).

The longitudinal pattern of MP concentration among the river sections (S1–S5) was similar in both measuring years (Figure 5.32). A significant drop occurred between S1 and S2 (in 2021: 52.3%), followed by a gradual decline between S2 and S4 (2021: 22%; 2022: 29.5%), and a subsequent increase between S4 and S5 (2021: 55.9%; 2022: 28.4%). The Kruskal-Wallis H test revealed the absence of any statistical differences in the MP concentration among the river sections in both measuring years.
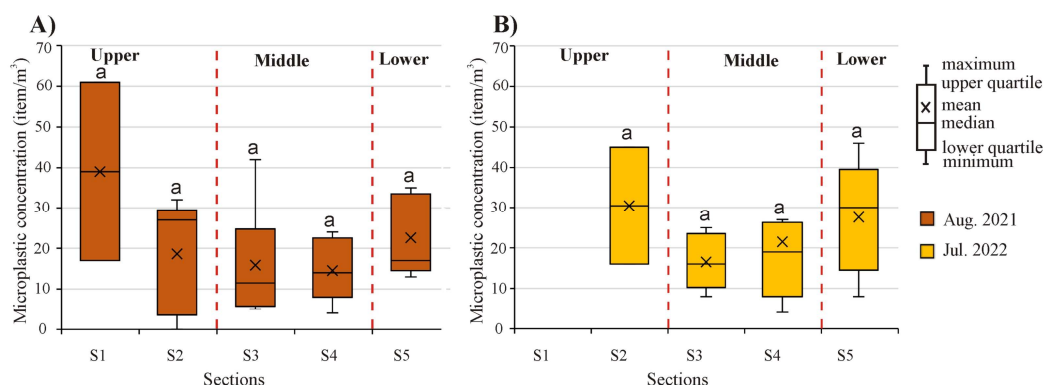
Figure 5.32. Distribution of the microplastic (MP) concentration at the five sections (S1–S5) of the Tisza River based on 26 sites in 2021 (A) and 21 sites in 2022 (B). Alphabetical letters refer to statistical differences.

The longitudinal MP concentration data along the Tisza in 2021 and 2022 revealed that the upper and lower reaches are the most polluted, while the middle reach experience comparatively lower pollution. This can be interpreted by the suboptimal wastewater management practices (wastewater treatment <30%; Interreg, 2018) in Ukraine, northeastern Hungary, and Serbia, along with the application of primary and secondary treatment technologies in these countries, which could retain up to 83.5 % of MPs (mainly fiber) (Tang and Hadibarata, 2021). Also, waste disposal sites in the upper mountainous sub-catchments, directly connected to the river channel, contribute to conveying runoff-related MPs into the Tisza during storm events.

On the other hand, in the middle reach sub-catchments, wastewater management practices are more developed, and the third treatment technology is implemented. Therefore, this reach has a moderate MP contamination level. Also, this reach benefits from a 2940 km long artificial levee system, acting as a buffer for the river channel and its tributaries, effectively separating it from MP pollution sources.

The mean MP concentration at the section scale obscures its great spatial variability along the Tisza in both measuring years; hence, it was depicted at the site scale (Figure 5.33). In 2021, the most polluted sites were in the Upper Tisza at site "b" (Gyilove; 61 items/m³) and in the Middle Tisza at site "i" (Aranyosapáti; 42 items/m³). In 2022, the most polluted sites remained at the upper and middle reaches too; however, they shifted downstream to site "f" (Tiszabecs; 45 items/m³) and site "u" (Mindszent; 63 items/m³), respectively. Besides, site "x" (Ada; 46 item/m³) in the Lower Tisza became very contaminated. On the other hand, the least contaminated sites in 2021 [e.g., "g" (Tivadar) and "p" (Tiszaroff)] became moderately polluted in 2022. Similarly, some moderately contaminated sites in 2021 [e.g., "s" (Tiszaug) and "v" (Szeged)] became less contaminated in 2022. This great spatiotemporal variability may be connected to changes in flow conditions, pollution sources, anthropogenic activities, and wastewater management practices along the river and among the measuring years.
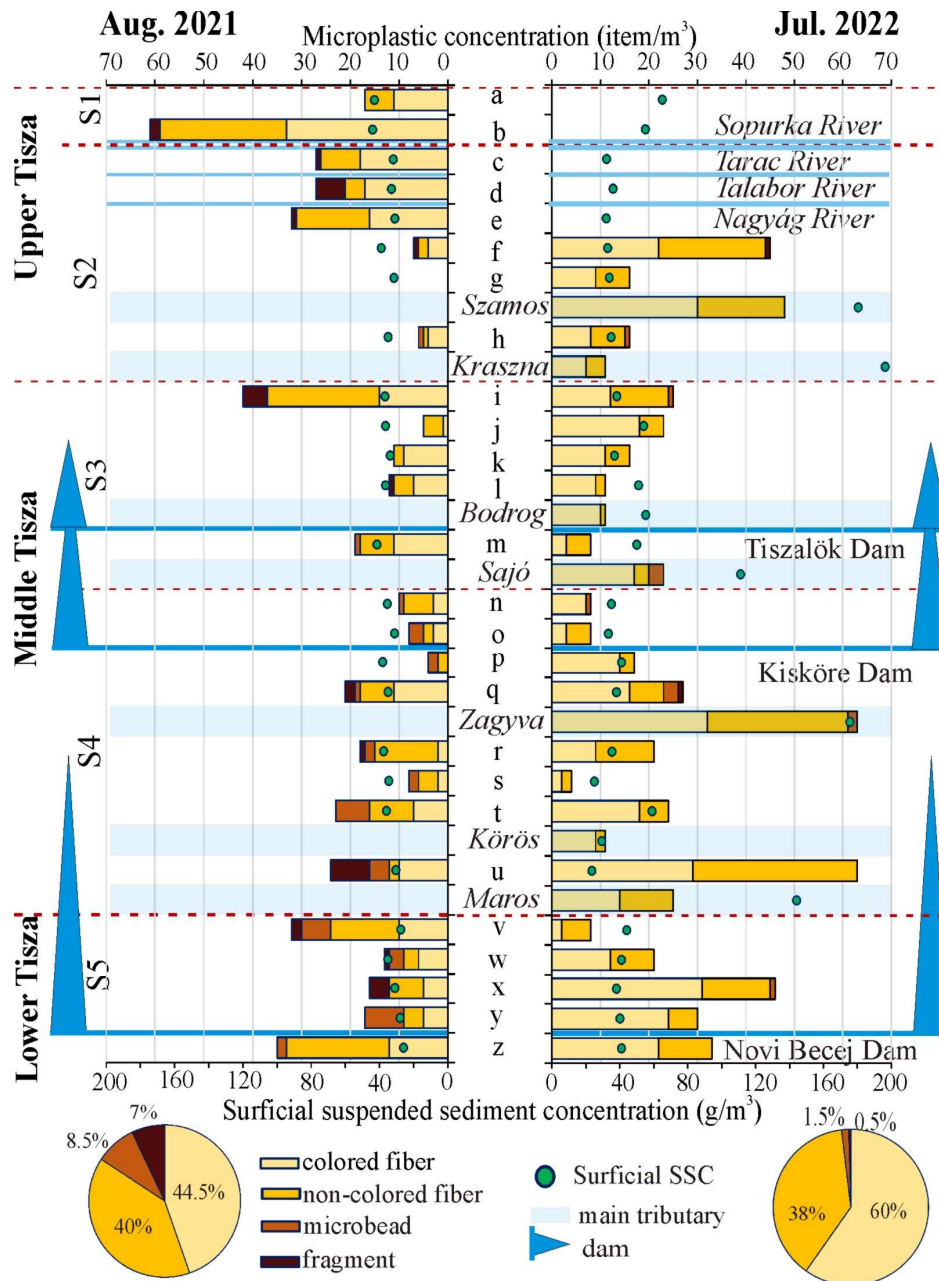
Figure 5.33. Differences between the longitudinal distribution of surficial suspended sediment (SS) and microplastic (MP) concentrations along the Tisza River (26 sites in 2021 and 21 sites in 2022). The surficial SS and MP concentrations of the main tributaries were measured only in 2022.

Based on the MP concentration measurements in 2022, tributaries had 1.2 times higher concentrations (mean: 27 ± 19 item/m^3) than the Tisza (mean: 22.4 ± 14.8 item/m^3). In 2021, most tributaries (e.g., Nagyág, Szamos, Kraszna, Bodrog, and Maros) raised the MP concentration in the mainstream by 19–600 % (Figure 5.33). Meanwhile, in 2022, only the Körös and Kraszna raised it by 56% and 163% respectively, though these rivers had relatively low MP concentrations (11 items/m^3). On the other hand, in 2021, the Tarac, Sajó, and Zagyva declined the MP concentration by 14–55 %; however, in 2022 this decline effect was typical in the Bodrog (−27%), and Maros Rivers (−87%).

Dams revealed an ambiguous influence on the MP transport in the Tisza during both measuring years (Figure 5.33). This can be inferred from the gradual decline in MP concentration (58%) upstream of the Kisköre Dam in 2021, which nearly stabilized in 2022. On the contrary, upstream of the Novi Becej Dam, MP concentration increased by 30% and 43% in 2021 and 2022, respectively.

Concerning the MP composition along the river, it was dominated by fiber in both years, mirroring the composition in the temporal monitoring site in Mindszent. In 2021, ca. 45% were colored fiber, 40% were non-colored fiber, while microbeads and fragments formed only 8% and 7%, respectively (Figure 5.33). In 2022, the proportion of colored fiber increased to 60%, the non-colored fiber (38%) nearly stabilized, while the abundance of microbeads (1.5%) and fragments (0.4 %) became rare. The Kruskal-Wallis H and post hoc tests revealed a statistically significant difference only in the microbeads and just in 2021 between S1–S3 and S4–S5 (Appendix: Table A11 and Figure A7A). Conversely, no significant difference appeared among the morpho-types in 2022 (Appendix: Figure A7B).

Microbeads were exclusively present in the middle and lower reaches (S3–S5) in both years; however, the peak occurred at different sections in both years (Figure 5.33). This particular morph-type primarily originates from cosmetics (Bashir et al., 2021), which interprets its less abundance in the upper reach, where Ukraine and northeastern Hungary have the lowest GDP, resulting in less consumption of such products in these regions compared to other sub-catchments. Fragments were observed throughout the river in 2021, and in the upper and middle reaches in 2022; however, its highest abundance occurred in the S2 section in both years (2021: 9.7 %; 2022: 1.6 %). The elevated abundance in the S2 section may be linked to lower waste management practices in Ukraine, where the highest gap between communal waste production and recycling ratio exists (Eurostat, 2021).

5.5.2.3. Longitudinal correlation between surficial suspended sediment and microplastic concentrations

The surficial SS and MP concentrations showed characteristic patterns along the river sections in both measuring years (Figure 5.30 and Figure 5.32). The highest surficial SSC occurred in the S1 (upper reach) and S3 (middle reach) sections in both years, while the most MP contaminated sections were the S2 (upper reach) and S5 (lower reach). Typically, sites with elevated MP contamination were coupled with low to moderate surficial SSC, exemplified in sites "e" (Mala Kopanya), "i" (Aranyosapáti), and "z" (Zrenjanin) in 2021, and sites "f" (Tiszabecs) and "u" (Mindszent) in 2022 (Figure 5.33).

Generally, tributaries revealed a distinct influence on the surficial SS and MP transport in the Tisza during both measuring years. The Kraszna (concentrating) and the Zagyva (diluting) were the only rivers that affected them equally in both years; meanwhile, the rest exhibited temporally different influences.

Likewise, dams showed a dissimilar influence on the surficial SS and MP transport in the Tisza during both measuring years. Usually, the SSC declines upstream in their reservoirs (e.g., Kisköre and Novi Becej Dams) and slightly increases downstream due to clear water erosion. Meanwhile, the MP concentration displayed an ambiguous pattern at different dams and in both years.

The Spearman's correlation test between surficial SS and MP concentrations along the Tisza revealed a moderate negative correlation in 2021 ($\rho_{SSC–MP}$: −0.35), which was strengthened in 2022 ($\rho_{SSC–MP}$: −0.41) (Table 5.10 and Appendix: Figure A8). This negative correlation might have occurred due to the timing of both measuring campaigns during low stages when the source of SS and MP are dissimilar. This was also evidenced by the temporal measurements in the Mindszent site during the low stages.

Considering the correlation between surficial SS and MP concentrations in the individual sections, the first section (S1) in the Upper Tisza was the only one where a very strong positive correlation occurred ($\rho_{SSC–MP}$: 0.99) (Table 5.10). In this section, the highest surficial SSC (43.5 ± 0.5 g/m^3) was associated with the highest MP (39 ± 22 item/m^3) concentration, owing to the mountainous nature of the sub-catchment and low level of communal waste and wastewater management practices, allowing storm event to mobilize both slope sediments and waste storages concurrently. Moving to the second section (S2), the surficial SSC

declines owing to a significant drop in the channel`s slope and the appearance of a floodplain in the valley. However, there is a simultaneous increase or stability in MP concentration in this section due to population growth and inadequate wastewater management practices in Ukraine and northeastern Hungary. The interplay of these natural and human factors resulted in a moderate negative correlation in 2021 (ρ_{SSC-MP}: -0.36), which was strengthened to a very strong (ρ_{SSC-MP}: -0.99) in 2022.

Table 5.10. Longitudinal correlation (ρ) between surficial suspended sediment (SS) and microplastic (MP) concentrations considering the entire river and its sections (S1–S5) in 2021 and 2022.

Reach	River section		2021 Surficial SSC	2022 Surficial SSC
Upper Tisza	Whole river (S1–S5)	MP	-0.35 (p=0.093)	-0.41 (p=0.066)
	S1	MP	0.99 (p<0.001)	–
	S2	MP	-0.36 (p=0.553)	-0.99 (p<0.001)
Middle Tisza	S3	MP	0.64 (p<0.173)	-0.10 (p=0.913)
	S4	MP	-0.30 (p=0.47)	0.20 (p=0.629)
Lower Tisza	S5	MP	-0.99 (p<0.001)	-0.82 (p<0.089)

A dissimilar correlation pattern with inverse signs occurred in the Middle Tisza sections (S3–S4) in both years; however, they were mostly weak (Table 5.10). This reflects the significant dynamism of SS and MP transport within this reach, primarily induced by various inputs from large tributaries. The weak correlations in these sections may be attributed to the relatively high SS input from tributaries, coupled with well-established wastewater management practices in these sub-catchments (77% of households connected to wastewater systems), resulting in a comparatively low MP pollution.

Lastly, a very strong negative correlation occurred in the Lower Tisza (S5) in both years (Table 5.10). This reach is heavily influenced by the impoundment effect of the Novi Becej Dam, leading to sediment and MP deposition. However, the low-degree wastewater management practices in Serbia resulted in a significant release of wastewater in the river, and consequently high MP concentrations. The combined influence resulted in a decline in the surficial SSC accompanied by high MP concentrations; hence a strong negative correlation occurred.

It should be emphasized that these interpretations might be constrained to our sampling periods during low stages with a moderate sampling intensity. Hence, further measurements during floods with a denser intensity are imperative to evaluate the validity of these interpretations during various hydrological conditions. However, conducting temporal measurements during floods in a large fluvial system, like the Tisza, has some challenges, including (1) flood waves usually transport at various velocities, and a sampling campaign could last for a week; therefore, it would be challenging to collect samples during the same hydrological phase across all sites; (2) not all tributaries experience floods simultaneously, potentially limiting flood waves to certain sections of the main river.

5.5.2.4. Influence of slope, tributaries and dams on sediment and microplastic transport

The transport of surficial SS and MP did not reveal a downstream trend along the Tisza. For instance, elevated MP concentrations occurred in both the upper mountains reach at S1 (slope: >13 cm/km) and the lower reach with a minimal slope (≤2.5 cm/km). This transport

pattern suggests that the influence of slope on the SS and MP transport was overshadowed by other factors, such as runoff, human activities, and sediment deposition patterns as reported by Schrank et al. (2022). In addition, our sampling campaigns were conducted during low stages, characterized by low slope conditions; thus, it may influence the surficial SS and MP transport minimally. However, its influence may vary during floods, thus additional longitudinal sampling during these periods is imperative for a thorough evaluation.

Tributaries have a significant influence on the SS and MP transport in the Tisza; however, their consistent influence on SS transport was more evident than MP`s. Over the course of both studied years, variations in MP and SS transport of the tributaries and differences in their impact on the mainstream were noticed, aligning with findings in other river systems (Mouri et al., 2014; Béjar et al., 2018). Although tributaries had concentrations three times higher for surficial SS and 20% higher for MP than the Tisza (in 2022), only slight concentration changes were noticed downstream of the confluences. This is attributed to low discharge inputs from tributaries during this period. Yet, denser spatial sampling upstream and downstream of confluences with sufficient replicates are vital to get better insights about their roles on surficial SS and MP transport in the main river, as the mixing patterns, flood wave propagation, and Q ratio between the tributary and mainstream might affect the snapshot-like findings.

Typically, dams influence the longitudinal profile of sediment transport, partially by stimulating sediment deposition upstream due to their impoundment effect and raising it downstream due to clear water erosion (Kondolf et al., 2014). However, they showed contradictory spatiotemporal patterns for surficial SS and MP transport in the Tisza in both measuring years, though the surficial SS transport pattern was more consistent than MP`s. This discrepancy may be attributed to the more uniform characteristics and settling behavior of sediment compared to MP`s (Kondolf et al., 2014). Also, the transport of MP in reservoirs is likely influenced by anthropogenic activities (e.g., WWTP effluents) compared to SS`s (Balla et al., 2022), which was evidenced in the Novi Becej reservoir. A similar finding was reached by Watkins et al. (2019) who reported both the increasing and decreasing MP concentration trends in their studied reservoirs, with the decreasing trend being dominant. Yet, denser longitudinal measurements upstream and downstream of dams with sufficient replicates are warranted to confirm the identified longitudinal transport patterns.

5.6. Remote sensing-based surficial suspended sediment and microplastic concentrations modelling in the Tisza River

5.6.1. *Correlation and spectral characteristics*

The Sentinel-2 and PlanetScope bands revealed a negligible (ρ=0.04) to a very strong (ρ =0.74) correlation with surficial SS and MP concentrations, meanwhile, they showed only a negligible correlation with the Sentinel-1 channels (ρ=0.03–0.08) (Figure 5.34A). The surficial SSC was highly correlated with bands of the optical sensors than MP concentration. The greatest correlation for surficial SSC was observed with Sentinel-2, while for MP concentration, it was with PlanetScope. Specifically, the VIS–NIR bands, especially B4 and B5 in Sentinel-2 and their counterparts B6 and B7 in PlanetScope were the most sensitive to surficial SS and MP concentration changes. Interestingly, the highest correlation between MP concentration and Sentinel-2 bands occurred with B9 (ρ=-0.26); however, this band is not the best for MP concentration estimation owing to its coarse spatial resolution (60 m) and heightened sensitivity to water vapor content.

The correlation between the most correlated bands in Sentinel-2 (i.e., B4 and B5) and PlanetScope (i.e., B6 and B7) with surficial SS and MP concentrations, along with the two channels of Sentienl-1 were depicted through scatter plots (Figure 5.34B–D). The plots suggested a non-linear correlation between surficial SS, MP concentrations, and Sentinel-2

and PlanetScope bands, while no correlation was found with the Sentinel-1 channels.

Remarkably, most bands of the Sentinel-2 and PlanetScope revealed a similar correlation pattern with surficial SS and MP concentrations, considering band compatibility between both sensors (Table 4.1 and Figure 5.34A). However, less bands (e.g., B8a in Sentinel-2 and B8 in PlanetScope) displayed a dissimilar pattern. This disparity may result from the variability in the spatial and spectral (e.g., bandwidth and SNR) characteristics of both sensors. Additionally, frequent imaging of PlanetScope provided more data than Sentienl-2, thus the correlation coefficients were calculated based on different datasets.
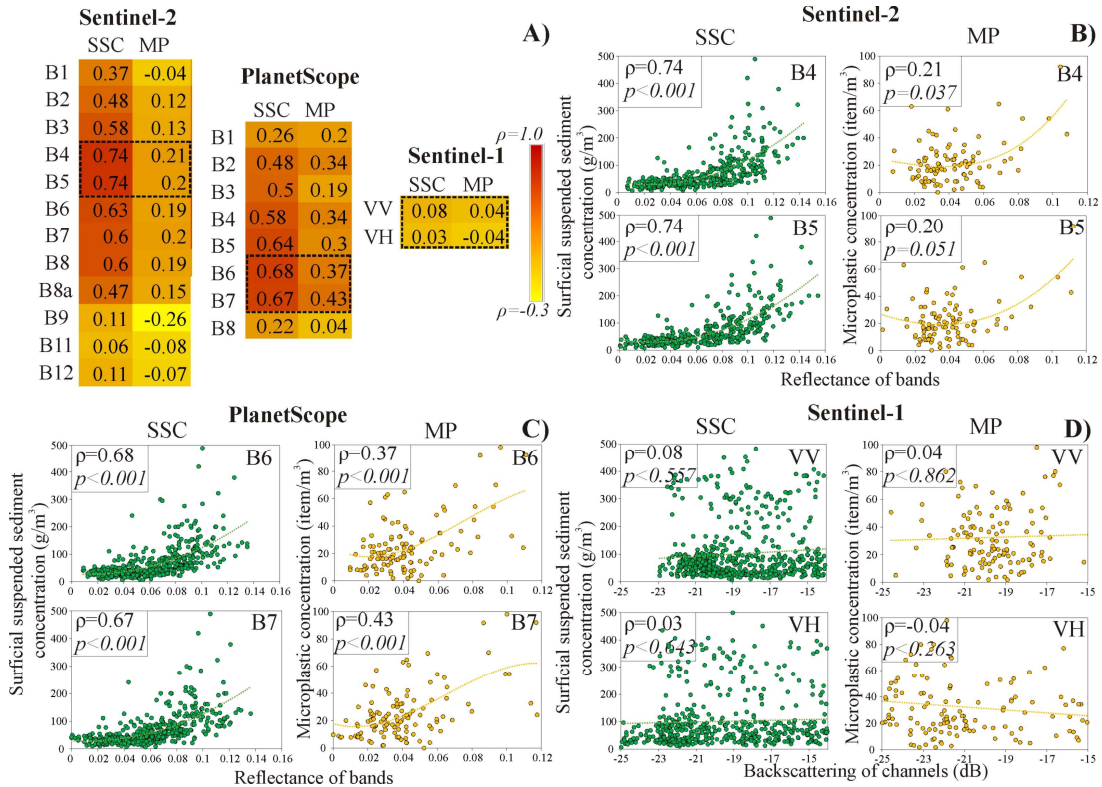
Figure 5.34. Correlation coefficient (ρ) among surficial suspended sediment (SS), microplastic (MP) concentrations, and bands of various optical (i.e., Sentinel-2 and PlanetScope) and active sensors (i.e., Sentinel-1) (A). The correlation between surficial SS, MP concentrations, and the first two bands or channels with the highest ρ were depicted by scatter plots (B–D).

The spectral signature of river water during low (low concentrations of surficial SS and MP) and high (high concentrations of surficial SS and MP) stages was compared to its counterpart in the clear water considering bands of Sentinel-2 and PlanetScope satellites (Figure 5.35). While the clear water showed a negligible reflectance in the red and NIR bands, the river water revealed a significant reflectance during both hydrological scenarios. Remarkably, the spectral signature of river water during low and high stages was very similar, differing mainly in reflectance magnitude. The most substantial difference in reflectance between clear and river water appeared in bands B3, B5, and B6 (Sentinel-2) and B5, B6, and B7 (PlanetScope). In addition, these bands had the highest reflectance difference between low and high stages, which explains their high correlations with the surficial SS and MP concentrations and suggests an elevated sensitivity to their concentration changes.

5.6.2. *Evaluation of the direct models of surficial suspended sediment and microplastic concentrations*

The evaluation metrics for remote sensing-based surficial SS and MP concentration models were represented, considering individual k-folds (5 data folds) and their average

(Figure 5.36). Remarkably, passive sensors (i.e., Sentinel-2 and PlanetScope) showed significantly higher metrics compared to the active sensor (Sentinel-1). While the best-performing surficial SSC model was derived based on the Sentinel-2 sensor (R^2=0.7; RMSE=35.7 g/m^3 and MAE=23.4 g/m^3), the MP's was based on the PlanetScope (R^2=0.2; RMSE=17.4 item/m^3 and MAE=13 item/m^3). However, it is noteworthy that the estimation accuracy of MP models is still comparatively low.
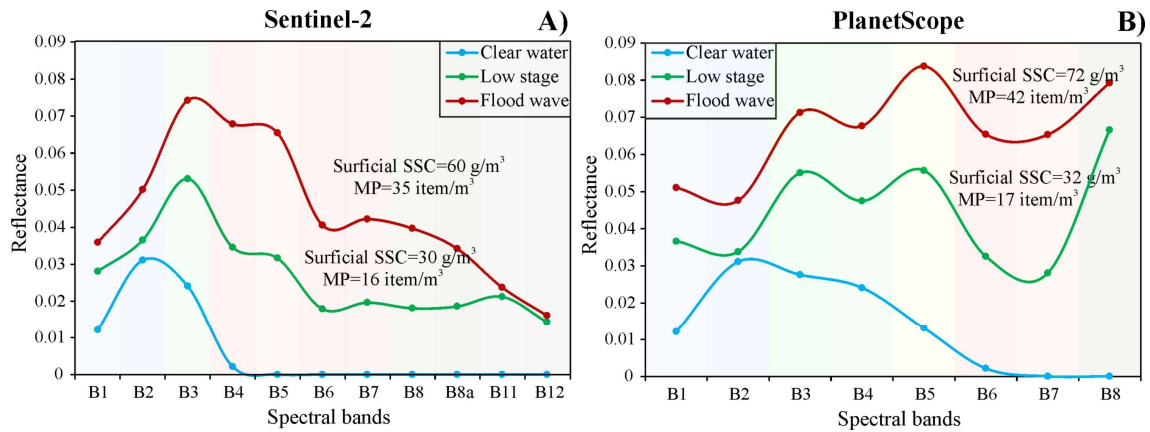
Figure 5.35. Spectral signature of river water during low and high stages in comparison to clear water, considering bands of Sentinel-2 (A) and PlanetScope (B) satellites.
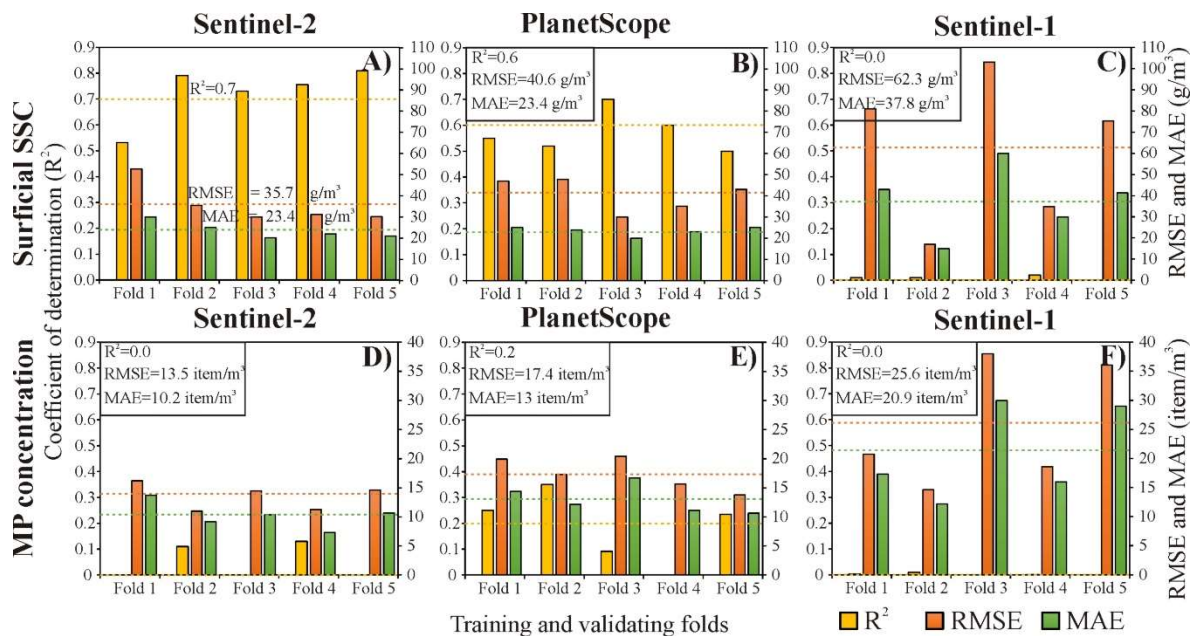
Figure 5.36. Evaluation metrics for remote sensing-based surficial suspended sediment (SS) (A–C) and microplastic (MP) (D–E) concentration models based on Sentinel-2, PlanetScope, and Sentinel-1 sensors. The metrics were represented for the five data folds and their average.

Passive sensors estimated surficial SSC with good accuracy, consistent with findings from previous studies (Atwood et al., 2019; Piehl et al., 2020; Mohsen et al., 2022a). However, they estimated MP concentration with relatively low accuracy. The reason for this discrepancy might be the elevated concentration and more uniform distribution of SS in water compared to MP, making it more effective on backscatter reflectance. This aligns with the results of Hu (2021) who reported the threshold of MP concentration to be detected by satellite sensors is ≥600 items/m^2, which is at least three times lower than the measured concentration in the Tisza. Another reason explaining this discrepancy is that most MP particles are transported below the water surface or concealed by a fine layer of water, making its detection by the VIS–NIR bands challenging.

The Sentinel-2 and PlanetScope satellites offered two different characteristic combinations of satellite constellations considering the tradeoff between accuracy and cost. Thus, they estimated surficial SS and MP concentrations with various accuracies. The best-performing surficial SSC model was based on Sentinel-2. This may return to the spectral superiority of the Sentinel-2 sensor over the PlanetScope, as it has a higher SNR (Sentinel-2: 12–15 dB and PlanetScope: 10–12 dB), wider bandwidth (Sentinel-2: 50 nm and PlanetScope: 31 nm; Table 4.1) (Mohsen et al., 2023c), and additional bands (i.e., red edge: B6 and B7; NIR: B8), which improve image quality.

On the other hand, the best-performing model for MP concentration was based on PlanetScope, which could be explained by its higher spatial resolution (3 m) and resolution uniformity among various bands compared to Sentinel-2 (10–60 m). Therefore, the proportion of sub-pixel coverage with MP was higher in PlanetScope than in Sentinel-2. The Sentinel-2 bands were resampled; however, the resampling process couldn`t substitute the higher details acquired by the native high spatial resolution PlanetScope sensor. The superiority of PlanetScope in estimating MP concentration may also arise from the existence of the yellow band (B5), absent in Sentienl-2 since this band showed the highest reflectance difference between river and clear water (Figure 5.35) and was the third-highest correlated band with MP concentration (Figure 5.34A). However, direct remote sensing of MP concentration is still uncertain, as the sub-pixel coverage is still far away from the detection threshold proposed by Hu (2021). Alternatively, it is likely that the MP concentration indirectly correlates with various bands through an active water constituent (e.g., chlorophyll-a, and SSC), which interprets the low estimation accuracy of the derived models.

The Sentinel-1-based surficial SS and MP concentration models showed poor accuracy, as evidenced by their low correlation with the backscattering of the VV and VH channels. This result disputes the initial hypothesis that the surficial SS and MP concentrations influence the dielectric constant of water, sensible by the active sensors (e.g., Sentinel-1). This might be explained by the relatively low surficial SSC of the Tisza during the studied period, as the maximum recorded concentration was 323 g/m^3. Shao et al. (2021) reported the existence of such correlation only for concentrations $\geq$1200 g/m^3, indicating the necessity of testing this approach in highly turbid rivers to evaluate its validity.

On the flip side, an alternative approach for estimating surficial SS and MP concentration in lowland rivers with a moderate surficial SSC by active sensors is imperative. This approach could leverage the existence of a correlation between water surface roughness and surficial SS and MP concentration changes. In this study, the backscattering of the VV and VH channels varied for even very similar concentrations (Figure 5.34D), which is likely attributed to surface roughness changes. Notably, the Mindszent site is located in a port with relatively heavy movements that stimulate water turbulence and consequently water surface roughness.

The MLP neural network yielded promising estimation accuracy for surficial SS and MP concentration models (especially surficial SSC) based on bands of optical sensors, consistent with Umar et al. (2018) and Mohsen et al. (2022a). The strength of this algorithm arises from its potential to discern intricate and non-linear patterns within the dataset, which align with the non-linearly correlated surficial SS, MP concentration, and remote sensing data (Figure 5.34B–D). The evaluation metrics of the MLP neural network-based model for surficial SSC (e.g., R^2=0.71) in the Tisza were similar to SSC models reported in the Yangtze River, China (R^2=0.72) (Liu et al., 2022a) and in the Missouri and Mississippi Rivers, USA (R^2=0.72) (Umar et al., 2018). Meanwhile, it outperformed models based on traditional linear regression, such as those developed on the Mississippi (R^2=0.62) and Maumee (R^2=0.56), Rivers, USA (Larson et al., 2018).

The SHAP analysis (Figure 5.37) was applied only to the passive-based surficial SS and MP concentration models since the active-based models demonstrated low evaluation metrics. Notably, the contribution order of bands identified by the SHAP analysis deviated

slightly from those that were obtained by correlation matrices (Figure 5.34 and Figure 5.37). Yet, certain bands with high correlations [e.g., B3 and B5 in the Sentinel-2-based surficial SSC model (Figure 5.37A) and B7 and B6 in the PlanetScope-based MP concentration model (Figure 5.37D)] persisted prominently at the cap of the violin plots, indicating their significant influence. This discrepancy in the contribution order of bands may return to the potential of the MLP neural network in detecting a high order of interaction between bands, in contrast to the pairwise correlation that is detected by the correlation coefficient (Youshen, 1996). Notably, the order of the most influential bands for surficial SSC models, based on Sentinel-2 and PlanetScope satellites, deviated from their counterparts in the MP models. In addition, they also deviated even for the same variable (i.e., surficial SSC or MP concentration) between both satellites (i.e., Sentinel-2 and PlanetScope).
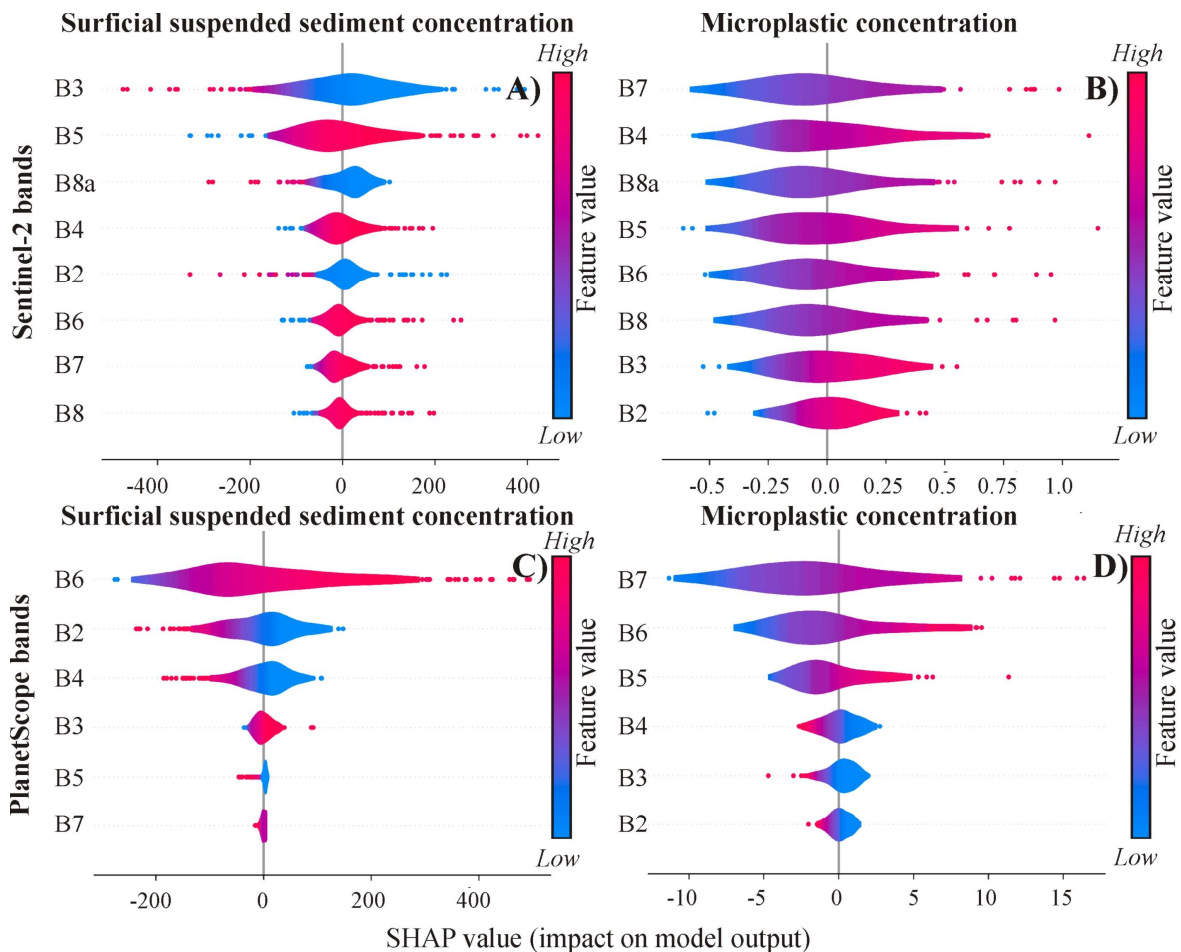
Figure 5.37. Summary plots represent the contribution of bands in the Sentinel-2 and PlanetScope-based surficial suspended sediment (SS) and microplastic (MP) concentration models in descending order based on SHAP values.

5.6.3. *Evaluation of the in-direct microplastic concentration models based on surficial suspended sediment concentration as a proxy*

Owing to the low estimation accuracy of the direct remote-sensing based MP concentration models, additional models considering surficial SSC as a proxy were developed, leveraging their elevated correlations, especially during floods (Figure 5.28). The models were developed for all hydrological conditions collectively and separately (i.e., low stages and flood phases) (Table 5.11). The collective model provided moderate accuracy for MP concentration, while the accuracy of the individual models varied from low in the case of low stage and falling conditions to very high in the case of rising and peak conditions.

Indirect estimation of MP concentration in rivers through a proxy emerges as an optimal alternative, offering significantly higher accuracy compared to direct estimates by remote sensing sensors. This method could circumvent the spatial and spectral limits of satellite sensors which restrict their direct detection of MP concentration (Hu, 2021). The utility of this approach could also arise from its potential to estimate MP concentration based on either measured or remotely sensed estimates of the proxy. However, the error propagation in the latter alternative should be considered.

Table 5.11. Predictive models for microplastic (MP) concentration based on surficial suspended sediment concentration (SSC) as a proxy.

Hydrological condition	Regression model	R^2	RMSE (item/m³)	MAE (item/m³)	Mean (item/m³)
All hydrological conditions	$MP = -0.0009 \, SSC^2 + 0.51 \, SSC + 10.67$	0.50	19.9	15.7	35±27
Low stage	$MP = -0.0006 \, SSC^3 + 0.0916 \, SSC^2 - 3.83 \, SSC + 64.5$	0.15	13.9	10.4	21±16
Rising limb	$MP = 0.256 \, SSC + 19.3$	0.72	12.8	10.5	42±24
Peak	$MP = -0.0026 \, SSC^2 + 1.141 \, SSC - 38.9$	0.8	8.8	11.12	50±28
Falling limb	$MP = 1 \times 10^{-5} \, SSC^3 - 0.0056 \, SSC^2 + 0.99 \, SSC + 8.35$	0.25	25.8	20.1	46±31

The surficial SSC has proven its validity as a reliable proxy for MP concentration estimation in the Tisza River, consistent with findings in the literature (Atwood et al., 2019; Piehl et al., 2020; Chen et al., 2021). However, certain limitations were observed, including (1) a low correlation between surficial SS and MP concentrations during low stages, leading to inaccurate estimates, albeit still reasonable; (2) sudden changes in the sources of SS and/or MP in space and/or time influence their established relationship, necessitating frequent calibration; (3) the established relationship along the river should be calibrated at sites by dams, tributaries, and WWTPs in advance. Based on these limitations, further research investigating the validity of additional water quality parameters (e.g., colored dissolved organic matter and chlorophyll-a) as a proxy could enhance estimation accuracy and overcome the limitation of SSC as a sole proxy.

5.6.4. Spatiotemporal generalization capability of the developed models

The temporal generalization capability of the derived surficial SS and MP concentration models was assessed using completely unseen data (during the training and validating process), from the Mindszent site, covering all hydrological scenarios (Figure 5.38A–C). The best-performing model was then applied to depict their spatial distribution during these periods (Figure 5.38D–F). Concerning the surficial SSC, the best estimation accuracy was achieved by the Sentinel-2-based model ($R^2=0.89$), revealing an elevated sensitivity to surficial SSC change under various hydrological conditions (Figure 5.38A and D). The worst accuracy was achieved by the Sentinel-1-based model ($R^2=0.35$). The PlanetScope-based model provided comparable accuracy to the Sentinel-2 model ($R^2=0.78$), yet it usually underestimates the actual surficial SSC, especially during the peak phase.

The temporal generalization capability of the MP models that were developed based on direct estimation by satellite images (Figure 5.38B) and indirectly through surficial SSC as a proxy (Figure 5.38C) were tested. Among the direct models, the PlanetScope-based model achieved the best estimation accuracy ($R^2=0.73$); however, it usually underestimates the real concentrations, particularly during the peak phase. Both Sentinel-2 and Sentinel-1-based

models revealed low sensitivity to MP concentration changes, with Sentinel-2 providing better estimates ($R^2=0.51$) than Sentinel-1 ($R^2=0$). On the other hand, the performance of the indirect method by a proxy significantly outweighed the direct method, as the R^2 raised by 44% on average (Figure 5.38B and C). Within the indirect method, MP concentration was estimated by both measured and satellite-based quantified surficial SSC. The best estimates of MP concentration, so far, were achieved by the measured surficial SSC ($R^2=0.98$). Although PlanetScope provided the best estimates of MP concentration in the direct method, Sentinel-2 surpassed its accuracy in the indirect method owing to its better accuracy in estimating surficial SSC.
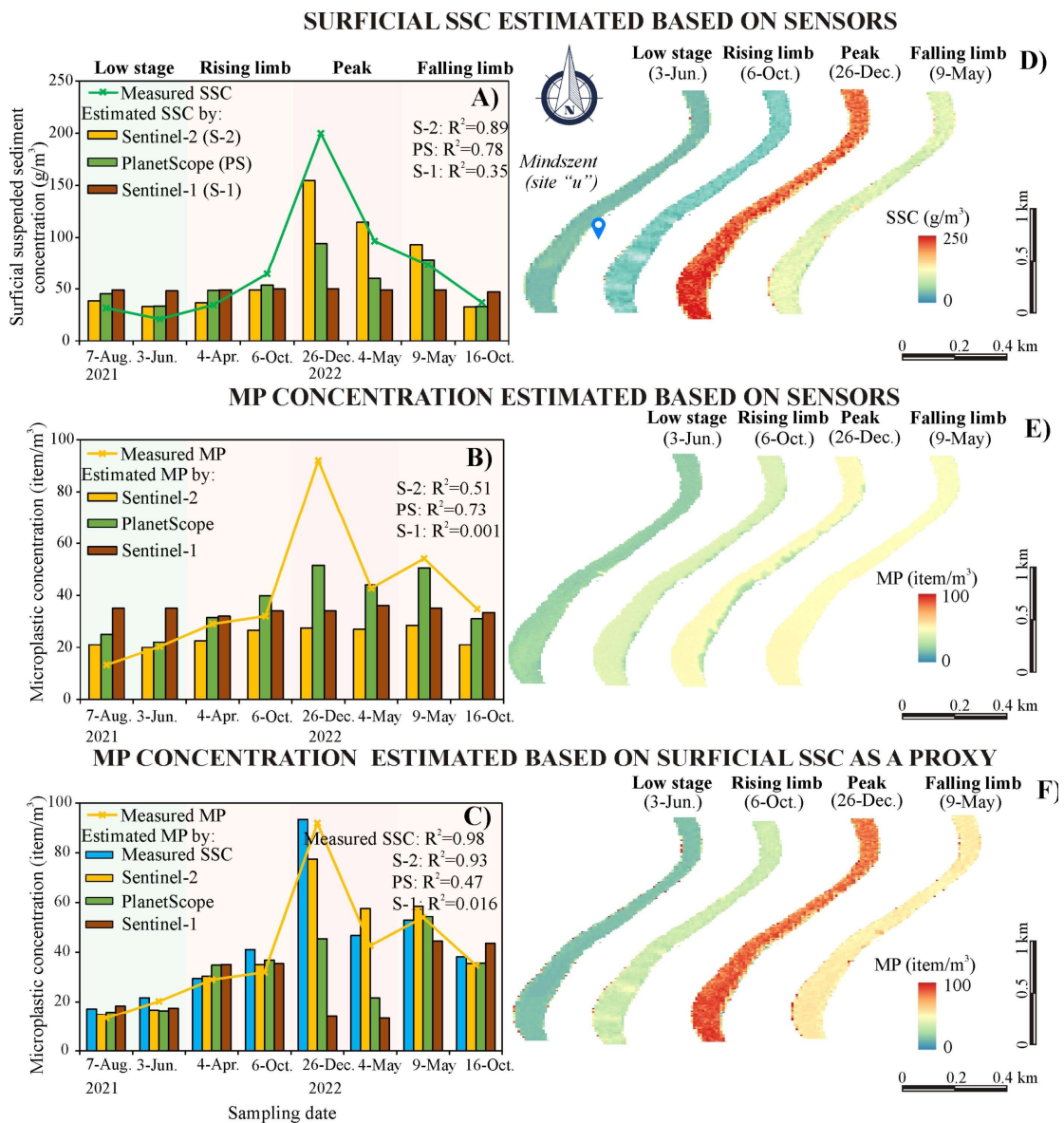
Figure 5.38. Temporal generalization capability of the developed surficial suspended sediment (SS) and microplastic (MP) concentration models under various hydrological conditions (A–C). The best-performing model was employed to depict the spatial distribution of both variables in Mindszent under the various hydrological conditions (D–F).

The spatial distribution of the surficial SS and MP concentrations in the Mindszent site during different hydrological conditions was almost uniform throughout the channel (Figure 5.38D–F). However, the estimates for certain pixels near the riverbank, particularly during the peak phase (Figure 5.38E), were under- or overestimated due to the influence of tree shadow on the reflectance of these pixels.

The longitudinal generalization capability of the derived surficial SS and MP concentration models was tested by totally unseen data too, covering the river between sites "i" (Aranyosapáti) and "p" (Tiszaroff), measured in July 2022 (Figure 5.39A–C). The best-performing model was used to depict the spatial distribution of both variables (i.e., surficial SS and MP concentrations) at these sites (Figure 5.39D–F). Almost all models performed badly during the longitudinal testing. Possibly, due to the timing of testing being conducted during low stages, when both variables have the lowest correlation coefficient and low correlation with remote sensing data. However, on a positive note, the mean estimates of the models were comparable to that of the in-situ measurements, particularly the passive-based models. For example, the mean surficial SSC estimated by Sentinel-2 (39.2 g/m^3), PlanetScope (35.1 g/m^3), and Sentinel-1 (50.1 g/m^3) closely matched the mean measured concentration (44.2 g/m^3) at the eight testing sites (Figure 5.39A).
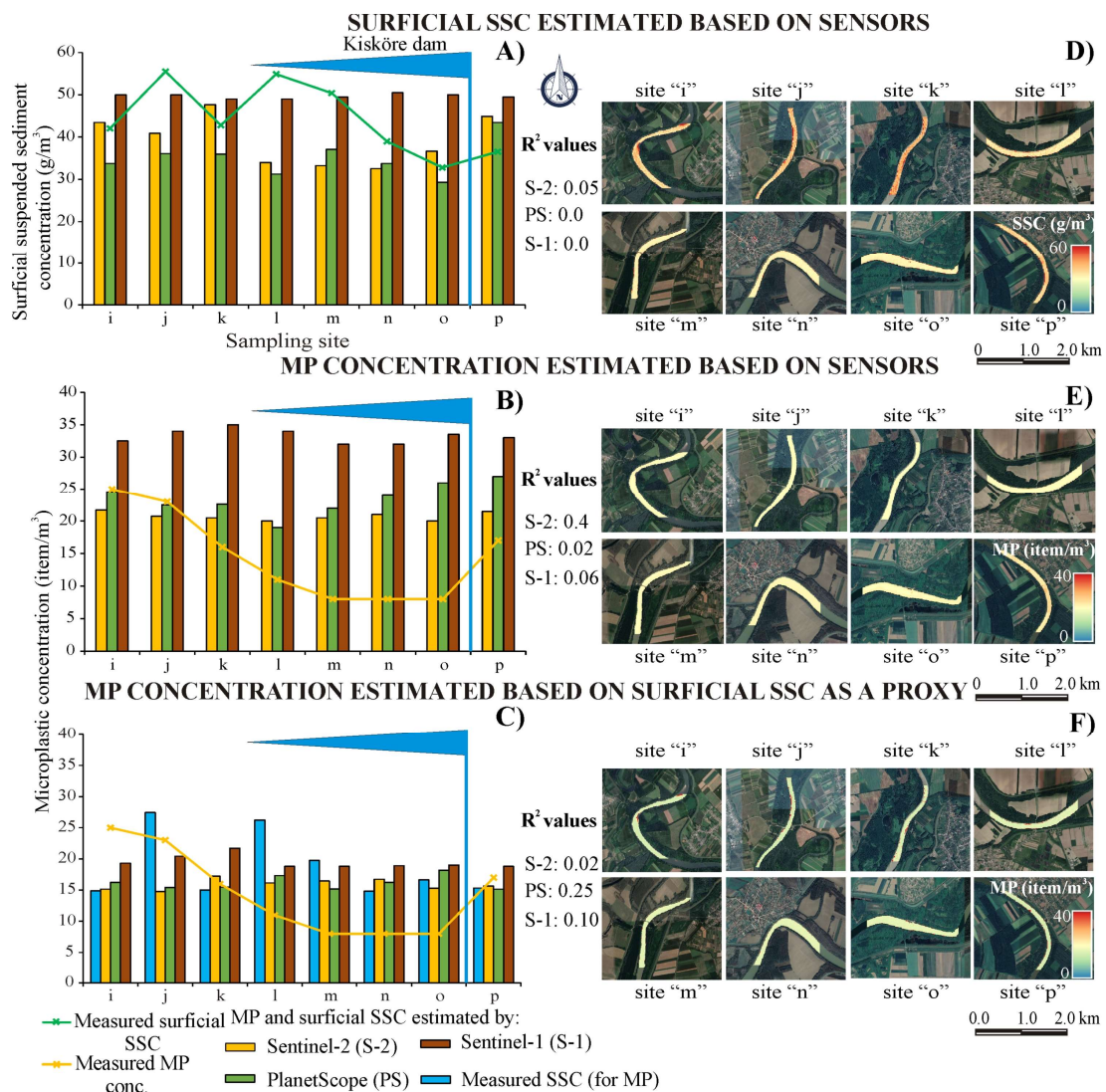
Figure 5.39. Longitudinal generalization capability of the developed surficial suspended sediment (SS) and microplastic (MP) concentration models between site "i" (Aranyosapáti) and "p" (Tiszaroff) (A–C). The best-performing model was employed to depict the spatial distribution of both variables at these sites (D–F).

In-situ measurements revealed a gradual decline in surficial SSC upstream of the Kisköre Dam [33.4% between site "l" (Tiszabercel) and "o" (Tiszadorogma)] and a sudden increase just downstream by 21% at the site "p" (Tiszaroff). This pattern was partially determined by optical-based models, while it was completely lost by active sensor (Figure 5.39A and D).

Both the direct and indirect MP concentration models revealed low estimation accuracy during the longitudinal testing (Figure 5.39B–C). The indirect models provided closer estimates (Sentinel-2: 15.9 item/m^3; PlanetScope: 16.6 item/m^3; Sentinel-1:19.5 item/m^3) to in-situ data (14.5 item/m^3) compared to the direct models (Sentinel-2: 20.7 item/m^3; PlanetScope: 23.5 item/m^3; Sentinel-1: 33.3 item/m^3). A similar MP concentration pattern to surficial SSC was observed upstream and downstream of the Kisköre Dam, though with different decreasing (27.3%) and increasing (112.5%) magnitudes. This pattern was partially detected by optical sensors and completely lost by the active sensor too.

The spatial distribution of the surficial SS and MP concentrations, depicted by the best-performing models, exhibited a generally uniform pattern across all eight sites. However, some false alarms appeared near the riverbanks. These alarms are likely attributed to low water levels during the study period and the concurrent appearance of point bars, which can affect pixel reflectance and, consequently, concentration estimates (Figure 5.39D–F).

In general, the derived surficial SS and MP concentration models provided higher performance during the temporal testing (Figure 5.38) than in spatial testing (Figure 5.39). This difference returns to the inclusion of various hydrological conditions in the temporal dataset, in contrast to the single low stage condition in the longitudinal data. Therefore, additional longitudinal data during floods are imperative for better evaluation. Within the temporal testing, the surficial SS and MP concentration models typically performed well during the low stage, rising, and falling phases, while underestimating the peak phase. This behavior suggests a bias toward lower concentrations, probably due to the relatively limited peak concentration data. During the longitudinal testing, no dominant under or over-estimation pattern was noticed as the models mixed between them (Figure 5.39A and B).

6. CONCLUSIONS

The presented Ph.D. research contributed to the current knowledge by providing deeper insights into the spatiotemporal dynamics of riverine suspended sediment and plastic pollution transport, considering the lowland, medium-sized Tisza River (Central Europe) as a case study. The key influencing factors and transport mechanisms of plastic pollution at both the microplastic (MP) and macroplastic (MaP) scales were revealed based on intensive in-situ measurements and satellite images. Furthermore, the complex interplay between SS and MP transport in response to different temporal and longitudinal variables was accurately analyzed. The river was investigated across multiple spatial and temporal scales, encompassing site-specific assessments, confluence-scale analyses, and river-long evaluations, with measurement frequencies spanning from every five days to monthly intervals. Besides, the study extended for long periods, spanning from two to seven years. Integrating this comprehensive dataset with various optical and active sensors, resulted in the development of reliable SS, MP, and MaP concentration models, providing valuable tools for future monitoring programs.

6.1. Spatiotemporal dynamics of riverine litter/macroplastic (MaP) in the Tisza River based on at-a-site survey and satellite images

Riverine litter transport, primarily consisting of organic material, is a natural phenomenon. However, it has become a pressing environmental problem since its amalgamation with plastic waste. A significant proportion of communal waste is mixed with organic litter along the Tisza`s sub-catchments where the communal waste production (mean: 340 kg/capita per year), is in some countries coupled with a low recycling ratio (1–38%). Unfortunately, there is limited available data on riverine litter transport not only in the Tisza but also globally. Therefore, this study participates in filling this data gap by investigating the spatiotemporal dynamics of riverine litter/macroplastics in the Tisza River, incorporating both satellite images (i.e., Google Earth satellites and Sentinel-2) and in-situ observations.

According to the results, the Tisza has a low to moderate riverine litter transport rate compared to rivers worldwide, with relatively low macroplastic abundance (5–20%). Typically, riverine litter accumulates upstream of hydraulic structures (dams and bridges), along riverbanks, and around floating docks owing to reduced water velocity and increased trapping efficiency in these areas. Hence, governmental and volunteer purification campaigns should be focused on these spots. Although the longitudinal distribution of riverine litter is mainly influenced by waste management levels in sub-catchments, local anthropogenic sources (e.g., illegal waste disposals, fishing, and tourist activities) may disrupt this distribution pattern. This indicates the complexity of the litter transport process and underscores the need for intensive observations to accurately evaluate the actual distribution and influencing factors.

Hydrology plays a significant role in riverine litter transport, through its profound influence on water discharge, flow velocity, kinetic energy, and channel morphology. Typically, the highest riverine litter transport rate occurs during high stages characterized by high stream power and floodplain inundation. Conversely, during low stages, the most important riverine litter sources are decoupled from the river, and the lowest transport rate occurs. Generally, the MaP transport rate showed a similar decreasing trend to litter transport, but with varying magnitudes, indicating potential differences in their sources, influencing factors, and transport mechanisms. Notably, the formation of substantial litter spots typically occurs at the end of flood waves, due to the gradual flux effect. Accordingly, purification campaigns are recommended to be held during or after these periods, when litter accumulates at well-defined hot spots with the largest quantity.

Remarkably, the areal coverage of certain riverine litter spots, mainly upstream of the Kisköre Dam, experienced an overall increasing trend over the seven-year study period (2015–2021). This trend is likely attributed to the absence of significant floods during this timeframe. However, to get deeper insights, more studies incorporating detailed communal waste data in the five shared countries with corresponding hydrological and meteorological data are necessary.

6.2. Remote sensing-based riverine litter/macroplastic (MaP) modelling in the medium-sized Tisza River

Several aspects of riverine litter transport, e.g., its spatiotemporal distribution, composition, transport rate, and accumulation hotspots remain insufficiently explored in most rivers worldwide, owing to the absence of comprehensive and comparable riverine litter data. Remote sensing, on the other hand, presents an opportunity to address this gap by providing valuable data through frequent monitoring and large-scale coverage, even for remote and inaccessible areas and under extreme weather conditions.

The combination of Sentinel-2 images, in-situ observations, VHR images (GE), and machine learning algorithms (DT, RF, NB, SVC, and ANN) resulted in highly accurate Sentinel-2-based riverine litter models (overall accuracy: 0.89–0.96), offering significant support for future monitoring programs. However, sub-pixel detection is still uncertain, as the models excelled with the large and medium spots, but often overlooked small spots (< pixel size). Therefore, further studies incorporating more representative small spots are warranted, as they constituted only 1% of the dataset used in this study. Besides, employing finer spatial resolution images, e.g., PlanetScope and WorldView-3 would provide more detailed riverine litter data, owing to its enhanced resolution and frequent imaging. Typically, the models exhibited good and comparable accuracies; however, they performed differently with various spot sizes due to inherited algorithmic differences and their alignment with current data assumptions. Accordingly, the SVC, ANN, and RF-based models are the most recommended for riverine litter detection, while the DT and NB are the least recommended.

According to the SHAP and spectral analysis, the NIR and SWIR bands, specifically B8, B11, and B12 in Sentinel-2 are optimal for riverine litter detection, aligning with the findings in the literature. These particular bands have a notable reflectance for riverine litter in comparison to lower values with obstructions (e.g., dams and bridges), and almost no reflectance with river water. Thus, litter manifests as bright spots in images within these spectral ranges. Accordingly, combining bands from NIR and SWIR could effectively enhance the contrast between the riverine litter and its background, rendering them a recommended choice for developing a riverine litter spectral index.

Although the derived models are beneficial for providing valuable riverine litter data, certain limitations should be noted: (1) Occasionally the models misclassify mixed pixels, especially along the riverbanks, thus incorporating more representative mixed pixel data during the training phase could enhance classification accuracy. (2) Temporal variations in the transported SS load may influence detection precision, especially with the DT model. However, the rest of the models avoided this issue, owing to the inclusion of water pixels with varying SSCs during the training phase; however, its influence on the simple DT model was significantly higher. (3) The moderate spatial resolution of Sentinel-2 images and its variability among bands (10–60 m) leads to the omission of small spots (<10 m) which forms the vast majority of the transported litter. Thus, testing finer spatial resolution images (e.g., SPOT 6 and WorldView-3) could improve monitoring efficiency. (4) The limited availability of riverine litter data has led to some disparities in evaluation metrics among validation and testing phases, especially for simpler models. Thus, the inclusion of additional data, especially small spots, is crucial to reinforce the robustness and reliability of the models.

6.3. Remote sensing-based suspended sediment discharge modelling in the medium-sized Tisza and Maros Rivers

Owing to the low number of representative gauging stations for Q_s in rivers globally, and the considerable decline in funding for monitoring programs, there is a pressing demand for developing remote sensing-based Q_s monitoring models. These models would enhance monitoring efficiency not only for sediment transport but also for various contaminants, including plastics. The previous efforts mainly focused on developing remote sensing-based SSC models and relied on measured Q to estimate Q_s. However, in this study, both variables (i.e., SSC and Q) were remotely sensed by integrating Sentinel-2 images with in-situ measurements of both variables, employing machine learning algorithms.

The hydraulic geometry theory, specifically, the water width–discharge (w-Q) relationship served as a reliable foundation for developing the Sentinel-2-based Q models. Among the three tested methods for Q modelling, my novel AHG machine learning model performed the best, followed by the AMHG models, while the worst performance was achieved by the AHG power law model. This outcome paves the road towards more intensive and regular Q monitoring of rivers, bypassing the intricate optimization process of numerous transects used in the AMHG method. Instead, the inherited nature of machine learning algorithms to identify intricate patterns in a dataset allows for accurate models based on a single transect with high adaptability to changing conditions.

On the other hand, these models have limitations: (1) They may provide inaccurate Q estimates above the bankfull level due to the loss of hydraulic geometry characteristics above this level, though the AHG machine learning models partially addressed this issue. (2) Certain cross-section shapes (e.g., rectangular shape) lack hydraulic geometry, while others (e.g., V-shape) have more effective hydraulic geometry than alternatives (e.g., trapezoidal shape). Consequently, the cross-section shape significantly impacts the estimation accuracy. (3) The precision of the remotely sensed water width data has a significant influence on the Q estimation accuracy. Hence, the spatial resolution of the employed satellite image and its suitability to the river size should be carefully considered. The combined NDWI and OTSU water extraction approach demonstrated high precision, making it highly recommended for future studies, especially with finer spatial resolution images.

The variation in watercolor (reflectance) in response to changes in SSC served as an effective proxy for developing Sentinel-2-based SSC models. The magnitude of the spectral signature (reflectance) of the highly turbid Maros River exceeded that of the Tisza, and during the high stage (elevated SS transport) was higher than during the low stages in both rivers. Based on my analysis and consistent with the literature, bands B3–B5 were identified as most beneficial for estimating SSC changes. However, my spectral analysis further pinpointed B3 as exceptionally sensitive to low concentrations and B5 to high concentrations, which might be beneficial for future SSC modeling in rivers worldwide.

The derived SSC models provided high and comparable estimation accuracy, with slightly better performance in the highly turbid Maros River compared to the Tisza River. The random forest algorithm and the combination of multiple algorithms are highly recommended for developing robust and reliable SSC models, as their estimation accuracy surpassed the others. Although the models revealed high potential in depicting the real SSCs during different hydrological scenarios at both lateral and longitudinal dimensions, they faced certain limitations: (1) The modelled concentrations along the riverbanks could be influenced by the shadow of trees and mixed pixels, thus the SSC at these sites should be carefully interpreted. (2) Estimation accuracy is significantly influenced by sun glint, waves, ripples, wind, and water depth. Therefore, meteorological conditions, especially wind speed, should be considered when interpreting SSC results.

Based on the best-derived Q and SSC models, the Q_s was efficiently estimated in the Lower Tisza and Maros Rivers between 2015 and 2021. Aligning with the existing literature, the models proved the elevated (2–3.5 times higher) Q_s load of the Tisza than the Maros, despite the Maros having 2–3 times higher SSCs. This difference is attributed to the Maros transporting four times lower Q than the Tisza. In addition, the models revealed a higher probability of occurrence for SSC–Q hysteresis in the Tisza than in the Maros. They also allowed better evaluation of the Q_s lateral distribution at river cross sections, revealing that it is not only influenced by flow velocity distribution but also the occurrence and location of a joining tributary upstream. Thus, the mixing pattern of the waters of joining rivers should be considered during measurements, especially at gauging sites like Szeged, which are located very close to the confluence.

6.4. Spatiotemporal dynamics of water mixing in the Tisza–Maros confluence: A support for future measurements

Confluences play a significant role in shaping the hydrological, ecological, water quality, and morphological characteristics of a river system. These sites undergo an intricate mixing process of waters, influenced by a multitude of interfering factors that change over time and between rivers. However, many of these factors remain understudied and completely unraveled due to data shortages and challenges in in-situ measurements at confluences. Furthermore, support for future measurements for various substances (e.g., pollutants, sediments, and plastics) in confluence is needed by identifying the mixing pattern to avoid misinterpretation of the collected data. Therefore, the mixing process in the Tisza–Maros confluence and its relationship to the hydrological parameters was analyzed by Sentinel-2 images, measured, and calculated hydrological parameters in the Tisza and Maros Rivers.

Based on the analyzed 143 Sentinel-2 images, the mean areal coverage of the water of the Tisza River (TW) exceeded that of the mixed water (MIX), while the lowest coverage was observed for the water of the Maros (MW). Both the areal and lateral changes in TW, MW, and MIX showed similar temporal patterns, with a gradual decline in TW and MW downstream, replaced by an increasing proportion of the MIX, indicating gradual mixing. The Q ratio between the joining rivers was the most influential hydrological parameter affecting the areal coverage of TW and MIX, regardless of the water stage condition. The slope and slope difference revealed significant correlations too, but only under separating the low and medium discharges from high discharges (flood periods). On the other hand, the areal coverage of MW and its longitudinal extent into the Tisza (L) exhibited less dependence on hydrology. Their highest correlations occurred exclusively with the hydrological parameters of the tributary itself (e.g., $H_{Makó}$ and $Q_{Makó}$). The findings suggest that the hydrology of the joining rivers is a primary factor influencing the mixing process in the confluence area, especially for the water of the main river and the mixed one, and it can serve as an effective indicator of the mixing patterns.

The mixing process in the Tisza–Maros confluence was condensed into 11 representative mixing patterns, categorized based on the domination of each water type and the likelihood of upwelling downstream. Typically, the water of the main river (TW) prevails over the confluence area, with full coverage (TW1) in January and November, when the Tisza`s elevated stream power impedes Maros distribution and limits the mixing process. The domination of the tributary water (MW) occurs just on limited occasions, usually during early summer (June or July), when simultaneous floods in the rivers, coupled with the steep slope of the Maros, enable MW to interact with TW. However, the MW typically extends longitudinally with a 30–80% lateral extent (MW6). MIX prevails during low stages in summer when rivers have minimal kinetic energy, while it has almost no coverage during floods. In 22% of cases, the water of either the Tisza (TW) or the Maros (MW) upwells downstream indicating the complexity of the mixing process affected by various densities of different water types (TW, MW, and MIX).

Based on the findings, the confluence area has distinct mixing patterns that alternate throughout the year, spanning from no mixing to complete mixing and to upwelling patterns. Therefore, SS or MP sampling downstream of the confluence must be applied with caution, and it is suggested to collect samples from several points, covering all water types, as individual samples may lead to misinterpretation of the collected substance. Therefore, defining the expected mixing pattern is crucial when planning the sampling schema. The developed predictive equations in this study could provide valuable insights in this regard, based on measured and calculated hydrological parameters at the three gauging sites (i.e., Szeged, Algyő, and Makó) in the Lower Tisza and Maros Rivers.

6.5. Spatiotemporal distribution and correlation of surficial suspended sediment and microplastic concentrations along the Tisza

Suspended sediment (SS) particles share several characteristics with MPs, suggesting potential similarities in their transport mechanisms. Although several studies have investigated their transport in rivers globally, these investigations often study them individually and based on limited spatiotemporal measurements, especially for MPs. Besides, there is a lack of studies that compared the influence of the longitudinal variables, such as dams, tributaries, and WWTPs on their transport simultaneously. Therefore, the spatiotemporal distribution and correlation between surficial SS and MP concentrations and their relationships with the hydrology were investigated in detail in the Lowland Tisza River based on intensive spatial (26 sites in August 2021 and 21 sites in July 2022) and temporal (140 samples in Mindszent May 2021–May 2023) measurements. Remarkably, these intensive measurements have not been applied in the existing literature so far. Therefore, the findings and conclusions of this study could significantly impact global knowledge in this scientific field.

The surficial SS and MP concentrations revealed similar temporal change patterns, with elevated concentrations recorded during flood waves and lower concentrations during low stages. However, surficial SSC demonstrated a stronger association with hydrology (water stage changes) than MP. The assessment of individual hydrological periods revealed a negligible correlation between surficial SSC, MP concentration, and water stage during low stages, strengthening during flood waves. Based on the study`s conceptual model the sources of sediment and MP are dissimilar during low stages leading to a negligible correlation. Specifically, during low stages, sediment might originate from bank erosion (e.g., landslides), tributaries, and mining activities, while MP could originate mainly from WWTP effluents and direct wastewater drainage. However, during flood waves, new sources common for both variables appear in the system, leading to heightened correlation. These sources include surface runoff, mainly in the mountainous and hilly sub-catchments, as well as (re)-mobilization of channel bed materials.

The findings underscored the significance of event sequence, especially in surficial SS transport. Typically, the first flood wave following a prolonged dry, low-stage season transports higher surficial SS and MP loads than subsequent waves. This was also applicable to the rising flood phase compared to the falling phase, which is likely attributed to the availability of sediment and MP during these periods, depleting with subsequent events. The study emphasizes the necessity to consider the river`s hydrology when designing monitoring programs for surficial SS and MP concentrations since comparable outcomes can be achieved solely within the context of a similar hydrological framework.

The recurrent longitudinal observations along the Tisza highlighted the significant influence of natural (e.g., flow velocity, discharge, slope, and confluence) and anthropogenic (e.g., WWTP effluents, dams, and proximity to pollution sources) factors on surficial SS and MP transport. However, over the study period, no clear downstream trend was observed for surficial SS and MP concentrations, and they revealed moderate to strong negative correlations. Yet, this result may be constrained to the low-stage sampling period when the

surficial SS and MP have dissimilar sources, as evidenced during the temporal measurements. Therefore, additional longitudinal measurements during floods, especially at the onset of a flood wave, are warranted for deeper insights and a comprehensive evaluation. On the other hand, the evaluation of individual sections (S1–S5) revealed great variability, with the highest positive and negative correlations between both variables occurring in the uppermost (S1) and last (S5) sections, respectively, and weak correlations in the middle sections (S3–S4). This indicates the great dynamics of sources and influencing factors on surficial SS and MP transport along the river, resulting in simultaneous influences at some sections and distinct at others, in relation to the specific hydrological, morphological, and pollution characteristics of these sections.

Tributaries and dams play a crucial role in the transport of surficial SS and MP; however, their influence tends to change not only between both variables but also over time. Nevertheless, their influence on surficial SS transport was more consistent than on MP transport, owing to more uniform characteristics and sedimentation patterns of sediments than MPs. The influence of a tributary on surficial SS and MP transport is mainly governed by its water discharge. For instance, downstream of the Tisza's confluences, there were slight changes in surficial SS and MP concentrations, even though tributaries exhibited higher SS and MP concentrations than the Tisza. It could be explained by the circumstances of the measurements during the low stages, thus tributaries had low water discharge. On the other hand, dams usually trap SS and MP upstream due to their impoundment effect and remobilize them downstream through clear water erosion. Nevertheless, both increasing and decreasing trends in surficial SS and MP concentrations were noticed upstream and downstream of the Tisza`s dams. This discrepancy was more pronounced for MP concentration than for SSC, primarily due to the higher influence of local anthropogenic activities (e.g., WWTP effluents) on MP concentration than on SSC.

The temporal dynamics in the hydrological, meteorological, hydraulic, and morphological characteristics of sub-catchments and channels pose additional complexity to the spatial distribution patterns of surficial SS and MP concentrations. Furthermore, surficial SS and probably MP usually transport in pulses and clouds, with their concentrations primarily influenced by pulse propagation rather than local sources, which introduces additional complexity to their transport dynamics. Therefore, snapshot-like monitoring may provide incomplete insights and contradictory findings, especially downstream of tributaries, in reservoirs, and downstream of dams. To address these challenges, denser spatiotemporal monitoring is warranted. Increased monitoring upstream and downstream of tributaries and dams is recommended to confirm the identified patterns in this study.

6.6. Remote sensing-based surficial suspended sediment and microplastic concentrations modelling in the medium-sized Tisza River

The limitations of in-situ spatiotemporal measurements of MP transport in rivers and the necessity of numerous auxiliary data for developing MP transport models could be addressed by remote sensing techniques. However, there are still many conflicting results concerning the applicability of remote sensing sensors, especially satellite images, in MP concentration estimation in aquatic environments, with no study being conducted in rivers so far. Therefore, this study aimed to fill this scientific gap, considering the Tisza River as a case study. MLP artificial neural network (ANN)-based models for surficial SS and MP concentrations were developed based on direct correlation with reflectance of Sentinel-2 and PlanetScope bands and backscattering of Sentinel-1 channels. Besides, indirect models for MP concentration were developed based on surficial SSC as a proxy.

The low MP concentration in rivers (maximum recorded in the Tisza 129 item/m^3) coupled with the relatively limited spectral and spatial characteristic of the tested sensors hindered accurate and effective direct estimation of MP concentrations. However, the proxy

method revealed promising estimation accuracy, especially during flood waves, making it capable of providing reliable MP concentration estimates by either measured or remotely sensed surficial SSCs. On the other side, this proxy approach still has some limitations: (1) It may provide less accurate estimates during low stages, yet still reasonable. (2) The established relationship between both variables is quite sensitive to sudden changes in their sources in space or time and needs validation at certain locations (e.g., dams and tributaries).

Based on the performance of the models during the spatiotemporal generalization capability test, I argue that the Sentinel-2-based models outperformed the others. This superiority can be attributed to the availability of extra spectral bands, higher SNR, and wider bandwidth in this sensor, resulting in higher-quality images. However, it still has moderate spatial and temporal resolutions. Although the best performance for MP concentration models was achieved by PlanetScope, it is still unreliable due to its low estimation accuracy. Instead, the Sentinel-2 sensor could effectively estimate surficial SSC and consequently MP concentration through the proxy model. However, the active sensor failed to directly estimate either surficial SS or MP concentrations through backscattering signals. Thus, developing proxy models based on surface roughness in rivers is warranted, as they may provide better results for active sensors.

The developed MP concentration models in this study represent an initial step toward the automatic monitoring of riverine MPs by satellite sensors. Thus, further research is necessary to improve the model`s estimation accuracy, reliability, and effectiveness across various hydrological scenarios. Given the superior performance of proxy models, I suggest exploring additional water quality parameters, such as chlorophyll-a and colored dissolved organic materials, as potential proxies. The integration of these parameters with surficial SSC may improve the estimation accuracy and overcome the limitations of current models.

6.7. Evaluation of remote sensing models as a potential monitoring tool for suspended sediment and plastic pollution transport in rivers

The developed remote sensing-based (surficial) suspended sediment, macro-, and microplastic models in this study have the potential not only to effectively monitor their concentrations but also their transport rates, thanks to the developed AHG machine learning water discharge models. The fusion of intensive in-situ measurements with several machine learning algorithms and satellite sensors resulted in reliable models that can provide valuable data for SS, MP, and MaP at multiple spatiotemporal scales not only in the Tisza River but probably on other lowland rivers as well. This approach mitigates the limited scale validity, high cost, and time consumption associated with in-situ measurements. Also, the widespread application of these models in rivers worldwide holds promise for researchers and decision-makers, offering deeper insight into the origins, pathways, and fates of SS and plastic pollution. Besides, it opens avenues to analyze the influencing factors and mechanisms shaping plastic pollution transport and its connection to natural sediment transport.

On the other hand, the technical limitations of the sensors and the constraints of the theoretical background of the employed method should be carefully considered. For instance, sub-pixel detection of both variables (i.e., SS and plastics) is still uncertain and requires further research. The current specifications of satellite sensors fall short of directly detecting the micro-scale of plastic particles, particularly given the low concentration levels in rivers. The potential of water discharge models to provide accurate estimates diminishes beyond the bankfull level, especially with traditional AHG power law and AMHG methods. Besides, their accuracy is significantly influenced by the applied water extraction method to estimate water width data from satellite images. Finally, frequent monitoring of these variables is occasionally hindered by cloud cover in optical sensors; however, this challenge can be addressed by integrating active sensors in future studies. This topic still requires further research toward better estimation accuracies and surpassing existing challenges and limitations.

ACKNOWLEDGEMENT

"First and foremost, I express my deepest gratitude to Allah for his unwavering grace, which has been a guiding force not only during my doctoral studies but also throughout my entire life."

I wish to extend my heartfelt gratitude to my esteemed supervisors Dr. Tímea Kiss and Dr. Ferenc Kovács for their invaluable guidance, unwavering support, dedicated effort, exceptional patience, and continuous motivation throughout my Ph.D. studies. Their profound involvement has played a pivotal role in shaping me into a more refined individual, not only in the realm of academia but also on a personal level. I will never forget their dedication to achieving the highest standards in our research endeavors and their relentless efforts during in-situ measurements, regardless of weather conditions. Without their comprehensive support, this thesis would not have come to fruition.

I would like to acknowledge the Hungarian and Egyptian Governments for providing me with a valuable chance to pursue my Ph.D. studies at a distinguished university in Hungary through the Stipendium Hungaricum Scholarship Program. Additionally, I extend my appreciation to the Hydrological Water Directorate of the Lower Tisza (ATIVIZIG), particularly Mr. Ferenc Szarvas, for their support in supplying the essential data for my research. Special thanks go to OTKA for their generous funding that has supported the necessary measurements and data analysis.

To all staff members of the Department of Geoinformatics, Physical and Environmental Geography, I really would like to thank all of you for your warm welcome, continuous help, and support. I am thankful to my Hungarian and international Ph.D. colleagues who have embraced me as a member of their extensive academic family. My thanks extend to the secretary of the department, who aided me in various administrative matters. I will not forget the mosque community in Szeged whose presence made me feel at home and eased many new environment challenges.

Finally, and of utmost importance, my heartfelt appreciation and gratitude go to my parents and family members. Without their motivation, understanding, and unwavering support, I would never have reached this milestone. I will always remember their steadfast encouragement and the challenges they have helped me overcome, not only throughout my Ph.D. studies but also during the pursuit of a Ph.D. opportunity abroad. I offer special thanks to my wife (Reem) and children (Talia and Hamza); I genuinely miss you all tremendously.

REFERENCES

Ahmed, I., Pan, N.D., Debnath, J., 2016. A study on Suspeded Sediment Discharge and Bed Load Grain Size of the Gumti River of Tripura at Some Selected Tributary Confluence Points. International Journal of Geology, Earth & Environmental Sciences, 6(1): 43-53.

Amissah, G.J., 2020. Channel Processes of a Large Alluvial River Under Human Impacts. Ph.D. Thesis, University of Szeged, Szeged, Hungary.

Amissah, J., Kiss, T., Fiala, K., 2018. Morphological Evolution of the Lower Tisza River (Hungary) in the 20th century in Response to Human Interventions. Water, 10(7): 884. DOI:https://doi.org/10.3390/w10070884

Ammenberg, P., Flink, P., Lindell, T., Pierson, D., Strombeck, N., 2002. Bio-optical Modelling Combined with Remote Sensing to Assess Water Quality. International Journal of Remote Sensing 23(8): 1621-1638. DOI:https://doi.org/10.1080/01431160110071860

Arisanty, D., Saputra, A.N., 2017. Remote Sensing Studies of Suspended Sediment Concentration Variation in Barito Delta. The 5th Geoinformation Science Symposium 2017. IOP Publishing, Yogyakarta, Indonesia.

Armitage, S., Awty-Carroll, K., Clewley, D., Martinez-Vicente, V., 2022. Detection and Classification of Floating Plastic Litter Using a Vessel-Mounted Video Camera and Deep Learning. Remote Sensing, 14(14): 3425. DOI:https://doi.org/10.3390/rs14143425

ASTM, 2007. Standard Test Method for Determining Sediment Concentration in Water Samples, West Conshohocken, PA. D3977-97R07. DOI:https://doi.org/10.1520/D3977-97R07

Atwood, E.C., Falcieri, F.M., Piehl, S., Bochow, M., Matthies, M., Franke, J., Carniel, S., Sclavo, M., Laforsch, C., Siegert, F., 2019. Coastal Accumulation of Microplastic Particles Emitted From the Po River, Northern Italy: Comparing Remote Sensing and Hydrodynamic Modelling With In situ Sample Collections. Marine Pollution Bulletin, 138: 561-574. DOI:https://doi.org/10.1016/j.marpolbul.2018.11.045

BaČA, P., 2008. Hysteresis Effect in Suspended Sediment Concentration in the Rybárik basin, Slovakia / Effet d'hystérèse Dans la Concentration des Sédiments en Suspension dans le Bassin Versant de Rybárik (Slovaquie). Hydrological Sciences Journal, 53(1): 224-235. DOI:https://doi.org/10.1623/hysj.53.1.224

Balla, A., Mohsen, A., Gönczy, S., Kiss, T., 2022. Spatial Variations in Microfiber Transport in a Transnational River Basin. Applied Sciences, 12(21): 10852. DOI:https://doi.org/10.3390/app122110852

Barrows, A.P.W., Christiansen, K.S., Bode, E.T., Hoellein, T.J., 2018. A watershed-scale, Citizen Science Approach to Quantifying Microplastic Concentration in a Mixed Land-use River. Water Research, 147: 382-392. DOI:https://doi.org/10.1016/j.watres.2018.10.013

Bashir, S.M., Kimiko, S., Mak, C.-W., Fang, J.K.-H., Gonçalves, D., 2021. Personal Care and Cosmetic Products as a Potential Source of Environmental Contamination by Microplastics in a Densely Populated Asian City. Frontiers in Marine Science, 8. DOI:https://doi.org/10.3389/fmars.2021.683482

Bates, P., Horritt, M., Smith, C., Mason, D., 1997. Integrating Remote Sensing Observations of Flood Hydrology and Hydraulic Modelling. Hydrological Processes, 11(14): 1777-1795. DOI:https://doi.org/10.1002/(SICI)1099-1085(199711)11:14<1777::AID-HYP543>3.0.CO;2-E

Béjar, M., Vericat, D., Batalla, R.J., Gibbins, C.N., 2018. Variation in Flow and Suspended Sediment Transport in a Montane River Affected by Hydropeaking and Instream

Mining. Geomorphology, 310: 69-83. DOI:https://doi.org/10.1016/j.geomorph.2018.03.001

Bentley, J., 2019. Detecting Ocean Microplastics with Remote Sensing in the Near-infrared: A Feasibility Study. Ph.D. Thesis, Bridgewater State University.

Bernardo, N., Alcântara, E., Watanabe, F., Rodrigues, T., Imai, N., Curtarelli, M., Barbosa, C., 2015. Bio-optical Model Tuning for Retrieving the Total Suspended Matter Concentration in Barra Bonita Reservoir. Rev. Bras. Cartogr, 67(7): 1497-1507.

Best, J.L., Reid, I., 1984. Separation Zone at Open-channel Junctions. Journal of Hydraulic Engineering, 110(11): 1588-1594. DOI:https://doi.org/10.1061/(ASCE)0733-9429(1984)110:11(1588)

Bettes, R., 2008. Sediment Transport & Alluvial Resistance in Rivers. Bristol: Environment Agency.

Biermann, L., Clewley, D., Martinez-Vicente, V., Topouzelis, K., 2020. Finding Plastic Patches in Coastal Waters Using Optical Satellite Data. Scientific Reports, 10(1): 1-10. DOI:https://doi.org/10.1038/s41598-020-62298-z

Birkinshaw, S.J., O'Donnell, G.M., Moore, P., Kilsby, C.G., Fowler, H.J., Berry, P.A.M., 2010. Using Satellite Altimetry Data to Augment Flow Estimation Techniques on the Mekong River. Hydrological Processes, 24(26): 3811-3825. DOI:https://doi.org/10.1002/hyp.7811

Bjerklie, D.M., Birkett, C.M., Jones, J.W., Carabajal, C., Rover, J.A., Fulton, J.W., Garambois, P.-A., 2018. Satellite Remote Sensing Estimation of River Discharge: Application to the Yukon River Alaska. Journal of Hydrology, 561: 1000-1018. DOI:https://doi.org/10.1016/j.jhydrol.2018.04.005

Bjerklie, D.M., Lawrence Dingman, S., Vorosmarty, C.J., Bolster, C.H., Congalton, R.G., 2003. Evaluating the Potential for Measuring River Discharge from Space. Journal of Hydrology, 278(1): 17-38. DOI:https://doi.org/10.1016/S0022-1694(03)00129-X

Bogárdi, J., 1971. Sediment Transport of Rivers. Budapest, Hungary: Akadémiai Kiadó.(In Hungarian).

Bogárdi, J., 1974. Sediment Transport in Alluvial Streams, 826. Akademiai Kiado Budapest.

Bordós, G., Urbányi, B., Micsinai, A., Kriszt, B., Palotai, Z., Szabó, I., Hantosi, Z., Szoboszlay, S., 2019. Identification of Microplastics in Fish Ponds and Natural Freshwater Environments of the Carpathian Basin, Europe. Chemosphere, 216: 110-116. DOI:https://doi.org/10.1016/j.chemosphere.2018.10.110

Breiman, Jerome H. Friedman, Richard A. Olshen, Charles J. Stone, 1984. Classification and Regression Trees. North-Holland, The Wadsworth Statistics/Probability Series, Wadsworth, Belmont.

Breiman, L., 2001. Random forests. Machine Learning, 45(1): 5-32. DOI:https://doi.org/10.1023/A:1010933404324

Bryksa, J. (2021) Microplastics from the North Saskatchewan River in the Edmonton Region. https://esaa.org/wp-content/uploads/2021/10/RT21-Bryksa.pdf. (Accessed September 6th, 2023)

Bussi, G., Dadson Simon, J., Bowes Michael, J., Whitehead Paul, G., 2017. Seasonal and Interannual Changes in Sediment Transport Identified through Sediment Rating Curves. Journal of Hydrologic Engineering, 22(2): 06016016. DOI:https://doi.org/10.1061/(ASCE)HE.1943-5584.0001466

Buwono, N.R., Risjani, Y., Soegianto, A., 2021. Distribution of Microplastic in Relation to Water Quality Parameters in the Brantas River, East Java, Indonesia. Environmental Technology & Innovation, 24: 101915. DOI:https://doi.org/10.1016/j.eti.2021.101915

Castro-Jiménez, J., González-Fernández, D., Fornier, M., Schmidt, N., Sempéré, R., 2019. Macro-litter in Surface Waters From the Rhone River: Plastic Pollution and Loading to the NW Mediterranean Sea. Marine Pollution Bulletin, 146: 60-66.

DOI:https://doi.org/10.1016/j.marpolbul.2019.05.067

Cewep (2021) Latest Eurostat Figures: Municipal Waste Treatment 2019. https://www.cewep.eu/municipal-waste-treatment-2019/. (Accessed February 6th, 2022)

Chen, H.L., Gibbins, C.N., Selvam, S.B., Ting, K.N., 2021. Spatio-temporal Variation of Microplastic Along a Rural to Urban Transition in a Tropical River. Environmental Pollution, 289: 117895. DOI:https://doi.org/10.1016/j.envpol.2021.117895

Chen, J., Wilson, C., Chambers, D., Nerem, R., Tapley, B., 1998. Seasonal Global Water Mass Budget and Mean Sea Level Variations. Geophysical Research Letters, 25(19): 3555-3558. DOI:https://doi.org/10.1029/98GL02754

Church, M., Rice, S.P., 2009. Form and Growth of Bars in a Wandering Gravel-bed River. Earth Surface Processes and Landforms, 34(10): 1422-1432. DOI:https://doi.org/10.1002/esp.1831

Congalton, R.G., 1991. A review of Assessing the Accuracy of Classifications of Remotely Sensed Data. Remote Sensing of Environment, 37(1): 35-46. DOI:https://doi.org/10.1016/0034-4257(91)90048-B

Cortes, C., Vapnik, V., 1995. Support-vector Networks. Machine Learning, 20(3): 273-297. DOI:https://doi.org/10.1007/BF00994018

Cowger, W., Gray, A.B., Guilinger, J.J., Fong, B., Waldschläger, K., 2021. Concentration Depth Profiles of Microplastic Particles in River Flow and Implications for Surface Sampling. Environmental Science & Technology, 55(9): 6032-6041. DOI:https://doi.org/10.1021/acs.est.1c01768

Crosti, R., Arcangeli, A., Campana, I., Paraboschi, M., González-Fernández, D., 2018. 'Down to the River': Amount, Composition, and Economic Sector of Litter Entering the Marine Compartment, Through the Tiber River in the Western Mediterranean Sea. Rendiconti Lincei. Scienze Fisiche E Naturali, 29(4): 859-866. DOI:https://doi.org/10.1007/s12210-018-0747-y

Csépes, E., Bancsi, I., Végvári, P., Aranyné Rózsavári, A., 2003. Sediment Transport Study on the Middle Tisza (Between Kisköre and Szolnok). MHT Szolnok, (CD), 2: 1-10 (in Hungarian).

Csépes, E., Nagy, M., Bancsi, I., Végvári, P., Kovács, P., Szilágyi, E., 2000. The Phases of Water Quality Characteristics in the Middle Section of River Tisza in the Light of the Greatest Flood of the Century. Hidrológiai Közlöny 80: 285-287 (in Hungarian).

D'Hont, A., Gittenberger, A., Leuven, R.S.E.W., Hendriks, A.J., 2021. Dropping the Microbead: Source and Sink Related Microplastic Distribution in the Black Sea and Caspian Sea Basins. Marine Pollution Bulletin, 173: 112982. DOI:https://doi.org/10.1016/j.marpolbul.2021.112982

Dancey, C.P., Reidy, J., 2007. Statistics Without Maths for Psychology, Fourth edition. Pearson education limited, England.

Davaasuren, N., Marino, A., Boardman, C., Alparone, M., Nunziata, F., Ackermann, N., Hajnsek, I., 2018. Detecting Microplastics Pollution in World Oceans Using SAR Remote Sensing. IGARSS 2018-2018 IEEE International Geoscience and Remote Sensing Symposium. IEEE, pp. 938-941. DOI:https://doi.org/10.1109/IGARSS.2018.8517281

de Carvalho, A.R., Garcia, F., Riem-Galliano, L., Tudesque, L., Albignac, M., ter Halle, A., Cucherousset, J., 2021. Urbanization and Hydrological Conditions Drive the Spatial and Temporal Variability of Microplastic Pollution in the Garonne River. Science of The Total Environment, 769: 144479. DOI:https://doi.org/10.1016/j.scitotenv.2020.144479

De Giglio, M., Dubbini, M., Cortesi, I., Maraviglia, M., Parisi, E.I., Tucci, G., 2021. Plastics Waste Identification in River Ecosystems by Multispectral Proximal Sensing: A

preliminary Methodology Study. Water and Environment Journal, 35(2): 569-579. DOI:https://doi.org/10.1111/wej.12652

Dehkordi, A.T., Ghasemi, H., Zoej, M.J.V., 2021. Machine Learning-Based Estimation of Suspended Sediment Concentration along Missouri River using Remote Sensing Imageries in Google Earth Engine, 2021. 7th International Conference on Signal Processing and Intelligent Systems (ICSPIS), pp. 1-5. DOI:https://doi.org/10.1109/ICSPIS54653.2021.9729382

Dekker, A.G., Vos, R., Peters, S., 2002. Analytical Algorithms for Lake Water TSM Estimation for Retrospective Analyses of TM and SPOT Sensor Data. International Journal of Remote Sensing, 23(1): 15-35. DOI:https://doi.org/10.1080/01431160010006917

Dris, R., Gasperi, J., Rocher, V., Saad, M., Renault, N., Tassin, B., 2015. Microplastic Contamination in an Urban Area: A case Study in Greater Paris. Environmental Chemistry, 12(5): 592-599. DOI:https://doi.org/10.1071/EN14167

Du, M., Mu, X., Zhao, G., Gao, P., Sun, W., 2021. Changes in Runoff and Sediment Load and Potential Causes in the Malian River Basin on the Loess Plateau. Sustainability, 13(2): 443. DOI:https://doi.org/10.3390/su13020443

Duan, H., Ma, R., Xu, J., Zhang, Y., Zhang, B., 2010. Comparison of Different Semi-empirical Algorithms to Estimate Chlorophyll-a Concentration in Inland Lake Water. Environmental Monitoring and Assessment, 170(1): 231-244. DOI:https://doi.org/10.1007/s10661-009-1228-7

Durga Rao, K.H.V., Shravya, A., Dadhwal, V.K., 2020. A novel Method of Satellite Based River Discharge Estimation Using River Hydraulic Geometry Through Genetic Algorithm Technique. Journal of Hydrology, 589: 125361. DOI:https://doi.org/10.1016/j.jhydrol.2020.125361

Elert, A.M., Becker, R., Duemichen, E., Eisentraut, P., Falkenhagen, J., Sturm, H., Braun, U., 2017. Comparison of Different Methods for MP Detection: What Can We Learn From Them, and Why Asking the Right Question Before Measurements Matters? Environmental Pollution, 231: 1256-1264. DOI:https://doi.org/10.1016/j.envpol.2017.08.074

ESA. https://step.esa.int/main/download/snap-download/. (Accessed June 20th, 2021)

ESA. https://scihub.copernicus.eu/. (Accessed March 6th, 2023)

Eurostat (2021) Municipal Waste Statistics. https://ec.europa.eu/eurostat/statistics-explained/index.php?title=Municipal_waste_statistics. (Accessed February 6th, 2022)

Evans, M.C., Ruf, C.S., 2022. Toward the Detection and Imaging of Ocean Microplastics with a Spaceborne Radar. IEEE Transactions on Geoscience and Remote Sensing, 60: 1-9. DOI:https://doi.org/10.1109/TGRS.2021.3081691

Feng, L., Hu, C., Chen, X., Tian, L., Chen, L., 2012. Human Induced Turbidity Changes in Poyang Lake Between 2000 and 2010: Observations from MODIS. Journal of Geophysical Research: Oceans, 117(C7). DOI:https://doi.org/10.1029/2011JC007864

Feng, S., Lu, H., Tian, P., Xue, Y., Lu, J., Tang, M., Feng, W., 2020. Analysis of Microplastics in a Remote Region of the Tibetan Plateau: Implications for Natural Environmental Response to Human Activities. Science of The Total Environment, 739: 140087. DOI:https://doi.org/10.1016/j.scitotenv.2020.140087

Fischer, H.B., 1979. Mixing in Inland and Coastal Waters. Academic press. DOI:https://doi.org/10.1016/C2009-0-22051-4

Flores, J., Wu, J., Stöckle, C., Ewing, R., Yang, X., 2020. Estimating River Sediment Discharge in the Upper Mississippi River Using Landsat Imagery. Remote Sensing, 12(15): 2370. DOI:https://doi.org/10.3390/rs12152370

Freedman, D., Pisani, R., Purves, R., Adhikari, A., 2007. Statistics. WW Norton & Company New York.

Friedman, N., Geiger, D., Goldszmidt, M., 1997. Bayesian Network Classifiers. Machine Learning, 29(2): 131-163. DOI:https://doi.org/10.1023/A:1007465528199

Fryirs, K., 2013. (Dis)Connectivity in Catchment Sediment Cascades: A fresh Look at the Sediment Delivery Problem. Earth Surface Processes and Landforms, 38(1): 30-46. DOI:https://doi.org/10.1002/esp.3242

Fryirs, K.A., Brierley, G.J., 2012. Geomorphic Analysis of River Systems: An approach to Reading the Landscape. John Wiley & Sons. DOI:https://doi.org/10.1002/9781118305454

Fulton, J.W., Mason, C.A., Eggleston, J.R., Nicotra, M.J., Chiu, C.-L., Henneberg, M.F., Best, H.R., Cederberg, J.R., Holnbeck, S.R., Lotspeich, R.R., Laveau, C.D., Moramarco, T., Jones, M.E., Gourley, J.J., Wasielewski, D., 2020. Near-Field Remote Sensing of Surface Velocity and River Discharge Using Radars and the Probability Concept at 10 U.S. Geological Survey Streamgages. Remote Sensing, 12(8): 1296. DOI:https://doi.org/10.3390/rs12081296

Geraeds, M., van Emmerik, T., de Vries, R., bin Ab Razak, M.S., 2019. Riverine Plastic Litter Monitoring Using Unmanned Aerial Vehicles (UAVs). Remote Sensing 11(17): 2045. DOI:https://doi.org/10.3390/rs11172045

Gleason, C.J., Durand, M.T., 2020. Remote Sensing of River Discharge: A Review and a Framing for the Discipline. Remote Sensing, 12(7): 1107. DOI:https://doi.org/doi:10.3390/rs12071107

Gleason, C.J., Smith, L.C., 2014. Toward Global Mapping of River Discharge Using Satellite Images and At-Many-Stations Hydraulic Geometry. Proceedings of the National Academy of Sciences, 111(13): 4788-4791. DOI:https://doi.org/10.1073/pnas.1317606111

Goddijn-Murphy, L., Peters, S., Van Sebille, E., James, N.A., Gibb, S., 2018. Concept for a Hyperspectral Remote Sensing Algorithm for Floating Marine Macro Plastics. Marine Pollution Bulletin, 126: 255-262. DOI:https://doi.org/10.1016/j.marpolbul.2017.11.011

Guy, H.P., 1969. Laboratory Theory and Methods for Sediment Analysis, Techniques of Water-Resources Investigations. U.S. G.P.O. DOI:https://doi.org/10.3133/twri05C1

Guyot, J.-L., Filizola, N., Guimarães, V., 1998. Amazon Suspended Sediment Yield Measurements Using an Acoustic Doppler Current Profiler (ADCP): First Results. In: Johnson, A.I., Fernandez Jauregui, C. (Eds.), Hydrology in the Humid Tropic Environment. IAHS-AISH publication, pp. 109-115.

Hartanto, I.M., van der Kwast, J., Alexandridis, T.K., Almeida, W., Song, Y., van Andel, S.J., Solomatine, D.P., 2017. Data Assimilation of Satellite-based Actual Evapotranspiration in a Distributed Hydrological Model of a Controlled Water System. International Journal of Applied Earth Observation and Geoinformation, 57: 123-135. DOI:https://doi.org/10.1016/j.jag.2016.12.015

Hashiba, M., Kai, T., Yorozuya, A., Motonaga, Y., 2014. Field Observation of the River Flood Flow and Suspended Sediment Distribution Using ADCP. 9th International Symposium on Ultrasonic Doppler Methods for Fluid Mechanics and Fluid Engineering Germany pp. 125-128.

He, B., Wijesiri, B., Ayoko, G.A., Egodawatta, P., Rintoul, L., Goonetilleke, A., 2020. Influential Factors on Microplastics Occurrence in River Sediments. Science of The Total Environment, 738: 139901. DOI:https://doi.org/10.1016/j.scitotenv.2020.139901

He, D., Chen, X., Zhao, W., Zhu, Z., Qi, X., Zhou, L., Chen, W., Wan, C., Li, D., Zou, X., Wu, N., 2021. Microplastics Contamination in the Surface Water of the Yangtze River from Upstream to Estuary Based on Different Sampling Methods. Environmental Research, 196: 110908.

DOI:https://doi.org/10.1016/j.envres.2021.110908

Hegde, R., Patel, S., Naik, R.G., Nayak, S.N., Shivaprakasha, K.S., Bhandarkar, R., 2021. Underwater Marine Life and Plastic Waste Detection Using Deep Learning and Raspberry Pi. In: Kalya, S., Kulkarni, M., Shivaprakasha, K.S. (Eds.), Advances in VLSI, Signal Processing, Power Electronics, IoT, Communication and Embedded Systems. Springer Singapore, Singapore, pp. 263-272. DOI:https://doi.org/10.1007/978-981-16-0443-0_22

Hoellein, T.J., Shogren, A.J., Tank, J.L., Risteca, P., Kelly, J.J., 2019. Microplastic Deposition Velocity in Streams Follows Patterns for Naturally Occurring Allochthonous Particles. Scientific Reports, 9(1): 3740. DOI:https://doi.org/10.1038/s41598-019-40126-3

Holland, J.H., 1992. Genetic Algorithms. Scientific American, 267(1): 66-73. DOI:https://doi.org/10.1038/scientificamerican0792-66

Hu, C., 2021. Remote Detection of Marine Debris Using Satellite Observations in the Visible and Near Infrared Spectral Range: Challenges and Potentials. Remote Sensing of Environment, 259: 112414. DOI:https://doi.org/10.1016/j.rse.2021.112414

Huang, Y., Tian, M., Jin, F., Chen, M., Liu, Z., He, S., Li, F., Yang, L., Fang, C., Mu, J., 2020. Coupled Effects of Urbanization Level and Dam on Microplastics in Surface Waters in a Coastal Watershed of Southeast China. Marine Pollution Bulletin, 154: 111089. DOI:https://doi.org/10.1016/j.marpolbul.2020.111089

Hurley, R., Braaten, H.F.V., Nizzetto, L., Steindal, E.H., Lin, Y., Clayer, F., van Emmerik, T., Buenaventura, N.T., Eidsvoll, D.P., Økelsrud, A., Norling, M., Adam, H.N., Olsen, M., 2023. Measuring Riverine Macroplastic: Methods, Harmonisation, and Quality Control. Water Research, 235: 119902. DOI:https://doi.org/10.1016/j.watres.2023.119902

Hurley, R., Woodward, J., Rothwell, J.J., 2018. Microplastic Contamination of River Beds Significantly Reduced by Catchment-wide Flooding. Nature Geoscience, 11(4): 251-257. DOI:https://doi.org/10.1038/s41561-018-0080-1

IBM Statistical Package for Social Sciences (SPSS) software. https://www.ibm.com/analytics/us/en/technology/spss/. (Accessed 25th May, 2022)

ICPDR, 2007. Analysis of the Tisza River Basin 2007, International Commission for the Protection of the Danube River, Vienna International Centre / D0412. https://www.icpdr.org/main/sites/default/files/Tisza_RB_Analysis_2007.pdf. (Accessed 22nd March, 2021)

ICPDR, 2018. Tisza River Basin Characterization Report on Surface Water, Interreg (Danube Transational Programme). https://www.interreg-danube.eu/uploads/media/approved_project_output/0001/37/ed1b7198ffc57c6d2d528717650cd6d94280004e.pdf. (Accessed May 15th, 2022)

Index.hu 2019. Ten-thousand-ton Waste and Woody Debris were Collected from the Tisza at the Kisköre Dam. https://index.hu/belfold/2019/12/11/tizezer_tonna_hulladekot_. (Accessed January 30th, 2022)

Interreg, 2018. Report on Significant Pressures Relevant for the Tisza River Basin. Deliverable 3.2.1 Report on Significant Pressures Relevant for the TRB, Danube Transnational Programme. https://www.interreg-danube.eu/approved-projects/jointisza. (Accessed May 15th, 2022)

Jakovljević, G., Govedarica, M., Taboada, F.Á., 2019. Remote Sensing Data in Mapping Plastics at Surface Water Bodies, FIG Working Week 2019. Geospatial Information for a Smarter Life and Environmental Resilience, Hanoi, Vietnam.

Jirka, G.H., 2004. Mixing and Dispersion in Rivers. In: Massimo Greco, A.C.R.D.M. (Ed.). Second International Conference on Fluvial Hyraulics. AA Balkema Publishers, a member of Taylor & Francis Group plc London, Napoli, Italy, pp. 13-27.

Katona, G., 2019. A Tisza folyó hulladékszennyezése (Waste pollution of the Tisza River). Műszaki Katonai Közlöny, 29(4): 65-80 (In Hungarian).

Kendall, M., 1975. Rank Correlation Measures. Charles Griffin, London, 202, 15.

Kiss, T., Amissah, G.J., Fiala, K., 2019a. Bank Processes and Revetment Erosion of a Large Lowland River: Case Study of the Lower Tisza River, Hungary. Water, 11(6). DOI:https://doi.org/10.3390/w11061313

Kiss, T., Balogh, M., Fiala, K., Sipos, G., 2018. Morphology of Fluvial Levee Series Along a River Under Human Influence, Maros River, Hungary. Geomorphology, 303: 309-321. DOI:https://doi.org/10.1016/j.geomorph.2017.12.014

Kiss, T., Fiala, K., Sipos, G., Szatmári, G., 2019b. Long-term Hydrological Changes After Various River Regulation Measures: Are we Responsible for Flow Extremes? Hydrology Research, 50(2): 417-430. DOI:https://doi.org/10.2166/nh.2019.095

Kiss, T., Fórián, S., Szatmári, G., Sipos, G., 2021. Spatial Distribution of Microplastics in the Fluvial Sediments of a Transboundary River – A case Study of the Tisza River in Central Europe. Science of the Total Environment, 785: 147306. DOI:https://doi.org/10.1016/j.scitotenv.2021.147306

Kiss, T., Gönczy, S., Nagy, T., Mesaroš, M., Balla, A., 2022. Deposition and Mobilization of Microplastics in a Low-Energy Fluvial Environment from a Geomorphological Perspective. Applied Sciences, 12(9): 4367. DOI:https://doi.org/10.3390/app12094367

Kiss, T., Oroszi, V.G., Sipos, G., Fiala, K., Benyhe, B., 2011. Accelerated Overbank Accumulation After Nineteenth Century River Regulation Works: A case Study on the Maros River, Hungary. Geomorphology, 135(1): 191-202. DOI:https://doi.org/10.1016/j.geomorph.2011.08.017

Knighton, D., 2014. Fluvial Forms and Processes: A new Perspective. Routledge. DOI:https://doi.org/10.4324/9780203784662

Kondolf, G.M., Gao, Y., Annandale, G.W., Morris, G.L., Jiang, E., Zhang, J., Cao, Y., Carling, P., Fu, K., Guo, Q., Hotchkiss, R., Peteuil, C., Sumi, T., Wang, H.-W., Wang, Z., Wei, Z., Wu, B., Wu, C., Yang, C.T., 2014. Sustainable Sediment Management in Reservoirs and Regulated Rivers: Experiences from Five Continents. Earth's Future, 2(5): 256-280. DOI:https://doi.org/10.1002/2013EF000184

Koyuncuoğlu, P., Erden, G., 2023. Microplastics in Municipal Wastewater Treatment Plants: A case Study of Denizli/Turkey. Frontiers of Environmental Science & Engineering, 17(8): 99. DOI:https://doi.org/10.1007/s11783-023-1699-8

Kröger, R., Brandt, J.R., Fleming, J.P., Huenemann, T., Stubbs, T., Prevost, J.D., Delta, F., Littlejohn, K.A., Pierce, S., 2010. Total Suspended Sediment Concentrations in Wolf Lake, Mississippi: An EPA 319 (h) Landscape Improvement Project, Mississippi Water Resources Conference. Mississippi State University.

Kruskal, W.H., Wallis, W.A., 1952. Use of Ranks in One-Criterion Variance Analysis. Journal of the American Statistical Association, 47(260): 583-621. DOI:https://doi.org/10.1080/01621459.1952.10483441

Kukkola, A., Runkel, R.L., Schneidewind, U., Murphy, S.F., Kelleher, L., Sambrook Smith, G.H., Nel, H.A., Lynch, I., Krause, S., 2023. Prevailing Impacts of River Management on Microplastic Transport in Contrasting US Streams: Rethinking Global Microplastic Flux Estimations. Water Research, 240: 120112. DOI:https://doi.org/10.1016/j.watres.2023.120112

Kumar, R., Sharma, P., Verma, A., Jha, P.K., Singh, P., Gupta, P.K., Chandra, R., Prasad, P.V.V., 2021. Effect of Physical Characteristics and Hydrodynamic Conditions on Transport and Deposition of Microplastics in Riverine Ecosystem. Water, 13(19). DOI:https://doi.org/10.3390/w13192710

Laermanns, H., Reifferscheid, G., Kruse, J., Földi, C., Dierkes, G., Schaefer, D., Scherer, C.,

Bogner, C., Stock, F., 2021. Microplastic in Water and Sediments at the Confluence of the Elbe and Mulde Rivers in Germany. Frontiers in Environmental Science, 9: 794895. DOI:https://doi.org/10.3389/fenvs.2021.794895

Lahens, L., Strady, E., Kieu-Le, T.C., Dris, R., Boukerma, K., Rinnert, E., Gasperi, J., Tassin, B., 2018. Macroplastic and Microplastic Contamination Assessment of a Tropical River (Saigon River, Vietnam) Transversed by a Developing Megacity. Environmental Pollution, 236: 661-671. DOI:https://doi.org/10.1016/j.envpol.2018.02.005

Larson, M.D., Simic Milas, A., Vincent, R.K., Evans, J.E., 2018. Multi-depth Suspended Sediment Estimation Using High-resolution Remote-sensing UAV in Maumee River, Ohio. International Journal of Remote Sensing, 39(15-16): 5472-5489. DOI:https://doi.org/10.1080/01431161.2018.1465616

Lászlóffy, W., 1982. Tisza River: Construction and Water Management in the Tisza Water Regime. Akadémiai Kiadó, Budapest, Hungary.

Law, K.L., 2017. Plastics in the Marine Environment. Annual Review of Marine Science, 9: 205-229. DOI:https://doi.org/10.1146/annurev-marine-010816-060409

Lebreton, L.C., Van Der Zwet, J., Damsteeg, J.-W., Slat, B., Andrady, A., Reisser, J., 2017. River Plastic Emissions to the World's Oceans. Nature Communications, 8(1): 1-10. DOI:https://doi.org/10.1038/ncomms15611

Lenaker, P.L., Baldwin, A.K., Corsi, S.R., Mason, S.A., Reneau, P.C., Scott, J.W., 2019. Vertical Distribution of Microplastics in the Water Column and Surficial Sediment from the Milwaukee River Basin to Lake Michigan. Environmental Science & Technology, 53(21): 12227-12237. DOI:https://doi.org/10.1021/acs.est.9b03850

Lenz, R., Labrenz, M., 2018. Small Microplastic Sampling in Water: Development of an Encapsulated Filtration Device. Water, 10(8): 1055. DOI:https://doi.org/10.3390/w10081055

Leopold, L.B., Maddock, T., 1953. The Hydraulic Geometry of Stream Channels and Some Physiographic Implications. US Government Printing Office, United states government printing office, vol. 252, Washington 1-53 pp.

Likas, A., Vlassis, N., Verbeek, J., 2003. The Global K-means Clustering Algorithm. Pattern Recognition, 36(2): 451-461. DOI:https://doi.org/10.1016/S0031-3203(02)00060-2

Liu, H., Li, Q., Shi, T., Hu, S., Wu, G., Zhou, Q., 2017. Application of Sentinel 2 MSI Images to Retrieve Suspended Particulate Matter Concentrations in Poyang Lake. Remote Sensing, 9(7): 761. DOI:https://doi.org/10.3390/rs9070761

Liu, Y.-M., Zhang, L., Zhou, M., Liang, J., Wang, Y., Sun, L., Li, Q.-L., 2022a. A neural Networks Based Method for Suspended Sediment Concentration Retrieval from GF-5 Hyperspectral Images. Journal of Infrared and Millimeter Waves, 41(1). DOI:https://doi.org/10.11972/j.issn.1001-9014.2022.01.029

Liu, Y., Cao, W., Hu, Y., Zhang, J., Shen, W., 2022b. Horizontal and Vertical Distribution of Microplastics in Dam Reservoir After Impoundment. Science of The Total Environment, 832: 154962. DOI:https://doi.org/10.1016/j.scitotenv.2022.154962

Lloyd, S., 1982. Least Squares Quantization in PCM. IEEE Transactions on Information Theory, 28(2): 129-137. DOI:https://doi.org/10.1109/TIT.1982.1056489

Louis, J., Debaecker, V., Pflug, B., Main-Knorn, M., Bieniarz, J., Mueller-Wilm, U., Cadau, E., Gascon, F., 2016. Sentinel-2 sen2cor: L2a processor for users. Proceedings Living Planet Symposium 2016. Spacebooks Online, pp. 1-8.

Lu, X., Wang, X., Liu, X., Singh, V.P., 2023. Dispersal and Transport of Microplastic Particles Under Different Flow Conditions in Riverine Ecosystem. Journal of Hazardous Materials, 442: 130033. DOI:https://doi.org/10.1016/j.jhazmat.2022.130033

Lundberg, S.M., Lee, S.-I., 2017. A unified Approach to Interpreting Model Predictions.

Advances in Neural Information Processing Systems, 30. DOI:https://doi.org/10.48550/arXiv.1705.07874

Maes, T., Jessop, R., Wellner, N., Haupt, K., Mayes, A.G.J.S.r., 2017. A rapid-screening Approach to Detect and Quantify Microplastics Based on Fluorescent Tagging with Nile Red. Scientific Reports, 7(1): 1-10. DOI:https://doi.org/10.1038/srep44501

Mai, Y., Peng, S., Lai, Z., Wang, X., 2021. Measurement, Quantification, and Potential Risk of Microplastics in the Mainstream of the Pearl River (Xijiang River) and its Estuary, Southern China. Environmental Science and Pollution Research, 28(38): 53127-53140. DOI:https://doi.org/10.1007/s11356-021-14395-3

Mann, H.B., 1945. Nonparametric Tests Against Trend. Econometrica: Journal of the Econometric Society: 245-259. DOI:https://doi.org/10.2307/1907187

Manuel, A., Blanco, A.C., Tamondong, A.M., Jalbuena, R., Cabrera, O., Gege, P., 2020. Optmization of Bio-optical Model Parameters for Turbid Lake Water Quality Estimation Using Landsat 8 and Wasi-2D. The International Archives of Photogrammetry, Remote Sensing and Spatial Information Sciences, 42: 67-72. DOI:https://doi.org/10.5194/isprs-archives-XLII-3-W11-67-2020

Marinho, R.R., Harmel, T., Martinez, J.-M., Filizola Junior, N.P., 2021. Spatiotemporal Dynamics of Suspended Sediments in the Negro River, Amazon Basin, from In Situ and Sentinel-2 Remote Sensing Data. ISPRS International Journal of Geo-Information, 10(2). DOI:https://doi.org/10.3390/ijgi10020086

Marinho, T., Filizola, N., Martinez, J.-M., Armijos, E., Nascimento, A., 2018. Suspended Sediment Variability at the Solimões and Negro Confluence Between May 2013 and February 2014. Geosciences, 8(7): 265. DOI:https://doi.org/10.3390/geosciences8070265

Martin, J.L., McCutcheon, S.C., 1998. Hydrodynamics and Transport for Water Quality Modeling. CRC press, Boca Raton. DOI:https://doi.org/10.1201/9780203751510

Martinez, J.-M., Guyot, J.-L., Filizola, N., Sondag, F., 2009. Increase in Suspended Sediment Discharge of the Amazon River Assessed by Monitoring Network and Satellite Data. Catena, 79(3): 257-264. DOI:https://doi.org/10.1016/j.catena.2009.05.011

Masoumi, H., Safavi, S.M., Khani, Z., 2012. Identification and Classification of Plastic Resins using Near infrared Reflectance. International Journal of Mechanical and Industrial Engineering, 6: 213-20.

Masura, J., Baker, J., Foster, G., Arthur, C., 2015. Laboratory Methods for the Analysis of Microplastics in the Marine Environment: Recommendations for Quantifying Synthetic Particles in Waters and Sediments. NOAA Marine Debris Division. https://repository.library.noaa.gov/view/noaa/10296 (Accessed 25th May, 2022).

Mattos, L.d., Kruger, L.D.M., Affonso, A.L.S., Perbiche-Neves, G., Pressinatte, S., 2017. Small Dams also Change the Benthic Macroinvertebrates Community in Rocky Rivers. Acta Limnologica Brasiliensia, 29. DOI:https://doi.org/10.1590/s2179-975x5316

McCormick, A.R., Hoellein, T.J., London, M.G., Hittie, J., Scott, J.W., Kelly, J.J., 2016. Microplastic in Surface Waters of Urban Rivers: Concentration, Sources, and Associated Bacterial Assemblages. Ecosphere, 7(11): e01556. DOI:https://doi.org/10.1002/ecs2.1556

McCulloch, W.S., Pitts, W., 1943. A logical Calculus of the Ideas Immanent in Nervous Activity. The Bulletin of Mathematical Biophysics, 5(4): 115-133. DOI:https://doi.org/10.1007/BF02478259

McFeeters, S.K., 1996. The use of the Normalized Difference Water Index (NDWI) in the Delineation of Open Water Features. International Journal of Remote Sensing, 17(7): 1425-1432. DOI:https://doi.org/10.1080/01431169608948714

Meijer, L.J.J., van Emmerik, T., van der Ent, R., Schmidt, C., Lebreton, L., 2021. More than

1000 Rivers Account for 80% of Global Riverine Plastic Emissions into the Ocean. Science Advances, 7(18): eaaz5803. DOI:https://doi.org/10.1126/sciadv.aaz5803

Mengen, D., Ottinger, M., Leinenkugel, P., Ribbe, L., 2020. Modeling River Discharge Using Automated River Width Measurements Derived from Sentinel-1 Time Series. Remote Sensing, 12(19): 3236. DOI:https://doi.org/10.3390/rs12193236

Mercedes, M., Esther, G., Francesc, P., Jordi, C., 2003. Drifting Plastic Debris as a Potential Vector for Dispersing Harmful Algal Bloom (HAB) Species, Los plásticos flotantes son potenciales vectores de dispersión de especies formadoras de proliferaciones algales nocivas. Consejo Superior de Investigaciones Científicas (España). DOI:https://doi.org/10.3989/scimar.2003.67n1107

Metz, T., Koch, M., Lenz, P., 2020. Quantification of Microplastics: Which Parameters are Essential for a Reliable Inter-study Comparison? Marine Pollution Bulletin, 157: 111330. DOI:https://doi.org/10.1016/j.marpolbul.2020.111330

Michailovsky, C.I., McEnnis, S., Berry, P.A.M., Smith, R., Bauer-Gottwein, P., 2012. River Monitoring from Satellite Radar Altimetry in the Zambezi River Basin. Hydrology and Earth System Sciences, 16(7): 2181-2192. DOI:https://doi.org/10.5194/hess-16-2181-2012

Mifdal, J., Longépé, N., Rußwurm, M., 2021. Towards Detecting Floating Objects on a Global Scale with Learned Spatial Features using Sentinel 2. ISPRS Annals of the Photogrammetry, Remote Sensing and Spatial Information Sciences, V-3-2021: 285-293. DOI:https://doi.org/10.5194/isprs-annals-V-3-2021-285-2021

Mohsen, A., Balla, A., Kiss, T., 2023a. High Spatiotemporal Resolution Analysis on Suspended Sediment and Microplastic Transport of a Lowland River. Science of The Total Environment, 902: 166188. DOI:https://doi.org/10.1016/j.scitotenv.2023.166188

Mohsen, A., Elshemy, M., Zeidan, B., 2020. Water Quality Monitoring of Lake Burullus (Egypt) using Landsat Satellite Imageries. Environmental Science and Pollution Research, 28(13): 15687-15700. DOI:https://doi.org/10.1007/s11356-020-11765-1

Mohsen, A., Elshemy, M., Zeidan, B.A., 2018. Change Detection for Lake Burullus, Egypt using Remote Sensing and GIS Approaches. Environmental Science and Pollution Research, 25(31): 30763-30771. DOI:https://doi.org/10.1007/s11356-016-8167-y

Mohsen, A., Kiss, T., Kovács, F., 2023b. Machine learning-based Detection and Mapping of Riverine Litter Utilizing Sentinel-2 Imagery. Environmental Science and Pollution Research, 30(25): 67742-67757. DOI:https://doi.org/10.1007/s11356-023-27068-0

Mohsen, A., Kovács, F., Kiss, T., 2022a. Remote Sensing of Sediment Discharge in Rivers using Sentinel-2 Images and Machine-learning Algorithms. Hydrology, 9(5): 88. DOI:https://doi.org/10.3390/hydrology9050088

Mohsen, A., Kovács, F., Kiss, T., 2023c. Riverine Microplastic Quantification: A Novel Approach Integrating Satellite Images, Neural Network, and Suspended Sediment Data as a Proxy. Sensors, 23(23): 9505. DOI:https://doi.org/10.3390/s23239505

Mohsen, A., Kovács, F., Mezősi, G., Kiss, T., 2021. Sediment Transport Dynamism in the Confluence Area of Two Rivers Transporting Mainly Suspended Sediment Based on Sentinel-2 Satellite Images. Water, 13(21): 3132. DOI:https://doi.org/10.3390/w13213132

Mohsen, A., Zeidan, B., Elshemy, M., 2022b. Water Quality Assessment of Lake Burullus, Egypt, Utilizing Statistical and GIS Modeling as Environmental Hydrology Applications. Environmental Monitoring and Assessment, 195(1): 93. DOI:https://doi.org/10.1007/s10661-022-10710-8

Moore, T.S., Dowell, M.D., Bradt, S., Verdu, A.R., 2014. An optical Water Type Framework for Selecting and Blending Retrievals from Bio-optical Algorithms in Lakes and Coastal Waters. Remote Sensing of Environment, 143: 97-111.

DOI:https://doi.org/10.1016/j.rse.2013.11.021

Morét-Ferguson, S., Law, K.L., Proskurowski, G., Murphy, E.K., Peacock, E.E., Reddy, C.M., 2010. The Size, Mass, and Composition of Plastic Debris in the Western North Atlantic Ocean. Marine Pollution Bulletin, 60(10): 1873-1878. DOI:https://doi.org/10.1016/j.marpolbul.2010.07.020

Mosley, M.P., 1976. An Experimental Study of Channel Confluences. The Journal of Geology, 84(5): 535-562.

Mouri, G., Ros, F.C., Chalov, S., 2014. Characteristics of Suspended Sediment and River Discharge During the Beginning of Snowmelt in Volcanically Active Mountainous Environments. Geomorphology, 213: 266-276. DOI:https://doi.org/10.1016/j.geomorph.2014.02.001

Mouyen, M., Longuevergne, L., Steer, P., Crave, A., Lemoine, J.-M., Save, H., Robin, C., 2018. Assessing Modern River Sediment Discharge to the Ocean using Satellite Gravimetry. Nature Communications, 9(1): 1-9. DOI:https://doi.org/10.1038/s41467-018-05921-y

Mukonza, S.S., Chiang, J.-L., 2022. Satellite Sensors as an Emerging Technique for Monitoring Macro- and Microplastics in Aquatic Ecosystems. Water Emerging Contaminants & Nanoplastics, 1(4): 17. DOI:https://doi.org/10.20517/wecn.2022.12

Napper, I.E., Baroth, A., Barrett, A.C., Bhola, S., Chowdhury, G.W., Davies, B.F.R., Duncan, E.M., Kumar, S., Nelms, S.E., Hasan Niloy, M.N., Nishat, B., Maddalene, T., Thompson, R.C., Koldewey, H., 2021. The Abundance and Characteristics of Microplastics in Surface Water in the Transboundary Ganges River. Environmental Pollution, 274: 116348. DOI:https://doi.org/10.1016/j.envpol.2020.116348

Neal, J., Schumann, G., Bates, P., Buytaert, W., Matgen, P., Pappenberger, F., 2009. A data Assimilation Approach to Discharge Estimation from Space. Hydrological Processes: An International Journal, 23(25): 3641-3649. DOI:https://doi.org/10.1002/hyp.7518

Newbould, R.A., Powell, D.M., Whelan, M.J., 2021. Macroplastic Debris Transfer in Rivers: A Travel Distance Approach. Frontiers in Water, 3. DOI:https://doi.org/10.3389/frwa.2021.724596

Ngo, P.L., Pramanik, B.K., Shah, K., Roychand, R., 2019. Pathway, Classification and Removal Efficiency of Microplastics in Wastewater Treatment Plants. Environmental Pollution, 255: 113326. DOI:https://doi.org/10.1016/j.envpol.2019.113326

Ockelford, A., Cundy, A., Ebdon, J.E., 2020. Storm Response of Fluvial Sedimentary Microplastics. Scientific Reports, 10(1): 1865. DOI:https://doi.org/10.1038/s41598-020-58765-2

Oeurng, C., Sauvage, S., Sánchez-Pérez, J.-M., 2010. Dynamics of Suspended Sediment Transport and Yield in a Large Agricultural Catchment, Southwest France. Earth Surface Processes and Landforms, 35(11): 1289-1301. DOI:https://doi.org/10.1002/esp.1971

Optuna. https://optuna.org/. (Accessed January 4th, 2023)

Otsu, N., 1979. A threshold Selection Method from Gray-level Histograms. IEEE Transactions on Systems, Man, and Cybernetics, 9(1): 62-66. DOI:https://doi.org/10.1109/TSMC.1979.4310076

OVF, 2019. Yearbook (2016) of the Hydrographical Service of Hungary, 350, OVF, Budapest.

Park, E., Latrubesse, E.M., 2015. Surface Water Types and Sediment Distribution Patterns at the Confluence of Mega Rivers: The Solimões-Amazon and Negro Rivers Junction. Water Resources Research, 51(8): 6197-6213. DOI:https://doi.org/10.1002/2014WR016757

Pavelsky, T.M., Smith, L.C., 2008. RivWidth: A Software Tool for the Calculation of River Widths From Remotely Sensed Imagery. IEEE Geoscience and Remote Sensing

Letters, 5(1): 70-73. DOI:https://doi.org/10.1109/LGRS.2007.908305

Peterson, K.T., Sagan, V., Sidike, P., Cox, A.L., Martinez, M., 2018. Suspended Sediment Concentration Estimation from Landsat Imagery along the Lower Missouri and Middle Mississippi Rivers Using an Extreme Learning Machine. Remote Sensing, 10(10): 1503. DOI:https://doi.org/10.3390/rs10101503

PETKUPA (2021). https://petkupa.hu/eng/7-tons-of-trash-from-the-tisza-river-will-be-recycled.html. (Accessed February 9th, 2022)

Piehl, S., Atwood, E.C., Bochow, M., Imhof, H.K., Franke, J., Siegert, F., Laforsch, C., 2020. Can Water Constituents be used as Proxy to Map Microplastic Dispersal within Transitional and Coastal Waters? Frontiers in Environmental Science, 8: 92. DOI:https://doi.org/10.3389/fenvs.2020.00092

Pilechi, A., Mohammadian, A., Murphy, E., 2022. A numerical Framework for Modeling Fate and Transport of Microplastics in Inland and Coastal Waters. Marine Pollution Bulletin, 184: 114119. DOI:https://doi.org/10.1016/j.marpolbul.2022.114119

Planet. https://www.planet.com/explorer. (Accessed February 2nd, 2023)

Porterfield, G., 1972. Computation of Fluvial-sediment Discharge, Techniques of Water-Resources Investigations of the United States Geological Survey US Government Printing Office, Washington, DC, USA,, pp. 1-66. DOI:https://doi.org/10.3133/twri03C3

Prata, J.C., da Costa, J.P., Duarte, A.C., Rocha-Santos, T., 2019. Methods for Sampling and Detection of Microplastics in Water and Sediment: A critical Review. TrAC Trends in Analytical Chemistry, 110: 150-159. DOI:https://doi.org/10.1016/j.trac.2018.10.029

Qiu, Q., Tan, Z., Wang, J., Peng, J., Li, M., Zhan, Z., 2016. Extraction, Enumeration and Identification Methods for Monitoring Microplastics in the Environment. Estuarine, Coastal and Shelf Science, 176: 102-109. DOI:https://doi.org/10.1016/j.ecss.2016.04.012

Quinn, B., Murphy, F., Ewins, C., 2017. Validation of Density Separation for the Rapid Recovery of Microplastics from Sediment. Analytical Methods, 9(9): 1491-1498. DOI:https://doi.org/10.1039/C6AY02542K

Rodrigues, M.O., Gonçalves, A.M.M., Gonçalves, F.J.M., Abrantes, N., 2020. Improving Cost-efficiency for MPs Density Separation by Zinc Chloride Reuse. MethodsX, 7: 100785. DOI:https://doi.org/10.1016/j.mex.2020.100785

Rodrigues, S.M., Almeida, C.M.R., Silva, D., Cunha, J., Antunes, C., Freitas, V., Ramos, S., 2019. Microplastic Contamination in an Urban Estuary: Abundance and Distribution of Microplastics and Fish Larvae in the Douro Estuary. Science of the Total Environment, 659: 1071-1081. DOI:https://doi.org/10.1016/j.scitotenv.2018.12.273

Ronkay, F., Molnar, B., Gere, D., Czigany, T., 2021. Plastic Waste from Marine Environment: Demonstration of Possible Routes for Recycling by Different Manufacturing Technologies. Waste Management, 119: 101-110. DOI:https://doi.org/10.1016/j.wasman.2020.09.029

Rouse, J.W., Haas, R.H., Schell, J.A., Deering, D.W., 1974. Monitoring Vegetation Systems in the Great Plains with ERTS. NASA Special Publication 351(1974): 309.

Rußwurm, M., Venkatesa, S.J., Tuia, D., 2023. Large-scale Detection of Marine Debris in Coastal Areas with Sentinel-2. iScience, 26(12). DOI:https://doi.org/10.1016/j.isci.2023.108402

Saadu, I., Farsang, A., Kiss, T., 2023. Quantification of Macroplastic Litter in Fallow Greenhouse Farmlands: Case Study in Southeastern Hungary. Environmental Sciences Europe, 35(1): 63. DOI:https://doi.org/10.1186/s12302-023-00777-6

Sang, W., Chen, Z., Mei, L., Hao, S., Zhan, C., Zhang, W.b., Li, M., Liu, J., 2021. The Abundance and Characteristics of Microplastics in Rainwater Pipelines in Wuhan,

China. Science of The Total Environment, 755: 142606. DOI:https://doi.org/10.1016/j.scitotenv.2020.142606

Scherer, C., Weber, A., Stock, F., Vurusic, S., Egerci, H., Kochleus, C., Arendt, N., Foeldi, C., Dierkes, G., Wagner, M., Brennholt, N., Reifferscheid, G., 2020. Comparative Assessment of Microplastics in Water and Sediment of a Large European River. Science of The Total Environment, 738: 139866. DOI:https://doi.org/10.1016/j.scitotenv.2020.139866

Schmidt, C., Krauth, T., Wagner, S., 2017. Export of Plastic Debris by Rivers into the Sea. Environmental Science & Technology, 51(21): 12246-12253. DOI:https://doi.org/10.1021/acs.est.7b02368

Schrank, I., Löder, M.G.J., Imhof, H.K., Moses, S.R., Heß, M., Schwaiger, J., Laforsch, C., 2022. Riverine Microplastic Contamination in Southwest Germany: A Large-scale Survey. Frontiers in Earth Science, 10: 794250. DOI:https://doi.org/10.3389/feart.2022.794250

Serra, T., Soler, M., Barcelona, A., Colomer, J., 2022. Suspended Sediment Transport and Deposition in Sediment-replenished Artificial Floods in Mediterranean Rivers. Journal of Hydrology, 609: 127756. DOI:https://doi.org/10.1016/j.jhydrol.2022.127756

Serranti, S., Bonifazi, G., 2010. Post-consumer Polyolefins (PP-PE) Recognition by Combined Spectroscopic Sensing Techniques. The Open Waste Management Journal, 3(1): 35-45. DOI:https://doi.org/10.2174/1876400201003010035

Setälä, O., Magnusson, K., Lehtiniemi, M., Norén, F., 2016. Distribution and Abundance of Surface Water Microlitter in the Baltic Sea: A comparison of Two Sampling Methods. Marine Pollution Bulletin, 110(1): 177-183. DOI:https://doi.org/10.1016/j.marpolbul.2016.06.065

Shaheed, R., Mohammadian, A., Kheirkhah Gildeh, H., 2019. A comparison of Standard k–ε and Realizable k–ε Turbulence Models in Curved and Confluent Channels. Environmental Fluid Mechanics, 19(2): 543-568. DOI:https://doi.org/10.1007/s10652-018-9637-1

Shamskhany, A., Li, Z., Patel, P., Karimpour, S., 2021. Evidence of Microplastic Size Impact on Mobility and Transport in the Marine Environment: A Review and Synthesis of Recent Research. Frontiers in Marine Science, 8. DOI:https://doi.org/10.3389/fmars.2021.760649

Shao, W., Zhao, C., Jiang, X., Sun, Z., Wang, X., Wang, J., Cai, L., 2021. Characteristics of Suspended Sediment in Sentinel-1 Synthetic Aperture Radar Observations. Remote Sensing Letters, 12(11): 1167-1179. DOI:https://doi.org/10.1080/2150704X.2021.1974119

Sipos, G., Blanka, V., Mezősi, G., Kiss, T., van Leeuwen, B., 2014. Effect of Climate Change on the Hydrological Character of River Maros, Hungary-Romania. Journal of Environmental Geography, 7(1-2): 49-56. DOI:https://doi.org/10.2478/jengeo-2014-0006

Sipos, G., Fiala, K., 2008. Changes of Cross-sectional Morphology and Channel Capacity During an Extreme Flood Event, Lower Tisza and Maros Rivers, Hungary. Journal of Environmental Geography, 1(1-2): 41-51. DOI:https://doi.org/10.14232/jengeo-2008-43856

Sipos, G., Kiss, T., Fiala, K., 2007. Morphological Alterations due to Channelization along the Lower Tisza and Maros Rivers (Hungary). Geografia Fiscica e Dinamica Quaternaria, 30(2): 239-247.

Solé Gómez, À., Scandolo, L., Eisemann, E., 2022. A learning Approach for River Debris Detection. International Journal of Applied Earth Observation and Geoinformation, 107: 102682. DOI:https://doi.org/10.1016/j.jag.2022.102682

Stigler, S.M., 1989. Francis Galton's Account of the Invention of Correlation. Statistical Science, 4(2): 73-79.

Stisen, S., Jensen, K.H., Sandholt, I., Grimes, D.I.F., 2008. A remote sensing Driven Distributed Hydrological Model of the Senegal River Basin. Journal of Hydrology, 354(1): 131-148. DOI:https://doi.org/10.1016/j.jhydrol.2008.03.006

Stumpf, R.P., Goldschmidt, P.M., 1992. Remote Sensing of Suspended Sediment Discharge into the Western Gulf of Maine During the April 1987 100-year Flood. Journal of Coastal Research, 8: 218-225.

Sun, Y., Bakker, T., Ruf, C., Pan, Y., 2023. Effects of Microplastics and Surfactants on Surface Roughness of Water Waves. Scientific Reports, 13(1): 1978. DOI:https://doi.org/10.1038/s41598-023-29088-9

Szeliski, R., 2010. Computer Vision: Algorithms and Applications. Springer London.

Talbot, R., Chang, H., 2022. Microplastics in Freshwater: A global Review of Factors Affecting Spatial and Temporal Variations. Environmental Pollution, 292: 118393. DOI:https://doi.org/10.1016/j.envpol.2021.118393

Tamminga, M., Hengstmann, E., Fischer, E.K., 2018. Microplastic Analysis in the South Funen Archipelago, Baltic Sea, Implementing Manta Trawling and Bulk Sampling. Marine pollution Bulletin, 128: 601-608. DOI:https://doi.org/10.1016/j.marpolbul.2018.01.066

Tan, B., Wolfe, R., Lin, G., 2021. PlanetScope Imagery Geolocation Accuracy Assessment, AGU Fall Meeting, New Orleans, LA, pp. B15I-1545.

Tang, K.H.D., Hadibarata, T., 2021. Microplastics Removal Through Water Treatment Plants: Its Feasibility, Efficiency, Future Prospects and Enhancement by Proper Waste Management. Environmental Challenges, 5: 100264. DOI:https://doi.org/10.1016/j.envc.2021.100264

Tarpai, J., 2013. The Role of Natural and Social Resources in the Touristical Development of the Transcarpathian Region, Ukraine. PhD Thesis, University of Pécs.

TERRA (2000) Structure of the Tisza Catchment Area. https://www.terra.hu/cian/vizgyujto-en.html. (Accessed September 11th, 2023)

Themistocleous, K., Papoutsa, C., Michaelides, S., Hadjimitsis, D., 2020. Investigating Detection of Floating Plastic Litter from Space Using Sentinel-2 Imagery. Remote Sensing 12(16): 2648. DOI:https://doi.org/10.3390/rs12162648

Thompson, R.C., Olsen, Y., Mitchell, R.P., Davis, A., Rowland, S.J., John, A.W., McGonigle, D., Russell, A.E., 2004. Lost at Sea: Where is all the Plastic? Science(Washington) 304(5672): 838. DOI:https://doi.org/10.1126/science.1094559

Topouzelis, K., Papakonstantinou, A., Garaba, S.P., 2019. Detection of Floating Plastics from Satellite and Unmanned Aerial Systems (Plastic Litter Project 2018). International Journal of Applied Earth Observation and Geoinformation, 79: 175-183. DOI:https://doi.org/10.1016/j.jag.2019.03.011

Tramoy, R., Gasperi, J., Colasse, L., Tassin, B., 2020. Transfer Dynamic of Macroplastics in Estuaries—New Insights from the Seine Estuary: Part 1. Long Term Dynamic Based on Date-prints on Stranded Debris. Marine Pollution Bulletin, 152: 110894. DOI:https://doi.org/10.1016/j.marpolbul.2020.110894

Umar, M., Rhoads, B.L., Greenberg, J., 2018. Use of Multispectral Satellite Remote Sensing to Assess Mixing of Suspended Sediment Downstream of Large River Confluences. Journal of Hydrology, 556: 325-338. DOI:https://doi.org/10.1016/j.jhydrol.2017.11.026

Van Emmerik, T., Kieu-Le, T.-C., Loozen, M., van Oeveren, K., Strady, E., Bui, X.-T., Egger, M., Gasperi, J., Lebreton, L., Nguyen, P.-D., 2018. A methodology to Characterize Riverine Macroplastic Emission into the Ocean. Frontiers In Marine Science, 5: 372. DOI:https://doi.org/10.3389/fmars.2018.00372

Van Emmerik, T., Mellink, Y., Hauk, R., Waldschläger, K., Schreyers, L., 2022. Rivers as Plastic Reservoirs. Frontiers in Water, 3: 786936. DOI:https://doi.org/10.3389/frwa.2021.786936

Van Emmerik, T., Schwarz, A., 2020. Plastic Debris in Rivers. Wiley Interdisciplinary Reviews: Water, 7(1): e1398. DOI:https://doi.org/10.1002/wat2.1398

Vercruysse, K., Grabowski, R.C., Rickson, R., 2017. Suspended Sediment Transport Dynamics in Rivers: Multi-scale Drivers of Temporal Variation. Earth-Science Reviews, 166: 38-52. DOI:https://doi.org/10.1016/j.earscirev.2016.12.016

Vriend, P., Van Calcar, C., Kooi, M., Landman, H., Pikaar, R., Van Emmerik, T., 2020. Rapid Assessment of Floating Macroplastic Transport in the Rhine. Frontiers in Marine Science, 7. DOI:https://doi.org/10.3389/fmars.2020.00010

Waldschläger, K., Brückner, M.Z.M., Carney Almroth, B., Hackney, C.R., Adyel, T.M., Alimi, O.S., Belontz, S.L., Cowger, W., Doyle, D., Gray, A., Kane, I., Kooi, M., Kramer, M., Lechthaler, S., Michie, L., Nordam, T., Pohl, F., Russell, C., Thit, A., Umar, W., Valero, D., Varrani, A., Warrier, A.K., Woodall, L.C., Wu, N., 2022. Learning from Natural Sediments to Tackle Microplastics Challenges: A multidisciplinary Perspective. Earth-Science Reviews, 228: 104021. DOI:https://doi.org/10.1016/j.earscirev.2022.104021

Waldschläger, K., Schüttrumpf, H., 2019. Erosion Behavior of Different Microplastic Particles in Comparison to Natural Sediments. Environmental Science & Technology, 53(22): 13219-13227. DOI:https://doi.org/10.1021/acs.est.9b05394

Waldschläger, K., Schüttrumpf, H., technology, 2019. Effects of Particle Properties on the Settling and Rise Velocities of Microplastics in Freshwater Under Laboratory Conditions. Environmental Science, 53(4): 1958-1966. DOI:https://doi.org/10.1021/acs.est.8b06794

Walling, D.E., 1983. The Sediment Delivery Problem. Journal of Hydrology, 65(1): 209-237. DOI:https://doi.org/10.1016/0022-1694(83)90217-2

Wang, Q., Atkinson, P.M., 2018. Spatio-temporal Fusion for Daily Sentinel-2 Images. Remote Sensing of Environment, 204: 31-42. DOI:https://doi.org/10.1016/j.rse.2017.10.046

Ward, J.H., 1963. Hierarchical Grouping to Optimize an Objective Function. Journal of the American Statistical Association, 58(301): 236-244. DOI:https://doi.org/10.1080/01621459.1963.10500845

Watkins, L., McGrattan, S., Sullivan, P.J., Walter, M.T., 2019. The Effect of Dams on River Transport of Microplastic Pollution. Science of The Total Environment, 664: 834-840. DOI:https://doi.org/10.1016/j.scitotenv.2019.02.028

Wendt-Potthoff, K., Avellán, T., van Emmerik, T., Hamester, M., Kirschke, S., Kitover, D., Schmidt, C., 2020. Monitoring Plastics in Rivers and Lakes: Guidelines for the Harmonization of Methodologies. United Nations Environment Programme.

Whitehead, P.G., Bussi, G., Hughes, J.M.R., Castro-Castellon, A.T., Norling, M.D., Jeffers, E.S., Rampley, C.P.N., Read, D.S., Horton, A.A., 2021. Modelling Microplastics in the River Thames: Sources, Sinks and Policy Implications. Water, 13(6): 861. DOI:https://doi.org/10.3390/w13060861

Wiesinger, H., Wang, Z., Hellweg, S., 2021. Deep Dive into Plastic Monomers, Additives, and Processing Aids. Environmental Science & Technology, 55(13): 9339-9351. DOI:https://doi.org/10.1021/acs.est.1c00976

Wolf, Mattis van den Berg, Katelijn Garaba, Shungudzemwoyo P Gnann, Nina Sattler, Klaus Stahl, Frederic Zielinski, Oliver, 2020. Machine Learning for Aquatic Plastic Litter Detection, Classification and Quantification (APLASTIC-Q). Environmental Research Letters, 15(11): 114042. DOI:https://doi.org/10.1088/1748-9326/abbd01

Wu, P., Tang, Y., Dang, M., Wang, S., Jin, H., Liu, Y., Jing, H., Zheng, C., Yi, S., Cai, Z.,

2020. Spatial-temporal Distribution of Microplastics in Surface Water and Sediments of Maozhou River within Guangdong-Hong Kong-Macao Greater Bay Area. Science of The Total Environment, 717: 135187. DOI:https://doi.org/10.1016/j.scitotenv.2019.135187

Wulf, H., Bookhagen, B., Scherler, D., 2012. Climatic and Geologic Controls on Suspended Sediment Flux in the Sutlej River Valley, Western Himalaya. Hydrology and Earth System Sciences, 16(7): 2193-2217. DOI:https://doi.org/10.5194/hess-16-2193-2012

Xia, F., Wang, Y., Wang, D., Cai, Y., Zhang, J., 2023. Seasonal Pulse Effect of Microplastics in the River Catchment-From Tributary Catchment to Mainstream. Journal of Environmental Management, 342: 118316. DOI:https://doi.org/10.1016/j.jenvman.2023.118316

Yan, M., Wang, L., Dai, Y., Sun, H., Liu, C., 2021. Behavior of Microplastics in Inland Waters: Aggregation, Settlement, and Transport. Bulletin of Environmental Contamination and Toxicology, 107(4): 700-709. DOI:https://doi.org/10.1007/s00128-020-03087-2

Yang, H., Kong, J., Hu, H., Du, Y., Gao, M., Chen, F., 2022. A Review of Remote Sensing for Water Quality Retrieval: Progress and Challenges, Remote Sensing. DOI:https://doi.org/10.3390/rs14081770

Youshen, X., 1996. A new Neural Network for Solving Linear and Quadratic Programming Problems. IEEE Transactions on Neural Networks, 7(6): 1544-1548. DOI:https://doi.org/10.1109/72.548188

Yu, L., Pan, Y., Wu, Y., 2009. Research on Data Normalization Methods in Multi-attribute Evaluation. International Conference on Computational Intelligence and Software Engineering. IEEE, pp. 1-5.

Yuan, S.-y., Xu, L., Tang, H.-w., Xiao, Y., Gualtieri, C., 2022. The Dynamics of River Confluences and Their Effects on the Ecology of Aquatic Environment: A review. Journal of Hydrodynamics, 34(1): 1-14. DOI:https://doi.org/10.1007/s42241-022-0001-z

Yuan, S., Tang, H., Li, K., Xu, L., Xiao, Y., Gualtieri, C., Rennie, C., Melville, B., 2021. Hydrodynamics, Sediment Transport and Morphological Features at the Confluence Between the Yangtze River and the Poyang Lake. Water Resources Research, 57(3): e2020WR028284. DOI:https://doi.org/10.1029/2020WR028284

Zalasiewicz, J., Gabbott, S., Waters, C.N., 2019. Chapter 23 - Plastic Waste: How Plastics Have Become Part of the Earth's Geological Cycle. In: Letcher, T.M., Vallero, D.A. (Eds.), Waste (Second Edition). Academic Press, pp. 443-452. DOI:https://doi.org/10.1016/B978-0-12-815060-3.00023-2

Zhang, K., Gong, W., Lv, J., Xiong, X., Wu, C., 2015. Accumulation of Floating Microplastics Behind the Three Gorges Dam. Environmental Pollution, 204: 117-123. DOI:https://doi.org/10.1016/j.envpol.2015.04.023

Zhang, L., Liu, J., Xie, Y., Zhong, S., Yang, B., Lu, D., Zhong, Q., 2020. Distribution of Microplastics in Surface Water and Sediments of Qin River in Beibu Gulf, China. Science of the Total Environment, 708: 135176. DOI:https://doi.org/10.1016/j.scitotenv.2019.135176

Zhao, S., Zhu, L., Wang, T., Li, D., 2014. Suspended Microplastics in the Surface Water of the Yangtze Estuary System, China: First Observations on Occurrence, Distribution. Marine Pollution Bulletin, 86(1-2): 562-568. DOI:https://doi.org/10.1016/j.marpolbul.2014.06.032

Zou, Q., Xie, S., Lin, Z., Wu, M., Ju, Y., 2016. Finding the Best Classification Threshold in Imbalanced Classification. Big Data Research, 5: 2-8. DOI:https://doi.org/10.1016/j.bdr.2015.12.001

SUMMARY

Rivers play a crucial role in connecting terrestrial plastic pollution sources to oceans. Although several studies have recently investigated riverine plastic pollution (MP and MaP) transport, many aspects, including spatiotemporal distribution dynamics, transport mechanisms, and influencing factors are still unclear. Furthermore, the connection between SS and plastic transport, especially MP, in response to various hydrological conditions and longitudinal variables (e.g., dams and tributaries) has not been thoroughly investigated. Moreover, the influence of hydrology on water mixing in confluences is still unexplored, despite their profound influence on mainstream sediment and plastic transport downstream. On the other side, remote sensing techniques could support these investigations and serve as a valuable and cost-effective monitoring tool for riverine sediment and plastic transport. However, the feasibility of satellite sensors in detecting plastic debris, especially MP, remains questionable. Also, there is a pressing need for developing satellite-based Q models with adequate accuracy, as most of the literature relied on in-situ Q measurements for estimating SS and plastic pollution transport.

The investigation was based on intensive measurements collected at multiple spatiotemporal scales in the lowland Tisza River (Central Europe) coupled with several optical and active satellite sensors and the utilization of machine learning algorithms. The composition, transport rate, and spatiotemporal distribution of riverine litter (including MaP) were investigated through four in-situ surveys in Szeged (during the early spring flood in 2021) and the exploration of VHR images (GE satellites) along the Tisza (2015–2021). Concurrent 16 Sentinel-2 images for the identified litter spots were acquired to develop Sentinel-2-based riverine litter models utilizing machine learning algorithms (DT, NB, RF, SVC, and ANN). The models underwent validation and testing at spots with various sizes, and the best-derived model was used to explore the spatiotemporal dynamics of litter in the Middle Tisza (276–451 river km) in detail, based on 61 Sentinel-2 images (2015–2021).

Both components of Q_s (i.e., Q and SSC) were modelled by five years (2015–2020) of monthly in-situ measurements of Q and SSC conducted at three gauging sites in the Lower Tisza (Algyő and Szeged) and Maros Rivers (Makó) by the ATIVIZIG, and concurrent 29 Sentinel-2 images. The hydraulic geometry theory, specifically the water width–Q relationship served as the basis for developing the Q models. Sentinel-2-based width estimates at the three gauging sites were integrated with measured Q through AHG power law, AMHG, and novel AHG machine learning methods. Simultaneously, SSC was modelled by correlating measured SSC at five verticals in the cross-sections in Szeged (Tisza) and Makó (Maros) with reflectance data from Sentinel-2 images, using RF, SVM, ANN, and combined algorithms. The best-performing Q and SSC models were then employed to explore the spatiotemporal dynamics of Q_s in the Lower Tisza and Maros Rivers, based on 93 Sentinel-2 images (2015–2021).

The influence of hydrology on water mixing, sediment, and pollutant transport was examined in detail in the Tisza–Maros confluence through 143 Sentinle-2 images, measured and calculated hydrological parameters at the three gauging sites (i.e. Tisza: Algyő and Szeged; Maros: Makó). The K-means algorithm classified the water of the confluence into TW, MW, and MIX, and their lateral and longitudinal dynamics in response to variations in hydrological parameters (e.g., Q, H, S, and their ratio and differences) were tested through a correlation analysis test. Predictive equations for these mixing water variables (i.e., TW, MW, MIX, and L) were developed based on rivers` hydrology, providing support for future measurements at the confluence.

The spatiotemporal distribution dynamics of surficial SS and MP transport in response to hydrological changes and longitudinal variables (e.g., dams and tributaries) were investigated in the Tisza River, through intensive spatial (26 sites in 2021; 21 sites in 2022) and temporal

(140 samples in Mindszent; May 2021–May 2023) surficial SS and MP concentration measurements. The Kruskal-Wallis, ANOVA and post hoc tests were applied to reveal their statistical differences among river sections (S1–S5) and during various hydrological conditions (i.e., low stages, minor and medium floods, and flood phases). Besides, a correlation analysis was applied to assess the strength of their correlation along the river sections and their correlation with H under different hydrological conditions. In the meantime, these measurements were coupled with additional surficial SSC measurements in Szeged (70 samples: March 2021–March 2022) to develop surficial SS and MP concentration models, through various satellite sensors (Sentinel-2, PlanetScope, and Sentinel-1) and ANN algorithm. Also, the surficial SSC was tested as a potential proxy for MP concentration, and predictive MP concentration equations were developed.

The findings revealed a domination of organic material in riverine litter of the Tisza, with only 5–20% comprising MaPs, owing to continuous input of organic debris, particularly at the meandering sections with high bank erosion. Riverine litter and MaPs exhibited a strong association with water stage and discharge conditions, as the highest transport rates (litter: 264 spot/h; MaP: 300 items/h) occurred during high stages, while the lowest (litter: 12 spot/h; MaP: 24 items/h) occurred during low stages. This is attributed to the elevated kinetic energy and connectivity between the floodplain and the river channel during high stages; meanwhile, they become isolated during low stages. Most of the identified litter spots were noticed along riverbanks, upstream of bridges, dams, and floating docks, influenced by decreased flow velocity and the elevated trapping efficiency of these obstructions. Although the longitudinal profile of riverine litter was highly influenced by the applied waste management practices at sub-catchments, occasionally it was disrupted by local anthropogenic activities. Remarkably, the temporal analysis suggested conducting riverine litter purification campaigns at the end of flood periods, when gradual flux forms the largest acclamations at well-defined locations.

The developed Sentinel-2-based riverine litter models revealed high and comparable estimation accuracy (F1-score; 0.83–0.94), suggesting an elevated potential of satellite sensors in detecting litter spots. However, the models excelled with large and medium spot sizes but struggled with sub-pixel size spots. This is partially attributed to the limited impact of small spots on sensor reflectance as well as the low percentage (1%) of small litter data applied during the training phase. There is a necessity for a larger riverine litter dataset to enhance the generalization capability, robustness, and reliability of the models, as a disparity in the magnitude of evaluation metrics was observed between the validating and testing datasets. The SVC, RF, and ANN are the most recommended algorithms for future riverine litter detection studies owing to their elevated performance, while the DT and NB are less favorable, as the DT occasionally misclassifies river water as litter, and the NB struggles to discriminate obstructions from litter. Also, more emphasis should be applied to NIR and SWIR bands, as the spectral and SHAP analysis revealed a unique spectral signature for riverine litter in these bands. Notably, the integration of spectral indices, especially PI, NDWI, and NDVI, during the derivation of the riverine litter model may enhance its performance.

The AMHG Q models outperformed the AHG power law models at the three gauging sites; however, the performance of my novel AHG machine learning models surpassed both methods (mean: $R^2=0.7$; RMSE=140 m^3/s). This finding paves the way for automatic Q monitoring in rivers by remote sensing satellites at more river sections, avoiding the intricate optimization process applied in the AMHG method. However, the limitations of this approach should be considered: (1) It tends to misestimate discharges above the bankfull level due to losing hydraulic geometry characteristics. (2) Certain cross-section shapes (e.g., V-shape) have better hydraulic geometry characteristics than others (e.g., trapezoidal shape); and (3) Q estimates are highly influenced by remotely sensed width data. On the other hand, the three tested algorithms for developing SSC models revealed high and comparable

accuracy (Tisza: R^2=0.8; Maros: R^2=0.85), with RF and combined algorithms revealing superiority. The best-derived Q and SSC models successfully estimated Q_s in the Lower Tisza and Maros, proving the lower Q_s load in the Maros (1264 t/day) than the Tisza (2584 t/d), despite its elevated SSC (Maros: 129 g/m^3; Tisza: 59 g/m^3) due to its lower Q (Maros: 157 m^3/s; Tisza: 702 m^3/s). Moreover, they also effectively depicted the real distribution of Q_s not only longitudinally, but also laterally, highlighting that the lateral distribution of Q_s is influenced not only by flow velocity but also by the occurrence and location of a tributary upstream. However, the Q_s estimates near the riverbanks, at shallow sections, and during extreme weather conditions should be interpreted with caution since the sensor reflectance is influenced by mixed pixels, riverbeds, and surface water roughness.

The measured and calculated hydrological parameters in the Tisza–Maros confluence area revealed the flashy regime of the Maros compared to the Tisza. They also emphasize the significant influence of rivers` hydrology on the water mixing process and consequently sediment and pollutant transport downstream. Specifically, the discharge ratio ($Q_{Makó}/Q_{Szeged}$), slope (S), and slope difference (S_{Tisza}-S_{Maros}) were the most correlated parameters with the mixing water variables (i.e., TW, MW, MIX, and L); meanwhile, the daily water stage difference (ΔH) and variance between the joining rivers ($\Delta H_{Algyő}$-$\Delta H_{Makó}$) were the least correlated. Analysis of 143 Sentinel-2 images identified 11 mixing patterns around the year. These patterns were considered based on the domination of each water type in the confluence area and the likelihood of upwelling downstream, resulting in five patterns in the TW dominant class, a single pattern in the MW dominant class, and five patterns in the MIX dominant class. Generally, TW dominates the confluence area during floods when the Tisza impounds the Maros. Occasionally, MW dominates during concurrent floods in both rivers, but with elevated kinetic energy in the Maros to overcome the impoundment effect of the Tisza. Notably, during these flood periods, MIX is very limited, while it dominates during simultaneous low stages. Predictive equations for mixing water variables were developed with moderate to strong accuracy (R^2=0.4–0.82), offering a valuable tool for supporting future measurements in the confluence area, based on rivers` hydrology.

The Tisza showed a moderate MP pollution level (mean 35±27 item/m^3) compared to European Rivers and slight pollution globally. Microfibers dominated its composition, revealing WWTP effluents and untreated wastewater discharge as major sources of MP pollution. Hydrology played a significant role in shaping the temporal dynamics of surficial SS and MP transport, as the highest concentrations were recorded during flood waves (SSC: 97±75 g/m^3; MP: 47±27 item/m^3) and the lowest during low stages (SSC: 34±14 g/m^3; MP: 21±16 item/m^3). However, surficial SSC showed a stronger association with river hydrology than MP concentration, as evidenced by its higher correlation with H (ρ_{SSC-H}=0.7), than MP with H (ρ_{MP-H}=0.55). The correlation between surficial SS and MP concentrations themselves was the highest during flood waves (ρ_{SSC-MP}=0.61), particularly during the rising (ρ_{rising}=0.6) and peak (ρ_{peak}=0.81) phases, declining to negligible during low stages (ρ_{SSC-MP}=0.0). This discrepancy suggests similarity in sources and influencing factors of SS and MP during floods, while differences may arise during low stages. This suggestion was confirmed from the longitudinal measurements along the Tisza, as a negative correlation occurred during both measuring campaigns in low stages (in 2021 and 2022), when SS likely originates from tributaries and bank erosion, while MP from wastewater discharge. However, their correlation varied along individual river sections (S1–S5), from weak in the middle sections (S3–S4), to strong in the upper (S1–S2) and lower sections (S5), suggesting the great dynamics of their sources and influencing factors along the river. This can also be inferred from the contradictory influence of tributaries and dams on surficial SS and MP transport. Specifically, the Kraszna and the Zagyva Rivers were the only tributaries that revealed similar influences on surficial SS and MP concentrations downstream of their confluences in both measuring years, while it differed at the rest of the tributaries. Hence, the contribution of

a tributary in MP pollution is mainly governed by the applied wastewater management practices in its sub-catchment, which is not related to sediment sources. Dams, on the other hand, usually stimulate sediment deposition in reservoirs and clear water erosion downstream, resulting in a gradual decline in surficial SSC upstream and a sudden increase downstream. However, ambiguous patterns were noticed with MP concentrations at the three dams of the Tisza and during both measuring campaigns, as MP distribution is more vulnerable to local sources of pollution than SS.

Direct estimation of MP concentration in rivers by satellite sensors remains unattainable, as models developed with Sentinel-2, PlanetScope, and Sentinel-1 achieved low accuracy (R^2=0–0.2). Besides, MP concentration demonstrated a weak to moderate correlation with the optical bands and a negligible correlation with SAR channels. This limitation is attributed to the low concentration level of MP in the river, its transport being covered by a thin layer of water, and the limited spatial and spectral characteristics of current satellite sensors. Thus, the concentration level is insufficient to affect reflectance or backscattering, and the sensors lack the sensitivity to capture such slight influences. On the other hand, proxy MP concentration models based on SSC were promising, as they achieved high accuracy (R^2=0.15–0.8), especially during flood waves. Given the elevated potential of Sentinel-2 (R^2=0.7) and PlanetScope (R^2=0.6) in estimating surficial SSC, they could be employed to estimate MP concentration indirectly through the proxy models. However, some limitations should be considered: (1) Error propagation may influence MP concentration estimation accuracy. (2) Proxy models typically provide inaccurate estimates during low stages due to dissimilar sources of SS and MP, though still reasonable; and (3) The established SS–MP concentrations relationship should be calibrated recurrently, as sudden changes in their sources, either in space or time, could affect its accuracy.

The findings of this Ph.D. dissertation contribute to current research knowledge by elucidating the spatiotemporal dynamics of SS, MP, and MaP along lowland rivers in response to varying hydrological conditions and longitudinal variables (e.g., dams and tributaries). The river was systematically investigated at multiple spatiotemporal scales with exclusive intensive spatiotemporal measurements, leading to more reliable findings and conclusions. The study revealed the interconnection between sediment and plastic pollution transport, providing a comparative analysis of their sources, influencing factors, and transport mechanisms. Furthermore, the study introduced remote sensing-based models for not only SS, MP, and MaP concentrations, but also for water discharge, paving the way towards more sustainable and cost-effective monitoring of sediment and plastic transport in rivers. However, this research field is still ongoing, and identified challenges and limitations necessitate further exploration. For instance: (1) Sub-pixel detection of MaPs is still uncertain and further research is needed incorporating larger riverine litter datasets with finer spatial resolution images. This would improve the reliability of models and broaden their visibility to smaller spots. (2) Employing SAR images in estimating river width data for Q modelling, could enable more frequent monitoring, overcoming cloud cover issues in optical sensors. Besides, exploring other forms of hydraulic geometry equations may offer additional opportunities for Q estimation by satellite sensors. (3) Further improvement of the predictive equations for mixing water variables in confluences is warranted, incorporating additional hydraulic and morphological data. (4) Additional longitudinal measurements of surficial SS and MP concentrations during floods, coupled with denser sampling upstream and downstream of confluence, dams, and WWTPs, are required to gain deeper insights into their spatiotemporal distribution and validate the identified patterns; and (5) Additional testing of optically active water quality parameters as a potential proxy for MP concentration is warranted, addressing current limitations of SSC as a single proxy.

DECLARATION

I, Ahmed Mohsen Abdelsadek Metwaly, hereby declare the originality and authorship of the submitted dissertation to the Doctoral School of Geosciences, University of Szeged, for obtaining the doctoral degree. I affirm that this work has not been previously submitted to any educational institution to attain an academic degree or title. All assistance and data sources employed in the preparation of this work have been appropriately cited and acknowledged.

APPENDIX

Table A1. Summary of the applied in-situ and remote sensing data in this study collected at various spatiotemporal scales in the Tisza and Maros Rivers.

| Site ID/name	In-situ data				Remote sensing data			
	Purpose	Study period	Frequency	Collected sample	Sentinel-2 images	PlanetScope images	Sentinel-1 images	Google satellite images
Szeged (Figure 4.1)	Temporal monitoring of riverine litter (including MaP)	Feb. 18th, 23rd and Mar. 5th, 10th, 2021	Every 5 days	–	–	–	–	–
Tisza River in Hungary (Figure 5.2)	Spatiotemporal monitoring/investigation of riverine litter and developing remote sensing-based models	Jul. 2015–May 2021	Available images	–	77	–	–	13
Tisza River Algyő and Szeged gauging sites **Maros River** Makó gauging site. (Figure 3.1B)	Developing remote sensing-based suspended sediment discharge (Q_s) models	Feb. 2015–Nov. 2020	Monthly	**SSC**: depth-integrated sampling by a pump **Q**: acoustic doppler current profiler (ADCP) by ATIVIZIG	Altogether 122 (Tisza: 29; Maros: 27) Q_s time-series: 93	–	–	–
Tisza–Maros confluence to an extent of 4.2 km downstream (Figure 3.1D)	Investigate water mixing dynamics and its relationship to hydrological parameters of the rivers	Jul. 2015–May 2021	Every 3–5 days	–	143	–	–	–
Longitudinal measurements at sites a–z (Figure 3.1A)	Investigate the spatiotemporal distribution and correlation of surficial SS and MP concentrations in the Tisza, as well as develop remote sensing-based models for both variables	Aug. 2021 and Jul. 2022	Once/year	**Surficial SSC**: 1.5 L of water **MP conc.**: pumping 1 m³ of water	Altogether 15 (2021: 8; 2022: 7)	Altogether 47 (2021: 26; 2022: 21)	Altogether 15 (2021: 8; 2022: 7)	–
Temporal measurements in Mindszent and Szeged (Figure 3.1D and E)		**Mindszent** Mar. 2021–May 2023 **Szeged** Mar.2021–Mar. 2022	Every 3–5 days		**Mindszent**: 75 **Szeged**: 47	**Mindszent**: 79 **Szeged**: 51	**Mindszent**: 154 **Szeged**: 70	–
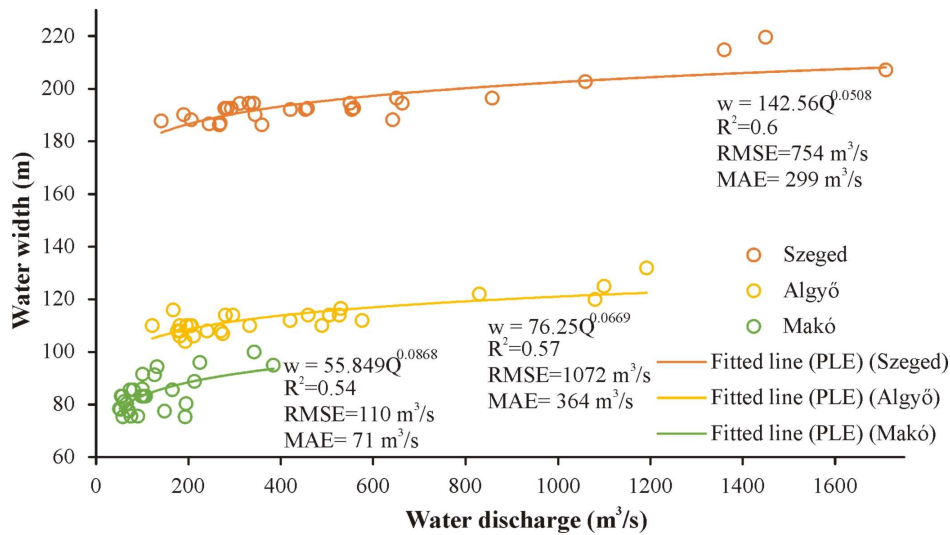
Figure A1. Fitted AHG power-law (PLE) models between water width and measured water discharge (2015–2020) at the three gauging sites in the Tisza (Algyő and Szeged) and Maros (Makó) Rivers.
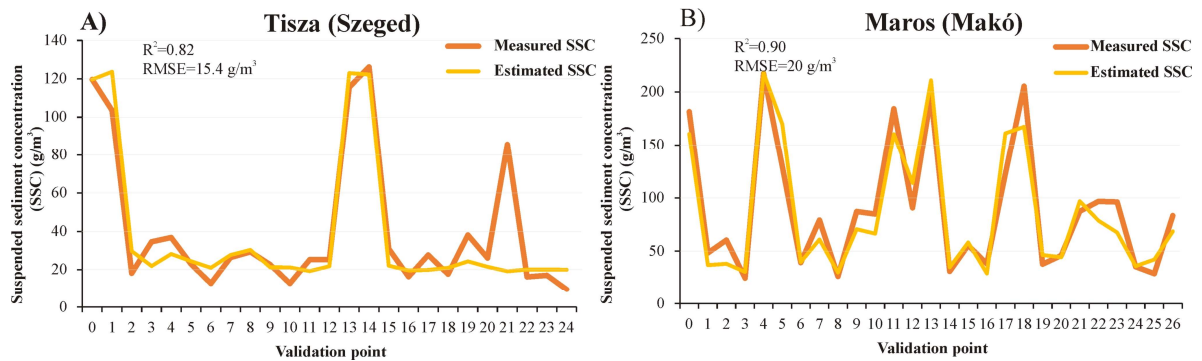

Figure A2. The estimated suspended sediment concentration (SSC) by the best-developed model (i.e., Tisza: combine model; Maros: random forest model) was compared to the measured one across the validation dataset (20% of data).

Table A2. Descriptive statistics of the various hydrological parameters (i.e., measured and calculated) in the three gauging sites in the Tisza (at Algyő and Szeged) and Marso (at Makó) Rivers, during the study period: January 2015–May 2021.

	Gauging site	Range	Min.	Max.	Mean	Std. dev.	Median	Mode
Water stage (cm)	$H_{Algyő}$	604	36	640	190	144	140	64
	H_{Szeged}	549	66	615	195	123	149	94[1]
	$H_{Makó}$	487	-112	375	-7	74	-24	-77
Absolute water level (m)	abs. $H_{Algyő}$	6.04	74.36	80.40	75.91	1.44	75.40	74.64
	abs. H_{Szeged}	5.49	74.36	79.85	75.65	1.23	75.2	74.64[1]
	abs. $H_{Makó}$	4.87	78.38	83.25	79.43	.74	79.26	78.73
Slope (cm/km)	S_{Tisza}	5.5	0.0	5.5	1.4	1.2	1.1	0.0
	S_{Maros}	16.9	2.7	19.6	13.0	2.8	13.9	14.3
	S_{Tisza}-S_{Maros}	20.8	-18.8	2.0	-11.6	3.9	-13.1	-14.4[1]
Discharge (m³/s)	$Q_{Algyő}$	1812	128	1940	627	425	501	180[1]
	Q_{Szeged}	2105	128	2233	659	448	520	180[1]
	$Q_{Makó}$	701	30	731	137	91	110	75
	$Q_{Algyő}$-$Q_{Makó}$	1629	60	1689	490.5	363.5	376.5	139
	$Q_{Makó}$/Q_{Szeged}	0.51	0.06	0.57	0.23	0.09	0.22	0.20

[1] *Multiple modes exist. The smallest value is shown.*
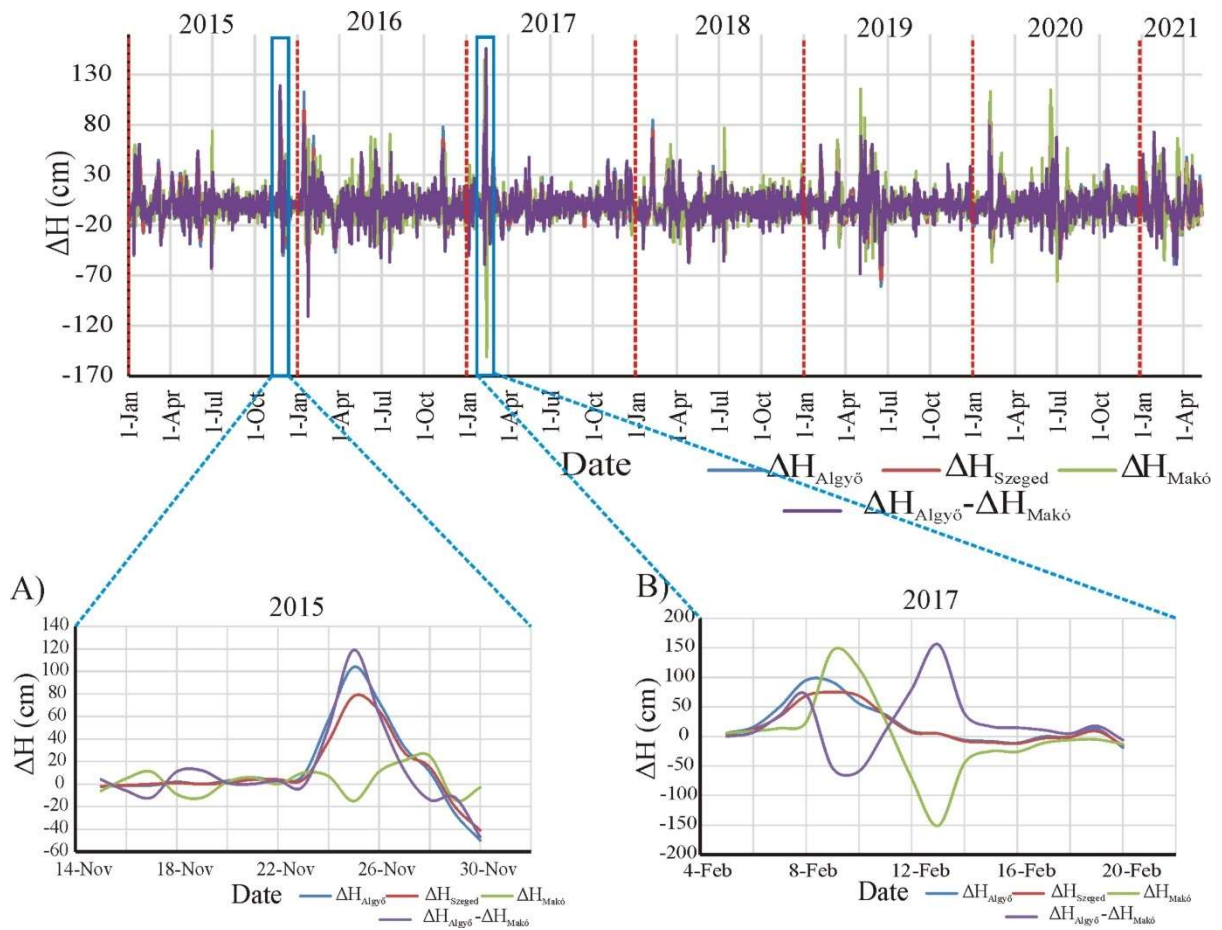
Figure A3. Daily water level change (ΔH) at the three gauging sites (i.e., Algyő, Szeged, and Makó) along with the absolute difference in the ΔH between the Tisza (at Algyő) and Maros (at Makó) ($\Delta H_{Algyő}$-$\Delta H_{Makó}$), throughout the study period (2015–2021). Close-up of the 2015 (A) and 2017 (B) floods, as an example, for more clarification.

Figure A4. Heat maps representing the lateral coverage (%) of the Tisza water (TW) (A), Maros water (MW) (B), and mixture (MIX) (C), across five transects (T1–T5) in the confluence area. These percentages were obtained by analyzing 143 Sentinel-2 images (2015–2021).

137

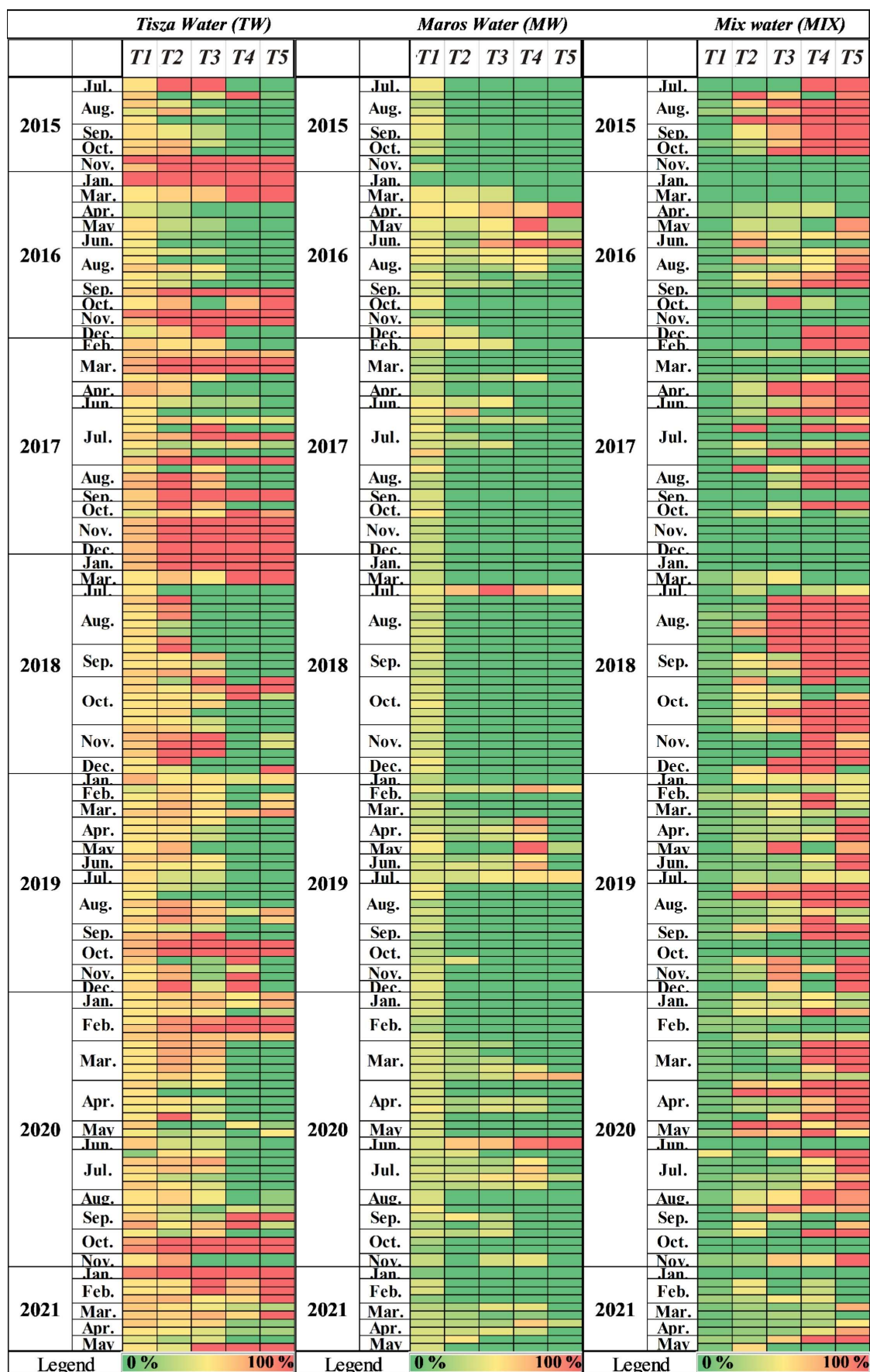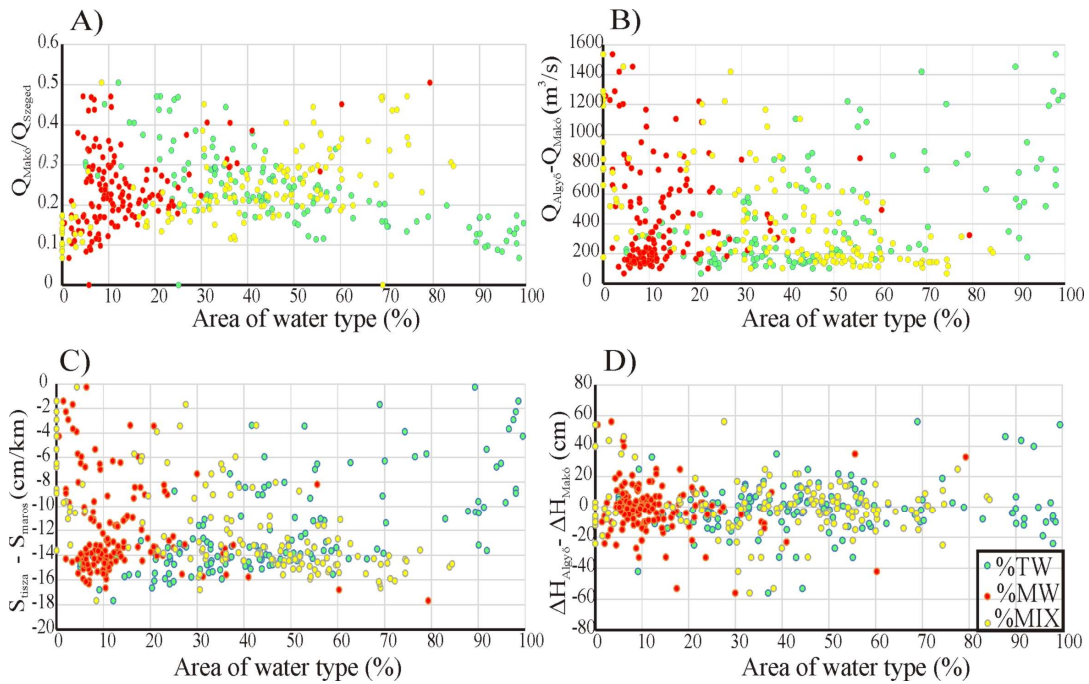Figure A5. The relationship between the areal percentage of Tisza water (TW), Maros water (MW) and mixture (MIX) and hydrological parameters in both rivers, including discharge ratio ($Q_{Makó}/Q_{Szeged}$) (A), discharge difference ($Q_{Algyő}-Q_{Makó}$) (B), slope difference ($S_{Tisza}-S_{Maros}$) (C) and daily water stage difference between rivers ($\Delta H_{Algyő}-\Delta H_{Makó}$) (D).

Table A3. The Spearman's rank correlation coefficient (ρ) among water stage (H), surficial suspended sediment (SS), and microplastic (MP) concentrations during various hydrological conditions (A) and flood phases (B) in Mindszent site (May 2021–May 2023).

A)	**Hydrological periods**			B)	**Flood phase**		
	Low stage	**Minor flood**	**Medium flood**		**Rising**	**Peak**	**Falling**
Parameter	*Surficial SSC*	*Surficial SSC*	*Surficial SSC*	*Parameter*	*Surficial SSC*	*Surficial SSC*	*Surficial SSC*
H	0.16 ($p = 0.356$)	0.49 ($p = 0.009$)	0.56 ($p < 0.001$)	*H*	0.67 ($p < 0.001$)	0.81 ($p = 0.005$)	0.61 ($p <0.001$)
	MP	*MP*	*MP*		*MP*	*MP*	*MP*
H	0.31 ($p = 0.02$)	0.34 ($p = 0.077$)	0.1 ($p = 0.471$)	*H*	0.16 ($p = 0.435$)	0.83 ($p = 0.003$)	0.16 ($p = 0.278$)
	Surficial SSC	*Surficial SSC*	*Surficial SSC*		*Surficial SSC*	*Surficial SSC*	*Surficial SSC*
MP	-0.02 ($p = 0.883$)	0.462 ($p = 0.013$)	0.46 ($p <0.001$)	*MP*	0.6 ($p = 0.001$)	0.81 ($p = 0.005$)	0.43 ($p = 0.003$)

Table A4. The statistical difference in the surficial suspended sediment concentration (SSC) among different hydrological periods, based on the Kruskal-Wallis and post hoc tests.

Hydrological periods	**Test statistic**	**Std. error**	**Std. test statistic**	**Sig. (p)**	**Adj. sig.[a]**
low stage–minor flood	-18.93	9.36	-2.02	**.043**	.129
low stage–medium flood	-52.46	7.67	-6.84	**.000**	.000
minor flood–medium flood	33.53	9.42	3.56	**.000**	.001

[a] Significance values have been adjusted by the Bonferroni correction for multiple tests.

The significance level is 0.05.

The statistical difference in the microplastic (MP) concentration among different hydrological periods, based on the Kruskal-Wallis and post hoc tests.

Hydrological periods	Test statistic	Std. error	Std. test statistic	Sig. (*p*)	Adj. sig.[a]
low stage–minor flood	-34.51	9.36	-3.69	**.000**	.001
low stage–medium flood	-47.01	7.67	-6.13	**.000**	.000
minor flood–medium flood	12.49	9.42	1.33	**.185**	.554

[a] Significance values have been adjusted by the Bonferroni correction for multiple tests.
The significance level is 0.05.

Table A6. The statistical difference in the surficial suspended sediment concentration (SSC) among different flood phases, based on the Kruskal-Wallis and post hoc tests.

Flood phases	Test statistic	Std. error	Std. test statistic	Sig. (*p*)	Adj. sig.[a]
rising–falling	-9.66	5.78	-1.67	**.095**	.568
peak–falling	-29.20	8.79	-3.32	**.001**	.005
peak–rising	19.55	9.24	2.12	**.034**	.206

[a] Significance values have been adjusted by the Bonferroni correction for multiple tests.
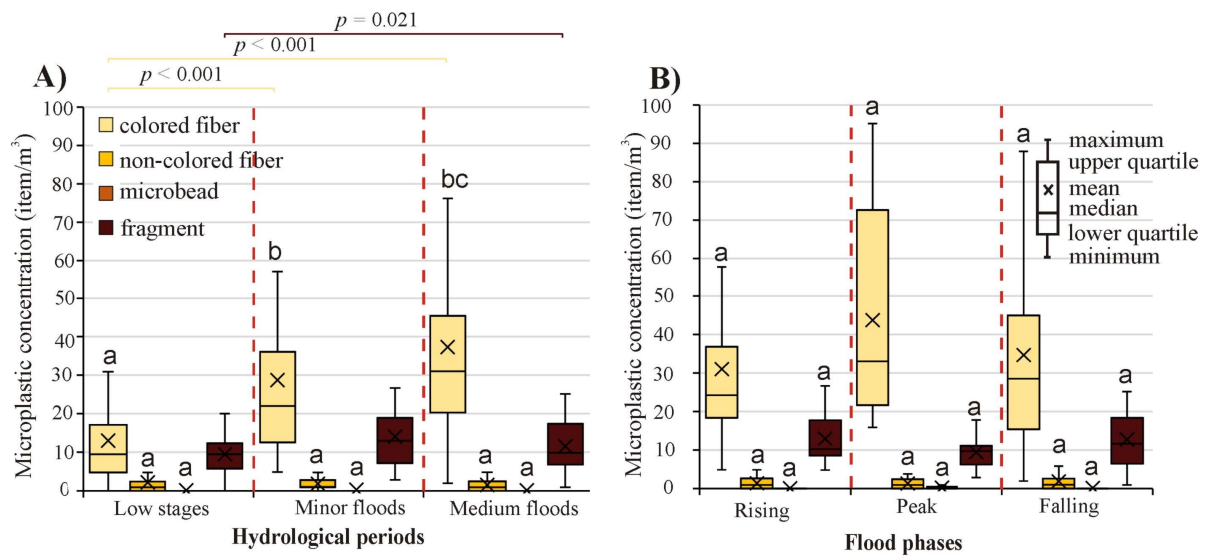The significance level is 0.05.

Figure A6. Distribution of various microplastic (MP) morpho-types during various hydrological periods (A) and flood phases (B) in Mindszent (May 2021–May 2023). Alphabetical letters indicate the statistical differences.

Table A7. The statistical difference in the colored fiber among different hydrological periods, based on the Kruskal-Wallis and post hoc tests.

Hydrological periods	Test statistic	Std. error	Std. test statistic	Sig. (*p*)	Adj. sig.[a]
low stage–minor flood	34.826	9.359	3.721	**.000**	.001
low stage–medium flood	51.556	7.665	6.726	**.000**	.000
minor flood–medium flood	16.729	9.415	1.777	**.076**	.227

[a] Significance values have been adjusted by the Bonferroni correction for multiple tests.
The significance level is 0.05.

Table A8. The statistical difference in the fragment among different hydrological periods, based on the Kruskal-Wallis and post hoc tests.

Hydrological periods	Test statistic	Std. error	Std. test statistic	Sig. (p)	Adj. sig.[a]
low stage–minor flood	13.523	7.664	1.765	**.078**	.233
low stage–medium flood	21.551	9.357	2.303	**.021**	.064
minor flood–medium flood	-8.029	9.413	-.853	**.394**	1.000

[a] Significance values have been adjusted by the Bonferroni correction for multiple tests.
The significance level is 0.05.

Table A9. Statistical difference in the surficial suspended sediment concentration (SSC) among the five sections (S1–S5) of the Tisza River in 2021 based on the Tukey post hoc test.

Sections	Mean difference	Std. error	Sig. (p)	95% Confidence interval	
				Lower bound	Upper bound
S1–S2	10.20[*]	2.47	**.004**	2.83	17.56
S1–S3	6.83	2.41	**.067**	-.35	14.01
S1–S4	8.68[*]	2.33	**.010**	1.72	15.64
S1–S5	13.97[*]	2.47	**.000**	6.60	21.33
S2–S3	-3.36	1.78	**.357**	-8.69	1.96
S2–S4	-1.51	1.68	**.894**	-6.52	3.50
S2–S5	3.77	1.86	**.292**	-1.79	9.33
S3–S4	1.85	1.59	**.772**	-2.89	6.60
S3–S5	7.13[*]	1.78	**.005**	1.80	12.46
S4–S5	5.28[*]	1.68	**.036**	.26	10.30

* The mean difference is significant at 0.05 level.

Table A10. Statistical difference in the surficial suspended sediment concentration (SSC) among the five sections (S1–S5) of the Tisza River in 2022, based on the Tukey post hoc test.

Sections	Mean difference	Std. error	Sig. (p)	95% Confidence interval	
				Lower bound	Upper bound
S1–S2	26.64[*]	6.52	**.004**	7.19	46.08
S1–S3	15.87	6.37	**.131**	-3.10	34.85
S1–S4	23.73[*]	6.16	**.007**	5.35	42.10
S1–S5	19.20	6.52	**.054**	-.24	38.64
S2–S3	-10.76	4.72	**.191**	-24.84	3.30
S2–S4	-2.90	4.44	**.964**	-16.16	10.34
S2–S5	-7.44	4.93	**.569**	-22.14	7.26
S3–S4	7.85	4.21	**.366**	-4.69	20.41
S3–S5	3.32	4.72	**.953**	-10.74	17.40
S4–S5	-4.53	4.44	**.844**	-17.78	8.72

* The mean difference is significant at 0.05 level.

Table A11. Statistical difference in the microbeads among the five sections (S1–S5) of the Tisza River in 2021, based on the Kruskal-Wallis and post hoc tests.

Sections	Test statistic	Std. error	Std. test statistic	Sig. (p)	Adj. sig.[a]
S1–S2	.00	6.05	.00	**1.00**	1.00
S1–S3	-2.66	5.90	-.45	**.652**	1.00
S1–S4	-12.75	5.72	-2.22	**.026**	.38
S1–S5	-12.80	6.05	-2.11	**.034**	.51
S2–S3	-2.66	4.38	-.60	**.543**	1.00
S2–S4	-12.75	4.12	-3.09	**.002**	.03
S2–S5	-12.80	4.57	-2.79	**.005**	.07
S3–S4	-10.08	3.90	-2.58	**.010**	.14
S3–S5	-10.13	4.38	-2.31	**.021**	.31
S4–S5	-.05	4.12	-.01	**.990**	1.00

[a] Significance values have been adjusted by the Bonferroni correction for multiple tests.
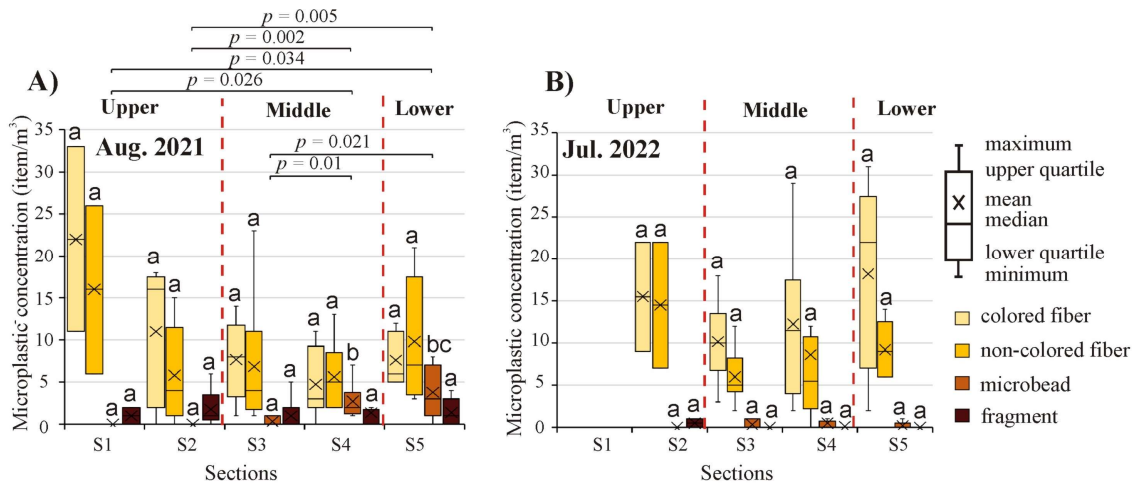The significance level is 0.05.

Figure A7. Distribution of the microplastic (MP) morpho-types at the five sections (S1–S5) of the Tisza River based on 26 sites in 2021 (A) and 21 sites in 2022 (B). Alphabetical letters refer to statistical differences.
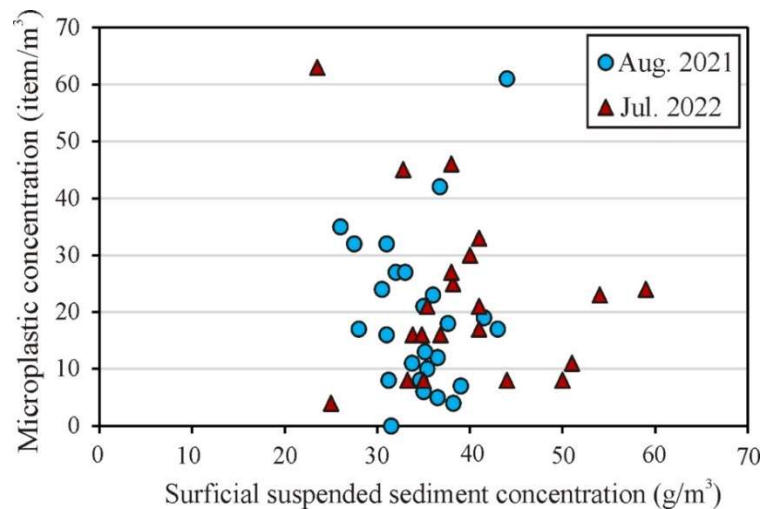

Figure A8. Graphical representation of the longitudinal correlation between surficial suspended sediment (SS) and microplastic (MP) concentrations in the Tisza in August 2021 and July 2022.

141

Statement of supervisors

We, Dr. Tímea Kiss and Dr. Ferenc Kovács, as supervisors, declare that the thesis written by *"Ahmed Mohsen Abdelsadek Metwaly"*, titled *"A multi-scale investigation of sediment and plastic pollution transport in the Tisza River applying remote sensing and machine learning: A hydrological perspective"* is his own writing prepared under our supervision. The candidate's contribution to the results used in the discussion of the thesis is approved. We also declare that the thesis meets the formal and professional requirements of the Doctoral School of Geosciences of the University of Szeged and the Faculty of Science and Informatics/Department of Geoinformatics, Physical and Environmental Geography. In light of these considerations, we endorse the submission of his thesis.

Szeged, January 3rd, 2024

Dr. Tímea Kiss ....

....

Dr. Ferenc Kovács